Lanthanide Doped Nanoparticles for Low Threshold Upconverting Microlasers

By

Yunfei Shang

Institute for Biomedical Materials & Devices

School of Mathematical and Physical Sciences, Faculty of Science

Supervisors:

Prof. Jiajia Zhou & Prof. Dayong Jin

This thesis is presented for the degree of Doctor of Philosophy

November, 2022

Certificate of Original Authorship

I, Yunfei Shang, declare that this thesis, submitted in fulfilment of the requirements for the award of Doctor of Philosophy, in the School of Mathematical and Physical Sciences, Faculty of Science at the University of Technology Sydney.

This thesis is wholly my own work unless otherwise reference or acknowledged. In addition, I certify that all information sources and literature used are indicated in the thesis.

This document has not been submitted for qualifications at any other academic institution. This thesis is the result of a Collaborative Doctoral Research Degree program with Harbin Institute of Technology as part of a Collaborative Doctoral Training Program.

This research is supported by the Australian Government Research Training Program.

Signature Production Note:
Signature removed prior to publication.

Date 17th, November, 2022

Acknowledgments

It is really a meaningful and unforgettable experience for me to study at University of Technology Sydney (UTS). As a cotutelle PhD student at University of Technology Sydney (UTS) and Harbin Institute of Technology (HIT), I have been assisted by many kind-hearted people during my PhD period. Herein, I would like to express my sincere gratitude to all of them.

Firstly, I would like to extend my deepest gratitude to my supervisor Prof. Dayong Jin and Prof. Jiajia Zhou, who give me the valuable opportunity of cotutelle PhD project. It’s a great honor and pleasure to be Prof. Dayong Jin and Prof. Jiajia Zhou’s PhD student. Prof. Jin is always considerate, patient, encouraging, and has great personal charisma. His self-motivated and optimistic attitude to life really infected us, and his passion and insights on scientific research inspired me. I learned a lot from Prof. Jin’s research thinking, and improved my ability on how to conduct research project logically. I really appreciate his sincere help and thoughtful suggestions on my PhD project and research career development.

Meanwhile, I also would like to express my heartfelt thanks to my supervisor Prof. Jiajia Zhou, for her precious supervision and guidance through all the years I studied at UTS. She helped me a lot with research project design, results discussion and we overcame the challenges in my research together. Her tender care and warm encouragement were of vital importance to my growth. I thank her for the great support in my experiments and daily life.

Next, I would like to thank Prof. Fan Wang for his guidance on optical systems. He is a man of deep learning, and his professional advice on the related optical issue of my research really helps a lot. Also, I would like to thank Dr. Shihui Wen, Dr. Xiaoxue Xu, Dr. Qian Su, Dr. Gungun Lin for their help suggestions.

I would also like to express my thanks to our group members and lab colleagues, who

have given me great help. They are Dr. Chaohao Chen, Dr. Yongtao Liu, Dr. Chao Mi, Dr. Zhiguang Zhou, Dr. Baolei Liu, Dr. Xuchen Shan, Dr. Yuan Liu, Dr. Ming Guan, Dr. Du Li, Dr. Wei Ren, Dr. Hao He, Dr. Jiayan Liao, Dr. Sheng Mei, Dr. Guochen Bao, Dr. Guocheng Fang, Dr. Yinghui Chen, Dr. Guan Huang, Dr. Xiangjun Di, Dr. Dejiang Wang, Dr. Lei Ding, Dr. Chi Li, Dr. Huan Wu, Dr. Le Zhang. Thank them a lot for beneficial discussions and helps in both research and daily life. I really appreciate their supports and friendship.

Special thanks to school manager Elizabeth Gurung Tamang, lab manager Katie McBean, and Ronald Shimmon for their technical support. Thanks to Jing Zhao, Chris O'Neill and the related staff who helped me for the cotutelle PhD project. Especially, when I was stuck in China due to the Covid-19. I could not image how to continue this project without their kind helps.

I give my deep appreciation to my family for endless love and great support during my study. Words fail me when I want to express my gratitude. I hope they are healthy and happy.

Finally, I would like to acknowledge the China Scholarship Council Scholarships and UTS for providing me with PhD scholarship and research opportunities.

Abstract

Lasers with small physical dimension at the micro or nanoscale enable emerging applications of optoelectronic nanoscience and nanotechnologies, due to their advantages of miniatured size. However, the reduced cavity size requires high pumping power to achieve lasing emissions, due to the increased optical losses. Moreover, the current gain media, including organic dyes, inorganic semiconductors, quantum dots, are limited by poor stability under air, thermal, and long-time pumping conditions. Lanthanide doped upconversion nanoparticles with ultra-long radiative lifetimes, which is of benefit to the excited energy accumulation for population inversion, are developed for micro lasing emissions. The outstanding frequency conversion properties of upconversion nanoparticles provide numerous opportunities for fantastic applications. But the ultrahigh pumping threshold is still a big challenge. Herein, this thesis mainly focuses on the design and construction of efficient upconverting gain media for continuous wave (CW) pumped room temperature low threshold upconversion lasing emission.

Chapter 1 summaries the basic mechanism of lanthanide doped upconversion nanoparticles and microlasers by reviewing the advances of this field. Upconverting lasers including random laser, whispering gallery mode (WGM)/fabry-perot (FP) cavity modulated lasers and photon lattice/plasmonic cavities related lasers are discussed and analyzed. The key elements, containing efficient upconversion gain media, coupling strategies, optical losses restraining, for low threshold upconverting lasers are highlighted. Then, the major tasks of this thesis are outlined.

Chapter 2 provides a detailed introduction of materials and methods used for constructing upconverting gain media, equipment, instruments and home-built optical set-ups for sample characterization.

In Chapter 3, a strategy for excited state energy accumulation is explored. The doping concentration dependence of cross-relaxation process is investigated. Doping of 20 mol. % Yb^{3+} and 2 mol. % Tm^{3+} is identified as the appropriate condition to achieve population inversion at relatively low power density. Then, an efficient coupling method driven by electrostatic force is developed to construct a WGM microlaser. Finally, systematic characterizations are carried out for the confirmation and exploration of upconverting lasing emission, and a CW pumped threshold as low as

~150 W/cm^2 is achieved.

Chapter 4 is aim to investigate another key parameter for lasing emission: the scattering effects caused by size of upconversion gain media. Upconversion nanoparticles with the same dopants but varied size are used to explore the lasing emission performance. It verifies that the increased size leads to stronger scattering, which hinders the coupling of emission at the surface and increases the leaking of light inside the microcavity. Then, a ~43 nm $NaYF_4$:20% Yb^{3+},2% Tm^{3+} single nanoparticle with bright emission is further employed to couple with microcavity for lasing emission. The narrow FWHM of ~0.45 nm and high Q factor confirm the negligible scattering from single nanoparticle coupling strategy.

Chapter 5 further explore the possibility of upconversion nanoparticles doped with high concentration sensitizer for low threshold lasing emission. A sandwich structured core-shell upconversion nanoparticle is employed. Due to the increased Yb^{3+} sensitizers and shorted distance between sensitizer and emitter, the pumping threshold of lasing emission (@800 nm band) is lowered from ~2 kW/cm^2 to ~180 W/cm^2. What's more, the temperature dependent features of lasing emission, including blue shift (~ 0.1 nm/°C), is explored for in-situ temperature sensing. And microlasers with white emission are achieved by employing novel energy migration modulated $NaGdF_4$:40%Yb^{3+},2%Tm^{3+}@$NaGdF_4$:15%Tb^{3+} upconversion gain media.

In Chapter 6, a brief summary of the results is presented. Challenges, prospects for further regulation and applications of upconverting microlasers are discussed.

Keywords: lanthanide doped gain media, cross-relaxation, energy accumulation, population inversion, CW pumped low threshold upconverting microlaser, white lasing emission

Format of Thesis

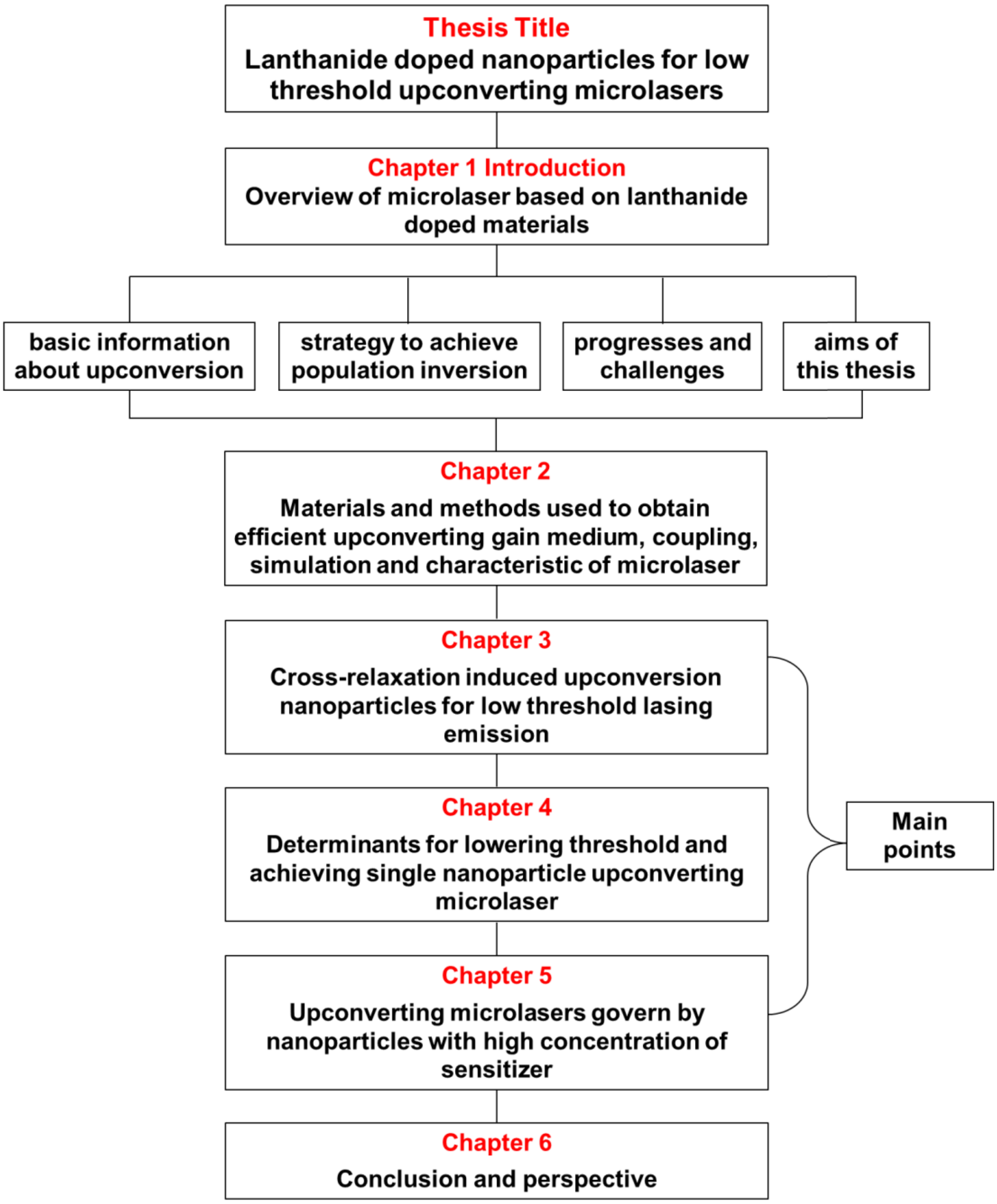

List of Publications

Published papers:

1. **Yunfei Shang**, Jiajia Zhou*, Yangjian Cai, Fan Wang, Angel Fernandez-Bravo, Chunhui Yang, Lei Jiang, Dayong Jin. Low threshold lasing emissions from a single upconversion nanocrystal. ***Nature Communications***, 2020, 11, 6156.
2. **Yunfei Shang**, Tong Chen, Tianhui Ma, Shuwei Hao*, Weiqiang Lv*, Dechang Jia, Chunhui Yang. Advanced lanthanide doped upconversion nanomaterials for lasing emission. ***Journal of Rare Earths***, 2022, 40, 5,687-695.
3. **Yunfei Shang**, Shuwei Hao*, Wei Shao, Tong Chen, Yuyan Zhu, Chunhui Yang*. Tuning the Upconversion Luminescence of Cubic $KMnF_3$:Yb^{3+}/Er^{3+} Nanocrystals through Inert Lanthanide Ions Doping. ***Journal of Materials Chemistry C***, 2020 ,8, 2847-2851.
4. **Yunfei Shang**, Qi Han, Shuwei Hao*, Tong Chen, Yuyan Zhu, Zhongyang Wang*, Chunhui Yang. Dual-mode Upconverting Nanoprobe Enables Broad-Range Thermometry from Cryogenic to Room Temperature. ***ACS Applied Materials & Interfaces***, 2019, 11, 45, 42455-42461.
5. **Yunfei Shang**, Shuwei Hao*, Weiqiang Lv, Tong Chen, Li Tian, Zuotao Lei, Chunhui Yang*. Confining Excitation Energy of Er^{3+}-sensitized Upconversion Nanoparticles through Introducing Various Energy Trapping Centers. ***Journal of Materials Chemistry C***, 2018, 6(15): 3869-3875.
6. **Yunfei Shang**, Guochen Bao, Jiajia Zhou, Wong KaLeung, Chunhui Yang, Dayong Jin*. Lanthanide-Doped Upconversion Luminescent Materials for Point of Care Diagnosis. ***Journal of the Chinese Rare Earth Society***, 2018, 36(2): 129-146.
7. Tong Chen, **Yunfei Shang***, Yuyan Zhu, Shuwei Hao*, Chunhui Yang. Activators Confined Upconversion Nanoprobe with Near-Unity FRET Efficiency for Ultrasensitive Detection. ***ACS Applied Materials & Interfaces***, 2022, 14, 17, 19826-19835.
8. Li Tian, **Yunfei Shang**, Shuwei Hao*, Qi Han, Tong Chen, Weiqiang Lv, Chunhui Yang*. Constructing a “Native” Oxyfluoride Layer on Fluoride Particles for Enhanced Upconversion Luminescence. ***Advanced Functional Materials***, 2018, 28(48): 1803946.
9. Tong Chen, **Yunfei Shang**, Shuwei Hao*, Li Tian, Yuedan Hou, Chunhui Yang*. Enhancement of dye sensitized solar cell efficiency through introducing concurrent upconversion/downconversion core/shell nanoparticles as spectral converters. ***Electrochimica Acta***, 2018, 282: 743-749.
10. Tong Chen, **Yunfei Shang**, Shuwei Hao*, Chongqiang Zhu, Zuotao Lei, Xiang Wang, Weiqiang Lv*, Chunhui Yang*. Reproducible single-droplet multiplexed detection through excitation-encoded tri-mode upconversion solid sensors.

Chemical Engineering Journal, 2022, 430, 4,131242.

11. Shuwei Hao, **Yunfei Shang**, Yuedan Hou, Tong Chen, Weiqiang Lv*, Pingan Hu, Chunhui Yang*. Enhance the performance of dye-sensitized solar cells by constructing upconversion-core/semiconductor-shell structured $NaYF_4$:Yb,Er @BiOCl microprisms. ***Solar Energy***, 2021,244: 563-568.
12. Aditya Tripathi, Sergey Kruk*, **Yunfei Shang**, Jiajia Zhou, Ivan Kravchenko, Dayong Jin, Yuri Kivshar. Topological nanophotonics for photoluminescence control, ***Nanophotonics***, 2021, 10(1), 435-441.
13. Tong Chen, Shuwei Hao*, Amina Azimbay, **Yunfei Shang**, Qingli Pi, Yuedan Hou, Chunhui Yang*. Optimizing concurrent extension of near-infrared and ultraviolet light harvesting of dye sensitized solar cells by introducing sandwich-nanostructured upconversion-core/inert-shell/downconversion-shell nanoparticles. ***Journal of Power Sources***, 2019, 430: 43-50.
14. Shuwei Hao, Hao Fu, **Yunfei Shang**, Vladimir Artemyev, Andrey Smirnov, Chongqiang Zhu, Zuotao Lei, Lili Zhao*, Chunhui Yang*. Numerical Simulation for Growing Large-scale and High-quality Zinc Germanium Phosphide Crystals. ***Journal of Crystal Growth***, 2021, 126354.
15. Taiguang Jin, Shuwei Hao *, **Yunfei Shang**, Zuotao Lei, Chunhui Yang. Recent Trends in Elpasolite Single Crystal Scintillators for Radiation Detection. ***Crystals***, 2022, 12(7), 887.

(These papers are related to my PhD thesis in UTS and home university (HIT) during the period from 2018 to 2022)

Conferences:

1. **Yunfei Shang**, et al. Low threshold lasing emissions from a single upconversion nanocrystal. UPCON2021, online.
2. **Yunfei Shang**, et al. Non-contact Cryogenic Thermometry Based on Upconverting Nanoprobes. 2020 Photonics Online Meetup.
3. **Yunfei Shang**, et al. Efficient lanthanide doped upconversion nanocrystals for low threshold microlaser. The 8th Conference on Luminescence Properties of Doped Nanomaterials, Changchun, China, 2021.

List of Abbreviations

A	Activator
CR	Cross-relaxation
CSU	Cooperative sensitization upconversion
CW	Continuous wave
DBR	Distributed Bragg reflector
DI water	Deionized water
EDS	Energy dispersive spectroscopy
EMCCD	Electron multiplying charge coupled device
EMU	Energy migration-mediated upconversion
ELNPs	Energy-looping nanoparticles
ESA	Excited state absorption
ETU	Energy transfer upconversion
FDTD	Finite difference time domain
FON	Fiber optic communications
FP	Fabry-Pérot
FSR	Free spectral range
FWHM	Full width at half-maximum
HMM	Hyperbolic meta-materials
L	Ladders like ions
Ln	Lanthanide ions
M	Migrators
NIR	Near infrared
OA	Oleic Acid
ODE	1-Octadecene
PA	Photon avalanche
PLQY	Photoluminescence quantum yield
PS	Polystyrene

Q	Quality factor
QDs	Quantum dots
R	Radius
S	Sensitizer ions
SEM	Scanning electron microscopy
SPAD	Single photon counting avalanche diode
TE	Transverse electric
TEM	Transmission electron microscope
TM	Transverse magnetic
UC	Upconversion
UCNPs	Upconversion nanoparticles
UV	Ultraviolet
WGM	Whispering gallery mode
3D	3 Dimensional

Table of Contents

Chapter 1 Introduction

1.1 Microlasers based on lanthanide doped materials

Laser is an abbreviation for light amplification by stimulated emission of radiation. A laser device can emit ultra-strong light through a process of optical amplification based on the inside stimulated emission of electromagnetic radiation[1]. Up to now, lasers have been developed into multiple sizes, forms, colors/wavelengths, levels of power, *etc.*[2-7]. Based on these, lasers have been widely employed for diverse applications ranging from intracellular sensing to long distance communication, laser surgery in hospital, bar code scanning in shopping store, and playing music, movies, and virtual reality at home, since the first invention of ruby laser in 1960 by Maiman[8-10]. Driven by new demand for the emerging technologies and applications, such as intracellular sensing[11-13], on-chip integrated devices[14, 15], fiber optic communications (FON)[16], high-density data storage[17], micro-laser display[18-20], lasers with a size at microscale or nanoscale have drawn considerable attentions in the last two decades[7, 21]. Due to the advantages of micro/nanometer leveled physical dimension, mico/nanolasers are promising in the application of next generation nanophotonic and optoelectronics[12, 21].

There are three elements to construct a laser including gain medium, optical resonator and pumping source, in which the former two are crucial components. The structures of resonator such as Fabry-Pérot (FP) cavity, whispering-gallery mode (WGM) cavity and distributed feedback (DFB) cavity, are used to confine the light with special wavelength and provide optical feedback through resonance. The gain medium, such as inorganic semiconductors, quantum dots, organic dyes, organic polymers, lanthanide doped materials, can generate the needed optical gain under the excitation of pumping source. However, due to the size induced optical losses, the pumping threshold would increase sharply as the cavity size reduces to micro/nano scale. Moreover, low temperature is needed to relieve the high pumping power induced thermal effect[22, 23]. The harsh pumping requirement, including the fs or ns pumping source to supply high power density, ultra-low temperature, water-free and oxygen-free conditions, etc., have become one of the bottlenecks for the widespread applications of micro/nano lasers.

Due to the advanced photoelectric property and relatively high refractive index, traditional inorganic semiconductors such as ZnO[24, 25], GaAs[26, 27], GaN[14, 28], and CdS[3, 29] have been widely employed as gain media for microlasers. However, the complex fabrication process, poor spectrum tunability, strong reabsorption and lack of excitons at room temperature impeded the development of inorganic semiconductors[30-32]. Organic dyes/molecules, polymers and semiconductors with large absorption cross-section and broad-spectrum tunable band have also been confirmed to be excellent gain media for lasing emissions[33, 34]. Unfortunately, the photostability, broad emission band, large reabsorption cross section and other issues are needed to be solved to lower the lasing threshold and relieve the limitation of high-power pulsed pumping laser (fs or ns). Alternatively, quantum dots (QDs) with high photoluminescence quantum yield (PLQY) are attractive for lasing applications[35-37]. However, the intrinsic photo-blinking and chemical, thermal and photostability limit the practical applications of QDs-based microlasers[38]. It is still a big challenge to design efficient gain media for widespread applications.

Lanthanide-doped nanomaterials with unique optical properties have captured increasing interests for micro/nanolasers in recent years. The trivalent lanthanide ions possess a $4f^n5s^25p^6$ electronic structure with 14 available orbitals ($0 < n < 14$), offering 14 possible electronic group configurations[39]. The quantum interaction of involved electrons endows lanthanide elements with abundant energy levels covering a broad spectrum range from NIR, visible to ultraviolet (UV)[40-42]. This allows versatile and diverse optical pumping strategies for lasing actions in terms of abundant output wavelengths. The abundant energy levels and long lifetime of lanthanide ions favor the process of excited energy accumulation and thus facilitate population inversion, which is a prerequisite for lasing emission[22, 43]. Besides, the large anti-/Stokes shifted emissions from lanthanides provide a low detection background, which are of high potential in biological detection[43-45].

Lanthanide doped upconversion materials are potential gain media for microlasers with the output wavelengths in the near infrared (NIR) to visible and UV regimes due to their multi ladder-like metastable energy levels and superior optical frequency conversion capability. However, knowledge gaps exist and hinder the development of upconversion laser, which include the mechanism to achieve energy accumulation and population inversion at low pumping power, and how the scattering affects the threshold and linewidth. The current threshold of pumping power for upconversion laser is unsatisfying. Thus, in this thesis, we focus on the construction of low threshold upconverting micro/nanolaser based on efficient upconversion nanocrystals, and to obtain tunable CW pumped room temperature low threshold upconverting microlasers.

1.2 Mechanism of upconversion process

The rare-earth family is comprised of 17 elements, which includes 15 lanthanide elements (from La to Lu) plus the elements of yttrium (Y) and scandium (Sc). The perfect shielding of 4*f* electrons by outer complete 5*s* and 5*p* shells enables electronic transitions to occur with limited influence from the surrounding environment, thus exhibiting high resistance to processes of photobleaching and photochemical degradation. As the symmetries of involved quantum states are identical, the intra-4*f* electronic transitions of lanthanide ions are electric-dipole forbidden, yet can be relaxed due to local-crystal-field-induced intermixing of the *f* states with higher electronic configurations. The primary forbidden nature yields metastable energy levels of lanthanide ions (lifetime can be as long as tens of milliseconds), thus favoring the occurrence of sequential excitations in excited states of a single lanthanide ion as well as permitting favorable ion-ion interactions in excited states to allow energy transfers between two or more lanthanide ions.

Upconversion is a typical nonlinear process that can emit photons with shorter wavelength and higher energy after sequential absorption of two or more photons with lower energy (Figure 1.1a)[46, 47]. Due to the abundant energy levels, lanthanide doped upconversion system exhibit excellent properties with tunable long decay times (from μs to ms)[48-50], broad emissions (from NIR to UV)[51-53], sharp emission peaks[20], large anti-Stokes shift[54, 55], photostability[56, 57], and so on. As shown in Figure 1.1, the upconversion emission color could be tuned in the full spectrum, and there are mainly five basic mechanisms to achieve these upconversion processes, including excited state absorption (ESA), energy transfer upconversion (ETU), photon avalanche (PA), energy migration-mediated upconversion (EMU) and cooperative sensitization upconversion (CSU)[54, 58-62]. Excited state absorption (ESA) takes the form of successive absorption of pump photons by a single ion utilizing the ladder-like structure of a simple multi-level system. Figure 1.1c illustrates a simplified three level system for two sequential photon absorption processes. The ETU process involves at least two types of ions, namely a sensitizer and an activator. In this process, ion I known as the sensitizer (S) is firstly excited from the ground state to its metastable level by absorbing a pump photon; it then successively transfers its harvested energy to the ground state and the first excited state of ion II, known as the activator (A), exciting A to its upper emitting state, which is followed by radiative decay to its ground state. The PA is a looping process that involves an efficient cross relaxation mechanism between in the S ground state and A in the second excited state, resulting in generation of two As in the metastable state. The population of A in the second excited state is created through absorption of laser photons at its metastable state (the first excited state), which is initially populated through non-resonant weak ground state absorption. When the looping process ensues, an avalanche population of A will be created at its metastable state, producing avalanche upconverted luminescence from the emitting state. The generation of PA UC typically occurs above a certain threshold of excitation density. Below the threshold, very little up-converted fluorescence is produced, while the luminescence intensity increases by orders of magnitude above the pump threshold. In addition, the looping nature enables the evoked UC luminescence to be strongly dependent on the laser pump power, especially around the threshold laser power. The lanthanide ions designed for realizing energy migration-mediated upconversion (EMU) comprise four types: the sensitizers (S), the accumulators/ladders (L), the migrators (M), and the activators (A). A sensitizer ion is used to harvest excitation photons and subsequently promotes a neighboring accumulator ion to its excited states. A migrator ion extracts the excitation energy from high-lying energy states of the accumulator, followed by random energy hopping through the migrator ion sublattice and trapping of the migrating energy by an activator ion that produces luminescence by decaying to the ground state. The excitation density for detectable upconversion is typically in the range of 10^{-1}~10^{2} W/cm^{2}. As for the cooperative sensitization upconversion, these two participants refer to different lanthanide dopants (I and II), *e.g.,* Yb^{3+}-Eu^{3+}, Yb^{3+}-Tb^{3+}, and Yb^{3+}-Pr^{3+} ion pairs. Due to the involvement of virtual pair levels during electronic transitions, a lower efficiency was typically observed in CSU (10^{-6}) than that of ESA and ETU processes[63-65]. And the typical upconversion emission colors (visible range) and related energy levels is shown in Figure 1.1b and Figure 1.2[66].

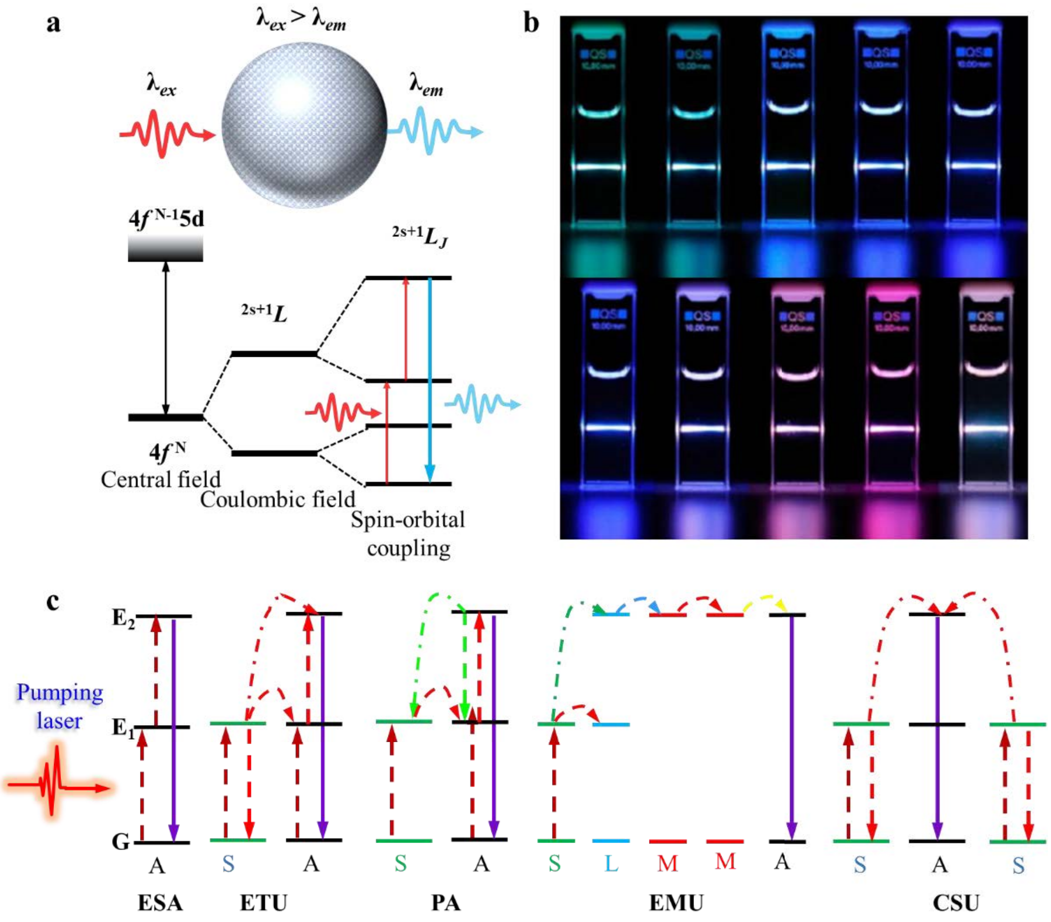

Figure 1.1 Schematic illustration of upconversion processes: (a) Energy level diagram of photon upconversion inside 4f orbital. (b) Typical photographs of upconversion emissions. (**c**) Typical upconversion processes, including Excited state absorption (ESA), Energy transfer upconversion (ETU), Photon avalanche (PA), Energy migration-mediated upconversion (EMU) and cooperative sensitization upconversion (CSU).

Lanthanide doped upconversion materials typically consist of an appropriate dielectric host matrix and doped Ln^{3+} ions that are dispersed as the guest in the lattice of the host matrix. Host materials with low phonon energy are able to produce upconversion luminescence at high efficiency, as multiphonon-assisted nonradiative relaxations between the closely spaced energy levels can be minimized, thus yielding increased lifetime of intermediate energy levels[60, 65, 67]. Investigated low phonon energy host materials typically include fluorides, chlorides, iodides, and bromides, while high phonon energy host materials such as silicates, borates, and phosphates are also under study[55, 61]. In general, host materials with low phonon energy are hygroscopic, while the high phonon energy ones are robust even under acute environment (strong acid, base, high temperature, *etc.*). Yet, the type of fluoride host material is unique and has attracted a lot of attentions in recent years. This is because fluoride host lattice not only has low phonon energy but also shows excellent chemical stability. In particular, hexagonal $NaYF_4$ lattice is considered to be one of the most efficient host materials to date[54, 68]. Thus, hexagonal $NaYF_4$ based upconversion host is used in the whole thesis.

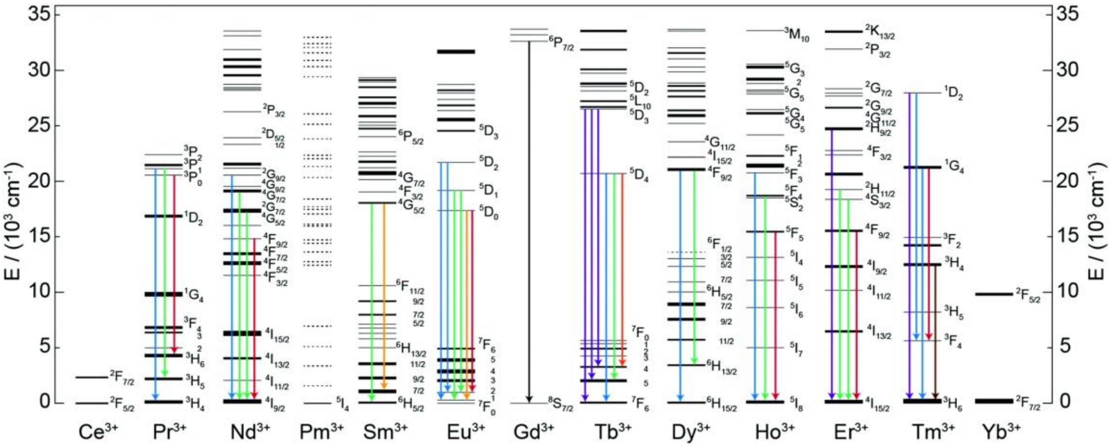

Figure 1.2 Partial energy level diagram of lanthanide ions commonly used to achieve upconversion emission. Adapted with permission from ref[66]

1.3 Modulation of photon distribution

Benefiting from the ladder-like long lifetime energy levels of lanthanide ions, photons can be excited to multiple energy levels through upconversion process. And the excited state energy distribution of each energy level would greatly affect the realization of population inversion, which is the precondition for lasing emission[69-72]. It is imperative to tune the photons distribution and achieve energy accumulation at specific energy levels, and thus achieve population inversion at a low power density. Here, several strategies to modulate the excited photons distribution are discussed.

1.3.1 Excitation power modulated photon distribution

It is well known that the upconversion is a kind of nonlinear process, which involves multi-photon absorption to achieve the emissions from the excited states with higher energy[54]. The long lifetime metastable energy levels make it possible for excited state ions to jump to an even higher excited state after absorbing energy from nearby sensitizers. Normally, the emission intensity (I) is proportional to nth power of the excitation power ($I \propto P^n$) at low excitation power density range, especially for upconverion process that linear decay dominates[73]. And the photon numbers (*n*) involved in each emission process varies in different doping systems and would be slightly power density dependent. Thus, it is straightforward to modulate excited photon distribution by changing excitation power density.

As shown in Figure 1.3, there are mainly seven emission peaks (802 nm, 782 nm, 744 nm, 650 nm, 514 nm, 475 nm and 450 nm) of Yb^{3+}/Tm^{3+} co-doped $NaYF_4$ nanocrystals, which are rising from various transition processes[56, 74, 75]. As reported by Jin's group[76], the dominant emission attributed to the transition from $^3H_4$ to $^3H_6$ at low power density, while the multi-photon process related short wavelength emissions (450, 475 nm *etc.*) increase rapidly at high power density. Similarly, in the Yb^{3+}/Er^{3+} co-doped $NaYF_4$ nanocrystals, Yb^{3+} ions are excited by 980 nm laser firstly, and then transfer the excited energy to adjacent Er^{3+} ions. After absorbing several photons energy from Yb^{3+} ions, blue, red and green upconversion emissions can be observed, correlating to the transitions from $^2H_{9/2}$, $^4F_{9/2}$, and $^2H_{11/2}$ ($^4S_{3/2}$) to ground state ($^4I_{15/2}$)[46, 77-79]. As shown in Figure 1.3 e and f, the emission ratio of green to red reduces as the increase of power density[80]. This typical nonlinear upconversion phenomenon has been widely reported and demonstrated in various doping systems[78, 80-87]. Although it is a powerful strategy to modulate the photons distribution of each energy level by adjusting the excitation power, it is not suitable for achieving popular inversion and lasing emissions at low power density. The power density needed for achieving high excited energy state distribution is almost very high, which is antithetical for the aim of realizing lasing emissions at low power density.

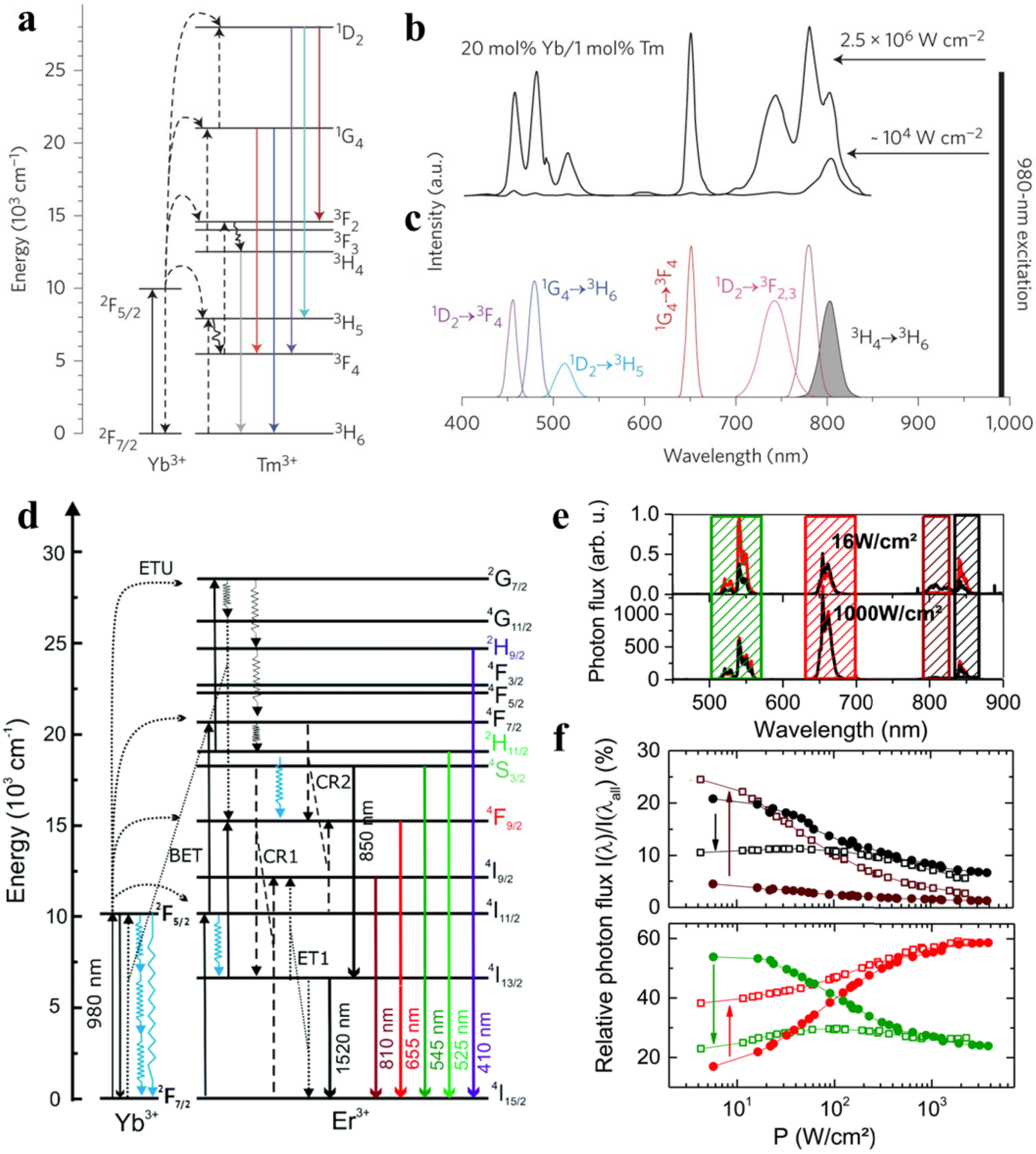

Figure 1.3 Typical power dependent upconversion processes. (**a**) Simplified energy-level scheme of NaYF$_4$:Yb^{3+}/Tm^{3+} nanocrystals indicating major upconversion processes. Dashed lines indicate non-radiative energy transfer, and curved arrows indicate multiphonon relaxation. (**b**) Typical evolution of spectra for 1 mol% Tm^{3+} as a function of excitation, showing substantial growth of emissions from the ^{1}G$_4$ and ^{1}D$_2$ levels with increasing excitation from 1 × 10^4 W cm^{-2} to 2.5 × 10^6 W cm^{-2}. (**c**) Decomposition of the spectra into individual Gaussian peaks. Integrated intensities are given by I_λ where λ is the peak wavelength. Different transitions are indicated by the colours shown in the energy-level scheme in (**a**). For example, the shaded area represents the ^{3}H$_4$ → ^{3}H$_6$ transitions. (**d**) Energy scheme of Yb^{3+}/Er^{3+} co-doped NaYF$_4$; ET: energy transfer, ETU: energy transfer upconversion, CR: cross relaxation, and BET: back energy transfer. (**e**) Emission spectra of 1,2-distearoyl-sn-glycero-3-phospho-

ethanolamine-N-[methoxy(polythylene glycol) (DSPE)-capped UCNPs in water (black lines) and D_2O (red lines) at low P of *ca.* 16 W cm^{-2} (top) and high P of *ca.* 1000 W cm^{-2} (bottom), respectively. (**f**) Contribution (in percentage) of the integral intensities of the different UC emission bands I (λ) to the overall integral intensity I (λ_{all}) of the UC emission of DSPE-capped UCNPs for the emission bands at up panel 850 nm (black) and 810 nm (brown) and down panel 655 nm (red) and 545 nm (green) in water (open squares) and in D_2O (solid circles), respectively, for P between 10 and 1000 W cm^{-2}. (a-c) are adapted with permission from Ref.[88] (d-f) are adapted with permission from Ref.[80]

1.3.2 Doping concentration modulated photon distribution

The doping concentration of sensitizers and activators lead to various spatial distances, which are vital for energy transfer and excited population distribution. However, the doping concentration for strong emission at moderate power is limited (<5 mol.%) due to the well-known concentration quenching[46, 89-92]. To further optimize the emission intensity, the doping concentration dependence has been investigated[93, 94]. Recently, the researchers found that the doping concentration plays an important role in the occurrence of energy transfer processes between adjacent dopants[95-97]. Normally, a higher doping concentration of Yb^{3+} (sensitizers) in favor of multi-photon (three, four or even higher) emissions, which indicated the powerful modulation of the high-lying excited state at high doping ratios of sensitizers[98, 99]. For example, Han et al. fabricated a series of α-$NaYF_4$:x%Yb^{3+},0.5%Tm^{3+}@CaF_2 nanoparticles with a Yb^{3+} doping ratio ranging from 30 to 99.5%, and the UV band emission located at 342 nm and 360 nm increased monotonically while increase the doping concentration of Yb^{3+} sensitizers (Figure 1.4a)[100]. As shown in Figure 1.4b, the blue band emission dominates while the doping concentration is lower than 1%, and the emission from $^3H_4$ energy level occupied the main emission when the doping concentration of Tm^{3+} is higher than 4%. The intense interaction between dopants lead to the excited state energy distribution. What's more, similar results were observed in Yb^{3+}-Er^{3+}/Ho^{3+} co-doped upconversion nanoparticles[97]. The cross relaxation modulated emission were observed no matter in Yb^{3+}-Er^{3+} co-doped upconversion nanoparticles or self-sensitized single Er^{3+} doped upconversion nanoparticles, and the emission color would be tuned from green to red as the increase of doping concentration[90, 101-103]. These all confirmed the powerful ability to modulate the excited energy distribution by tuning doping concentrations, which is useful to achieve population inversion at lower power.

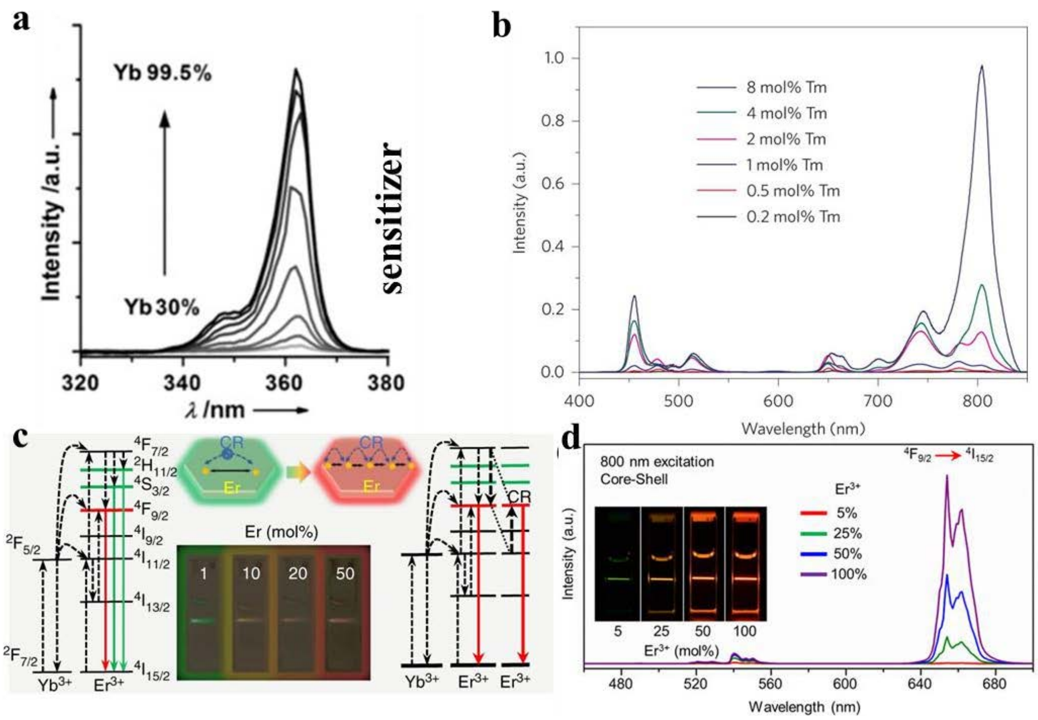

Figure 1.4 (**a**) UV emission spectra of α-$NaYF_4$:x%Yb^{3+},0.5%Tm^{3+}@CaF_2 with different Yb^{3+}-levels (30~99.5). Adapted from ref[100]. (**b**) Upconversion spectra of a series of $NaYF_4$:20%Yb^{3+},x%Tm^{3+} nanocrystals with Tm^{3+} concentrations varied from 0.2 mol% to 8 mol% under an excitation irradiance of 2.5×10^6 W cm^{-2}. Adapted from ref[76] (**c**) Upconversion mechanisms and fluorescence photographs of $NaYbF_4$:x%Er^{3+} upconversion nanoparticles with different doping concentrations of the activators. Adapted from ref[97]. (**d**) Upconversion spectra and upconversion emission photos of the core–shell nanocrystals with variable Er^{3+} dopant concentrations in the core ($NaYF_4$:x% Er^{3+}, x = 5, 25, 50, 100). Adapted from ref[90] .

1.3.3 Energy trapping centers modulated photon distribution

The internal energy transfer processes, including upward transitions, energy transfer from sensitizers to emitters and interactions between emitters, determine the population distribution of each high-lying energy level[98, 104-106]. The internal energy transfer usually occurs *via* cross-relaxation or direct energy transfer between nearby ions. Successful upconversion emission tuning from green to red has been achieved through introducing Ce^{3+} ions to $NaYF_4$: Yb^{3+},Ho^{3+} nanoparticles[107]. As shown in Figure 1.5a, there are mainly two cross-relaxation processes between Ce^{3+} and Ho^{3+} for the tuning of visible radiation: $^5I_6$ (Ho^{3+}) + $^5F_{5/2}$ (Ce^{3+}) → $^5I_7$ (Ho^{3+}) + $^2F_{7/2}$ (Ce^{3+}) and $^5S_2$/$^5F_4$ (Ho^{3+}) + $^5F_{5/2}$ (Ce^{3+}) → $^5I_5$ (Ho^{3+}) + $^2F_{7/2}$ (Ce^{3+}). Thus, the red emission from $^5F_5$ to $^5I_8$ dominates the visible spectral region with the doping of Ce^{3+} ions (Figure 1.5b). Similarly, the impurity doping of Yb^{3+}, Tm^{3+} and Eu^{3+} ions *etc.* show powerful modulation in the emission of $NaErF_4$ upconversion nanoparticles[101, 106]. As shown in Figure 1.5d, the introduced Yb^{3+}, Tm^{3+} and Eu^{3+} ions lead to energy trapping centers that can confine the excited state energy and transfer the energy back to the nearby Er^{3+} ions. The difference of introduced energy levels results in various energy transfer processes that can modulate the energy distribution of $^4F_{9/2}$ (Er^{3+}) and yield populating or depopulating of red emissions as a result. What's more, transition metal ions, including Mn^{2+}, Mo^{3+}, Ni^{2+} also have been used to mediate energy transfer pathways[108-111]. As shown in Figure 1.5e, the energy of the $^4S_{3/2}$ (Er^{3+}) state is higher than the $^4T_1$ (Mn^{2+}) excited level. So, the excited state $^4S_{3/2}$ could relax to a neighboring Mn^{2+} by energy transfer. Then, an energy back transfer from Mn^{2+} to the lower state $^4F_{9/2}$ of Er^{3+} would increase population of the red-emitting $^4F_{9/2}$ state of Er^{3+} greatly. Similar energy transfer and back transfer processes between Ho^{3+}/Tm^{3+} and Mn^{2+} were also achieved. And the excited energy would mainly accumulate at $^5F_5$ (Ho^{3+}) state and $^3H_4$ (Tm^{3+}) state, due to the energy transfer from high-lying state of activators to $^4T_1$ (Mn^{2+}) and then back to lower lying state of activators. In short, the energy trapping centers-controlled energy transfer is an efficient strategy to modulate excited energy distribution without the dependency of excitation power. Thus, it's promising to achieve low power population inversion for effective gain media.

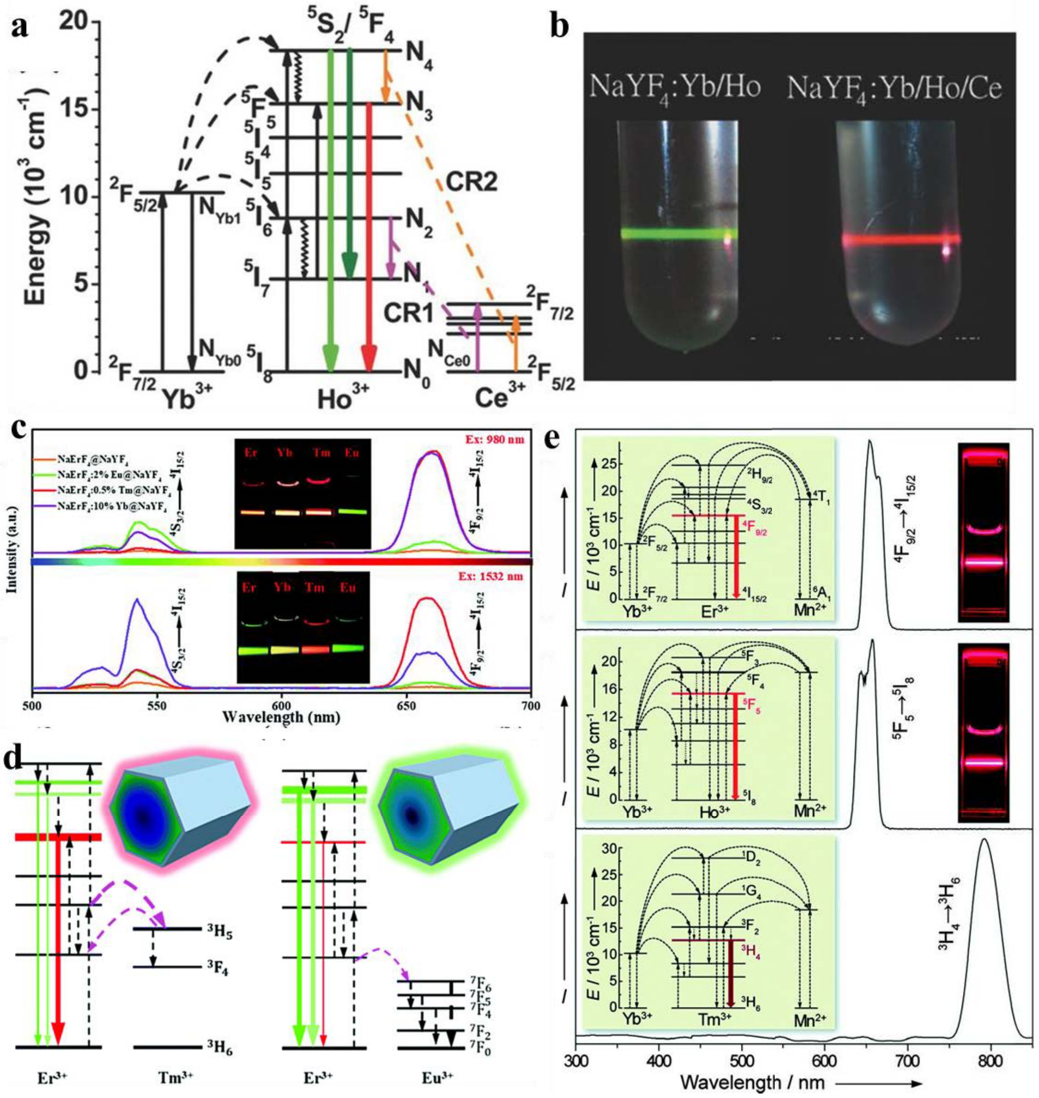

Figure 1.5 (**a**, **b**) Proposed mechanism and photographs of multiphoton cross-relaxation of $NaYF_4:Yb^{3+},Ho^{3+}$ and $NaYF_4:Yb^{3+},Ho^{3+},Ce^{3+}$ upconversion nanoparticles. Adapted from ref[107]. (**c**) Visible upconversion emission spectra and photographs of $NaErF_4@NaYF_4$, $NaErF_4:2\%Eu^{3+}@NaYF_4$, $NaErF_4:0.5\%Tm^{3+}@NaYF_4$ and $NaErF_4:10\%\ Yb^{3+}@NaYF_4$ core shell upconversion nanoparticles under the excitation of 980 nm (top) and 1532 nm (bottom) diode laser. (**d**) Typical energy transfer pathways for multiphoton cross-relaxations generated between Er^{3+}-Tm^{3+} pairs and Er^{3+}-Eu^{3+} pairs. Adapted from ref[101]. (**e**) Upconversion emission spectra, proposed energy transfer mechanisms and corresponding luminescent photos of $KMnF_3:Yb^{3+}/Er^{3+}$ (top), $KMnF_3:Yb^{3+}/Ho^{3+}$ (middle), and $KMnF_3:Yb^{3+}/Tm^{3+}$ (bottom) nanocrystals. Adapted from ref[112].

1.3.4 Thermal and other local field modulated photon distribution

Apart from the above-mentioned strategies, some other methods like shell coating, thermal effect, and localized field can also modulate the photons distribution at some extent[113-116]. Among which, the inert shell could isolate the surface quenching sites or ligands from the activators, and suppress surface quenching pathways[91, 93, 103, 117-119]. The surface related quenching relief would in favor of the redistribution of excited state energy[120]. What's more, thermal induced emission variation is also widely observed[121-124]. As shown in Figure 1.6 a-d, Jiang's group reported the thermally-induced multicolor emission originating from the gradually-attenuated H_2O quenching effect[121]. The color changes from green to red as temperature increases from 30°C to150°C. Especially, the thermal related Boltzmann distribution also helps for the pumping of upper energy level as shown in Figure 1.6e[125]. The energy gap between the thermally coupled energy levels of $^2H_{11/2}$ and $^4S_{3/2}$ of Er^{3+} ions is only several hundred cm^{-1}, which can be matched by heating. And thus, the photons at $^4S_{3/2}$ state could be pump to $^2H_{11/2}$ (upper) state with the assistance of heat activation[126]. In addition, the local structure, including bond distance, bond angle, coordination number and local symmetry strongly impact nonradiative energy transfer between lanthanide dopants[127]. For example, the Li^+, K^+, Lu^{3+}, Ca^{2+} doping would break the local crystal symmetry of $NaLnF_4$, and thus tune the photons distribution and emissions[128-131]. As shown in Figure 1.6g, the aliovalent ions can not only occupy the crystallographic site but also result in a vacancy or interstitial ion for charge equilibrium. Therefore, aliovalent doping could induce a larger degree of local lattice distortion than isovalent doping, which is benefit for population modulations. The local coordination structure could be further engineered by controlling the stoichiometric ratio of Na_xYF_{3+x}:Yb^{3+},Er^{3+} nanoparticles[132]. As the ratio of [Na]/[RE] declined from 1 to 0.5, obvious lattice contraction and a decreased coordination number in the Y–F shell were noticed, suggesting the emergence of Na^+ and F^- vacancies (Figure 1.6h). The changed local coordination structure led to enhanced cross-relaxation interactions between Er^{3+} and Yb^{3+} and thus result in emission variation. Moreover, high pressure is also used to modify the electronic structure, reduce internal ions distance, vary lattice volume and symmetry and so on[133-136], which are the key points of nonradiative energy transfer.

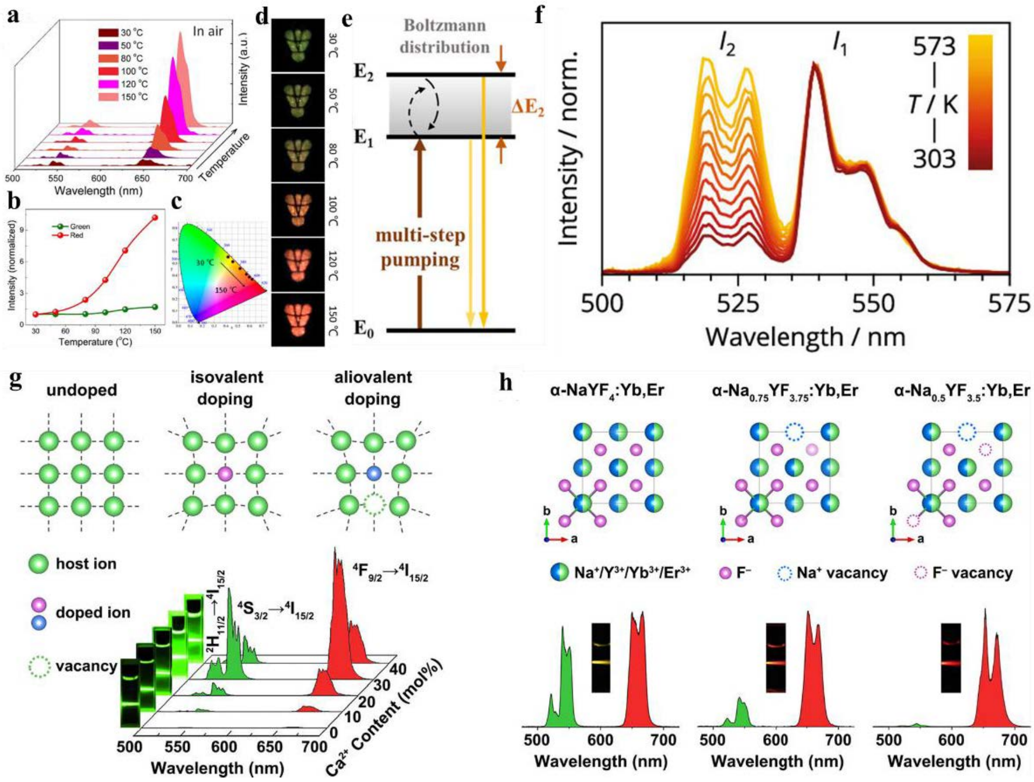

Figure 1.6 (**a**) Temperature-dependent upconversion spectra of β-$NaGdF_4$: Ce^{3+},Yb^{3+},Ho^{3+} nanocrystals in air. (**b**) Integrated emission intensities of red and green bands normalized to that at 30 °C. Temperature-dependent color coordinates of nanocrystals in CIE chromaticity diagram (**c**) and patterns printed with nanocrystal ink (**d**). (**a-d**) adapted from ref[121]. (**e**) Schematic illustration diagram of thermally coupled energy levels. Adapted from ref[125]. (**f**) Green upconversion luminescence of the cubic $NaYF_4$: Yb^{3+},Er^{3+} nanoparticles under 980 nm excitation at various temperatures ranging from 303 K (dark red) to 573 K (yellow). Adapted from ref[126]. (**g**) Schematic of the local structure affected by impurity doping (top). Upconversion emission spectra and photos of hexagonal $NaGdF_4$:Yb^{3+},Er^{3+},Ca^{2+} UCNs as a function of Ca^{2+} content under 980 nm excitation (bottom). Adapted from Ref[131]. (**h**) Schematic of the structure of cubic (α) Na_xYF_{3+x}:Yb^{3+},Er^{3+} with different stoichiometric ratios in the unit cell (top). Upconversion emissions and photos of Na_xYF_{3+x}:Yb^{3+},Er^{3+} UCNs under 980 nm excitation (bottom). Adapted from Ref[132].

1.4 Review of upconversion nanocrystals for microlasers

It has been widely reported that lanthanide doped bulk materials were used as gain media for commercialized solid-state lasers, such as the neodymium-doped yttrium aluminum garnet (YAG:Nd) laser[137]. In recent years, the elaborately polished core-shell-structured UC nanocrystals have showed the enhanced luminescence emitting efficiency and highly tunable excitation/emission properties. Integrating the core-shell UC nanocrystals with dielectric microcavities or hyperbolic metamaterials can further increase the efficiency in small laser, producing multi-wavelength upconverted lasing[69, 70, 138]. Here, the recent progress on upconversion nanocrystals-based-microlasers is summarized and discussed. As the composition of a microlaser device has already introduced above, this section mainly focuses on recent upconversion microlasers, such as upconversion random laser, WGM/FP cavity and photon lattice/plasmonic cavities modulated upconversion lasers.

1.4.1 Upconverting random laser

The upconversion nanoparticles can be employed as cavities for the feedback and resonance based on the scattering effect of themselves to produce random lasering emission. The construction of this type of upconverting microlaser devices is therefore simple. Benefiting from the multi ladder-like and long lifetime energy levels, lanthanide doped UCNPs facilitate the necessary photons accumulation for population inversion. The intrinsic weak and narrow absorption of lanthanide ions, however, severely limits the upconverting efficiency, which inevitably leads to a high threshold of lasing emission. Jin *et al.* designed a $LiYbF_4$:1%Tm^{3+}@$LiYbF_4$@$LiLuF_4$ core-shell-shell UCNP with strong absorption layer of pure $LiYbF_4$ and inert protecting outlayer (Figure 1.7a)[139]. This novel structure favors 15 times stronger ultraviolet (UV) upconversion emission under 980 nm excitation. These highly efficient UCNPs were spin-coated on the silicon substrate to form a uniform film with a thickness around 320 μm. Random and discrete emission peaks with a narrow linewidth of 0.4 nm were emerged as the pumping power increased above 2.19 mJ/cm^2 (980 nm, 6 ns, 10 Hz), as shown in Figure 1.7 b and c. This is currently the lowest reported threshold for multiphoton promoted UVB (280~315 nm) upconversion lasing emission.

Core-shell UCNPs structure can not only enhance upconversion luminescence emitting efficiency, but also lead to unprecedented expanding of the excitation/emission spectra[52, 140-142]. Especially, the efficient energy migration across the core-shell interface through Gd^{3+} sublattice bridges widely expanded the upconversion emissions[143, 144]. For instance, based on the preferred matching between 4f-5d excitation frequency of Ce^{3+} and emission of Gd^{3+}, a broadband UV upconversion emission from Ce^{3+} ions embedded in CaF_2 shell was generated in α-$NaYbF_4$:40%Gd^{3+},1%Tm^{3+}@$NaGdF_4$@CaF_2:Ce^{3+} nanocrystals (Figure 1.7d)[145]. Effective Yb^{3+}→Tm^{3+}→Gd^{3+}→Ce^{3+} energy migration transfer is established by the continuous crystalline interface and the redshift of 4f-5d absorption band of Ce^{3+} in CaF_2 relative to that in $NaLnF_4$ matrix. With this procedure, a broad-band and long lifetime UV upconversion emission under 980 nm excitation was achieved with a tunable lasing emission from 309 nm to 363 nm (Figure 1.7 e and f). The laser threshold was as low as 170 kW/cm^2. Similarly, Haider *et al.* reported a highly efficient single segment white random laser by using a solution-processed $NaYF_4$:50%Yb^{3+},0.5%Er^{3+},0.5%Tm^{3+}@$NaYF_4$:10%Eu^{3+} core–shell nanoparticle assisted with Au/MoO_3 multilayer hyperbolic meta-materials (HMM) [146]. The optical feedback gain was provided by photon scattering of the porous structure of UCNP clusters (inset of Figure 1.7g). Besides, by using the suitable HMM as substrate, the photon propagation loss can be greatly decreased, and the multicolor lasing emission can be enhanced due to the HMM induced high photonic density of states. Therefore, a lower lasing threshold of 0.65 kW/cm^2 was achieved in HMM substrate in comparison with SiO_2/Si substrate.

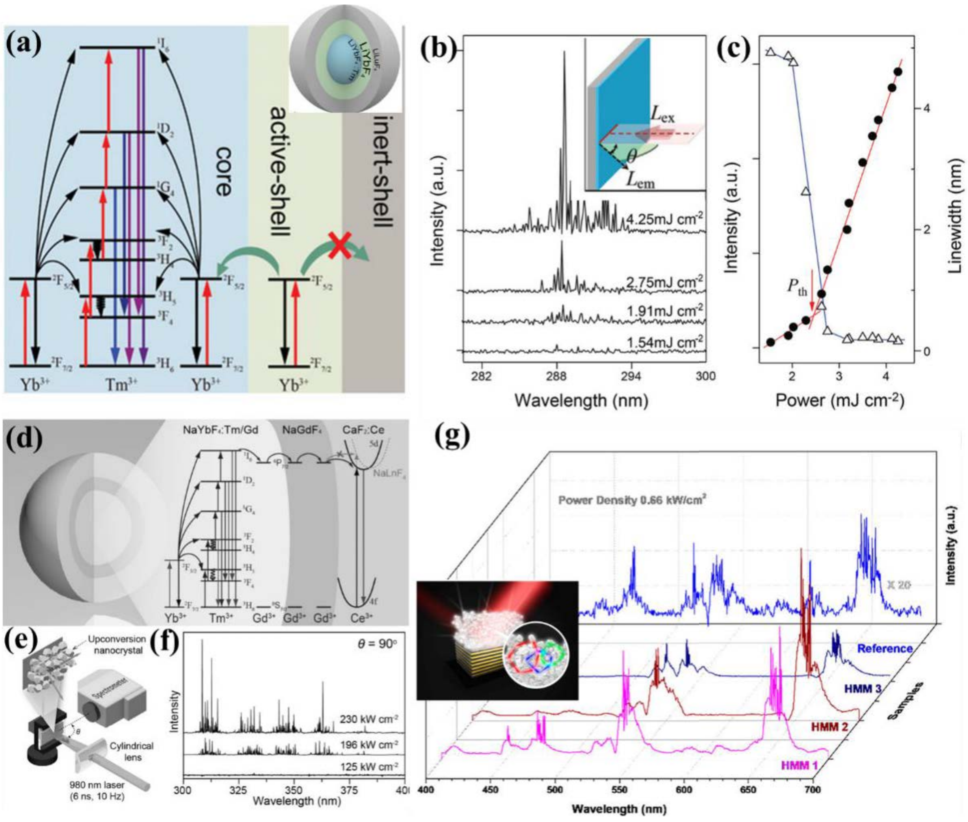

Figure 1.7 (**a**) Energy transfer processes in $LiYbF_4$:1%Tm^{3+}@$LiYbF_4$@$LiLuF_4$ core–shell–shell nanoparticle. (**b**) Power dependent emission spectra of UCNPs film. Inset

shows the schematic diagram of the optical setup. (**c**) Light–light curve of the spectra in (**b**). (**d**) Schematic of α-$NaYbF_4$:40%Gd^{3+},1%Tm^{3+}@$NaGdF_4$ @CaF_2:15%Ce^{3+} core-shell-shell architecture and proposed energy transfer process for migration upconversion of Ce^{3+} ions. (**e**) Schematic illustration of the optical setup for the measurement of random lasing emissions. (**f**) Power dependent emission spectra of the α-$NaYbF_4$: 40%Gd^{3+},1%Tm^{3+}@$NaGdF_4$@CaF_2:15%Ce^{3+} nanoparticles. (**g**) Emission spectra from UCNP/HMM composites under the excitation of 980 nm laser at a constant pumping power density of 0.66 kW/cm^2. Inset shows the schematic illustration of upconversion nanoparticles (UCNPs) coated HMM samples. Adapt from Ref. [139]. (**a-c**), (**d-h**) Ref. [145] and Ref. [146] (**g**).

Differing from Haider's work, Chen *et al.* proposed a new scheme of lasing emission at an ultralow threshold under 980 nm CW excitation through the use of gold sandwich UCNPs nanocomposite (gold-UCNP-gold) (Figure 1.8a)[147]. The localized surface plasmon resonance-based electromagnetic hotspots and the enhanced scattering coefficient benefit the formation of coherent closed loops by multiple scattering, which is responsible for the generation of 545 nm stimulated emissions. The random lasing actions were observed at the extremely ultralow threshold (~0.06 kW/cm^2) due to the unique structure for light trapping. It is well known that the high temperature induced multi-phonon relaxation often results in thermal quenching or lasing death phenomenon[148, 149]. Xu *et al.* presented a type of high-temperature operated compact self-cooling laser through using Ba_2LaF_7:Yb^{3+},Er^{3+} nanocrystals embedded glass-ceramics [150]. As shown in Figure 1.8 b, the phonon-assisted transition from $^4S_{3/2}$ to $^2H_{11/2}$ level is increased at the high temperature, favoring the optical gain for $^2H_{11/2}\rightarrow{}^4I_{15/2}$ transition (523 nm). The high refractive index contrast between Ba_2LaF_7 nanocrystals (~1.7476) and glass-ceramics host (~1.5510) promotes strong random scattering for lasing emission. The low lasing threshold of less than 536 nJ/cm^2 (980 nm, 6 ns, 10 Hz) was thus obtained at 473 K by the formation of a ridge waveguide through ion beam etching (Figure 1.8c). The effective phonon-assisted anti-Stokes strategy has great potential for applications in all-solid-state cryocoolers and radiation balanced microlasers.

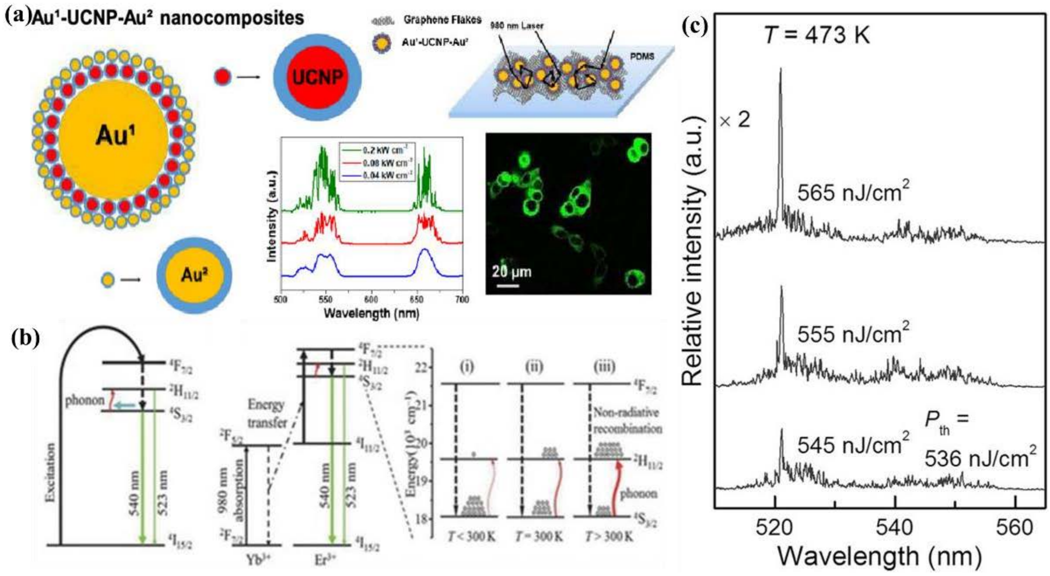

Figure 1.8 (**a**) Design and schematic diagram of gold-UCNPs-gold (Au^1-UCNP-Au^2) nanocomposites. The schematic diagram and pumping-power-density-dependent upconversion emission spectra of the stretchable rippled structure random lasing device consisting of Au^1-UCNPs-Au^2 nanocomposites. (**b**) Simplified model and population inversion *via* phonon-assisted process at temperature T (i) < 300 K, (ii) = 300 K, and (iii) >300 K between $^4S_{3/2}$ and $^2H_{11/2}$ states of Er^{3+}. (**c**) Lasing spectra of optical waveguides fabricated by etching a 2 μm wide and 1 μm height stripe on the surface of the glass-ceramic films on quartz substrate operating at 473 K. Adapt from Ref. [147] (**a**), and Ref. [150] (**b-c**).

The threshold of upconversion random lasers relies heavily on upconversion efficiency [139], the scattering effect (refractive index contrast) [150], propagation losses [146] and so on. Benefiting from core-shell structure and localized surface plasmonic enhancement, the upconverting random laser is expected to be much tunable at emission and excitation wavelength with a low threshold. However, another challenge for random laser is that the lasing emission mode is uncontrollable. Thus, great efforts have been made to achieve ordered and adjustable microlasers.

1.4.2 WGM/FP cavity modulated upconverting laser

Unlike scattering effect induced random laser, Fabry-Perot (FP) cavity and whispering gallery mode (WGM) are employed as common micro-resonator geometries for upconversion lasing emission due to their high quality (Q) factor[151, 152]. The FP microcavities constructed by two or more parallel mirrors enable the light bouncing back and forth between two reflective surfaces. The resonance occurs when the optical pathlength is equal to integer multiple light wavelengths. Based on this, Zhu *et al.* designed a FP cavity consisting of a quartz tube sandwiched between a distributed Bragg reflector (DBR) and an Al mirror (Figure 1.9a)[138]. Highly efficient NaYF$_4$:Yb^{3+},Er^{3+}@NaYF$_4$ core-shell nanocrystal solution with a concentration of 3.6 *wt*% in cyclohexane was used as gain medium. As shown in Figure 1.9b and c, the emission wavelength can be manipulated from blue to red bands by the precise adjustment of reflectivity of DBR and Al mirror. The linewidth of lasing emission is reduced by a factor of 4 times. However, the long cavity makes it difficult to obtain the fine-structured lasing spectrum.

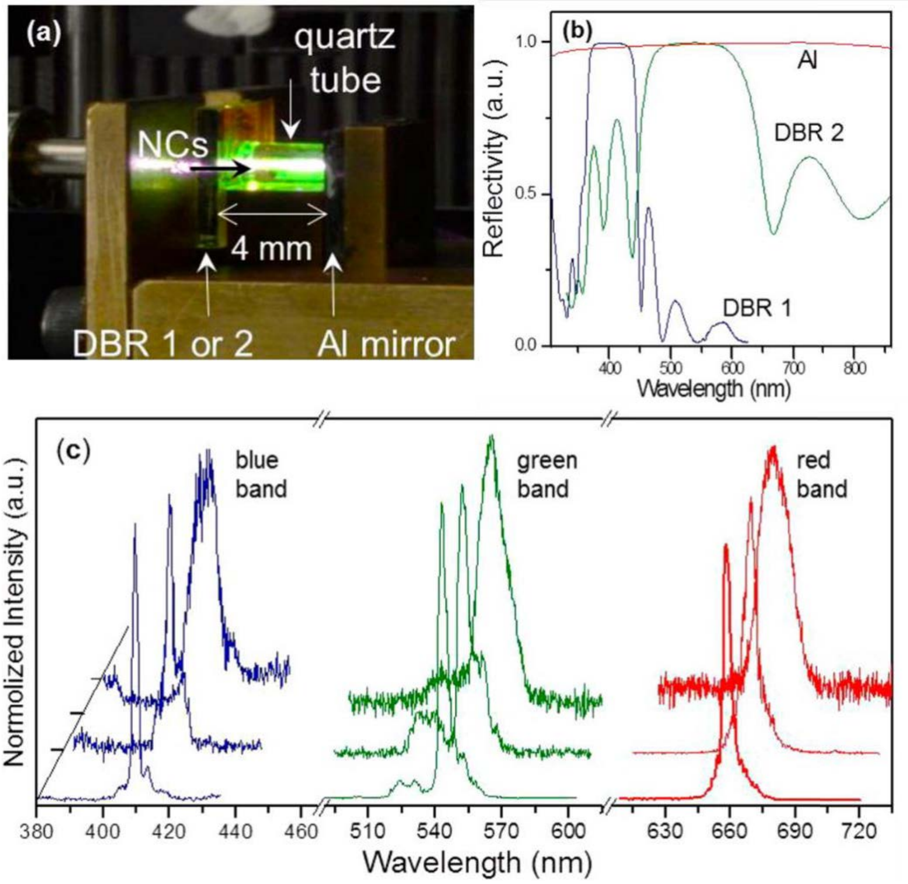

Figure 1.9 (**a**) Image of the FP cavity using NaYF$_4$:Yb^{3+},Er^{3+}@NaYF$_4$ core–shell nanoparticles cyclohexane solution as gain medium. (**b**) Reflection spectra of DBRs and Al mirror. (**c**) Plot of normalized photoluminescent spectra of the 3 color bands versus different excitation power based on the 3-pulse excitation scheme. Adapt from Ref. [138].

The WGM microcavities can confine lights in a narrow ring along the equatorial surface of the cavity *via* total internal reflection[152, 153]. WGM cavities, with various shapes, such as bottle, sphere, toroid and rings, have been further exploited and demonstrated as one of the best cavities for microlasers with low threshold and narrow linewidth due to the high quality (Q) factors and the small mode volumes[154]. Wang *et al.* studied the lasing behaviors of lanthanide doped upconversion nano and microparticles. A bottle-like WGM microcavity enabled upconversion lasing emission by coating a drop of silica resin containing UCNPs onto an optical fiber. Through the rational control on cavity size and the selection of UCNPs, multiple visible lasing emissions (408 nm, 540 nm and 654 nm) of Er^{3+} (Figure 1.10a)[138] and deep UV lasing emission (311 nm) of Gd^{3+} (Figure 1.10b, and c) can be obtained[155, 156]. It is worth noting that the linewidth of Ln^{3+} lasing emissions is usually narrower than 0.5 nm due to the high Q factor. Moreover, as shown in Figure 1.10d, multi-band upconversion lasing emissions (UV: 345 nm and 365 nm, and blue: 450 nm and 475 nm) of Tm^{3+} were also achieved by simply confining $NaYF_4:Yb^{3+},Tm^{3+}@NaYF_4$ core-shell structured nanoparticles in a microscale cylindrical cavity[157]. Despite highly efficient lasing emissions were obtained by the use of these high Q factor microcavities, these resonators with the size of dozens or even hundreds micrometer severely limited the practical applications of microlasers. To solve this issue, Yu and coworkers exploited a single-particle hexagonal $NaYF_4:Yb^{3+},Er^{3+},Tm^{3+}$ microrod for multicolor upconversion lasing emission (Figure 1.10e)[158]. Particularly, the total internal reflection between the six flat surfaces of this microrod could support a whispering gallery mode. This novel microrod served as both gain medium and laser cavity. The red, green, and blue lasing emissions were obtained through tuning the sensitizer (Yb^{3+}) and activator (Er^{3+}, Tm^{3+}) concentrations in the single $NaYF_4$ microrod. Sharp lasing peaks with a linewidth less than 0.4 nm dominated the emission spectra as the excitation power density exceeded a certain threshold, which is usually in a few mJ/cm^2 level (980 nm, 6 ns, 10 Hz). Furthermore, white-light lasing can be also generated through the co-doping of 40%Yb^{3+}, 0,5%Er^{3+} and 2%Tm^{3+} in a single $NaYF_4$ microrod. The pump threshold decreased with the increase of microrod diameter. However, these single-particle upconversion microlasers show low Q factors and inefficient gain mediums, limiting the exploration of low-threshold CW pumped upconversion lasers.

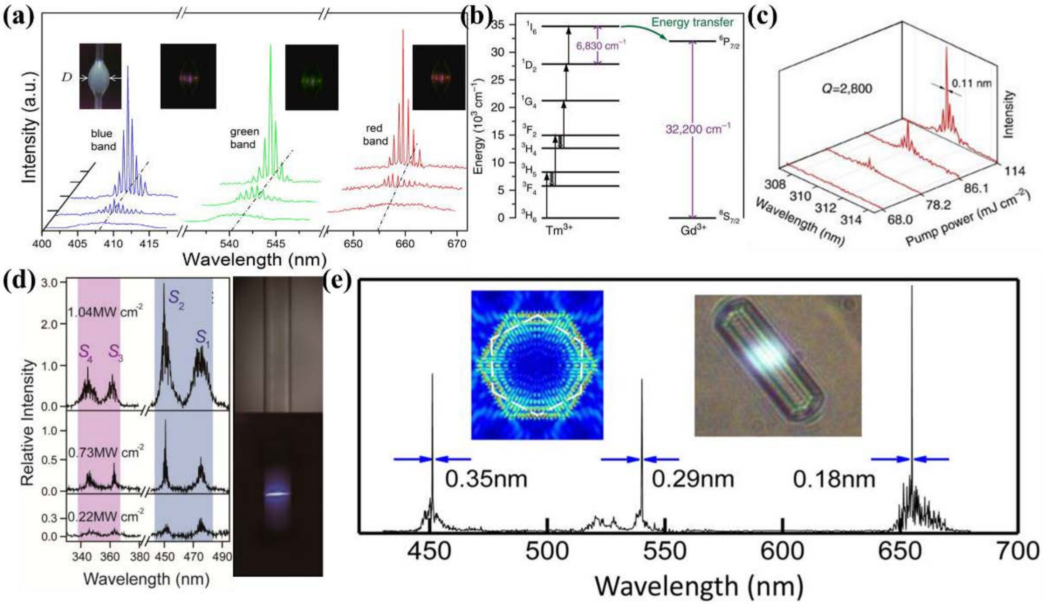

Figure 1.10 (**a**) Lasing spectra of the bottle-like microcavity with a diameter of 80 μm. The insets show the images of the microcavity under different excitation power. (**b**) Simplified energy level diagram showing the energy transfer from Tm^{3+} to Gd^{3+}. (**c**) The corresponding power dependent lasing spectra of the bottle-like microcavity with a diameter of 75 μm. (**d**) Upconversion lasing characteristics of cylindrical microcavities with diameter of 60 μm under 5-pulse 976 nm excitation. The optical image of cylindrical microcavity under a daylight lamp (top) and with (down) NIR pumping in the dark. (**e**) lasing emission spectra, and linewidth of the RGB modes for a single $NaYF_4$:40%Yb^{3+},0.2%Er^{3+},2%Tm^{3+} microrod with R equal to 4 μm. The inset shows the numerical simulation of the optical field distribution inside a β-$NaYF_4$ microrod emitted at 654 nm (left) and the corresponding microscopy image under 980 nm ns-pulsed excitation at room temperature (right). Adapt from Ref. [138] (**a**), Ref. [152] (**b-c**), Ref. [157] (**d**) and Ref. [158] (**e**).

Recently, efficient energy-looping nanocrystals (ELNPs) were designed to fabricate continuous-wave pumped upconverting microlaser with a pump threshold as low as 14 kW/cm^2 [71]. The designed $NaYF_4$:20%Gd^{3+},1.5%Tm^{3+}@$NaGdF_4$ core-shell nanoparticles with a unique energy looping upconversion mechanism under the excitation of 1064 nm CW laser can be used as highly efficient gain medium. The single doped Tm^{3+} can activate an avalanche-like upconversion process, which facilitates efficient population inversion in the NIR emitting state ($^3H_4$) (Figure 1.11d). After the deposition of these hydrophobic ELNPs onto the surface of a polystyrene microsphere, the WGM microlaser device with a high Q factor was fabricated (Figure 1.11a and b). The inert $NaGdF_4$ shell enabled the suppression of surface quenching and energy losses, reducing further the pump threshold. Notably, the microlaser can give out stable blue and NIR upconversion lasing emission for more than 5 h under continuous excitation at 300 kW/cm^2. Liu *et al.* improved the fabrication quality of these microlasers through manipulating the surface oleic acid ligands to tune UCNPs' assembly on the surface of microcavity (Figure 1.11e)[72]. As a result, a smooth and uniform submonolayer gain medium was created, leading to a 25-fold lower laser threshold (1.7 ± 0.7 kW/cm^2) and 30-fold narrower distribution compared to their previous work (Figure 1.11 f and g). The imaging of microlasers was also presented through a 1 mm thick phantom. These stand-alone room-temperature CW pumped low threshold microlasers show great potential for further *in-vivo* imaging or tracking applications. However, the size is still a bit large for intracellular applications, and it is a long way to reduce the threshold.

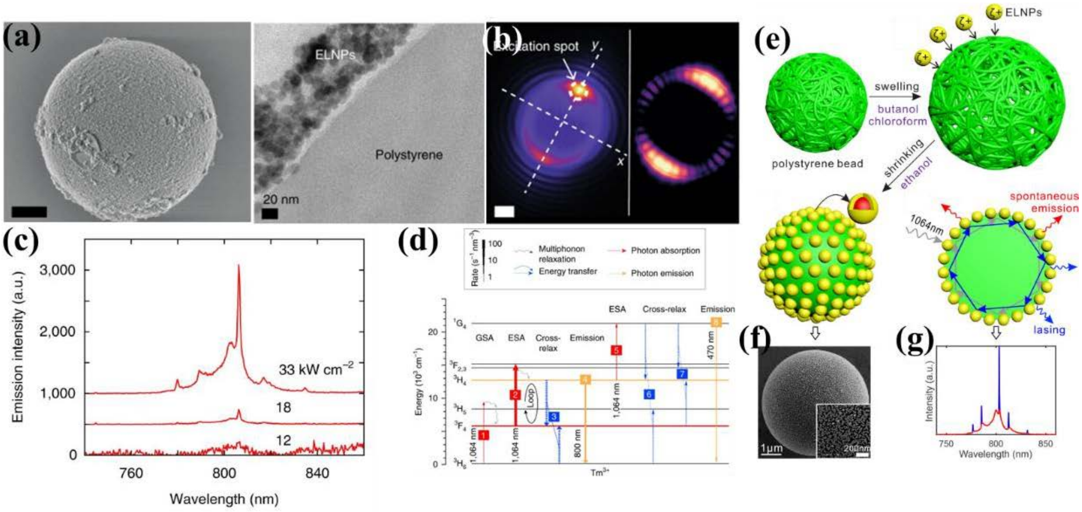

Figure 1.11 (**a**) SEM and cross-section TEM of a 5-µm-diameter cavity coated with ELNPs. (**b**) Wide-field image (left) and simulated field distributions in the x-y plane (right) of a lasing microsphere. (**c**) NIR spectra for pump laser intensities below, near and above the lasing threshold. (**d**) Energy looping upconversion mechanism of single Tm^{3+}-doped $NaYF_4$. (**e**) Fabrication processes of the ELNP-PS cavities, and WGM resonances generated in an ELNP-PS cavity under 1064 nm pumping. (**f**) SEM showing the morphology of an ELNP-PS cavity. The inset (right bottom) is the magnified view of the surface coated with single layer nanoparticles. (**g**) Emission spectrum of an ELNP-PS microlaser, showing sharp WGMs (blue) and spontaneous emission (red). Adapt from Ref. [71] (**a-d**), and Ref. [71] (**e-g**).

1.4.3 Photon lattice/plasmonic cavity modulated upconverting laser

One strategy to lower the threshold of lanthanide upconverting laser is to enhance upconversion efficiency of gain medium[22]. Despite the aforementioned highly-doped sensitizer and core-shell structure can enhance upconversion emission intensity, the corresponding microlasers still require high-threshold excitation. The plasmonic structures with locally enhanced electromagnetic fields can amplify the upconversion process within sub-diffraction volumes[159]. As typical plasmonic materials, silver and gold nanoparticles with tailorable resonance modes that matches upconversion excitation or emissions have shown enhanced upconversion efficiency[160-162]. Wu *et al.* demonstrated upconversion super-burst with directional, fast and ultrabright luminescence by coupling a gap-mode (20 nm) plasmonic nanoresonator (~90 nm Ag nanocube) with nanoparticle emitters (Figure 1.12 a and b)[163]. Due to the overlap of surface plasmon resonance and upconversion emission range (Figure 1.12c), the spontaneous upconversion emission could be boosted by four to five orders of magnitude by precisely manipulating the nanoparticle's local density of state through Purcell effects (Figure 1.12 e and f). And the spontaneous emission rate was also increased by 166-fold through Fermi's golden rule (Figure 1.12 g and h).

However, the typical surface plasmon resonance from a single nanoparticle is in broadband (dozens of nanometers) with low-mode quality. This broad resonance shows poor match with multiple narrowband upconversion transitions. Plasmonic arrays of metal nanoparticles were designed to overcome these challenges by providing narrow lattice plasmon resonance (< 5nm) and strong near-field enhancement[164-166]. Based on this, Schuck and Odom *et al.* designed an ultra-stable and directional emitting plasmon-nanoarray upconverting laser[70]. The plasmonic arrays consisting of Ag nanopillars were fabricated to provide a high-quality single-mode lattice plasmon with sharp resonance peak (Figure 1.12i). The heavily doped $NaYF_4$:20%Yb^{3+},20%Er^{3+}@$NaYF_4$ core-shell nanoparticles (~14 nm) with improved emission intensity and reduced saturation intensity[167, 168] were deposited onto the plasmonic nanoarray surface for microcavity (Figure 1.12j). In this well-designed plasmonic microcavity, the resonance peak centered at 650 nm matches well with the red $^4F_{9/2} \rightarrow ^4I_{15/2}$ emission transition from Er^{3+} ions (Figure 1.12 k and l). Continuous-wave upconversion lasing with an ultralow threshold of 70 W/cm^2 (orders of magnitude lower than other small lasers) was achieved, which offers exciting prospects for low-threshold coherent light sources at the nanoscale and lab-on-a-chip photonic devices. However, the Ohmic loss of metallic nanoantenna arrays is still a daunting task. The threshold and size will be acceptable with the development of the design and fabrication of high-quality optical cavities, as well as the highly efficient coupling between gain medium and resonant cavity.

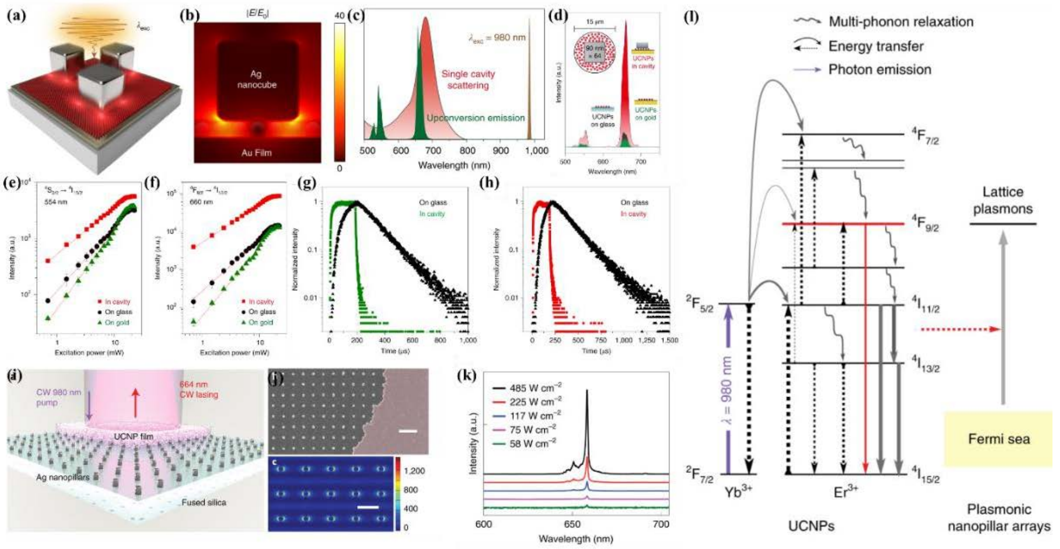

Figure 1.12 (**a**) Plasmonic cavity-coupled UCNPs composed of a gold thin film, a silver nanocube and a monolayer of UCNPs embedded in the sub-20-nm-wide gap. (**b**) Simulated plasmonic gap mode with a maximum electric field enhancement ($|E/E_0|$) of ~40. (**c**) Emission spectrum of the Er^{3+}-activated UCNPs and simulated scattering spectrum of a single nanocavity. (**d**) Emission spectra of a UCNP monolayer deposited on the glass substrate (black) and gold film (green) or in the nanocavity (red). (**e**, **f**) for the power dependent emission intensity for the three samples at emission wavelengths of 554 nm (**e**) and 660 nm (**f**). (**g**, **h**) Decay curves of UCNPs deposited on a glass slide (black) and in the nanocavity mode (green) at an emission wavelength of 554 nm and 660 nm. (**i**) Schematic of the UCNP coating on top of Ag arrays with inter-space of 450 nm. Ag nanopillars are with 80-nm diameter, 50-nm height and the arrays are scalable over cm^2 areas. The UCNP film is roughly 150 nm thick. (**j**) Scanning electron micrograph showing the Ag nanopillar array with partial conformal coating (right) with a film of 14 nm core–shell UCNPs. Scale bar, 1 μm. Representative near-field $|E|^2$ plot for the 450-nm spaced Ag nanopillars at resonance (n = 1.46) from a FDTD method simulation. Scale bar, 500 nm. (**k**) Power-dependent lasing spectra from lattice plasmon resonances at λ = 664 nm. (**l**) Yb^{3+}, Er^{3+} energy levels and coupling mechanism to the lattice plasmons. Adapt from Ref. [163] (**a-h**), and Ref. [70] (**i-l**).

Table 1: Summary of typical upconverting lasers.

Resonant cavity	Upconversion gain medium	Pumping sources	Threshold	Ref. and published year
Random (UCNPs layer on silicon substrate)	$LiYbF_4:Tm^{3+}$@$LiYbF_4$@$LiLuF_4$	980 nm, 6 ns, 10 Hz	2.19 mJ/cm^2 @UVB (280~315 nm)	Ref.[169]@2019
Random (UCNPs layer on quartz substrate)	α-$NaYbF_4:Gd^{3+},Tm^{3+}$@$NaGdF_4$@$CaF_2:Ce^{3+}$	980 nm, 6 ns, 10 Hz	170 kW/cm^2 @UV (309~363 nm)	Ref.[145]@2017
Random (UCNPs embedded glass-ceramics)	$Ba_2LaF_7:Yb^{3+},Er^{3+}$	980 nm, 6 ns, 10 Hz	536 nJ/cm^2 @520 nm	Ref.[150]@2016
Random (UCNPs assisted with Au/MoO_3 multilayer hyperbolic meta-materials)	$NaYF_4$: Yb^{3+},Er^{3+},Tm^{3+}@$NaYF_4:Eu^{3+}$	980 nm, CW	0.65 kW/cm^2 @ red, green and blue range	Ref.[146]@2018
Random (Rippled structure Au^1-UCNPs-Au^2 nanocomposites)	Au^1-UCNPs-Au^2 nanocomposites	980 nm, CW	0.06 kW/cm^2 @545 nm, 0.08 kW/cm^2 @658 nm	Ref.[147]@2020
WGM microcavities (Silica resin containing UCNPs coated optical fiber)	a) $NaYF_4:Yb^{3+},Er^{3+}$@$NaYF_4$ b) $NaYF_4$@$NaYbF_4$: Tm^{3+},Gd^{3+}@$NaYF_4$	a-b) 980 nm, 6 ns, 10 Hz	a) 5~9 kW/cm^2 @410nm, 540 nm and 655 nm b) ~86 mJ/cm^2 @310 nm	a) Ref. [138]@2013 b) Ref.[155]@2016
WGM microcavities (single hexagonal $NaYF_4$ microrod)	$NaYF_4:Yb^{3+},Er^{3+},Tm^{3+}$	980 nm, 6 ns, 10 Hz	5~25 mJ/cm^2 @450 nm, 545 nm, and 650 nm	Ref.[158]@2017
WGM microcavities (UCNPs coated PS beads)	a-b) $NaYF_4:Gd^{3+},Tm^{3+}$@$NaGdF_4$ c) $NaYF_4$: Yb^{3+},Tm^{3+}	a-b) 1064 nm, CW c) 980 nm, CW	800 nm lasing a) 14 kW/cm^2 b) 1.7 ± 0.7 kW/cm^2 c) 150 W/cm^2	a) Ref.[71]@2018 b) Ref.[72]@2020 c) Ref.[69]@2020
Photon lattice/plasmonic cavity (UCNPs coated Ag arrays)	$NaYF_4:Yb^{3+},Er^{3+}$@$NaYF_4$	980 nm, CW	70 W/cm^2@655 nm	Ref.[70]@2019

Though the tremendous progress, challenges remain. For instance, the small-size cavity is expected for the practical applications in life sciences and sensing. Despite the cavity size can be reduced by controlling upconversion nanoparticles, the quality factor and upconversion luminescence efficiency decrease greatly in small upconversion materials. This therefore limits severely the reduction of the laser size and the pumping threshold. As the pumping power is one of the key points of microlasers in practical applications, there are several parts need to be studied in depth. For example, 1) the ways to enhance the upconversion luminescence efficiency with tunable emission and excitation wavelengths in microlaser with ultralow threshold need to be explored. 2) Smart cavities with high Q factor WGM, FP cavity and plasmon enhancement should be further developed for various applications. 3) Deepening regulatory mechanism studies on highly efficient upconversion luminescence output and threshold reduction in microlaser need to be further revealed.

1.5 Thesis aims and outline

Novel micro- and nano-laser output strategies are always relying on the fast development of material science with new optical properties. The outstanding frequency conversion properties of upconversion nanoparticles provide numerous opportunities for upconverting lasering, such as the fabrication of upconversion random laser, WGM/FP cavity modulated upconversion lasing emission and photon lattice/plasmonic cavities upconversion lasers. However, the ultrahigh pumping threshold still restrained the further application of microlasers. Thus, this thesis mainly focuses on the design and construction of upconverting gain media for CW pumped room temperature low threshold upconversion microlasers.

In Chapter 1, the basic information of lanthanide doped upconversion nanoparticles and microlasers are provided by reviewing the recent advances of this field. Several kinds of upconverting lasers including random laser, WGM/FP cavity modulated lasers and photon lattice/plasmonic cavities related lasers are discussed. We highlight the key element for low threshold upconverting lasers, and point out the following research on upconversion gain media.

In Chapter 2, full details including, materials and methods used for constructing upconverting gain media, equipment, instruments and home-built set-ups for sample characterization, are introduced.

In Chapter 3, doping concentration modulated cross-relaxation process is investigated to achieve population inversion at low power density. Strategies to construct a WGM laser by coating efficient upconversion gain media are discussed. Then, systematic characterizations are carried out for the confirmation of upconverting lasing emission.

In Chapter 4, another key point for lasing emission, scattering effects caused by size of upconversion gain media, is fully explored. Then, single nanoparticle with bright emission and negligible scattering is further employed to couple with microcavity for lasing emission.

In Chapter 5, highly sensitizers doping strategy is investigated for low threshold lasing emission. The performance of temperature dependent lasing emission, especially blue shift, is demonstrated for further in-situ temperature sensing. What's more, microlaser with white emission is achieved by employing novel energy migration modulated upconversion gain media.

In Chapter 6, a brief summary of this thesis is presented. On the consideration of four years research, challenges and perspective of upconverting microlaser is discussed.

1.6 References

1. Maiman, T. H. Stimulated Optical Radiation in Ruby. *Nature* **1960,** 187 (4736), 493-494 DOI: 10.1038/187493a0.
2. Gmachl, C.; Sivco, D. L.; Colombelli, R.; Capasso, F.; Cho, A. Y. Ultra-broadband semiconductor laser. *Nature* **2002,** 415 (6874), 883-887 DOI: 10.1038/415883a.
3. Duan, X. F.; Huang, Y.; Agarwal, R.; Lieber, C. M. Single-nanowire electrically driven lasers. *Nature* **2003,** 421 (6920), 241-245 DOI: 10.1038/nature01353.
4. Maslov, A. V.; Ning, C. Z. Far-field emission of a semiconductor nanowire laser. *Opt Lett* **2004,** 29 (6), 572-574 DOI: Doi 10.1364/Ol.29.000572.
5. Qian, F.; Lieber, C. M. Semiconductor nanowire lasers. *Ieee Leos Ann Mtg* **2007**, 831-831.
6. Koblmuller, G.; Mayer, B.; Stettner, T.; Loitsch, B.; Kaniber, M.; Abstreiter, G.; Finley, J. J. Advances in Semiconductor Nanowire Lasers. *2016 Ieee Photonics Society Summer Topical Meeting Series (Sum)* **2016**, 39-39.
7. Jeong, K.-Y.; Hwang, M.-S.; Kim, J.; Park, J.-S.; Lee, J. M.; Park, H.-G. Recent Progress in Nanolaser Technology. *Adv Mater* **2020,** 32 (51), 2001996 DOI: https://doi.org/10.1002/adma.202001996.
8. Jeong, K. Y.; Hwang, M. S.; Kim, J.; Park, J. S.; Lee, J. M.; Park, H. G. Recent

Progress in Nanolaser Technology. *Adv Mater*, 14 DOI: 10.1002/adma.202001996.

9. Singh, S. C.; Zeng, H.; Guo, C.; Cai, W. In *Nanomaterials-Basel*; pp 1-34.

10. Garcia-Vidal, F. J.; Moreno, E. Lasers go nano. *Nature* **2009,** 461 (7264), 604-605 DOI: 10.1038/461604a.

11. Humar, M.; Hyun Yun, S. Intracellular microlasers. *Nat Photonics* **2015,** 9 (9), 572-576 DOI: 10.1038/nphoton.2015.129.

12. Fikouras, A. H.; Schubert, M.; Karl, M.; Kumar, J. D.; Powis, S. J.; Di Falco, A.; Gather, M. C. Non-obstructive intracellular nanolasers. *Nature Communications* **2018,** 9 (1), 4817 DOI: 10.1038/s41467-018-07248-0.

13. Martino, N.; Kwok, S. J. J.; Liapis, A. C.; Forward, S.; Jang, H.; Kim, H.-M.; Wu, S. J.; Wu, J.; Dannenberg, P. H.; Jang, S.-J.; Lee, Y.-H.; Yun, S.-H. Wavelength-encoded laser particles for massively multiplexed cell tagging. *Nat Photonics* **2019,** 13 (10), 720-727 DOI: 10.1038/s41566-019-0489-0.

14. Johnson, J. C.; Choi, H. J.; Knutsen, K. P.; Schaller, R. D.; Yang, P. D.; Saykally, R. J. Single gallium nitride nanowire lasers. *Nat Mater* **2002,** 1 (2), 106-110 DOI: 10.1038/nmat728.

15. Wright, J. B.; Li, Q. M.; Brener, I.; Luk, T. S.; Wang, G. T.; Chow, W. W.; Lester, L. F. Gallium Nitride Single-Mode Nanowire Lasers. *Conf Laser Electr* **2012**.

16. Jackson, S. D. Towards high-power mid-infrared emission from a fibre laser. *Nat Photonics* **2012,** 6 (7), 423-431 DOI: 10.1038/Nphoton.2012.149.

17. Grotjohann, T.; Testa, I.; Leutenegger, M.; Bock, H.; Urban, N. T.; Lavoie-Cardinal, F.; Willig, K. I.; Eggeling, C.; Jakobs, S.; Hell, S. W. Diffraction-unlimited all-optical imaging and writing with a photochromic GFP. *Nature* **2011,** 478 (7368), 204-208 DOI: 10.1038/nature10497.

18. Downing, E.; Hesselink, L.; Ralston, J.; Macfarlane, R. A three-color, solid-state, three-dimensional display. *Science* **1996,** 273 (5279), 1185-1189 DOI: DOI 10.1126/science.273.5279.1185.

19. Kador, L. A three-color, three-dimensional, solid-state display. *Adv Mater* **1997,** 9 (1), 83-& DOI: DOI 10.1002/adma.19970090121.

20. Deng, R.; Qin, F.; Chen, R.; Huang, W.; Hong, M.; Liu, X. Temporal full-colour tuning through non-steady-state upconversion. *Nat Nanotechnol* **2015,** 10 (3), 237.

21. Ma, R.-M.; Oulton, R. F. Applications of nanolasers. *Nat Nanotechnol* **2019,** 14 (1), 12-22.

22. Chen, X.; Sun, T.; Wang, F. Lanthanide-Based Luminescent Materials for Waveguide and Lasing. *Chemistry – An Asian Journal* **2020,** 15 (1), 21-33 DOI: 10.1002/asia.201901447.

23. Tang, S.-J.; Dannenberg, P. H.; Liapis, A. C.; Martino, N.; Zhuo, Y.; Xiao, Y.-F.; Yun, S.-H. Laser particles with omnidirectional emission for cell tracking. *Light: Science & Applications* **2021,** 10 (1), 23 DOI: 10.1038/s41377-021-00466-0.

24. Huang, M. H.; Mao, S.; Feick, H.; Yan, H. Q.; Wu, Y. Y.; Kind, H.; Weber, E.;

Russo, R.; Yang, P. D. Room-temperature ultraviolet nanowire nanolasers. *Science* **2001,** 292 (5523), 1897-1899 DOI: DOI 10.1126/science.1060367.

25. Gargas, D. J.; Moore, M. C.; Ni, A.; Chang, S. W.; Zhang, Z. Y.; Chuang, S. L.; Yang, P. D. Whispering Gallery Mode Lasing from Zinc Oxide Hexagonal Nanodisks. *Acs Nano* **2010,** 4 (6), 3270-3276 DOI: 10.1021/nn9018174.

26. Ha, S. T.; Fu, Y. H.; Emani, N. K.; Pan, Z. Y.; Bakker, R. M.; Paniagua-Dominguez, R.; Kuznetsov, A. I. Directional lasing in resonant semiconductor nanoantenna arrays. *Nat Nanotechnol* **2018,** 13 (11), 1042-+ DOI: 10.1038/s41565-018-0245-5.

27. Chen, R.; Tran, T. T. D.; Ng, K. W.; Ko, W. S.; Chuang, L. C.; Sedgwick, F. G.; Chang-Hasnain, C. Nanolasers grown on silicon. *Nat Photonics* **2011,** 5 (3), 170-175 DOI: 10.1038/Nphoton.2010.315.

28. Tamboli, A. C.; Haberer, E. D.; Sharma, R.; Lee, K. H.; Nakamura, S.; Hu, E. L. Room-temperature continuous-wave lasing in GaN/InGaN microdisks. *Nat Photonics* **2007,** 1 (1), 61-64 DOI: DOI 10.1038/nphoton.2006.52.

29. Di Stasio, F.; Polovitsyn, A.; Angeloni, I.; Moreels, I.; Krahne, R. Broadband Amplified Spontaneous Emission and Random Lasing from Wurtzite CdSe/CdS "Giant-Shell" Nanocrystals. *Acs Photonics* **2016,** 3 (11), 2083-2088 DOI: 10.1021/acsphotonics.6b00452.

30. Eaton, S. W.; Fu, A.; Wong, A. B.; Ning, C. Z.; Yang, P. D. Semiconductor nanowire lasers. *Nat Rev Mater* **2016,** 1 (6), DOI: Artn 16028 10.1038/Natrevmats.2016.28.

31. Ma, Y. G.; Guo, X.; Wu, X. Q.; Dai, L.; Tong, L. M. Semiconductor nanowire lasers. *Adv Opt Photonics* **2013,** 5 (3), 216-273 DOI: 10.1364/Aop.5.000216.

32. Pauzauskie, P. J.; Sirbuly, D. J.; Yang, P. D. Semiconductor nanowire ring resonator laser. *Phys Rev Lett* **2006,** 96 (14), DOI: Artn 143903 10.1103/Physrevlett.96.143903.

33. Samuel, I. D. W.; Turnbull, G. A. Organic semiconductor lasers. *Chem Rev* **2007,** 107 (4), 1272-1295 DOI: 10.1021/cr050152i.

34. Yu, J. C.; Cui, Y. J.; Xu, H.; Yang, Y.; Wang, Z. Y.; Chen, B. L.; Qian, G. D. Confinement of pyridinium hemicyanine dye within an anionic metal-organic framework for two-photon-pumped lasing. *Nature Communications* **2013,** 4, DOI: Artn 2719 10.1038/Ncomms3719.

35. Zhou, T. J.; Tang, M. C.; Xiang, G. H.; Xiang, B. Y.; Hark, S.; Martin, M.; Baron, T.; Pan, S. J.; Park, J. S.; Liu, Z. Z.; Chen, S. M.; Zhang, Z. Y.; Liu, H. Y. Continuous-wave quantum dot photonic crystal lasers grown on on-axis Si (001). *Nature Communications* **2020,** 11 (1), DOI: ARTN 977 10.1038/s41467-020-14736-9.

36. Roh, J.; Park, Y. S.; Lim, J.; Klimov, V. I. Optically pumped colloidal-quantum-dot lasing in LED-like devices with an integrated optical cavity. *Nature Communications* **2020,** 11 (1), DOI: ARTN 271 10.1038/s41467-019-14014-3.

37. Lim, J.; Park, Y. S.; Klimov, V. I. Optical gain in colloidal quantum dots achieved with direct-current electrical pumping. *Nat Mater* **2018,** 17 (1), 42-+ DOI: 10.1038/NMAT5011.

38. Fan, F.; Voznyy, O.; Sabatini, R. P.; Bicanic, K. T.; Adachi, M. M.; McBride, J. R.; Reid, K. R.; Park, Y.-S.; Li, X.; Jain, A.; Quintero-Bermudez, R.; Saravanapavanantham, M.; Liu, M.; Korkusinski, M.; Hawrylak, P.; Klimov, V. I.; Rosenthal, S. J.; Hoogland, S.; Sargent, E. H. Continuous-wave lasing in colloidal quantum dot solids enabled by facet-selective epitaxy. *Nature* **2017,** 544 (7648), 75-79 DOI: 10.1038/nature21424.
39. Liu, X. F.; Qiu, J. R. Recent advances in energy transfer in bulk and nanoscale luminescent materials: from spectroscopy to applications. *Chemical Society Reviews* **2015,** 44 (23), 8714-8746 DOI: 10.1039/c5cs00067j.
40. Bunzli, J. C. G. Benefiting from the unique properties of lanthanide ions. *Accounts Chem Res* **2006,** 39 (1), 53-61 DOI: 10.1021/ar0400894.
41. Bunzli, J. C. G. Lanthanide Luminescence for Biomedical Analyses and Imaging. *Chem Rev* **2010,** 110 (5), 2729-2755 DOI: 10.1021/cr900362e.
42. Carlos, L. D.; Ferreira, R. A. S.; Bermudez, V. D.; Julian-Lopez, B.; Escribano, P. Progress on lanthanide-based organic-inorganic hybrid phosphors. *Chemical Society Reviews* **2011,** 40 (2), 536-549 DOI: 10.1039/c0cs00069h.
43. Zheng, K. Z.; Loh, K. Y.; Wang, Y.; Chen, Q. S.; Fan, J. Y.; Jung, T.; Nam, S. H.; Suh, Y. D.; Liu, X. G. Recent advances in upconversion nanocrystals: Expanding the kaleidoscopic toolbox for emerging applications. *Nano Today* **2019,** 29, DOI: Artn 100797 10.1016/J.Nantod.2019.100797.
44. Song, C. X.; Zhang, S. B.; Zhou, Q. A.; Hai, H.; Zhao, D. F.; Hui, Y. Z. Upconversion nanoparticles for bioimaging. *Nanotechnol Rev* **2017,** 6 (2), 233-242 DOI: 10.1515/ntrev-2016-0043.
45. Zhou, B.; Shi, B. Y.; Jin, D. Y.; Liu, X. G. Controlling upconversion nanocrystals for emerging applications. *Nat Nanotechnol* **2015,** 10 (11), 924-936 DOI: 10.1038/Nnano.2015.251.
46. Chen, B.; Wang, F. Combating Concentration Quenching in Upconversion Nanoparticles. *Accounts Chem Res* **2020,** 53 (2), 358-367 DOI: 10.1021/acs.accounts.9b00453.
47. Liang, L.; Qin, X.; Zheng, K.; Liu, X. Energy flux manipulation in upconversion nanosystems. *Accounts Chem Res* **2018,** 52 (1), 228-236.
48. Lu, Y. Q.; Zhao, J. B.; Zhang, R.; Liu, Y. J.; Liu, D. M.; Goldys, E. M.; Yang, X. S.; Xi, P.; Sunna, A.; Lu, J.; Shi, Y.; Leif, R. C.; Huo, Y. J.; Shen, J.; Piper, J. A.; Robinson, J. P.; Jin, D. Y. Tunable lifetime multiplexing using luminescent nanocrystals. *Nat Photonics* **2014,** 8 (1), 33-37 DOI: 10.1038/Nphoton.2013.322.
49. Liu, B. L.; Liao, J. Y.; Song, Y. L.; Chen, C. H.; Ding, L.; Lu, J.; Zhou, J. J.; Wang, F. Multiplexed structured illumination super-resolution imaging with lifetime-engineered upconversion nanoparticles. *Nanoscale Adv* **2021,** 4 (1), 30-38 DOI: 10.1039/d1na00765c.
50. Liao, J. Y.; Zhou, J. J.; Song, Y. L.; Liu, B. L.; Chen, Y. H.; Wang, F.; Chen, C. H.; Lin, J.; Chen, X. Y.; Lu, J.; Jin, D. Y. Preselectable Optical Fingerprints of

Heterogeneous Upconversion Nanoparticles. *Nano Lett* **2021,** 21 (18), 7659-7668 DOI: 10.1021/acs.nanolett.1c02404.

51. Haase, M.; Schafer, H. Upconverting Nanoparticles. *Angew Chem Int Edit* **2011,** 50 (26), 5808-5829 DOI: 10.1002/anie.201005159.

52. Chen, G. Y.; Agren, H.; Ohulchanskyy, T. Y.; Prasad, P. N. Light upconverting core-shell nanostructures: nanophotonic control for emerging applications. *Chemical Society Reviews* **2015,** 44 (6), 1680-1713 DOI: 10.1039/c4cs00170b.

53. Zhang, Y.; Zhang, L.; Deng, R.; Tian, J.; Zong, Y.; Jin, D.; Liu, X. Multicolor barcoding in a single upconversion crystal. *J Am Chem Soc* **2014,** 136 (13), 4893-4896.

54. Auzel, F. Upconversion and anti-stokes processes with f and d ions in solids. *Chem Rev* **2004,** 104 (1), 139-173 DOI: 10.1021/cr020357g.

55. Sun, L.-D.; Dong, H.; Zhang, P.-Z.; Yan, C.-H. Upconversion of rare earth nanomaterials. *Annual review of physical chemistry* **2015,** 66, 619-642.

56. Liu, Y. J.; Lu, Y. Q.; Yang, X. S.; Zheng, X. L.; Wen, S. H.; Wang, F.; Vidal, X.; Zhao, J. B.; Liu, D. M.; Zhou, Z. G.; Ma, C. S.; Zhou, J. J.; Piper, J. A.; Xi, P.; Jin, D. Y. Amplified stimulated emission in upconversion nanoparticles for super-resolution nanoscopy. *Nature* **2017,** 543 (7644), 229-233 DOI: 10.1038/nature21366.

57. Nampi, P. P.; Vakurov, A.; Mackenzie, L. E.; Scrutton, N. S.; Millner, P. A.; Jose, G.; Saha, S. Selective cellular imaging with lanthanide-based upconversion nanoparticles. *Journal of biophotonics* **2019,** 12 (4), e201800256.

58. Huang, X.; Han, S.; Huang, W.; Liu, X. Enhancing solar cell efficiency: the search for luminescent materials as spectral converters. *Chemical Society Reviews* **2013,** 44 (16), 173-201.

59. Chen, G.; Seo, J.; Yang, C.; Prasad, P. N. Nanochemistry and nanomaterials for photovoltaics. *Chemical Society Reviews* **2013,** 42 (21), 8304-8338.

60. Zhou, J.; Liu, Q.; Feng, W.; Sun, Y.; Li, F. Y. Upconversion Luminescent Materials: Advances and Applications. *Chem Rev* **2015,** 115 (1), 395-465.

61. Liu, X.; Yan, C.-H.; Capobianco, J. A. Photon upconversion nanomaterials. *Chemical Society Reviews* **2015,** 44 (6), 1299-1301.

62. Shang, Y.; Hao, S.; Yang, C.; Chen, G. Enhancing solar cell efficiency using photon upconversion materials. *Nanomaterials-Basel* **2015,** 5 (4), 1782-1809.

63. Yu, D.; Yu, T.; van Bunningen, A. J.; Zhang, Q.; Meijerink, A.; Rabouw, F. T. Understanding and tuning blue-to-near-infrared photon cutting by the Tm^{3+}/Yb^{3+} couple. *Light: Science & Applications* **2020,** 9 (1), 107 DOI: 10.1038/s41377-020-00346-z.

64. Zhou, J.; Liu, Q.; Feng, W.; Sun, Y.; Li, F. Upconversion luminescent materials: advances and applications. *Chem Rev* **2014,** 115 (1), 395-465.

65. Chen, G.; Qiu, H.; Prasad, P. N.; Chen, X. Upconversion nanoparticles: design, nanochemistry, and applications in theranostics. *Chem Rev* **2014,** 114 (10), 5161-5214.

66. Wang, Y.; Zheng, K. Z.; Song, S. Y.; Fan, D. Y.; Zhang, H. J.; Liu, X. G. Remote

manipulation of upconversion luminescence. *Chemical Society Reviews* **2018,** 47 (17), 6473-6485 DOI: 10.1039/c8cs00124c.

67. Li, C. X.; Lin, J. Rare earth fluoride nano-/microcrystals: synthesis, surface modification and application. *J Mater Chem* **2010,** 20 (33), 6831-6847 DOI: 10.1039/c0jm00031k.

68. Zhou, J.; Liu, Z.; Li, F. Upconversion nanophosphors for small-animal imaging. *Chemical Society Reviews* **2012,** 41 (3), 1323-1349.

69. Shang, Y.; Zhou, J.; Cai, Y.; Wang, F.; Fernandez-Bravo, A.; Yang, C.; Jiang, L.; Jin, D. Low threshold lasing emissions from a single upconversion nanocrystal. *Nature Communications* **2020,** 11 (1), 6156 DOI: 10.1038/s41467-020-19797-4.

70. Fernandez-Bravo, A.; Wang, D.; Barnard, E. S.; Teitelboim, A.; Tajon, C.; Guan, J.; Schatz, G. C.; Cohen, B. E.; Chan, E. M.; Schuck, P. J. Ultralow-threshold, continuous-wave upconverting lasing from subwavelength plasmons. *Nat Mater* **2019,** 18 (11), 1172-1176.

71. Fernandez-Bravo, A.; Yao, K.; Barnard, E. S.; Borys, N. J.; Levy, E. S.; Tian, B.; Tajon, C. A.; Moretti, L.; Altoe, M. V.; Aloni, S.; Beketayev, K.; Scotognella, F.; Cohen, B. E.; Chan, E. M.; Schuck, P. J. Continuous-Wave Upconverting Nanoparticle Microlasers. *Nat. Nanotechnol.* **2018,** 13, 572.

72. Liu, Y. W.; Teitelboim, A.; Fernandez-Bravo, A.; Yao, K. Y.; Altoe, M. V. P.; Aloni, S.; Zhang, C. H.; Cohen, B. E.; Schuck, P. J.; Chan, E. M. Controlled Assembly of Upconverting Nanoparticles for Low-Threshold Microlasers and Their Imaging in Scattering Media. *Acs Nano* **2020,** 14 (2), 1508-1519 DOI: 10.1021/acsnano.9b06102.

73. Pollnau, M.; Gamelin, D. R.; Luthi, S. R.; Gudel, H. U.; Hehlen, M. P. Power dependence of upconversion luminescence in lanthanide and transition-metal-ion systems. *Phys Rev B* **2000,** 61 (5), 3337-3346 DOI: DOI 10.1103/PhysRevB.61.3337.

74. Zhou, J.; Chizhik, A. I.; Chu, S.; Jin, D. Single-particle spectroscopy for functional nanomaterials. *Nature* **2020,** 579 (7797), 41-50 DOI: 10.1038/s41586-020-2048-8.

75. Zhan, Q.; Liu, H.; Wang, B.; Wu, Q.; Pu, R.; Zhou, C.; Huang, B.; Peng, X.; Agren, H.; He, S. Achieving high-efficiency emission depletion nanoscopy by employing cross relaxation in upconversion nanoparticles. *Nature Communications* **2017,** 8 (1), 1058 DOI: 10.1038/s41467-017-01141-y.

76. Zhao, J.; Jin, D.; Schartner, E. P.; Lu, Y.; Liu, Y.; Zvyagin, A. V.; Zhang, L.; Dawes, J. M.; Xi, P.; Piper, J. A. Single-nanocrystal sensitivity achieved by enhanced upconversion luminescence. *Nat Nanotechnol* **2013,** 8 (10), 729.

77. Liu, D. M.; Xu, X. X.; Du, Y.; Liao, J. Y.; Wen, S. H.; Dong, X. T.; Jin, Y.; Liu, L.; Jin, D. Y.; Capobianco, J. A.; Shen, D. Z. Reconstructing the Surface Structure of NaREF4 Upconversion Nanocrystals with a Novel K+ Treatment. *Chem Mater* **2021,** 33 (7), 2548-2556 DOI: 10.1021/acs.chemmater.0c04956.

78. Wang, Q.; Liao, J. S.; Guo, J. F.; Huang, H. P.; Wen, H. R. Upconversion Emission and Temperature Sensing Behavior of LuF3:Yb3+,Er3+ Microcrystals Prepared by

One-Step Hydrothermal Synthesis. *Chinese J Inorg Chem* **2018,** 34 (3), 579-588 DOI: 10.11862/Crc.2018.067.

79. Xiong, H. P.; Min, Q. H.; Ma, H. Q.; Zhao, L.; Chen, W. B.; Qiu, J. B.; Yu, X.; Xu, X. H. Ultra-high sensitivity of rhodamine B sensing based on NaGdF4:Yb3+, Er3+@NaGdF4 core-shell upconversion nanoparticles. *Journal of Rare Earths* **2019,** 37 (4), 339-344 DOI: 10.1016/j.jre.2018.08.004.

80. Wurth, C.; Kaiser, M.; Wilhelm, S.; Grauel, B.; Hirsch, T.; Resch-Genger, U. Excitation power dependent population pathways and absolute quantum yields of upconversion nanoparticles in different solvents. *Nanoscale* **2017,** 9 (12), 4283-4294 DOI: 10.1039/c7nr00092h.

81. Stanton, I. N.; Ayres, J. A.; Stecher, J. T.; Fischer, M. C.; Scharpf, D.; Scheuch, J. D.; Therien, M. J. Power-Dependent Radiant Flux and Absolute Quantum Yields of Upconversion Nanocrystals under Continuous and Pulsed Excitation. *J Phys Chem C* **2018,** 122 (1), 252-259 DOI: 10.1021/acs.jpcc.7b11929.

82. Liao, J. Y.; Jin, D. Y.; Chen, C. H.; Li, Y. M.; Zhou, J. J. Helix Shape Power-Dependent Properties of Single Upconversion Nanoparticles. *Journal of Physical Chemistry Letters* **2020,** 11 (8), 2883-2890 DOI: 10.1021/acs.jpclett.9b03838.

83. Sagaidachnaya, E. A.; Konyukhova, J. G.; Kazadaeva, N. I.; Doronkina, A. A.; Yanina, I. Y.; Skaptsov, A. A.; Pravdin, A. B.; Kochubey, V. I. Dependence of the luminescent properties of thermostabilized upconversion NaYF4:Yb, Er particles on the excitation power and temperature. *Opt Eng* **2020,** 59 (6), DOI: Artn 061609
10.1117/1.Oe.59.6.061609.

84. Ji, S. H.; Lin, X. J.; Chen, M. N.; Rong, X. F.; Xu, H. Y.; Li, W. S.; Cai, Z. P. Green Wavelength-Tunable and High Power Ho3+-Doped Upconversion Fiber Lasers. *Ieee Photonic Tech L* **2020,** 32 (6), 313-316 DOI: 10.1109/Lpt.2020.2972077.

85. Bae, H.; Lee, E.; Lee, K. T. Power-dependent photophysical pathways of upconversion in BaTiO3:Er3+. *Physical Chemistry Chemical Physics* **2021,** 23 (27), 14587-+ DOI: 10.1039/d1cp01679b.

86. Krishnan, R.; Menon, S. G.; Poelman, D.; Kroon, R. E.; Swart, H. C. Power-dependent upconversion luminescence properties of self-sensitized Er2WO6 phosphor. *Dalton T* **2021,** 50 (1), 229-239 DOI: 10.1039/d0dt03081c.

87. Pang, T.; Jian, R. H.; Mao, J. W.; Guo, H. Improved Response of Upconversion Luminescence Color to Pump Power through the Coupling of Er3+ and Tm3+. *J Phys Chem C* **2022**, DOI: 10.1021/acs.jpcc.1c08853.

88. Zhao, J. B.; Jin, D. Y.; Schartner, E. P.; Lu, Y. Q.; Liu, Y. J.; Zvyagin, A. V.; Zhang, L. X.; Dawes, J. M.; Xi, P.; Piper, J. A.; Goldys, E. M.; Monro, T. M. Single-nanocrystal sensitivity achieved by enhanced upconversion luminescence. *Nat Nanotechnol* **2013,** 8 (10), 729-734 DOI: 10.1038/nnano.2013.171.

89. Liu, X.; Kong, X.; Zhang, Y.; Tu, L.; Wang, Y.; Zeng, Q.; Li, C.; Shi, Z.; Zhang, H. Breakthrough in concentration quenching threshold of upconversion luminescence via

spatial separation of the emitter doping area for bio-applications. *Chem Commun (Camb)* **2011,** 47 (43), 11957-9 DOI: 10.1039/c1cc14774a.

90. Johnson, N. J. J.; He, S.; Diao, S.; Chan, E. M.; Dai, H. J.; Almutairi, A. Direct Evidence for Coupled Surface and Concentration Quenching Dynamics in Lanthanide-Doped Nanocrystals. *J Am Chem Soc* **2017,** 139 (8), 3275-3282 DOI: 10.1021/jacs.7b00223.

91. Ma, C.; Xu, X.; Wang, F.; Zhou, Z.; Liu, D.; Zhao, J.; Guan, M.; Lang, C. I.; Jin, D. Optimal Sensitizer Concentration in Single Upconversion Nanocrystals. *Nano Lett* **2017,** 17 (5), 2858-2864 DOI: 10.1021/acs.nanolett.6b05331.

92. Rabouw, F. T.; Prins, P. T.; Villanueva-Delgado, P.; Castelijns, M.; Geitenbeek, R. G.; Meijerink, A. Quenching pathways in NaYF4: Er3+, Yb3+ upconversion nanocrystals. *Acs Nano* **2018,** 12 (5), 4812-4823.

93. Zuo, J.; Li, Q. Q.; Xue, B.; Li, C. X.; Chang, Y. L.; Zhang, Y. L.; Liu, X. M.; Tu, L. P.; Zhang, H.; Kong, X. G. Employing shells to eliminate concentration quenching in photonic upconversion nanostructure. *Nanoscale* **2017,** 9 (23), 7941-7946 DOI: 10.1039/c7nr01403a.

94. Wang, M. Y.; Tian, Y.; Zhao, F. Y.; Li, R. F.; You, W. W.; Fang, Z. L.; Chen, X. Y.; Huang, W.; Ju, Q. Alleviating the emitter concentration effect on upconversion nanoparticles via an inert shell. *J Mater Chem C* **2017,** 5 (6), 1537-1543 DOI: 10.1039/6tc05289d.

95. Li, D.; Wen, S. H.; Kong, M. Y.; Liu, Y. T.; Hu, W.; Shi, B. Y.; Shi, X. Y.; Jin, D. Y. Highly Doped Upconversion Nanoparticles for In Vivo Applications Under Mild Excitation Power. *Anal Chem* **2020,** 92 (16), 10913-10919 DOI: 10.1021/acs.analchem.0c02143.

96. Wen, S. H.; Zhou, J. J.; Zheng, K. Z.; Bednarkiewicz, A.; Liu, X. G.; Jin, D. Y. Advances in highly doped upconversion nanoparticles. *Nature Communications* **2018,** 9, DOI: Artn 2415
10.1038/S41467-018-04813-5.

97. Wei, W.; Zhang, Y.; Chen, R.; Goggi, J.; Ren, N.; Huang, L.; Bhakoo, K. K.; Sun, H.; Tan, T. T. Y. Cross relaxation induced pure red upconversion in activator-and sensitizer-rich lanthanide nanoparticles. *Chem Mater* **2014,** 26 (18), 5183-5186.

98. Dong, H.; Sun, L.-D.; Yan, C.-H. Energy transfer in lanthanide upconversion studies for extended optical applications. *Chemical Society Reviews* **2015,** 44 (6), 1608-1634.

99. Yin, A.; Zhang, Y.; Sun, L.; Yan, C. Colloidal synthesis and blue based multicolor upconversion emissions of size and composition controlled monodisperse hexagonal NaYF 4: Yb, Tm nanocrystals. *Nanoscale* **2010,** 2 (6), 953-959.

100. Shen, J.; Chen, G. Y.; Ohulchanskyy, T. Y.; Kesseli, S. J.; Buchholz, S.; Li, Z. P.; Prasad, P. N.; Han, G. Tunable Near Infrared to Ultraviolet Upconversion Luminescence Enhancement in (alpha-$NaYF_4$:Yb,Tm)/CaF_2 Core/Shell Nanoparticles

for In situ Real-time Recorded Biocompatible Photoactivation. *Small* **2013,** 9 (19), 3213-3217 DOI: 10.1002/smll.201300234.

101. Shang, Y.; Hao, S.; Lv, W.; Chen, T.; Tian, L.; Lei, Z.; Yang, C. Confining excitation energy of Er 3+-sensitized upconversion nanoparticles through introducing various energy trapping centers. *J Mater Chem C* **2018,** 6 (15), 3869-3875.

102. Chen, Q. S.; Xie, X. J.; Huang, B. L.; Liang, L. L.; Han, S. Y.; Yi, Z. G.; Wang, Y.; Li, Y.; Fan, D. Y.; Huang, L.; Liu, X. G. Confining Excitation Energy in Er^{3+} -Sensitized Upconversion Nanocrystals through Tm^{3+} -Mediated Transient Energy Trapping. *Angew Chem Int Edit* **2017,** 56 (26), 7605-7609 DOI: 10.1002/anie.201703012.

103. Cui, X. S.; Cheng, Y.; Lin, H.; Wu, Q. P.; Xu, J.; Wang, Y. S. Boosting single-band red upconversion luminescence in colloidal NaErF4 nanocrystals: Effects of doping and inert shell. *Journal of Rare Earths* **2019,** 37 (6), 573-579 DOI: 10.1016/j.jre.2018.10.012.

104. Chen, G. Y.; Yang, C. H.; Prasad, P. N. Nanophotonics and Nanochemistry: Controlling the Excitation Dynamics for Frequency Up- and Down-Conversion in Lanthanide-Doped Nanoparticles. *Accounts Chem Res* **2013,** 46 (7), 1474-1486 DOI: 10.1021/ar300270y.

105. Qin, X.; Xu, J.; Wu, Y.; Liu, X. Energy-transfer editing in lanthanide-activated upconversion nanocrystals: a toolbox for emerging applications. *ACS Central Science* **2019,** 5 (1), 29-42.

106. Chan, E. M.; Han, G.; Goldberg, J. D.; Gargas, D. J.; Ostrowski, A. D.; Schuck, P. J.; Cohen, B. E.; Milliron, D. J. Combinatorial discovery of lanthanide-doped nanocrystals with spectrally pure upconverted emission. *Nano Lett* **2012,** 12 (7), 3839-3845.

107. Chen, G. Y.; Liu, H. C.; Somesfalean, G.; Liang, H. J.; Zhang, Z. G. Upconversion emission tuning from green to red in Yb3+/Ho3+-codoped NaYF4 nanocrystals by tridoping with Ce3+ ions. *Nanotechnology* **2009,** 20 (38), DOI: Artn 385704, 10.1088/0957-4484/20/38/385704.

108. Wenger, O. S.; Gamelin, D. R.; Gudel, H. U. Chemical modification of transition metal upconversion properties: Exchange enhancement of Ni2+ upconversion rates in Ni2+: RbMnCl3. *J Am Chem Soc* **2000,** 122 (30), 7408-7409 DOI: Doi 10.1021/Ja000979o.

109. Gamelin, D. R.; Gudel, H. U. Two-photon spectroscopy of d(3) transition metals: Near-IR-to-visible upconversion luminescence by Re4+ and Mo3+. *J Am Chem Soc* **1998,** 120 (46), 12143-12144 DOI: Doi 10.1021/Ja982742m.

110. Shang, Y. F.; Hao, S. W.; Shao, W.; Chen, T.; Zhu, Y. Y.; Yang, C. H. Tuning the upconversion luminescence of cubic KMnF3:Yb3+/Er3+ nanocrystals through inert lanthanide ion doping. *J Mater Chem C* **2020,** 8 (8), 2847-2851 DOI: 10.1039/c9tc06288b.

111. Tian, G.; Gu, Z.; Zhou, L.; Yin, W.; Liu, X.; Yan, L.; Jin, S.; Ren, W.; Xing, G.; Li, S. Mn^{2+} dopant-controlled synthesis of $NaYF_4$: Yb/Er upconversion nanoparticles for in vivo imaging and drug delivery. *Adv Mater* **2012,** 24 (9), 1226-1231.

112. Wang, J.; Wang, F.; Wang, C.; Liu, Z.; Liu, X. Single-band upconversion emission in lanthanide-doped $KMnF_3$ nanocrystals. *Angewandte Chemie International Edition* **2011,** 50 (44), 10369-10372.

113. Wang, F.; Liu, X. G. Multicolor Tuning of Lanthanide-Doped Nanoparticles by Single Wavelength Excitation. *Accounts Chem Res* **2014,** 47 (4), 1378-1385 DOI: 10.1021/ar5000067.

114. Chen, X.; Peng, D.; Ju, Q.; Wang, F. Photon upconversion in core–shell nanoparticles. *Chemical Society Reviews* **2015,** 44 (6), 1318-1330.

115. Yan, L.; Zhou, B.; Song, N.; Liu, X.; Huang, J.; Wang, T.; Tao, L.; Zhang, Q. Self-sensitization induced upconversion of Er^{3+} in core–shell nanoparticles. *Nanoscale* **2018,** 10 (37), 17949-17957.

116. Meng, Z. P.; Zhang, S. F.; Wu, S. L. Power density dependent upconversion properties of NaYbF4: Er3+@NaYbF4: Tm3+@NaYF4 nanoparticles and their application in white-light emission LED. *Journal of Luminescence* **2020,** 227, DOI: Artn 117566, 10.1016/J.Jlumin.2020.117566.

117. Shao, W.; Chen, G.; Damasco, J.; Wang, X.; Kachynski, A.; Ohulchanskyy, T. Y.; Yang, C.; Agren, H.; Prasad, P. N. Enhanced upconversion emission in colloidal $NaYF_4$:Er^{3+}/$NaYF_4$ core/shell nanoparticles excited at 1523 nm. *Opt Lett* **2014,** 39 (6), 1386-9 DOI: 10.1364/OL.39.001386.

118. Fischer, S.; Bronstein, N. D.; Swabeck, J. K.; Chan, E. M.; Alivisatos, A. P. Precise Tuning of Surface Quenching for Luminescence Enhancement in Core-Shell Lanthanide-Doped Nanocrystals. *Nano Lett* **2016,** 16 (11), 7241-7247 DOI: 10.1021/acs.nanolett.6b03683.

119. Fischer, S.; Swabeck, J. K.; Alivisatos, A. P. Controlled Isotropic and Anisotropic Shell Growth in beta-NaLnF4 Nanocrystals Induced by Precursor Injection Rate. *J Am Chem Soc* **2017,** 139 (35), 12325-12332 DOI: 10.1021/jacs.7b07496.

120. Lay, A.; Siefe, C.; Fischer, S.; Mehlenbacher, R. D.; Ke, F.; Mao, W. L.; Aliyisatos, A. P.; Goodman, M. B.; Dionne, J. A. Bright, Mechanosensitive Upconversion with Cubic-Phase Heteroepitaxial Core-Shell Nanoparticles. *Nano Lett* **2018,** 18 (7), 4454-4459 DOI: 10.1021/acs.nanolett.8b01535.

121. Hu, Y. Q.; Shao, Q. Y.; Deng, X. Y.; Jiang, J. Q. Thermal-responsive multicolor emission of single NaGdF4:Yb/Ce/Ho upconversion nanocrystals for anticounterfeiting application. *Nanophotonics-Berlin* **2020,** 9 (9), 2879-2885 DOI: 10.1515/nanoph-2020-0136.

122. Li, A. H.; Sun, Z. J.; Lu, Q. Laser heating effect on the power dependence of upconversion luminescence in Er3+-doped nanopowders. *Journal of Nanoparticle Research* **2013,** 15 (1), DOI: Artn 1377

10.1007/S11051-012-1377-4.

123. Zhou, J. J.; Wen, S. H.; Liao, J. Y.; Clarke, C.; Tawfik, S. A.; Ren, W.; Mi, C.; Wang, F.; Jin, D. Y. Activation of the surface dark-layer to enhance upconversion in a thermal field. *Nat Photonics* **2018,** 12 (3), 154-+ DOI: 10.1038/s41566-018-0108-5.

124. Liao, J. S.; Kong, L. Y.; Wang, M. H.; Sun, Y. J.; Gong, G. L. Tunable upconversion luminescence and optical temperature sensing based on non-thermal coupled levels of Lu3NbO7:Yb3+/Ho3+ phosphors. *Optical Materials* **2019,** 98, DOI: Artn 109452, 10.1016/J.Optmat.2019.109452.

125. Shang, Y.; Han, Q.; Hao, S.; Chen, T.; Zhu, Y.; Wang, Z.; Yang, C. Dual-Mode Upconversion Nanoprobe Enables Broad-Range Thermometry from Cryogenic to Room Temperature. *Acs Appl Mater Inter* **2019,** 11 (45), 42455-42461 DOI: 10.1021/acsami.9b11751.

126. van Swieten, T. P.; van Omme, T.; van den Heuvel, D. J.; Vonk, S. J. W.; Spruit, R. G.; Meirer, F.; Garza, H. H. P.; Weckhuysen, B. M.; Meijerink, A.; Rabouw, F. T.; Geitenbeek, R. G. Mapping Elevated Temperatures with a Micrometer Resolution Using the Luminescence of Chemically Stable Upconversion Nanoparticles. *Acs Appl Nano Mater* **2021,** 4 (4), 4208-4215 DOI: 10.1021/acsanm.1c00657.

127. Dong, H.; Sun, L. D.; Yan, C. H. Local Structure Engineering in Lanthanide-Doped Nanocrystals for Tunable Upconversion Emissions. *J Am Chem Soc* **2021,** 143 (49), 20546-20561 DOI: 10.1021/jacs.1c10425.

128. Cheng, Q.; Sui, J.; Cai, W. Enhanced upconversion emission in Yb3+ and Er3+ codoped NaGdF4 nanocrystals by introducing Li+ ions. *Nanoscale* **2012,** 4 (3), 779-84 DOI: 10.1039/c1nr11365h.

129. Zhao, C.; Kong, X.; Liu, X.; Tu, L.; Wu, F.; Zhang, Y.; Liu, K.; Zeng, Q.; Zhang, H. Li+ ion doping: an approach for improving the crystallinity and upconversion emissions of NaYF4:Yb3+, Tm3+ nanoparticles. *Nanoscale* **2013,** 5 (17), 8084-9 DOI: 10.1039/c3nr01916k.

130. Wisser, M. D.; Fischer, S.; Maurer, P. C.; Bronstein, N. D.; Chu, S.; Alivisatos, A. P.; Salleo, A.; Dionne, J. A. Enhancing Quantum Yield via Local Symmetry Distortion in Lanthanide-Based Upconverting Nanoparticles. *Acs Photonics* **2016,** 3 (8), 1523-1530 DOI: 10.1021/acsphotonics.6b00166.

131. Lei, L.; Chen, D. Q.; Xu, J.; Zhang, R.; Wang, Y. S. Highly Intensified Upconversion Luminescence of Ca2+-doped Yb/Er:NaGdF4 Nanocrystals Prepared by a Solvothermal Route. *Chem-Asian J* **2014,** 9 (3), 728-733 DOI: 10.1002/asia.201301514.

132. Dong, H.; Sun, L. D.; Wang, Y. F.; Ke, J.; Si, R.; Xiao, J. W.; Lyu, G. M.; Shi, S.; Yan, C. H. Efficient Tailoring of Upconversion Selectivity by Engineering Local Structure of Lanthanides in NaxREF3+x Nanocrystals. *J Am Chem Soc* **2015,** 137 (20), 6569-6576 DOI: 10.1021/jacs.5b01718.

133. Jayaraman, A. Diamond Anvil Cell and High-Pressure Physical Investigations.

Rev Mod Phys **1983,** 55 (1), 65-108 DOI: DOI 10.1103/RevModPhys.55.65.

134. Wisser, M. D.; Chea, M.; Lin, Y.; Wu, D. M.; Mao, W. L.; Salleo, A.; Dionne, J. A. Strain-Induced Modification of Optical Selection Rules in Lanthanide-Based Upconverting Nanoparticles. *Nano Lett* **2015,** 15 (3), 1891-1897 DOI: 10.1021/nl504738k.

135. Mei, S.; Guo, Y.; Lin, X. H.; Dong, H.; Sun, L. D.; Li, K.; Yan, C. H. Experimental and Simulation Insights into Local Structure and Luminescence Evolution in Eu3+-Doped Nanocrystals under High Pressure. *Journal of Physical Chemistry Letters* **2020,** 11 (9), 3515-3520 DOI: 10.1021/acs.jpclett.0c00895.

136. Runowski, M.; Shyichuk, A.; Tymiński, A.; Grzyb, T.; Lavín, V.; Lis, S. Multifunctional Optical Sensors for Nanomanometry and Nanothermometry: High-Pressure and High-Temperature Upconversion Luminescence of Lanthanide-Doped Phosphates-LaPO4/YPO4:Yb3+-Tm3+. *ACS Appl. Mater. Interfaces* **2018,** 10, 17269.

137. Ikesue, A.; Kinoshita, T.; Kamata, K.; Yoshida, K. Fabrication and Optical-Properties of High-Performance Polycrystalline Nd-Yag Ceramics for Solid-State Lasers. *J Am Ceram Soc* **1995,** 78 (4), 1033-1040 DOI: DOI 10.1111/j.1151-2916.1995.tb08433.x.

138. Zhu, H.; Chen, X.; Jin, L. M.; Wang, Q. J.; Wang, F.; Yu, S. F. Amplified spontaneous emission and lasing from lanthanide-doped up-conversion nanocrystals. *Acs Nano* **2013,** 7 (12), 11420-11426.

139. Jin, L. M.; Wu, Y. K.; Wang, Y. J.; Liu, S.; Zhang, Y. Q.; Li, Z. Y.; Chen, X.; Zhang, W. F.; Xiao, S. M.; Song, Q. H. Mass-Manufactural Lanthanide-Based Ultraviolet B Microlasers. *Adv Mater* **2019,** 31 (7), DOI: Artn 1807079
10.1002/Adma.201807079.

140. Xie, X.; Gao, N.; Deng, R.; Sun, Q.; Xu, Q.-H.; Liu, X. Mechanistic investigation of photon upconversion in Nd^{3+}-sensitized core–shell nanoparticles. *J Am Chem Soc* **2013,** 135 (34), 12608-12611.

141. Li, Z.; Zhang, Y.; Jiang, S. Multicolor core/shell-structured upconversion fluorescent nanoparticles. *Adv Mater* **2008,** 20 (24), 4765-4769.

142. Wang, F.; Deng, R.; Wang, J.; Wang, Q.; Han, Y.; Zhu, H.; Chen, X.; Liu, X. Tuning upconversion through energy migration in core–shell nanoparticles. *Nat Mater* **2011,** 10 (12), 968.

143. Tu, L. P.; Liu, X. M.; Wu, F.; Zhang, H. Excitation energy migration dynamics in upconversion nanomaterials. *Chemical Society Reviews* **2015,** 44 (6), 1331-1345 DOI: 10.1039/c4cs00168k.

144. Su, Q.; Han, S.; Xie, X.; Zhu, H.; Chen, H.; Chen, C.-K.; Liu, R.-S.; Chen, X.; Wang, F.; Liu, X. The effect of surface coating on energy migration-mediated upconversion. *J Am Chem Soc* **2012,** 134 (51), 20849-20857.

145. Chen, X.; Jin, L. M.; Sun, T. Y.; Kong, W.; Yu, S. F.; Wang, F. Energy Migration Upconversion in Ce(III)-Doped Heterogeneous Core-Shell-Shell Nanoparticles. *Small*

2017, 13 (43), DOI: Artn 1701479
10.1002/Smll.201701479.

146. Haider, G.; Lin, H. I.; Yadav, K.; Shen, K. C.; Liao, Y. M.; Hu, H. W.; Roy, P. K.; Bera, K. P.; Lin, K. H.; Lee, H. M.; Chen, Y. T.; Chen, F. R.; Chen, Y. F. A Highly-Efficient Single Segment White Random Laser. *Acs Nano* **2018,** 12 (12), 11847-11859 DOI: 10.1021/acsnano.8b03035.

147. Kataria, M.; Yadav, K.; Nain, A.; Lin, H.; Hu, H. W.; Inbaraj, C. R. P.; Chang, T. J.; Liao, Y. M.; Cheng, H. Y.; Lin, K. H.; Chang, H. S.; Tseng, F. G.; Wang, W. H.; Chen, Y. F. Self-Sufficient and Highly Efficient Gold Sandwich Upconversion Nanocomposite Lasers for Stretchable and Bio-applications. *Acs Appl Mater Inter* **2020,** 12 (17), 19840-19854 DOI: 10.1021/acsami.0c02602.

148. Qin, C. J.; Sandanayaka, A. S. D.; Zhao, C. Y.; Matsushima, T.; Zhang, D. Z.; Fujihara, T.; Adachi, C. Stable room-temperature continuous-wave lasing in quasi-2D perovskite films. *Nature* **2020,** 585 (7823), 53-+ DOI: 10.1038/s41586-020-2621-1.

149. Jia, Y. F.; Kerner, R. A.; Grede, A. J.; Rand, B. P.; Giebink, N. C. Continuous-wave lasing in an organic-inorganic lead halide perovskite semiconductor. *Nat Photonics* **2017,** 11 (12), 784-+ DOI: 10.1038/s41566-017-0047-6.

150. Xu, X. H.; Zhang, W. F.; Yang, D. C.; Lu, W.; Qiu, J. B.; Yu, S. F. Phonon-Assisted Population Inversion in Lanthanide-Doped Upconversion Ba2LaF7 Nanocrystals in Glass-Ceramics. *Adv Mater* **2016,** 28 (36), 8045-8050 DOI: 10.1002/adma.201601405.

151. Hill, M. T.; Gather, M. C. Advances in small lasers. *Nat Photonics* **2014,** 8 (12), 908.

152. Ward, J.; Benson, O. WGM microresonators: sensing, lasing and fundamental optics with microspheres. *Laser & Photonics Reviews* **2011,** 5 (4), 553-570.

153. Jiang, X. F.; Qavi, A. J.; Huang, S. H.; Yang, L. Whispering-Gallery Sensors. *Matter* **2020,** 3 (2), 371-392 DOI: 10.1016/j.matt.2020.07.008.

154. Foreman, M. R.; Swaim, J. D.; Vollmer, F. Whispering gallery mode sensors. *Adv Opt Photonics* **2015,** 7 (2), 168-240 DOI: 10.1364/AOP.7.000168.

155. Chen, X.; Jin, L.; Kong, W.; Sun, T.; Zhang, W.; Liu, X.; Fan, J.; Yu, S. F.; Wang, F. Confining energy migration in upconversion nanoparticles towards deep ultraviolet lasing. *Nature communications* **2016,** 7, 10304.

156. Du, Y. Y.; Wang, Y. F.; Deng, Z. Q.; Chen, X.; Yang, X. Q.; Sun, T. Y.; Zhang, X.; Zhu, G. Y.; Yu, S. F.; Wang, F. Blue-Pumped Deep Ultraviolet Lasing from Lanthanide-Doped Lu6O5F8 Upconversion Nanocrystals. *Adv Opt Mater* **2020,** 8 (2), DOI: Artn 1900968
10.1002/Adom.201900968.

157. Jin, L. M.; Chen, X.; Siu, C. K.; Wang, F.; Yu, S. F. Enhancing multiphoton upconversion from NaYF4: Yb/Tm@ NaYF4 core–shell nanoparticles via the use of laser cavity. *Acs Nano* **2017,** 11 (1), 843-849.

158. Wang, T.; Yu, H.; Siu, C. K.; Qiu, J.; Xu, X.; Yu, S. F. White-light whispering-gallery-mode lasing from lanthanide-doped upconversion NaYF4 hexagonal microrods. *ACS photonics* **2017,** 4 (6), 1539-1543.

159. Qin, X.; Neto, A. N. C.; Longo, R. L.; Wu, Y. M.; Malta, O. L.; Liu, X. G. Surface Plasmon-Photon Coupling in Lanthanide-Doped Nanoparticles. *Journal of Physical Chemistry Letters* **2021,** 12 (5), 1520-1541 DOI: 10.1021/acs.jpclett.0c03613.

160. Bang, D.; Jo, E. J.; Hong, S.; Byun, J. Y.; Lee, J. Y.; Kim, M. G.; Lee, L. P. Asymmetric Nanocrescent Antenna on Upconversion Nanocrystal. *Nano Lett* **2017,** 17 (11), 6583-6590 DOI: 10.1021/acs.nanolett.7b02327.

161. Zhang, H.; Xu, D.; Huang, Y.; Duan, X. F. Highly spectral dependent enhancement of upconversion emission with sputtered gold island films. *Chem Commun* **2011,** 47 (3), 979-981 DOI: 10.1039/c0cc03566a.

162. Li, A. H.; Lu, M. Y.; Guo, L.; Sun, Z. J. Enhanced Upconversion Luminescence of Metal-Capped NaGd(0.3)Yb(0.7)F4:Er Submicrometer Particles. *Small* **2016,** 12 (15), 2092-2098 DOI: 10.1002/smll.201502934.

163. Wu, Y. M.; Xu, J. H.; Poh, E. T.; Liang, L. L.; Liu, H. L.; Yang, J. K. W.; Qiu, C. W.; Vallee, R. A. L.; Liu, X. G. Upconversion superburst with sub-2 mu s lifetime. *Nat Nanotechnol* **2019,** 14 (12), 1110-1115 DOI: 10.1038/s41565-019-0560-5.

164. Auguie, B.; Barnes, W. L. Collective resonances in gold nanoparticle arrays. *Phys Rev Lett* **2008,** 101 (14), DOI: Artn 143902
10.1103/Physrevlett.101.143902.

165. Wang, D. Q.; Guan, J.; Hu, J. T.; Bourgeois, M. R.; Odom, T. W. Manipulating Light-Matter Interactions in Plasmonic Nanoparticle Lattices. *Accounts Chem Res* **2019,** 52 (11), 2997-3007 DOI: 10.1021/acs.accounts.9b00345.

166. Wang, D. Q.; Wang, W. J.; Knudson, M. P.; Schatz, G. C.; Odom, T. W. Structural Engineering in Plasmon Nanolasers. *Chem Rev* **2018,** 118 (6), 2865-2881 DOI: 10.1021/acs.chemrev.7b00424.

167. Tian, B.; Fernandez-Bravo, A.; Najafiaghdam, H.; Torquato, N. A.; Altoe, M. V. P.; Teitelboim, A.; Tajon, C. A.; Tian, Y.; Borys, N. J.; Barnard, E. S. Low irradiance multiphoton imaging with alloyed lanthanide nanocrystals. *Nature Communications* **2018,** 9 (1), 3082.

168. Liu, Q.; Zhang, Y.; Peng, C. S.; Yang, T.; Joubert, L.-M.; Chu, S. Single upconversion nanoparticle imaging at sub-10 W cm^{-2} irradiance. *Nat Photonics* **2018,** 12 (9), 548-553.

169. Jin, L.; Wu, Y.; Wang, Y.; Liu, S.; Zhang, Y.; Li, Z.; Chen, X.; Zhang, W.; Xiao, S.; Song, Q. Mass-Manufactural Lanthanide-Based Ultraviolet B Microlasers. *Adv Mater* **2019,** 31 (7), 1807079.

Chapter 2 Materials and methods

In this chapter, the general chemicals and reagents used in this thesis are described; the key synthesis and characterization methods are introduced; the instrument and set-up for material and optical property characterization are provide and accounted in detail.

2.1 Chemicals and reagents

The general chemicals and reagents used in the synthesis of UCNPs and construction of microlaser.

Table 2.1 The chemicals and regents used in this thesis.

Name	Specifications	CAS or product number	Manufacturer
Yttrium (III) chloride hexahydrate ($YCl_3 \cdot 6H_2O$)	99.99% trace metals basis	10025-94-2	Sigma-Aldrich
Ytterbium (III) chloride hexahydrate ($YbCl_3 \cdot 6H_2O$)	99.998% trace metals basis	10035-01-5	Sigma-Aldrich
Thulium (III) chloride hexahydrate ($TmCl_3 \cdot 6H_2O$)	99.99% trace metals basis	1331-74-4	Sigma-Aldrich
Gadolinium (III) chloride hexahydrate ($GdCl_3 \cdot 6H_2O$)	99% (titration)	13450-84-5	Sigma-Aldrich
Terbium (III) chloride hexahydrate ($TbCl_3 \cdot 6H_2O$)	99.9% trace metals basis	13798-24-8	Sigma-Aldrich
Sodium hydroxide	semiconductor grade, 99.99%	1310-73-2	Sigma-Aldrich

(NaOH)	trace metals basis		
Ammonium fluoride (NH_4F)	≥99.99% trace metals basis	12125-01-8	Sigma-Aldrich
Oleic Acid (OA)	Technical grade, 90%	112-80-1	Sigma-Aldrich
1-Octadecene	Technical grade, 90%	112-88-9	Sigma-Aldrich
Ethanol	Undenatured 100%	64-17-5	Chem-Supply
Methanol	for HPLC, ≥99.9%	67-56-1	Sigma-Aldrich
Cyclohexane	for HPLC, ≥99.9%	110-82-7	Chem-Supply (Australia)
Hydrochloric acid (HCl)	1.0 ± 0.005 mol/L (20 °C)	7647-01-0	Chem-Supply
Micro particles based on polystyrene	5 µm std dev <0.1 µm, coeff var <2%	79633-5ML-F	Sigma-Aldrich

2.2 Instruments and equipment

The commercial instruments and equipment used in this thesis are listed as follow.

Table 2.2 Instruments and equipment for material synthesis and characterization.

Name	Specifications	Manufacturer
Magnetic stirrer	0-1800 rpm	Labquip
Heating mantle	Range room temperature (25-30 °C) to 400 °C	Labquip
Temperature controller	Range room temperature to 400 °C	Labquip

Three-neck round-bottom flask	50 mL, 100 mL	Synthware
Flow control adapter	19/22	Synthware
Teflon-coated, elliptical RE extra power stir bars	15 × 10 mm	Sigma-Aldrich
Micropipettes	ranges: 10–100 µL, 100–1000 µL and 500–5000 µL	Eppendorf
Centrifuge	Centrifuge 5424 Centrifuge 5804	Eppendorf
Vortex mixer	LSE	Corning
Ultrasonic cleaner	Commercial Benchtop Cleaners (FXP) 2.7 Litre	Unisonics
Laboratory balance	SJF2104 (0.1 mg)	ProSciTech
TEM	Model: Tecnai T20 JEM-ARM200F/ JEOL TEM-2200FS	FEI JEOL
TEM copper grids	300 mesh with carbon film	Pacific Grid-Tech
SEM	Supra 55VP	Zeiss
UV-Visible spectrophotometer	Agilent Cary 60	Agilent Technologies
Spectrometer	Shamrock 193i	Andor
Zetasizer	Malvern Zetasizer Nano ZS90 - ATA Scientific	Malvern Panalytical
Glass slide	25×57 mm	Hurst Scientific Pty. Ltd.
Cover slip	22×22 mm	Muraban Laboratories

2.3 Synthesis protocols of upconversion nanoparticles

2.3.1 General synthesis of $NaLnF_4$ core nanoparticles

In the whole thesis, the uniform lanthanide doped core upconversion nanoparticles with various doping concentration were obtained through optimized coprecipitation method[1-3]. In a typical experiment, $LnCl_3 \cdot 6H_2O$ is used as the source for lanthanide ions, while NH_4F and NaOH reagents are used to provide the needed Na^+ and F^- ions. Oleic acid (OA) with carboxy group that can chelate with lanthanide ions performs as solvent and surfactant to control the growth process of nanoparticles. 1-Octadecene (ODE) with high boiling point (> 300 °C) provides the high temperature reaction condition. Firstly, lanthanide ions are coupled with OA ligands to form $Ln(OA)_3$ complexes at ~150 °C. Then, nucleation occurs in the precursor solution at ~50 °C with the promotion of Na^+ and F^- ions. Finally, the size of nanoparticles grows at high temperature (~300 °C). Therefore, the amount of OA and ODE, the temperature and final reaction time, *etc.* are the key points to control the synthesis of $NaLnF_4$ nanoparticles. Due to the similarity of lanthanide ions, the doping and replacement of lanthanide ions in the nanoparticles are easy to achieve.

Typical synthesis process of β-$NaYF_4$:20%Yb, 2%Tm^{3+} nanoparticles:

The uniform oleic-acid-capped nanoparticles (β-$NaYF_4$:20%Yb, 2%Tm^{3+}) were synthesized by the coprecipitation method modified from previous report[3, 4]. A typical procedure is as follows: $YCl_3 \cdot 6H_2O$ (0.78 mmol), $YbCl_3 \cdot 6H_2O$ (0.2 mmol) and $TmCl_3 \cdot 6H_2O$ (0.02 mmol) were added into a 50 mL three-necked flask containing 6 mL oleic acid (OA) and 15 mL 1-octadecene (ODE). The mixture is first heated to 160 °C under argon for 30 min to form a transparent solution and remove residual water. The solution is cooled down to room temperature, and 10 mL of a methanol solution containing NaOH (2.5 mmol) and NH_4F (4 mmol) is slowly dropped into the flask and stirred for 30 min. Then, the solution is heated to 70-80 °C and maintained for 30 min to evaporate methanol. Subsequently, the solution is heated to 300 °C and maintained for 1 h under argon atmosphere. After cooling down to room temperature, the resulting products are precipitated by ethanol and collected by centrifugation at 6000 rpm for 5 min. The precipitate is then purified with ethanol three times, and finally dispersed in cyclohexane for further use.

2.3.2 Layer by layer growth of upconversion core shell nanoparticles

Seed mediated layer by layer coating strategy were used in this thesis to construct upconversion core-shell nanoparticles[5, 6]. The core nanoparticles are used as seeds, and the precursors are injected to the reaction system to form the needed outer shell layer. The set up for the synthesis of core shell nanoparticles are shown as below (Figure 2.1). This set up is similar with that used in the core nanoparticles synthesis process. The only difference is that the injection syringe is used to inject the precursors at the neck of this flask. And before the injection, precursors with various doping ions need to be prepared.

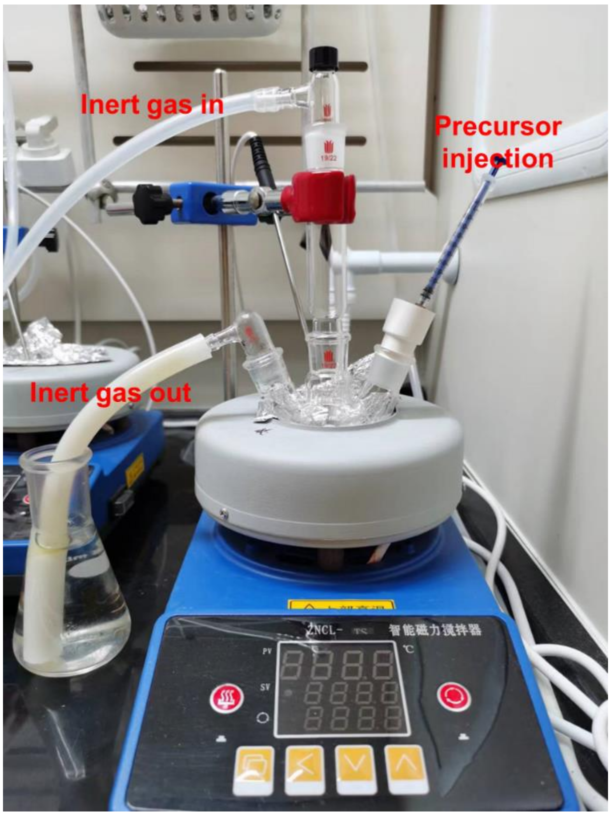

Figure 2.1 The reaction set up for the synthesis of upconversion nanoparticles.

And a typical NaYF$_4$ shell precursor procedure is as follows[2]: YCl$_3$·6H$_2$O (1 mmol) is added into a 50 mL three-necked flask containing 6 mL oleic acid (OA) and 15 mL

1-octadecene (ODE). The mixture is first heated to 160 ℃ under argon for 30 min to form a transparent solution and remove residual water. The solution is cooled down to room temperature, and 10 mL of a methanol solution containing NaOH (2.5 mmol) and NH_4F (4 mmol) is slowly dropped into the flask and stirred for 30 min. Then, the solution is heated to 70-80 ℃ and maintained for 30 min to evaporate methanol. And the reaction solution is further heated to 160 ℃for 30 min to remove the residual water before cooling down to room temperature.

For the seed-mediated layer by layer growth of upconversion nanocrystals with needed size: A total of 0.2 mmol seed nanocrystals in cyclohexane are added to a 50 mL flask containing 4 mL OA and 10 mL ODE. The mixture is heated to 160 °C under argon for 30 min to remove cyclohexene before the solution is further heated to 300 °C. Then, an appropriate amount of shell precursors is injected into the reaction mixture step-by-step with an injection rate of 0.25 mL every 3 min. After finish the injection of precursors, the reaction solution is ripened at 300 °C for additional 5 min. Finally, the reaction solution is cooled down to room temperature, and the resulting products are precipitated by ethanol and collected by centrifugation at 6000 rpm for 5 min. The precipitate is then purified with ethanol three times, and finally dispersed in cyclohexane for further use.

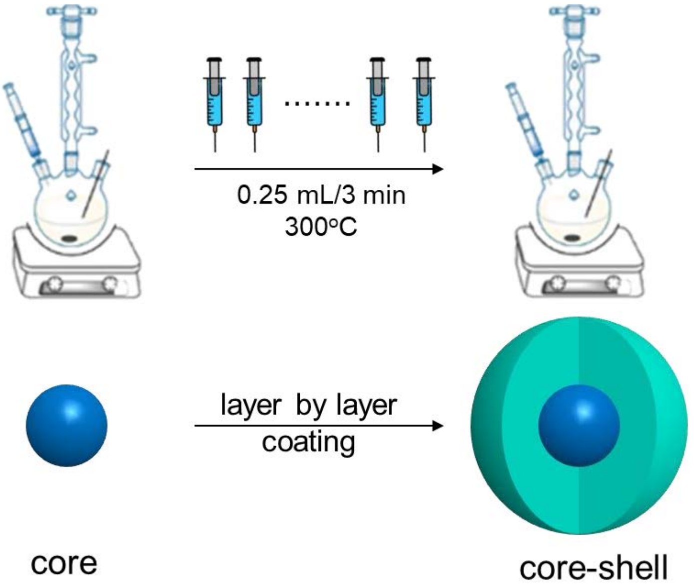

Figure 2.2 Schematic illustration of reaction equipment used in seed-mediated layer by layer growth method, and growth process of nanocrystals.

Due to the similarity of lanthanide ions and tiny crystal lattice mismatch of different types of $NaLnF_4$, homogenesis and heterogeneous core-shell structure can be obtained through this seed-mediated layer by layer growth strategy[7-9]. And the thickness of the shell layer can be easily controlled by the amount of precursor or the ratio between the added core nanoparticles and shell precursor. The needed amount of precursors for desired size can be calculated through a simplified homocentric sphere model[10-12].

2.4 Construction of microlaser

In this part, two strategies are introduced for the coating of upconversion nanoparticles gain media onto the surface of microcavity.

2.4.1 UCNPs coating through swelling-deswelling process of microcavity

As the microcavity we used is a kind of polystyrene microsphere, which can swell and de-swell at condition of different solvent. Upconversion nanoparticles can deposited on the surface of microsphere through Van Der Waals interactions[13-15]. In a typical process, the PS microsphere is swelled in the mixture of chloroform (10 μL) and butanol (100 μL) at room temperature. Then, upconversion nanoparticles in hexane are added to the mixed solution. The solution is vortexed for 30 s and sonicated for 2 mins to make the upconversion nanoparticles and PS microspheres are monodispersed. After incubation at room temperature for 4 h, the upconversion nanoparticles coated microspheres are collected by centrifuging at 3500 rpm. These microspheres are washed three times by alternating between ethanol and cyclohexane to remove the superfluous upconversion nanoparticles and stop the swelling process. The coating thickness can be controlled by the ratio of added microsphere and upconversion nanoparticles.

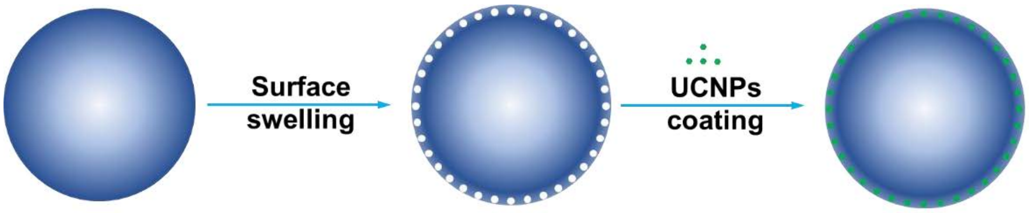

Figure 2.3 Schematic illustration of swelling and deswelling modulated upconversion nanoparticles coating process.

2.4.2 Electrostatic force driven UCNPs coating process

Although the swelling process promoted the deposition of upconversion nanoparticles onto the surface of microsphere, the smooth surface would be broken to some extent, which induce more scattering losses. Thus, another solution processed loading strategy driven by electrostatic force is developed[2]. The hydrophobic oleic acid ligands are removed from the surface of upconversion nanoparticles by acid washing. This makes the surface charge positive. Then, the electropositive upconversion nanoparticles can be coated onto the surface of electronegative microsphere easily.

Surface modification for water-soluble upconversion nanoparticles

The as-synthesized upconversion nanoparticles are coated with a layer of hydrophobic oleic acid ligands, which need to be removed for further usage. In a typical procedure, the nanoparticles were first precipitated by adding ethanol (2.0 mL) to a cyclohexane colloidal solution of the OA coated hydrophobic β-NaYF$_4$:20%Yb^{3+}, x%Tm^{3+} nanoparticles (1 mL, 10 mg/mL) and then collected by centrifugation at 6000 rpm for 5 min. The obtained nanoparticles were re-dispersed in a mixed solution of ethanol (1 mL) and HCl (1 mL, 2 M) upon sonication for 5 min[16, 17]. The ligand free nanoparticles were collected by centrifugation at 14680 rpm for 10 min and re-dispersed in deionized water (1 mL).

Figure 2.4 Schematic illustration of HCl assisted surface modification.

Fabrication of upconverting microlasers

Upconverting microlasers were also produced through a solution process. In a typical procedure, 10 μL PS microbeads (10% solids) were first dispersed in 1000 μL deionized (DI) water upon sonication for 5 min. Then 7 μL ligand free water-soluble upconversion nanoparticles (8 mg/mL) were mixed together with PS microbeads upon sonication. This mixed solution was kept for a gentle shake (750 rpm) for 2 hours before centrifugation. During this stage, the electropositive upconversion nanoparticles would attach onto the electronegative surface of PS microbeads through the electrostatic force assembly. All these processes were carried out at room temperature. Then, these upconversion nanoparticles coated microbeads were further washed with ethanol and water for three times to remove the surplus upconversion nanoparticles. Finally, these microbeads were re-dispersed in water or ethanol for further usage. Noting that, the coated surface and thickness can be controlled precisely by tuning the concentration ratio of microbeads and nanoparticles.

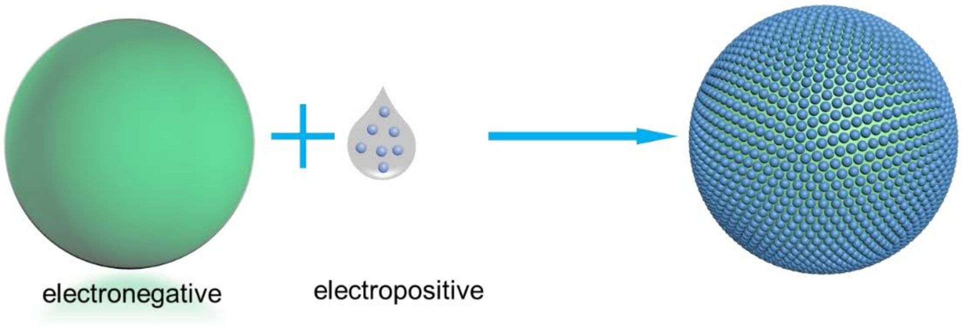

Figure 2.5 Schematic illustration of electrostatic force driven UCNPs coating process.

2.5 Characterization methods and home-built optical instruments

2.5.1 Conventional characterization method

The characterization of morphology, size, absorption spectrum and surface charge is introduced in this part. The conventional measurement including, TEM images, SEM images, Zeta potential, absorption spectra are shown as follow:

TEM

Transmission electron microscope (TEM) measurements were performed using an FEI Tecnai T20 instrument with an operating voltage of 120 kV. The samples for TEM analysis were prepared by placing a drop of a dilute suspension of nanoparticles onto carbon-coated copper grids, and dry in the oven at 60 °C for 5 mins.

SEM

The morphology of microcavity coated with upconversion nanoparticles was characterized via scanning electron microscope (SEM) imaging (Supra 55VP, Zeiss) operated at 3.00 kV. And the samples were prepared by adding a drop of solution sample to the silicon wafer, and dry in the oven. Then, a layer of 7 nm Au/Pt was coated (Leica EM ACE600 High Vacuum Coater) for better electrical conductivity and high resolution.

As for the EDS element mapping and spectrum, Zeiss EVO LS15 SEM was used and operated at 15.00 kW.

Zeta potential

The measurement of zeta potential (ζ-potential) was carried out in aqueous solution by Zetasizer (Malvern Panalytical).

Absorption spectra

The absorption spectra of upconversion nanoparticles were measured by using the Agilent Cary 60 UV-Vis spectrophotometer (400~1100 nm) with a step of 1 nm.

2.5.2 Spectra and lifetime measurement system for solution sample

The emission spectra of as-prepared UCNPs in solution were measured with a simple home-made system as shown in Figure 2.6. A fiber coupled 976 nm laser (BL976-PAG900, Thorlabs) with collimation lens was used as excitation source, and a commercial fiber coupled spectrometer (iHR550 and Shamrock 193i switchable) was used to collect the fluorescent signal. A short pass filter (FF01-842/SP-25, Semrock) was used to block the excitation laser and allow the transmission of 400-842 nm emission signal. The solution sample was placed in the sample cuvette, and the angle of excitation and collection is perpendicular to avoid the interference from laser signals. A collection lens was used to gather the anti-Stokes emissions from upconversion nanoparticles and coupled to an optical fiber for spectra measurement. The power dependent spectra were measured by recording the spectrum at different power density (adjust the output power of the excitation laser). Then we can plot the emission intensity with the function of excitation power density in the log-to-log graphs. The linear fitting slopes of this graph indicate the photons needed in each upconverting process.

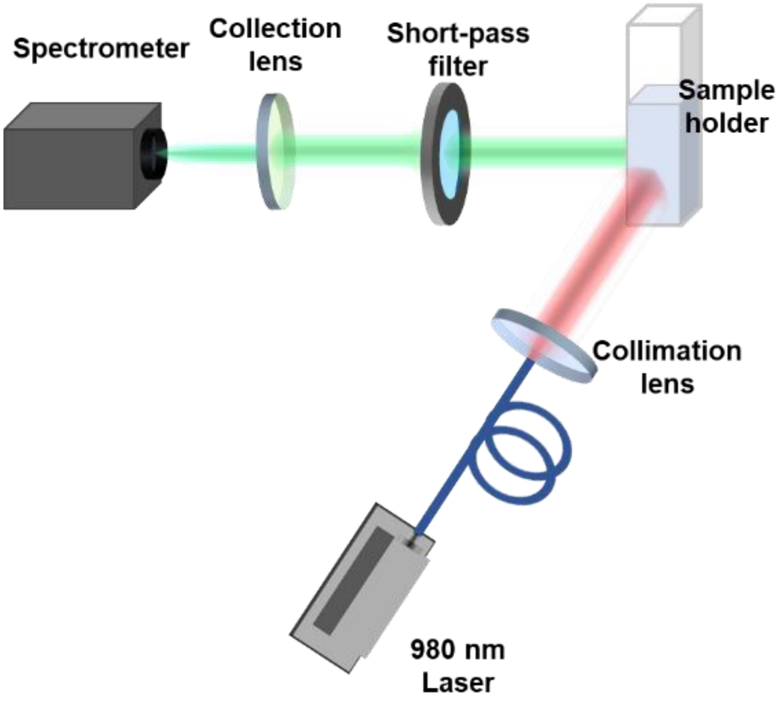

Figure 2.6 Schematic illustration of home-made emission spectrum measurement setup.

As for the emission lifetime measurement setup, it was modified from the spectra measurement setup. Due to the multi-band emission of lanthanide doped upconversion nanoparticles, a related band pass filter for selected emission peak is needed. The decay curve of a characteristic emission peak, corresponding energy level transition, is recorded by a gate mode single photon counting modules (SPCM-AQRH-14-FC, Excelitas Technologies). And the time gating counting is achieved by synchronizing the laser and SPCM with a NI data acquisition (USB-6353 DAQ). Then, the emission intensity of each gate-width is accumulated and recorded according to time-gating scale. The laser pulse width and signal collection width can be tuned for different emission peaks. The collection steps are as small as 1μs, and all of these parameters can be adjusted through a specially written LabVIEW program.

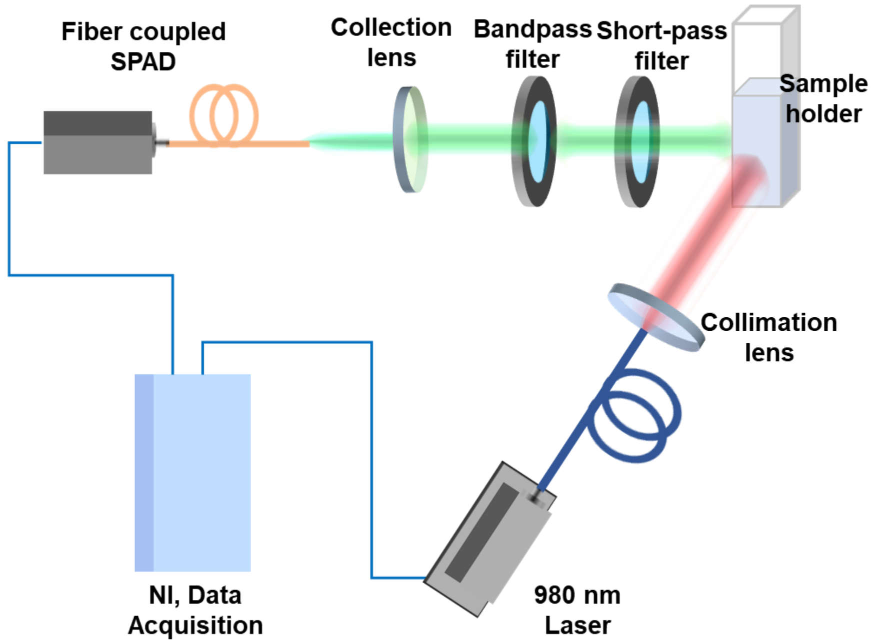

Figure 2.7 Schematic illustration of home-made emission lifetime (decay curve) measurement setup.

2.5.3 Confocal microscopy and spectroscopy

The inverted confocal optical system was built on a sample scanning configuration employing a 3D piezo stage[18-20]. A single-mode fiber-coupled 976 nm diode laser (BL976-PAG900, Thorlabs) was used as the excitation source and was focused onto the sample through an oil-immersion objective lens (100×, NA = 1.4; UPlanAPO, Olympus). The emission from sample was collected by the same objective lens then refocused into an optical fiber that has a core size matching with system Airy disk. A Single Photon Counting Avalanche Diode (SPAD) detector was connected to the collection optical fiber to detect the emission intensity. The single nanoparticles images were achieved by recording the emission intensity of each point when moving the 3D piezo stage. The spectra were measured with a fiber-coupled spectrometer (Shamrock 193i, Andor) with a grating of 1200 grooves/mm (resolution: 0.21 nm, data collection step: ~0.04 nm) and EMCCD detector (iXon Ultra 888, Andor). The detection of single nanoparticle image and spectrum is switchable by just exchanging the coupling fibers. And the lifetime measurement of single nanoparticle is similar to the solution ones. Time gating emission intensity is recorded by the SPAD and plotted with the function of time.

The wide field microscope images were acquired from the camera when the flexible mirror is switched to the camera paths. The polarization performance of this upconverting microlaser was characterized by rotating a λ/2 plate @808 nm while cooperated with a polarizer (620-1000 nm). Spectra at different polarization angles can be recorded.

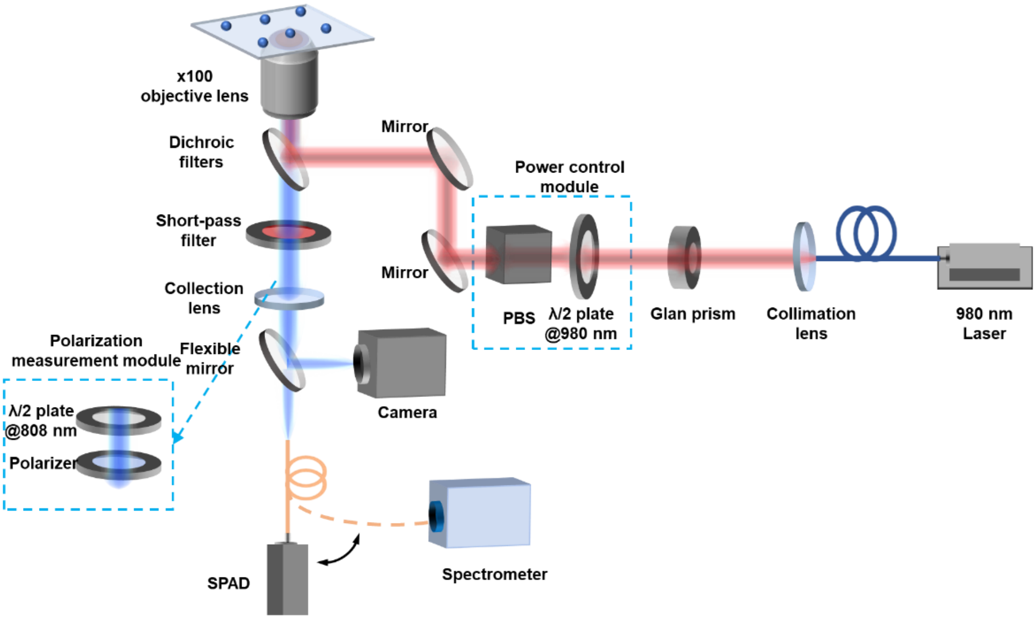

Figure 2.8 Schematic diagram of home-built inverted confocal optical system.

The temperature dependent spectra were measured with extra heating platform. A home built heating platform, containing a heater (HT24S, Thorlabs), thermocouple (TH100PT, Thorlabs), and temperature controller (TC200, Thorlabs), was integrated with the sample holder. The temperature of sample slides carrying microlasers can be measured and controlled by this heating platform with an accuracy of 0.1 K. Noting that the oil-immersion objective lens (100×, NA = 1.4; UPlanAPO, Olympus) was replaced with an air objective lens (100×, NA=0.9, Olympus). And the whole optical system was aligned before use.

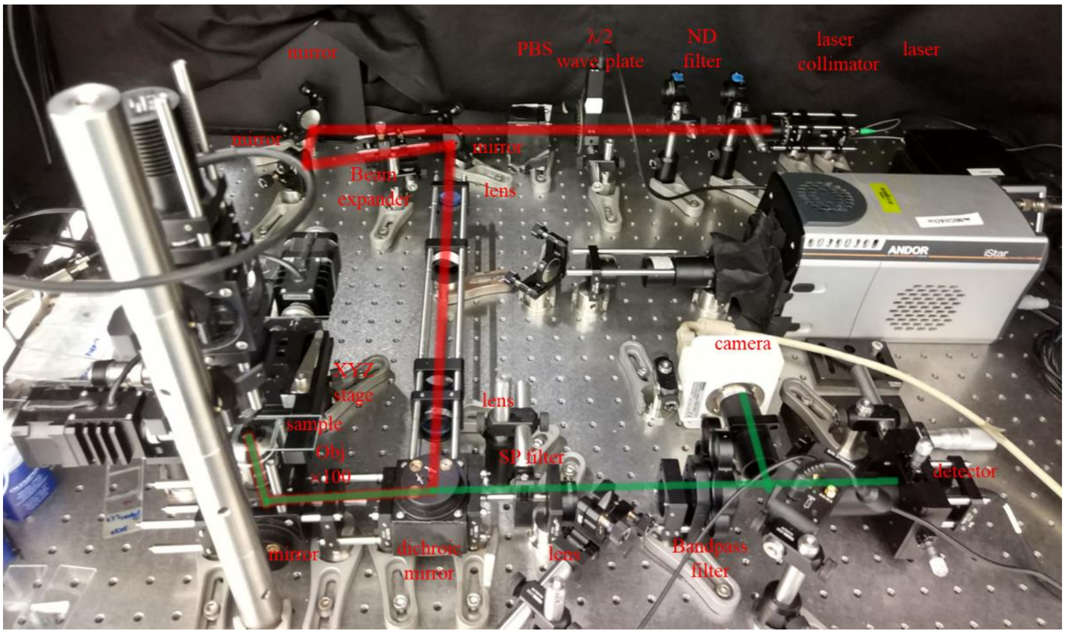

Figure 2.9 Photograph of home built inverted confocal optical system.

Due to the theoretical optical resolution of this home-built inverted confocal system is about 490 nm, adjacent nanoparticles with a distance smaller than 490 nm are indistinguishable[21-23]. To get individual distributed UCNPs, the sample slides need to be prepared carefully. In a typical procedure, the coverslips were firstly cleaned with ethanol and DI water by ultrasonication, and dry in the oven. Upconversion nanoparticles were diluted to 10 ng/mL in cyclohexane solution for further usage. Then, 10 μL nanoparticles was dropped onto the surface of coverslip, and dry in the oven. The nanoparticles would spread out evenly when the droplet containing nanoparticles distributed uniformly on the coverslip surface. Finally, the coverslip with individual distributed UCNPs was put over a clean glass slide, and packaged by glue before measuring.

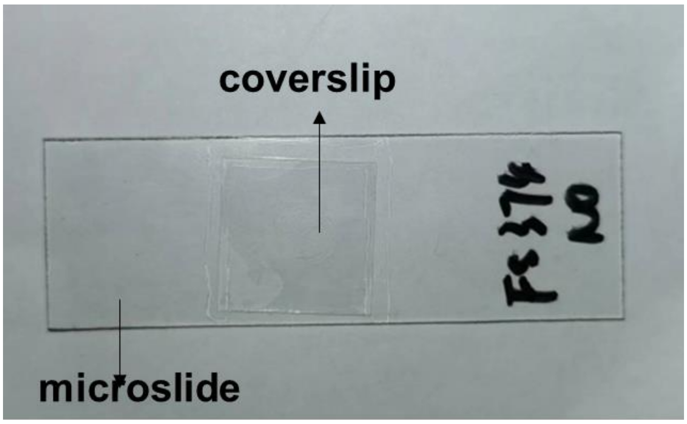

Figure 2.10 Photograph of sample slide carrying individual-distributed UCNPs.

The preparation of coverslip with microlaser is similar to the process of single nanoparticle slide. Noting that, the coverslip needs to be dry in the oven at 60 °C for 30 mins.

2.5.4 Finite difference time domain simulations

Numerical simulations of our microcavity were performed using Lumerical FDTD solutions and MATLAB code[24-26]. For the simulation of the electrical-field distributions and resonance spectrum, the perfectly matched layer (PML) was set as the boundary condition with a simulation region of 6μm× 6μm× 6μm; the monitored wavelength was 400-1000 nm; the meshes order was 10 nm; the light type was a dipole source. The simulated resonance spectrum and electric field distribution of microcavity were calculated separately. The cavity modes were achieved while changing the sizes of the microcavity. The electrical-field distributions at ~800 nm mode was plotted along the diameter.

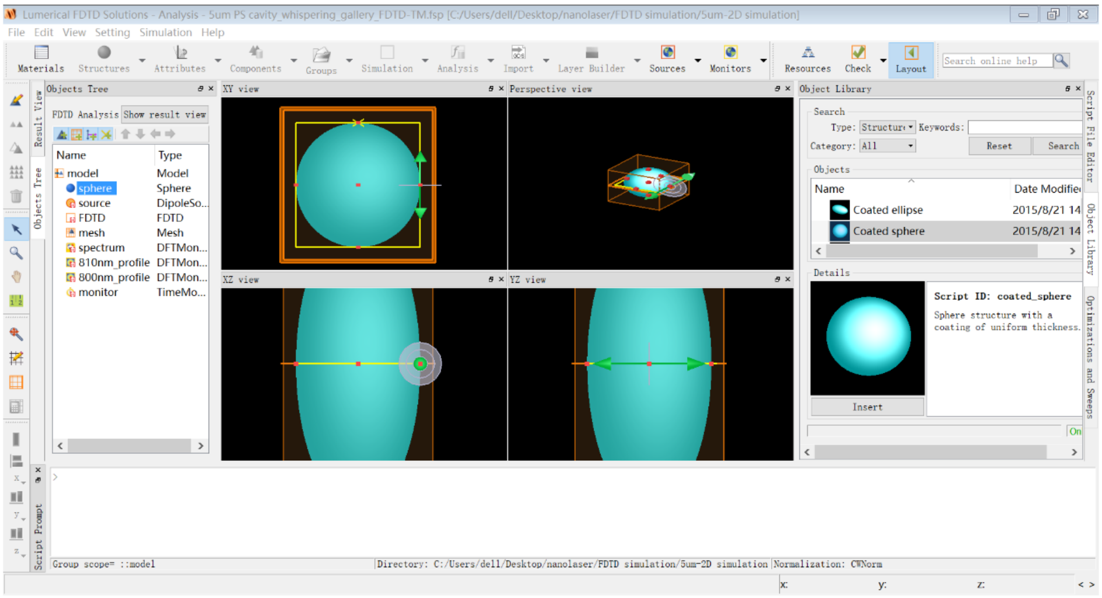

Name	Type
model	Model
sphere	Sphere
source	DipoleSo...
FDTD	FDTD
mesh	Mesh
spectrum	DFTMon...
810nm_profile	DFTMon...
800nm_profile	DFTMon...
monitor	TimeMo...

Name	Date Modified
Coated ellipse	2015/8/21 14
Coated sphere	2015/8/21 14

Script ID: coated_sphere

Sphere structure with a coating of uniform thickness.

Group scope= ::model

Directory: C:/Users/dell/Desktop/nanolaser/FDTD simulation/5um-2D simulation

Normalization: CWNorm

Figure 2.11 Simulations interface of Lumerical FDTD solutions.

2.6 Reference

1. Zhao, J.; Jin, D.; Schartner, E. P.; Lu, Y.; Liu, Y.; Zvyagin, A. V.; Zhang, L.; Dawes, J. M.; Xi, P.; Piper, J. A. Single-nanocrystal sensitivity achieved by enhanced upconversion luminescence. *Nat Nanotechnol* **2013,** 8 (10), 729.
2. Shang, Y.; Zhou, J.; Cai, Y.; Wang, F.; Fernandez-Bravo, A.; Yang, C.; Jiang, L.; Jin, D. Low threshold lasing emissions from a single upconversion nanocrystal. *Nature Communications* **2020,** 11 (1), 6156 DOI: 10.1038/s41467-020-19797-4.
3. Shang, Y.; Hao, S.; Lv, W.; Chen, T.; Tian, L.; Lei, Z.; Yang, C. Confining excitation energy of Er 3+-sensitized upconversion nanoparticles through introducing various energy trapping centers. *J Mater Chem C* **2018,** 6 (15), 3869-3875.
4. Liao, J. Y.; Jin, D. Y.; Chen, C. H.; Li, Y. M.; Zhou, J. J. Helix Shape Power-Dependent Properties of Single Upconversion Nanoparticles. *Journal of Physical Chemistry Letters* **2020,** 11 (8), 2883-2890 DOI: 10.1021/acs.jpclett.9b03838.
5. Liu, D.; Xu, X.; Du, Y.; Qin, X.; Zhang, Y.; Ma, C.; Wen, S.; Ren, W.; Goldys, E. M.; Piper, J. A. Three-dimensional controlled growth of monodisperse sub-50 nm heterogeneous nanocrystals. *Nature communications* **2016,** 7, 10254.
6. Li, D.; Wen, S. H.; Kong, M. Y.; Liu, Y. T.; Hu, W.; Shi, B. Y.; Shi, X. Y.; Jin, D. Y. Highly Doped Upconversion Nanoparticles for In Vivo Applications Under Mild Excitation Power. *Anal Chem* **2020,** 92 (16), 10913-10919 DOI: 10.1021/acs.analchem.0c02143.
7. Li, X. M.; Shen, D. K.; Yang, J. P.; Yao, C.; Che, R. C.; Zhang, F.; Zhao, D. Y. Successive Layer-by-Layer Strategy for Multi-Shell Epitaxial Growth: Shell Thickness and Doping Position Dependence in Upconverting Optical Properties. *Chem Mater* **2013,** 25 (1), 106-112 DOI: 10.1021/cm3033498.

8. Fischer, S.; Swabeck, J. K.; Alivisatos, A. P. Controlled Isotropic and Anisotropic Shell Growth in beta-NaLnF4 Nanocrystals Induced by Precursor Injection Rate. *J Am Chem Soc* **2017,** 139 (35), 12325-12332 DOI: 10.1021/jacs.7b07496.

9. Li, X. M.; Guo, Z. Z.; Zhao, T. C.; Lu, Y.; Zhou, L.; Zhao, D. Y.; Zhang, F. Filtration Shell Mediated Power Density Independent Orthogonal Excitations-Emissions Upconversion Luminescence. *Angew Chem Int Edit* **2016,** 55 (7), 2464-2469 DOI: 10.1002/anie.201510609.

10. Shao, W.; Chen, G.; Damasco, J.; Wang, X.; Kachynski, A.; Ohulchanskyy, T. Y.; Yang, C.; Agren, H.; Prasad, P. N. Enhanced upconversion emission in colloidal $NaYF_4$:Er^{3+}/$NaYF_4$ core/shell nanoparticles excited at 1523 nm. *Opt Lett* **2014,** 39 (6), 1386-9 DOI: 10.1364/OL.39.001386.

11. Johnson, N. J. J.; Korinek, A.; Dong, C. H.; van Veggel, F. C. J. M. Self-Focusing by Ostwald Ripening: A Strategy for Layer-by-Layer Epitaxial Growth on Upconverting Nanocrystals. *J Am Chem Soc* **2012,** 134 (27), 11068-11071 DOI: 10.1021/ja302717u.

12. Zhang, F.; Che, R. C.; Li, X. M.; Yao, C.; Yang, J. P.; Shen, D. K.; Hu, P.; Li, W.; Zhao, D. Y. Direct Imaging the Upconversion Nanocrystal Core/Shell Structure at the Subnanometer Level: Shell Thickness Dependence in Upconverting Optical Properties. *Nano Lett* **2012,** 12 (6), 2852-2858 DOI: 10.1021/nl300421n.

13. Fernandez-Bravo, A.; Yao, K.; Barnard, E. S.; Borys, N. J.; Levy, E. S.; Tian, B.; Tajon, C. A.; Moretti, L.; Altoe, M. V.; Aloni, S.; Beketayev, K.; Scotognella, F.; Cohen, B. E.; Chan, E. M.; Schuck, P. J. Continuous-Wave Upconverting Nanoparticle Microlasers. *Nat. Nanotechnol.* **2018,** 13, 572.

14. Liu, Y. W.; Teitelboim, A.; Fernandez-Bravo, A.; Yao, K. Y.; Altoe, M. V. P.; Aloni, S.; Zhang, C. H.; Cohen, B. E.; Schuck, P. J.; Chan, E. M. Controlled Assembly of Upconverting Nanoparticles for Low-Threshold Microlasers and Their Imaging in Scattering Media. *Acs Nano* **2020,** 14 (2), 1508-1519 DOI: 10.1021/acsnano.9b06102.

15. Yang, X. F.; Lyu, Z. Y.; Dong, H.; Sun, L. D.; Yan, C. H. Lanthanide Upconverted Microlasing: Microlasing Spanning Full Visible Spectrum to Near-Infrared under Low Power, CW Pumping. *Small* **2021,** 17 (41), DOI: Artn 2103140
10.1002/Smll.202103140.

16. Wang, F.; Deng, R.; Wang, J.; Wang, Q.; Han, Y.; Zhu, H.; Chen, X.; Liu, X. Tuning upconversion through energy migration in core–shell nanoparticles. *Nat Mater* **2011,** 10 (12), 968.

17. Su, Q.; Han, S.; Xie, X.; Zhu, H.; Chen, H.; Chen, C.-K.; Liu, R.-S.; Chen, X.; Wang, F.; Liu, X. The effect of surface coating on energy migration-mediated upconversion. *J Am Chem Soc* **2012,** 134 (51), 20849-20857.

18. Zhao, J. B.; Jin, D. Y.; Schartner, E. P.; Lu, Y. Q.; Liu, Y. J.; Zvyagin, A. V.; Zhang, L. X.; Dawes, J. M.; Xi, P.; Piper, J. A.; Goldys, E. M.; Monro, T. M. Single-nanocrystal sensitivity achieved by enhanced upconversion luminescence. *Nat Nanotechnol* **2013,**

8 (10), 729-734 DOI: 10.1038/nnano.2013.171.

19. Chen, C.; Wang, F.; Wen, S.; Su, Q. P.; Wu, M. C. L.; Liu, Y.; Wang, B.; Li, D.; Shan, X.; Kianinia, M. Multi-photon near-infrared emission saturation nanoscopy using upconversion nanoparticles. *Nature Communications* **2018,** 9 (1), 3290.

20. Ma, C.; Xu, X.; Wang, F.; Zhou, Z.; Liu, D.; Zhao, J.; Guan, M.; Lang, C. I.; Jin, D. Optimal Sensitizer Concentration in Single Upconversion Nanocrystals. *Nano Lett* **2017,** 17 (5), 2858-2864 DOI: 10.1021/acs.nanolett.6b05331.

21. Wang, F.; Wen, S.; He, H.; Wang, B.; Zhou, Z.; Shimoni, O.; Jin, D. Microscopic inspection and tracking of single upconversion nanoparticles in living cells. *Light: Science & Applications* **2018,** 7 (4), 18007-18007.

22. Zhou, J.; Chizhik, A. I.; Chu, S.; Jin, D. Single-particle spectroscopy for functional nanomaterials. *Nature* **2020,** 579 (7797), 41-50 DOI: 10.1038/s41586-020-2048-8.

23. Dong, H.; Sun, L. D.; Yan, C. H. Upconversion emission studies of single particles. *Nano Today* **2020,** 35, DOI: Artn 100956
10.1016/J.Nantod.2020.100956.

24. Gargas, D. J.; Moore, M. C.; Ni, A.; Chang, S. W.; Zhang, Z. Y.; Chuang, S. L.; Yang, P. D. Whispering Gallery Mode Lasing from Zinc Oxide Hexagonal Nanodisks. *Acs Nano* **2010,** 4 (6), 3270-3276 DOI: 10.1021/nn9018174.

25. Ward, J.; Benson, O. WGM microresonators: sensing, lasing and fundamental optics with microspheres. *Laser & Photonics Reviews* **2011,** 5 (4), 553-570.

26. Jiang, X. F.; Zou, C. L.; Wang, L.; Gong, Q. H.; Xiao, Y. F. Whispering-gallery microcavities with unidirectional laser emission. *Laser & Photonics Reviews* **2016,** 10 (1), 40-61 DOI: 10.1002/lpor.201500163.

Chapter 3 Cross-relaxation induced upconversion nanoparticles for low threshold lasing emission

3.1 Introduction

Lanthanide-doped upconversion nanoparticles (UCNPs), based on step-wise absorption of two or more photons through real energy levels with long lifetime, are one of the most efficient non-linear emitters[1]. The abundant metastable energy levels of lanthanide ions facilitate the establishment of population inversion (Figure 3.1), which makes it promising as lasing gain media, especially for nonlinear upconverting laser with huge anti-stokes shift[2-5]. Meanwhile the super long excited states lifetime (on the order of milliseconds or microseconds) usually lead to low saturation intensity, which allows set up of population inversion under continuous pumping[6-8]. Recently, miniaturized lasers have attracted intense interest due to the demand from the emerging optical interconnects, ultra-dense data storage, near-field spectroscopy, super-resolution imaging, optical probing and sensing[9-12]. However, the reduced cavity size leads to increased optical losses, insufficient gain and further induces the rise of lasing thresholds[9, 13, 14], which present a huge challenge for practical applications of these microlasers.

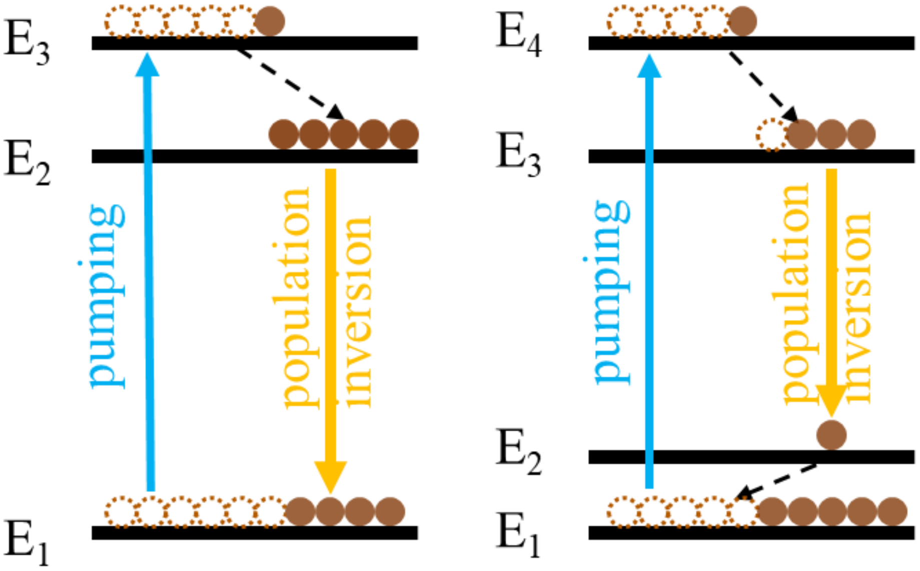

Figure 3.1 Three (left) and four (right) level system that can achieve population inversion.

The onset lasing emission threshold power is used for compensating the cavity losses and achieving population inversion of the gain medium[8]. Thus, it is possible to keep lowering the threshold through selecting a high-quality cavity and optimizing the gain medium. Among current microcavities, whispering-gallery mode (WGM) cavity has attracted considerable interests in the past decades due to the high quality (Q) factors and small mode volumes, which result in low pumping threshold and narrow linewidth. Multiphoton upconversion lasing have been achieved in several kinds of WGM microcavities ranging from microrods shaped upconversion crystals[15, 16], lanthanide doped amorphous microspheres[17, 18] or microtoroidals[19], to UCNPs doped bottle-like microcavity[3, 5, 20] and microdisk[21] et al. However, due to tough population inversion within multiphoton processes, upconverting microlasers are still suffering from high pumping power and require pulsed excitation. Meanwhile, energy accumulation in selected energy level arisen from energy cross relaxation[2, 22], energy looping[6, 23], excited state energy exchanges[24] would accelerate population enrichment, which has the potential to lower the threshold. Recently, room temperature continuous-wave (CW) pumped upconverting lasing at 450 nm and 800 nm was obtained through the usage of single Tm^{3+} doped $NaYF_4$ nanocrystals[6]. The avalanche-like energy looping mechanism is an efficient strategy to achieve energy accumulation in the selected $^3H_4$ (Tm^{3+}) state, which would further facilitate the formation of low threshold (~14 kW/cm^2) lasing emission with a high-quality polystyrene microsphere acting as resonant cavity. However, the tiny absorption cross section and low upconversion efficiency of recent single Tm^{3+} doped $NaYF_4$ energy looping nanosystem restrained the further reduction of threshold.

In this chapter, we demonstrate another low threshold upconverting micolaser by combining Yb^{3+}/Tm^{3+} co-doped efficient energy accumulation upconversion nanocrystals with a high-quality microscale whispering-gallery-mode cavity. The competitive processes of energy transfer upconversion and cross relaxation reach a situation of harmony within this efficient energy accumulation nanosystem. The well-designed Yb^{3+}/Tm^{3+} co-doped upconversion nanocrystals can not only tune the population distribution of each energy level, but also suppress serious nonradiative transition in excessively high doping particles. Taking the advantages of moderate cross relaxation process, powerful enrichment of population distribution in $^3H_4$ state can be obtained with restrained energy loss under lower pumping power density. Thus, CW pumped upconverting lasing emission is achieved with a threshold as low as ~150 W/cm^2.

3.2 Experimental Section

3.2.1 Synthesis of NaYF:20%Yb, x%Tm^{3+} based upconversion gain medium

Materials

All chemicals were of analytical grade and used without further purification. $YCl_3 \cdot 6H_2O$ (99.99%), $TmCl_3 \cdot 6H_2O$ (99.99%), $YbCl_3 \cdot 6H_2O$ (99.99%), NH_4F (99.99%), NaOH (99.9%), oleic acid (OA, 90%), 1-octadecene (ODE, 90%) and 5 μm PS microbeads were supplied by Sigma-Aldrich.

Synthesis of β-$NaYF_4$:20%Yb, x%Tm^{3+} nanoparticles (x=0.2, 0.5, 1, 2, 4, 8)

The uniform oleic-acid-capped nanoparticles (β-$NaYF_4$:20%Yb, x%Tm^{3+}) were synthesized by the coprecipitation method modified from previous report[25, 26]. A typical procedure is as follows: $YCl_3 \cdot 6H_2O$ (0.8-x mmol), $YbCl_3 \cdot 6H_2O$ (0.2 mmol) and $TmCl_3 \cdot 6H_2O$ (x mmol) were added into a 50 mL three-necked flask containing 6 mL oleic acid (OA) and 15 mL 1-octadecene (ODE). The mixture was first heated to 160 °C under argon for 30 min to form a transparent solution and remove residual water. The solution was cooled down to room temperature, and 10 mL of a methanol solution containing NaOH (2.5 mmol) and NH_4F (4 mmol) was slowly dropped into the flask and stirred for 30 min. Then, the solution was heated to 70-80 °C and maintained for 30 min to evaporate methanol. Subsequently, the solution was heated to 300 °C and maintained for 1 h under argon atmosphere. After cooling down to room temperature, the resulting products were precipitated by ethanol and collected by centrifugation at 6000 rpm for 5 min. The precipitate was then purified with ethanol three times, and finally dispersed in cyclohexane for further use.

Surface modification for water-soluble upconversion nanoparticles

The hydrophobic oleic acid ligands coated on the surface of as-synthesized upconversion nanoparticles need to be removed for further usage. In a typical procedure, the nanoparticles were first precipitated by adding ethanol (2.0 mL) to a cyclohexane colloidal solution of the OA coated hydrophobic β-$NaYF_4$:20%Yb, x%Tm^{3+} nanoparticles (1 mL, 10 mg/mL) and then collected by centrifugation at 6000 rpm for

5 min. The obtained nanoparticles were re-dispersed in a mixed solution of ethanol (1 mL) and HCl (1 mL, 2 M) upon sonication for 5 min[27, 28]. The ligand free nanoparticles were collected by centrifugation at 14680 rpm for 10 min and re-dispersed in deionized water (1 mL). As can be seen, the morphology and sizes of upconversion nanoparticles didn't change so much before and after HCl assisted ligands free treatment. However, due to the removement of surface ligands, the distribution in the TEM images changes slightly, for example, partial nanoparticles are attached with each other.

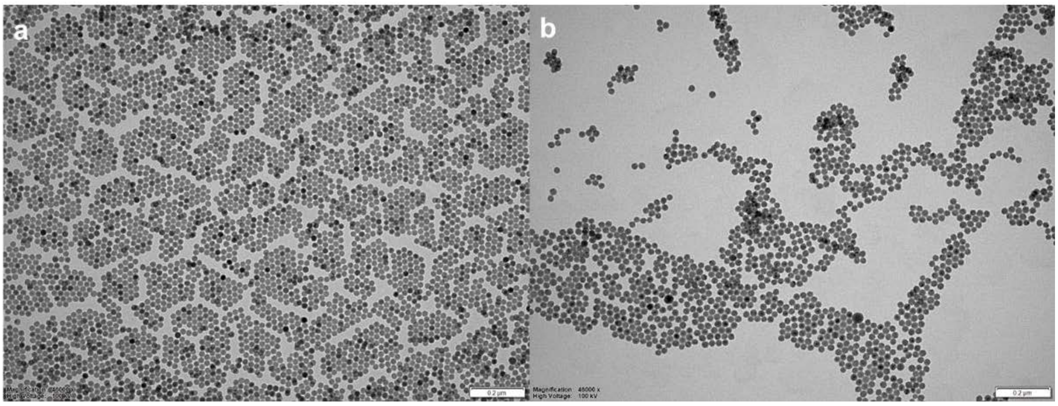

Figure 3.2 TEM images **a**, before and **b**, after HCl assisted ligands free.

3.2.2 Fabrication of upconverting microlasers

Methods I: Swelling and deswelling modulated UCNPs deposition

In a typical process, the PS microspheres (7 μL, 10% solids) were swelled in the mixture of 10 v/v% chloroform in butanol (110 μL) at room temperature. OA ligands coated hydrophobic β-$NaYF_4$:20%Yb, *x*%Tm^{3+} upconversion nanoparticles (10 μL, 10 mg/mL) in hexane are added to the mixed solution. The solution is vortexed for 30 s and sonicated for 2 mins to make the upconversion nanoparticles and PS microspheres intensive mixing. After incubation at room temperature for 4 h, the upconversion nanoparticles coated microspheres are collected by centrifuging at 3500 rpm. These microspheres are washed three times by alternating between ethanol and cyclohexane to remove the superfluous upconversion nanoparticles and stop the swelling process.

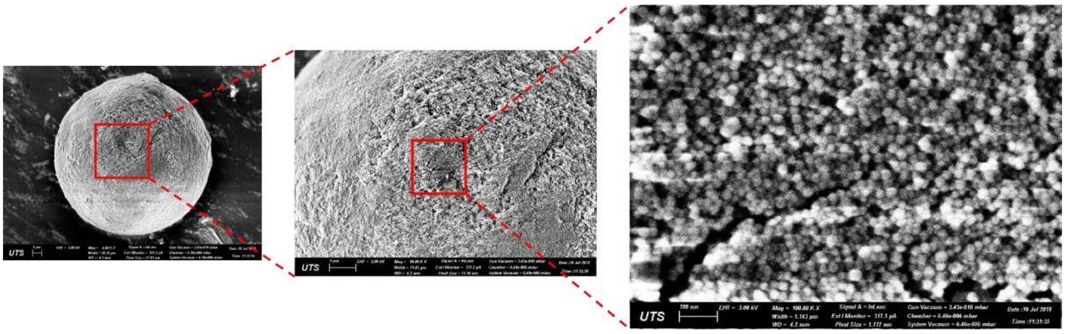

Figure 3.3 SEM images show that the UCNPs were coated on the surface of PS microbeads.

Methods II: Electrostatic force driven UCNPs coating strategy

In a typical procedure, 10 µL PS microbeads (10% solids) were first dispersed in 1000 µL DI water upon sonication for 5 min, then 7 µL ligand free water-soluble upconversion nanoparticles (8 mg/mL) were mixed together with PS microbeads upon sonication. Then, this mixed solution was kept for a gentle shake (750 rpm) for 2 hours before centrifugation. These upconversion nanoparticles coated microbeads were further washed with ethanol and water for three times, and finally were re-dispersed in water.

With the unform coating of UCNPs on the surface of microcavity, the upconversion emission from UCNPs can be coupled into the internal surface of this microsphere. Then, the coupled emissions would travel along the interface through total internal reflection. When the light goes back the same point during the looping process, amplification at these nodes can be achieved. Laing emission would arise when the gain is larger than losses.

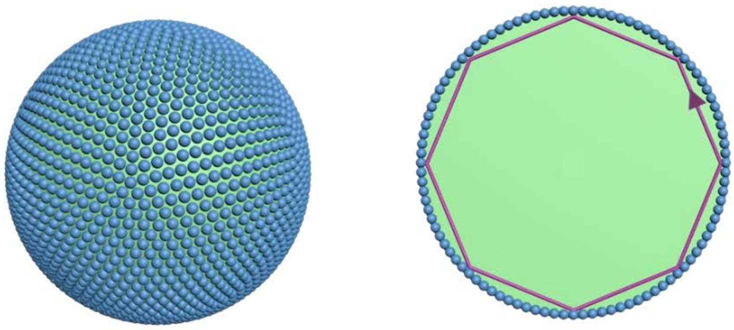

Figure 3.4 Schematic illustration and cross-section drawn of UCNPs coated WGM cavity

3.3 Results and Discussion

3.3.1 CR modulated upconversion gain media

Cross-relaxation (CR) refers to an efficient energy transfer process between a pair of nearby emitters, where one at a higher excited energy state transfers its photon energy to the other one at a lower excited state or ground state, so that both can simultaneously reach their intermediate excited states[29]. This process can be often observed in lanthanides ions those featured with a series of sophisticated intermediate energy levels and each with long lifetimes[2, 30]. CR accumulates energy in the intermediate excited states, as a conducive process to the formation of population inversion that is essential for the generation of lasing emissions. This explains why lanthanide ions doped laser crystals and glass are ascendant gain medium[4, 31, 32]. Though the concentration of lanthanide ions determines the extent of CR and thereby the threshold for lasing emission generation, in the bulk materials the doping uniformity and dynamic range of lanthanide ions are hard to control, *e.g.* typically 0.25 to 1 % for Tm^{3+} in YVO_4, $MgWO_4$ or YAG laser crystal ($< 8\times10^{20}$ ions/cm^3)[33-35]. High doping in bulk crystal and glass often leads to the non-uniform distribution of the ions and localized excessive CR, which results in luminescence quenching, self-heating, and high laser threshold.

At the nanoscale, wet chemistry synthesis strategies for lanthanides doped upconversion nanoparticles (UCNPs) have been well developed. The size, shape and doping concentrations of UCNPs can be precisely controlled with high accuracies to achieve morphological and optical uniformities[27, 36-40]. In a typical $NaYF_4$ host, the doping percentage of a lanthanide ion can be arbitrarily tuned between zero and its unity to form the "alloyed" nanocrystals[41, 42]. This allows several recent studies on the role of doping concentrations and the degree of cross-relaxation between ions in increasing the efficiency of optical depletion in super-resolution microscopy and facilitating the generation of near-infrared and single band emissions[2, 22, 24, 43-45]. As design, when the concentration of Tm^{3+} is fixed at low level, the population inversion purely depends on the high-power density of the pumping laser, as the activation of the emitters is mainly through the sensitization of Yb^{3+} and there is negligible CR due to the long distance between the lanthanide ions. The dependence on the high-power excitation can be alleviated by CRs, ($^1G_4$, $^3H_6 \rightarrow$ $^3H_5$, $^3H_4$), ($^1G_4$, $^3H_6 \rightarrow$ $^3F_{2,3}$, $^3F_4$), ($^3F_{2,3}$, $^3F_4 \rightarrow$ $^3H_4$, $^3H_5$)[22, 46], which facilitates the establishment of population inversion at intermediate levels, such as $^3H_4$. Besides, highly Tm^{3+} doped UCNPs leads to the decrease in the Yb^{3+}-Tm^{3+} distance and increase in the Yb^{3+}-Tm^{3+} energy transfer efficiency. But this strategy, as illustrated in Figure 3.5c, could lead to a quenching of the overall upconversion emissions, when doping too many emitters. To alleviate the concentration quenching and energy back transfer effects in the highly doped UCNPs, high excitation power density is required to pump the significant amount of the ground level Tm^{3+} emitters and Yb^{3+} sensitizers. These suggest the existence of a sweet spot of optimum Tm^{3+} doping concentration and excitation pumping power for the low threshold establishment of population inversion.

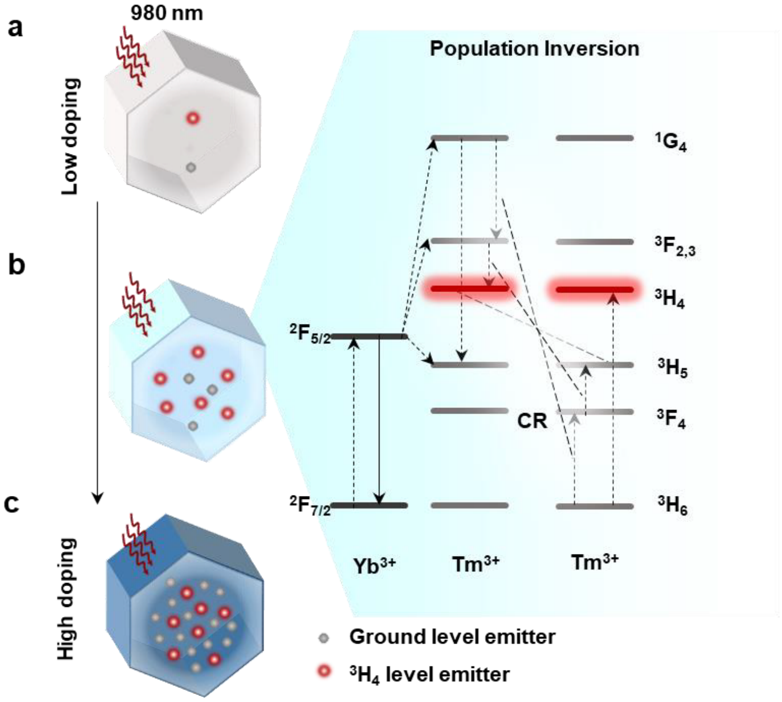

Figure 3.5 a-c, Schematic illustration of the simplified energy level diagram and the role of doping concentration of Tm^{3+} in establishing the CR enabled population inversion of $^3H_4$ level, compared to the ground level.

A series of hexagonal phase $NaYF_4$:20%Yb^{3+}/x%Tm^{3+} (x=~0.2-8 mol%) nanocrystals were synthesized through a coprecipitation method[26, 47]. The TEM images displayed the Figure 3.6 of a series of morphology-uniform UCNPs at different Tm^{3+} concentrations show the monodispersity of the as-prepared nanocrystals. Within the volume of ~7240 nm^3, in a 24 nm UCNP (the inset of Figure 3.6), we tune the amount of the Tm^{3+} ions from ~200 to ~8000, 0.2 mol.% to 8 mol.% correspondingly. And the averaged large distance can be calculated as ~3.3 nm at the doping concentration of 0.2 mol.%. Thus, the possibility of CR can be well tuned in these UCNPs from the point of distance between two nearby emitters.

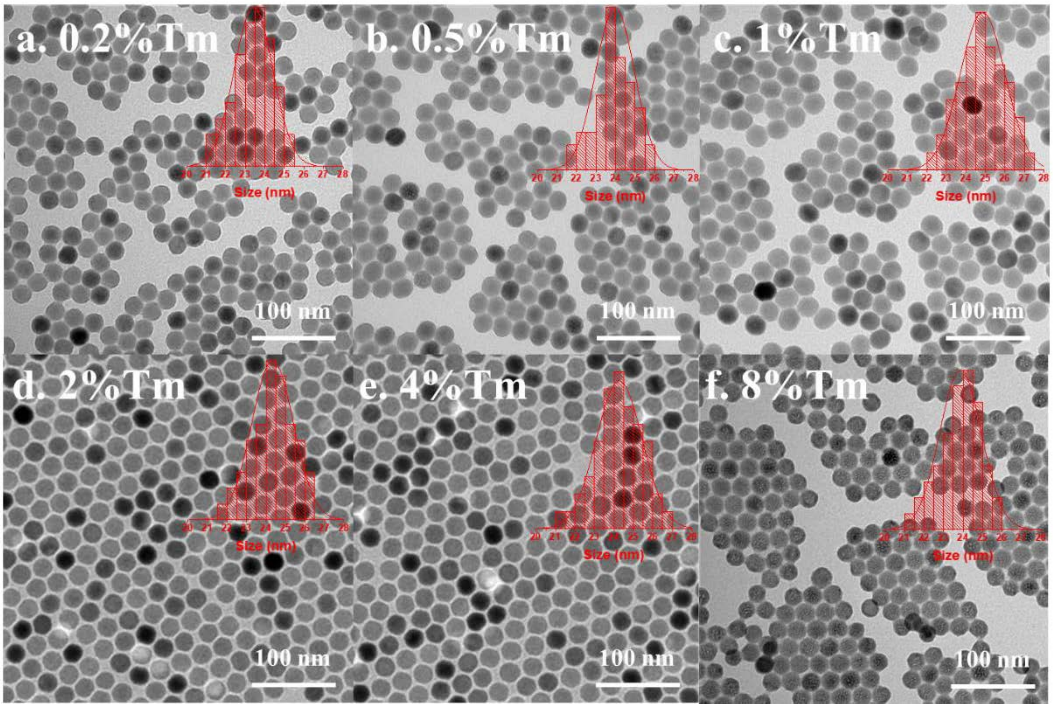

Figure 3.6. a-d, TEM images of a series of monodispersed 24 nm UCNPs varying the Tm^{3+} doping concentration from 0.2% to 8%. Scale bar 100 nm. And the inset in each figures shows the size distribution of related as-prepared UCNPs.

Absorption spectra were measured firstly to make sure the absorbing ability of upconversion nanoparticles with various Tm^{3+} doping concentrations. As can be seen, the absorption peak around 980 nm originates from $^2F_{5/2}$ (Yb^{3+}), while the peaks at ~690 nm and ~800 nm are from Tm^{3+} ions. The absorption at ~800 nm increase as the Tm^{3+} ions doping concentration increase from 0.2% to 8%. Meanwhile, the Yb^{3+} absorbance keeps constant at different Tm^{3+} concentrations, indicating the existence of Tm^{3+} ions don't affect the absorption of Yb^{3+} ions. Thus, the difference of upconversion emission spectra between this batch of samples are derived from the amount of Tm^{3+} ions.

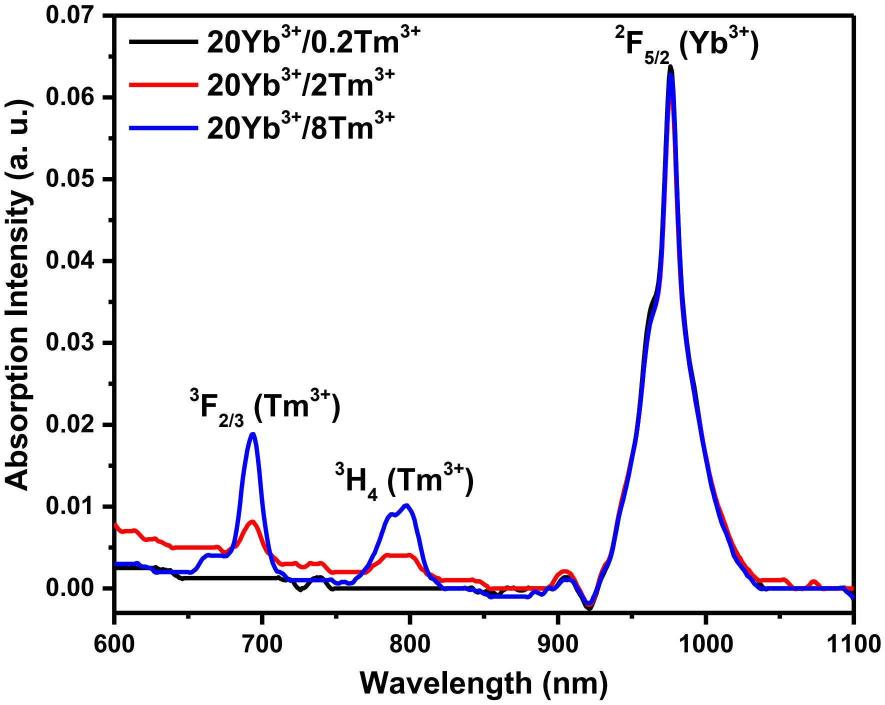

Figure 3.7 Absorption spectra of $NaYF_4$:20%Yb^{3+}/x%Tm^{3+} (x=0.2, 2, 8).

Then, the upconversion emission spectra of the series of 24 nm UCNPs were characterized and shown in Figure 3.8. The NIR emission peak at 802 nm originate from the transition of $^3H_4 \rightarrow {}^3H_6$, and the blue emission bands including 450 nm and 475 nm can be attributed to the transition of $^1D_2 \rightarrow {}^3H_5$ and $^1G_4 \rightarrow {}^3H_6$ respectively. The apparent diversified spectral distributions are observed when varying the Tm^{3+} concentrations, suggesting the concentration-dependent CR effect. The proportions of the emissions from $^3H_4$ to $^3H_6$ transition show an upward tendency with the increase of Tm^{3+} concentration, which indicates the CR-induced efficient energy accumulation (Figure 3.9). At the low concentration range, the energy, sensitized by and transferred from Yb^{3+}, is distributed onto all the excited states including $^1D_2$, $^1G_4$ and $^3H_4$. When the Tm^{3+} concentration increases from 1 mol. % to 2 mol.%, the peak intensities associated with the $^1G_4$ level decrease, while the $^3H_4$ initiated transition intensity increases. Figure 3.8b displays the quantitative intensity evolution and ratios as the function of Tm^{3+} concentration. The intensity at 802 nm ($^3H_4 \rightarrow {}^3H_6$) transition, the intensity ratios of 802 nm/473 nm and 802 nm/645 nm reach their peak values at 2 mol. % Tm^{3+} due to the CR induced population enrichment at the excitation power density of 100 W/cm^2. Further increase in the Tm^{3+} concentration, e.g. 4 mol% and 8 mol.%, depopulates the $^3H_4$ level with decreased intensity at 802 nm due to the excessive CR induced energy loss and the possible back energy transfer from Tm^{3+} to Yb^{3+}.

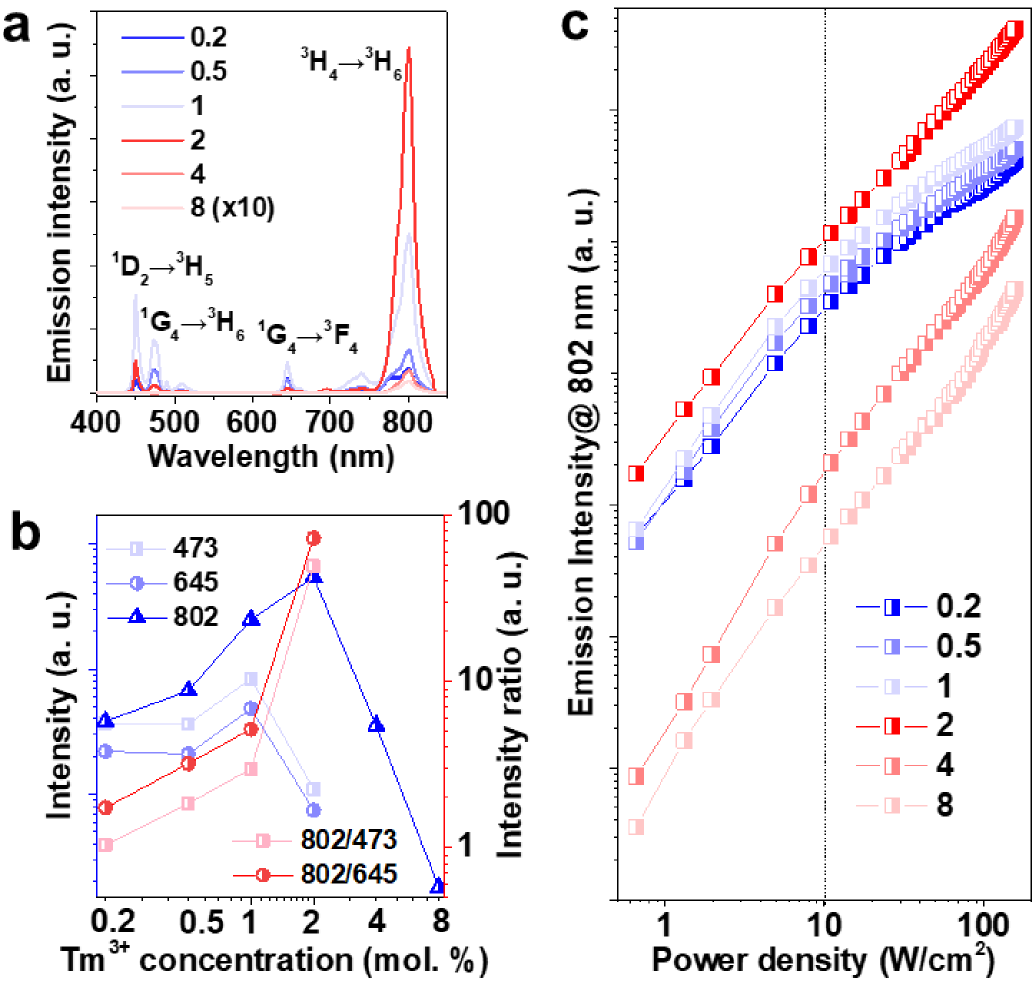

Figure 3.8 a, Comparison emission intensities and spectra of UCNPs doped with 20 mol.% Yb^{3+} and x mol.% Tm^{3+} (x=0.2, 0.5, 1, 2, 4, 8). **b**, Comparison emission intensities at the characteristic wavelengths and the intensity ratios of 802 nm/473 nm and 802 nm/645 nm. Both results displayed in a and b were acquired at the excitation power density of 100 W/cm^2 **c,** Power dependent emission intensity evaluation at 802 nm.

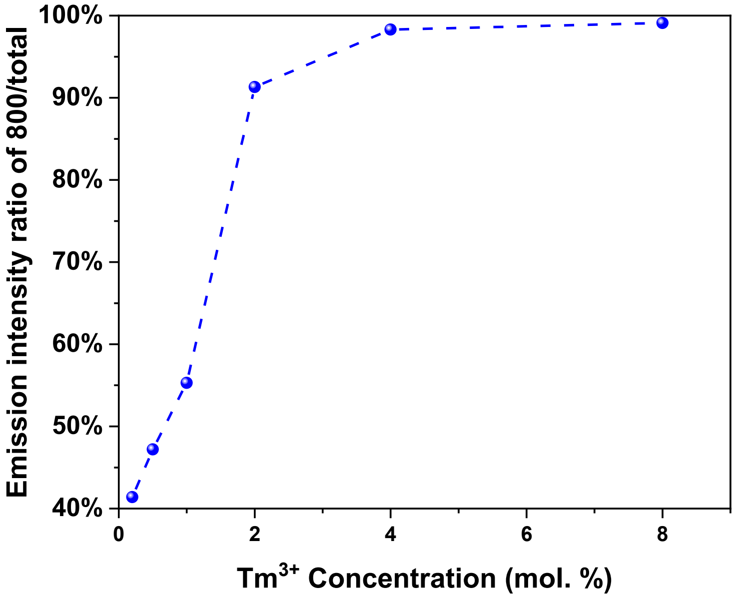

Figure 3.9 The emission intensity ratio of 800 nm peak/total emission under the excitation of 100 W/cm^2.

As CR involves different energy levels between a pair of nearby emitters, the population distribution of each energy level is strongly dependent on the excitation power density, so is the CR dynamics.[2, 48] And Figure 3.8c shows the power-dependent population of $^3H_4$ level by analyzing the peak intensity at 802 nm. The 2 mol.% Tm^{3+} doped sample shows the highest intensities of 802 nm emissions within the excitation power density range of 0.6-150 W/cm^2 due to the CR effect. Above the power density of 10 W/cm^2, the low doping samples are saturated while the highly doped samples exhibit an accelerated growth trend of the emission intensities, indicating the non-linear transition dynamics caused by the power-dependent and concentration-dependent CR effect.

In order to further confirm the energy transfer paths and efficiency between Yb^{3+} ions and Tm^{3+} ions, the decay curves of Yb^{3+} at 985 nm excited by 976 nm laser were measured. As shown in Figure 3.10 a, the Yb^{3+} lifetime decreases with the increase of Tm^{3+} concentrations. The energy transfer efficiency (η) from Yb^{3+} to Tm^{3+} can be calculated by the decay of lifetime ($\eta=(\tau_0-\tau_1)/\tau_0$, τ_0 and τ_1 refer to the lifetime of Yb^{3+} without and with Tm^{3+} doping). We therefore estimated the overall Yb^{3+}-Tm^{3+} energy transfer efficiency as a function of Tm^{3+} concentration, plotted in Figure 3.10b. The efficiencies increase with the increase of Tm^{3+} concentrations with a trend of saturation at the range of higher concentrations, which indicates the possible quenching and back energy transfer from Tm^{3+} to Yb^{3+}. Although the shorted distance between Yb^{3+} and

Tm^{3+} ions induce efficient energy transfer and possible back energy transfer[49], the CR still shows a powerful regulation of population distribution. These suggest the existence of a sweet spot of optimum Tm^{3+} doping concentration and excitation pumping power for the low threshold establishment of population inversion.

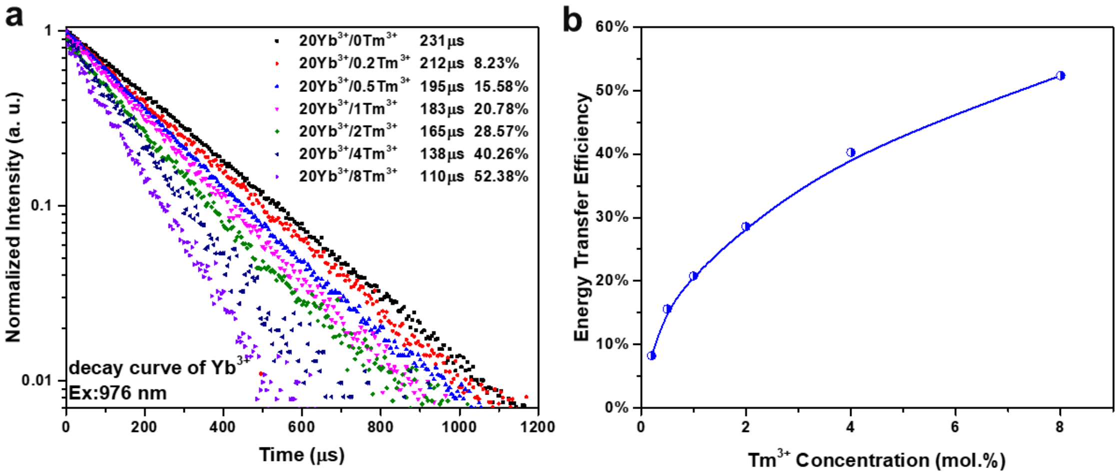

Figure 3.10 a, Lifetime decay curves of Yb^{3+} emissions at 985 nm for UCNPs with different Tm^{3+} doping concentrations. **b**, the energy transfer efficiencies from Yb^{3+} to Tm^{3+} for UCNPs with different Tm^{3+} doping concentrations, estimated based on the lifetime decay curves of Yb^{3+} emissions at 980 nm.

Thus, the upconversion mechanism can be simplified divided into two parts by CR process dominant or not as shown in Figure 3.11. When the doping concentration of Tm^{3+} ions is pretty low, the distance between two neighboring ions is pretty long. Then, the excited state population distribution mainly depends on the energy transfer process from Yb^{3+} to Tm^{3+}. When increase the doping concentration of Tm^{3+} ions, the interaction between adjacent Tm^{3+} ions should not be ignored. The CR processes, including ($^1G_4$, $^3H_6 \rightarrow {}^3H_5$, $^3H_4$), ($^1G_4$, $^3H_6 \rightarrow {}^3F_{2,3}$, $^3F_4$), and ($^3F_{2,3}$, $^3F_4 \rightarrow {}^3H_4$, $^3H_5$), are vital for the excited state population distribution. The powerful energy modulation, especially for $^3H_4$ state, make it possible to achieve population inversion at low excitation power density.

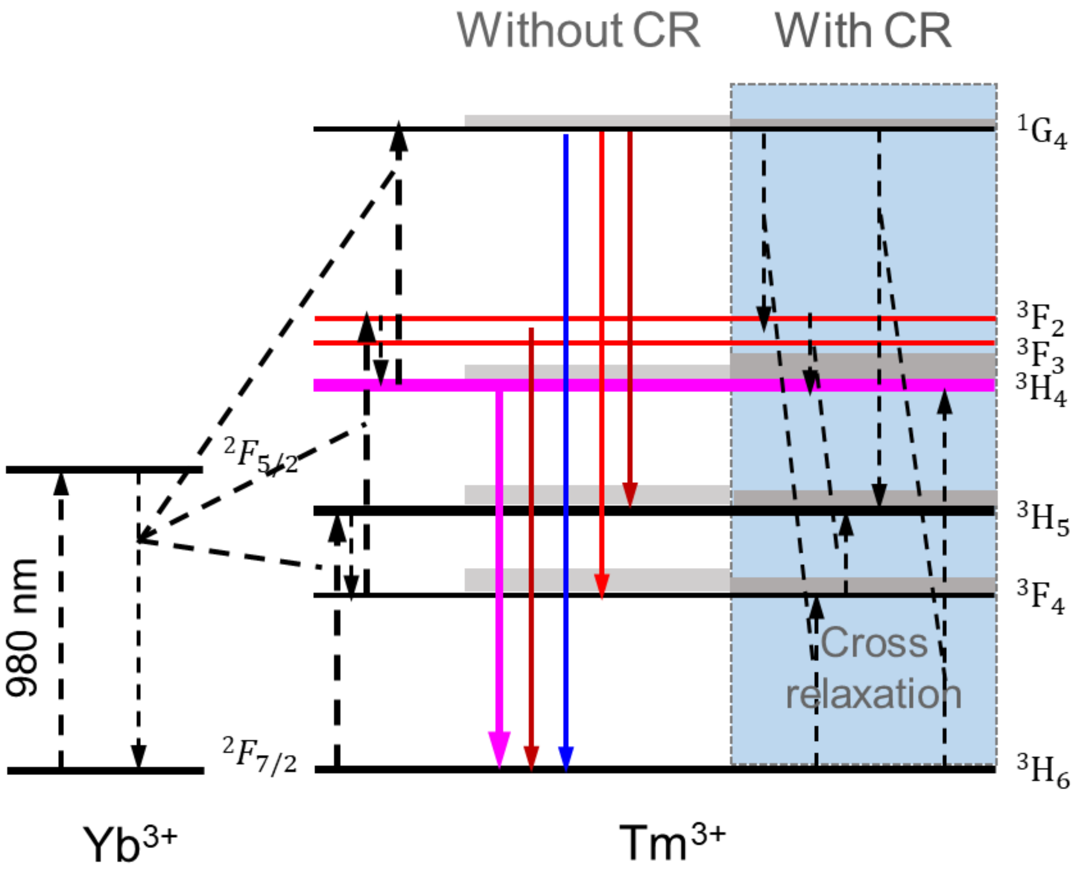

Figure 3.11 Energy level diagram of Yb^{3+}/Tm^{3+} co-doped UCNPs including typical cross-relaxation pathways among Tm^{3+} emitters.

3.3.2 Theoretical possibility of upconverting microlaser

To further explore the optical property of these UCNPs as gain media, we coupling them with a kind of high quality WGM cavity. A 5 μm PS beads were chosen as microcavity to hold the WGM emission modulation. The coupled light can be confined inside the microsphere due to the total internal reflection at surface, and thus provide essential loop to achieve stimulated emission (Figure 3.4). Before coupling the gain media with a microcavity, the theoretical transverse electric and transverse magnetic propagating modes of this 5 μm microcavity were simulated by using Lumerical FDTD solutions. As can be seen, the cavity optical WGMs fit well with the emission of our gain media (~800 nm band), and the mode number and peak position can be further modulated by varying the diameter of the microspheres. This indicates the possibility to achieve lasing emission while coupling our gain media with this microcavity.

As we mentioned in chapter 1, the lasing emission would not arise only if the gain in each looping process is larger than the losses. The coupling strategy of gain media and microcavity is further simulated. The electrical-field distributions of a selected mode (~795 nm) within a major plane were shown as follow. Figure 3.12b indicate that the jacinth-shaded region with high field intensity is almost at the surface of microcavity, which suggest the appropriate position for the coupling of gain media.

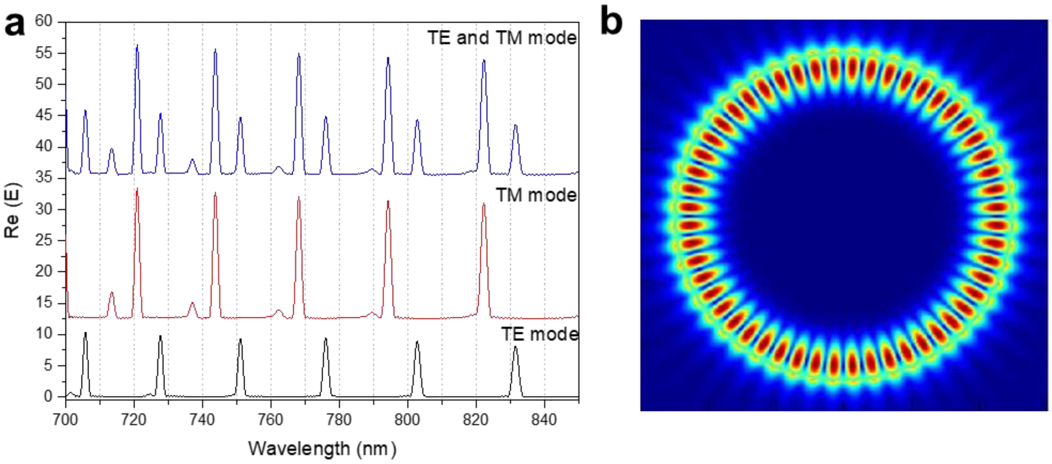

Figure 3.12 **a**, Numerical simulations of resonance spectra of microcavity with a diameter of 5 µm. **b**, the numerical simulation of the electrical-field distributions at 795 nm within a major plane.

3.3.3 Conventional construction of upconverting microlaser

As the simulation results, the UCNPs (gain media) need to be coupled well with the microcavity to construct a microlaser. There are several kinds of methods to couple the gain media, e. g. organic dyes, inorganic quantum dots, carbon dots, with microcavities[50-53]. As for an organic spherical microcavity, the swelling and deswelling strategy is one of the mostly used methods to loading gain media[54-56]. Thus, we prepared upconversion nanoparticles loaded PS microsphere with a modified swelling-deswelling strategy reported in the previous literatures[57-59]. Chloroform was used to swell the surface region of polystyrene microspheres, and the hydrophobic nanoparticles would attach onto the surface driven by Van Der Waals interactions. The uniformity and thickness of gain media layer can be adjusted by the dosage of upconversion nanoparticles and microspheres.

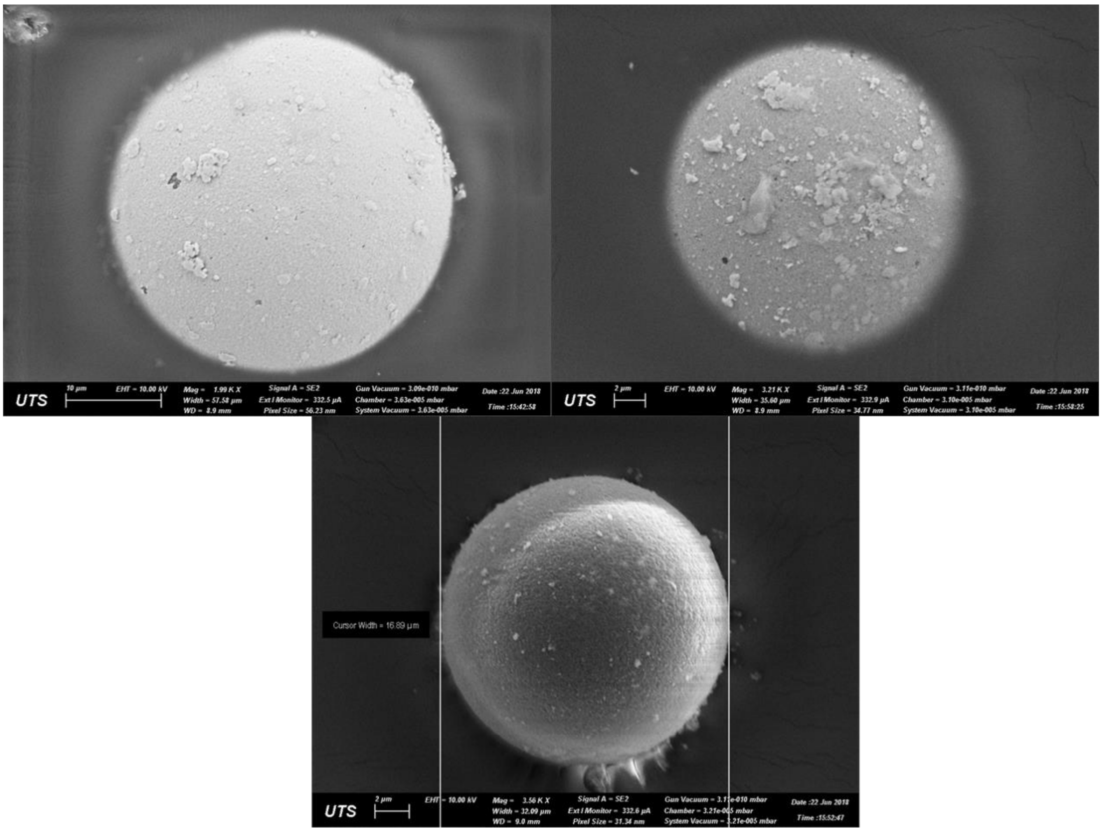

Figure 3.13 SEM images of upconversion nanoparticles coated microsphere obtained through swelling and deswelling strategy.

As can be seen in Figure 3.13, dense coating layer of upconversion nanoparticles was achieved. The shape of microsphere didn't change a lot except an additional layer of gain media. The aggregation of gain media can be controlled by tuning the reaction conditions. The EDS element mapping shown in Figure 3.14 and EDS element spectrum shown in Figure 3.15 indicate the existence of upconversion nanoparticles. Due to the sensitivity of EDS detector and the small amount of upconversion nanoparticles, the mapping contrast of Na, Y, F elements are not so obvious. However, the evident EDS spectrum signal of these elements and the integrated intensity ratio of Na, Y, F further confirmed the successfully loading of upconversion nanoparticles. What's more, the sphere-like elements distribution also reveals the upconverison nanoparticles are mainly attached on the surface of microsphere with a bit of aggregation.

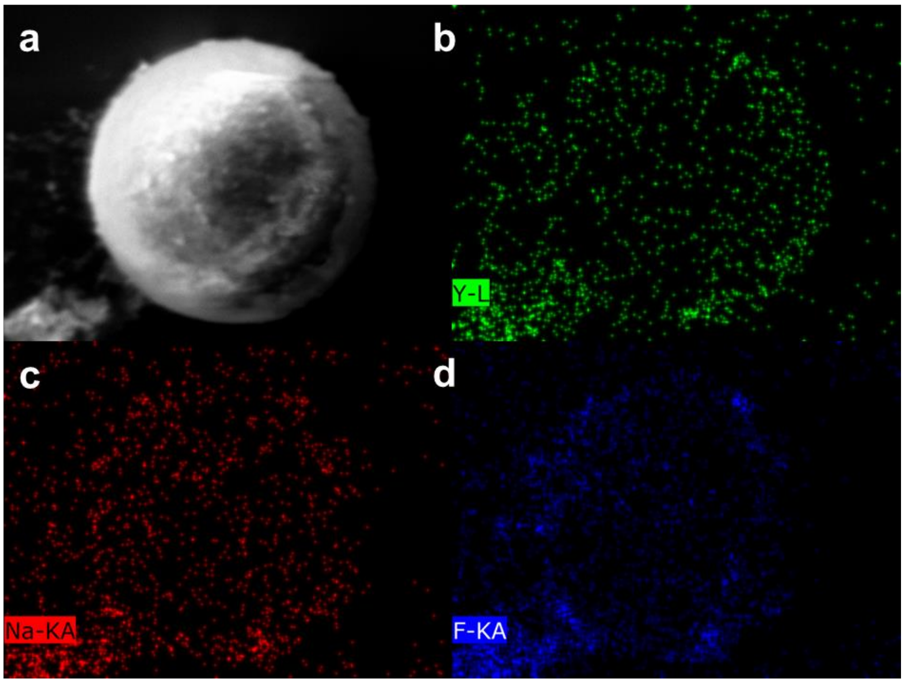

Figure 3.14 Energy-dispersive X-ray spectroscopy (EDS) mapping of upconversion nanoparticles coated microsphere, including a, SEM image, b, Y element, c, Na element, d, F element.

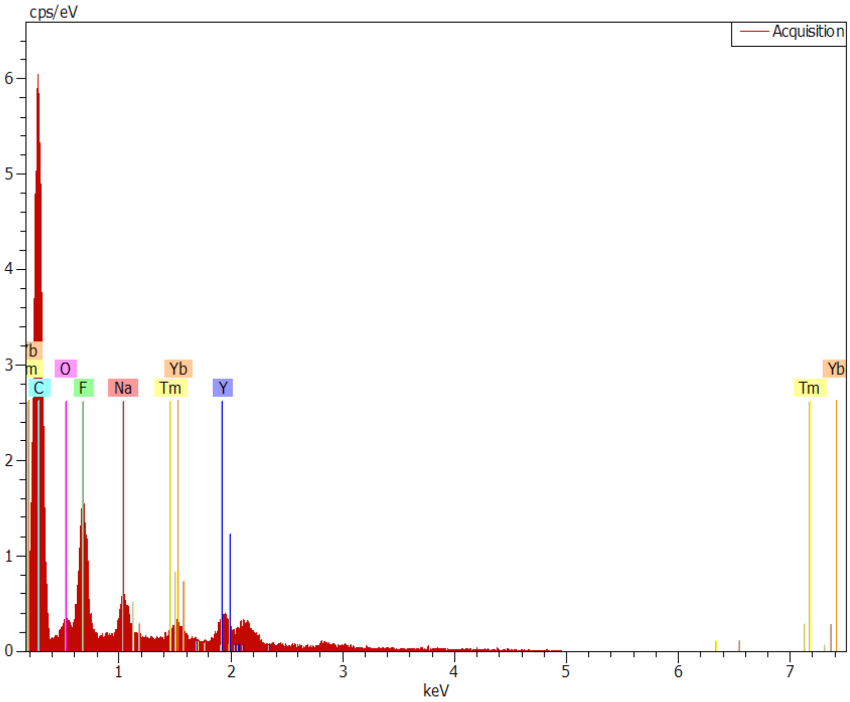

Figure 3.15 EDS elemental spectrum of upconversion nanoparticles coated microsphere.

Then, the emission spectra of upconversion nanoparticles coated microsphere were measured by using our home-built confocal system. Additional sharp emission peaks can be observed, indicating the modulation of spontaneous emission. However, the numbers and position of these sharp peaks were irregular. But most of them located around 800 nm (the transition from $^3H_4$ to $^3H_6$), indicating the population inversion and possibility to achieve lasing emissions. Due to the poor uniformity, only part of micro-resonator shown the property to achieve multiple sharp peaks.

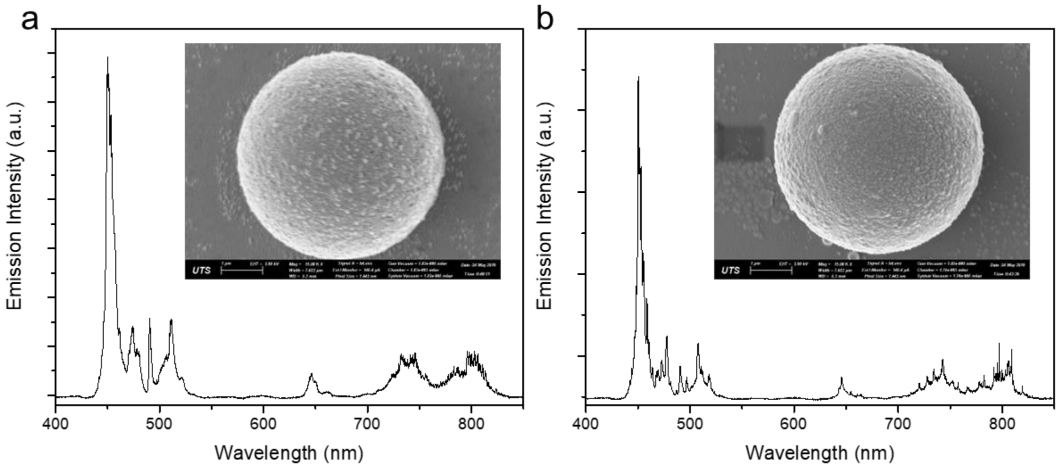

Figure 3.16 a, b, Typical upconversion emission spectrum and related SEM images of upconversion nanoparticles coated microsphere.

We found that the PS microsphere is very sensitive to organic solvent and the smooth surface would be destroyed by using swelling and deswelling method[57, 58]. As can be seen in the wide field image, the broken surface would lead to the leak of confined light. And the aggregation of upconversion nanoparticles also result in the increased scattering losses (Figure 3.17). What's more, the poor surface, including structure broken and aggregation, would induce the interactions of different modes. Thus, the sharp peaks in Figure 3.16 didn't fit well with the simulated modes, and the spontaneous emission background was very strong.

In short, the CR modulated upconversion nanoparticles show the powerful ability to promote the excited energy accumulation and population inversion of $^3H_4$ state. When equipped with a micro-resonator, emission can be confined inside the microcavity then achieve stimulated amplification. However, due to the limitation of coupling methods, the gain was slightly larger than the whole losses. In order to achieve lasing emission with much obvious stimulated radiation peak, new method to reduce the scattering losses are needed.

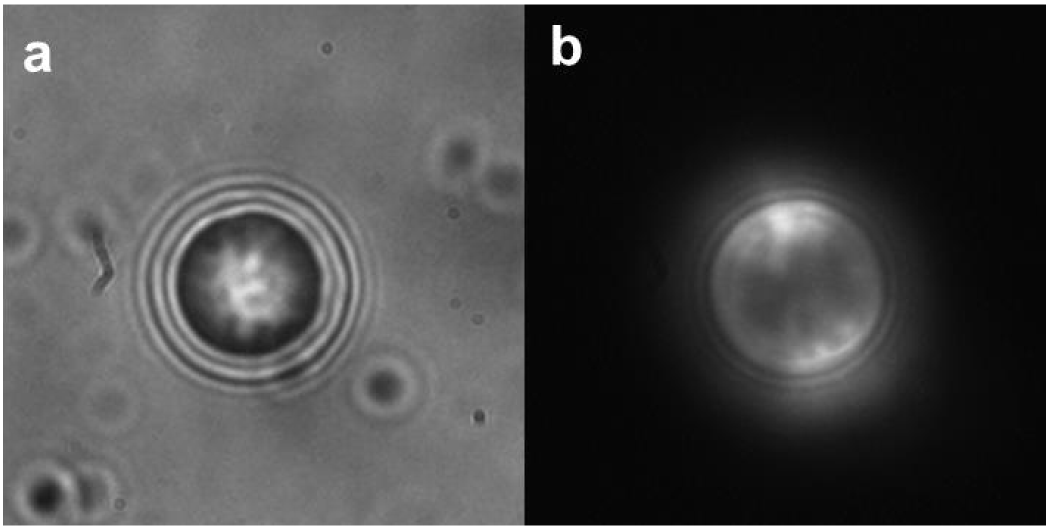

Figure 3.17 a, Bright field image and **b**, fluorescence field image of upconversion nanoparticles coated microsphere.

3.3.4 Novel construction of upconverting microlaser

As mentioned above, smooth surface of microcavity and uniform coating layer are needed for lasing emission. Herein, a simple and moderate aqueous solution phase process was developed and used in our experiment. In order to avoid the surface destruction of PS microspheres, organic solvents that can swell the PS microspheres were excluded. Considering the surface charge, a novel electrostatic force driven coating strategy was proposed. Upconversion nanoparticles with positive charge would be assembled uniformly on the surface of electronegative microcavity.

During the coating process, the hydrophobic UCNPs were firstly modified through ligands free method assisted with HCl solution (experimental section). The measured surface charge of PS beads and ligands-free UCNPs are ~-8 mV and 25 mV respectively (Figure 3.18). Then, the ligands-free UCNPs were mixed with PS microbeads and shaking for 2 h at room temperature. In this stage, UCNPs were coated onto the surface of cavity through the electrostatic assembly. And the uniformity and thickness of UCNPs layer can be simply tuned by adjusting the concentration ratio of UCNPs and PS beads.

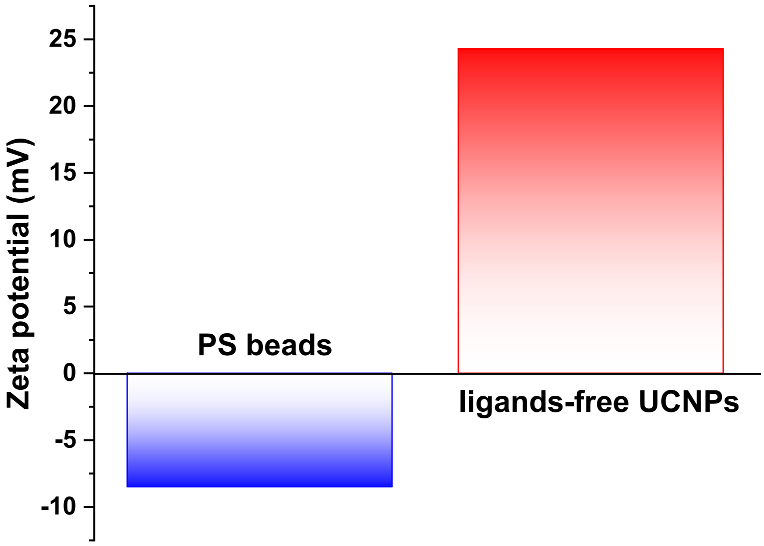

Figure 3.18 Zeta potentials of 5 μm PS beads and ligands-free UCNPs.

As mentioned above, the microsphere confines the light through total internal reflection and supports both transverse electric (TE) and transverse magnetic (TM) propagating modes with high quality (Q) factor, e.g. the Q factor for a 750 μm fused-silica microsphere could even reach ~10^9 [14, 55, 60, 61]. When nanoparticles are coated onto the surface, the increased roughness induces scattering losses and reduces Q factors [62], therefore homogeneous coatings avoid aggregations and minimize scattering.

To evaluate the coating process of microlasers, SEM and cross-sectional TEM images were measured. Figure 3.19a present the typical SEM image of a 5-μm UCNPs coated polystyrene microsphere, showing the uniform and smooth layer of 2 mol.% Tm^{3+} doped UCNPs on the surface of the cavity. The cross-sectional TEM measurements shown in Figure 3.19 b and c further confirmed the existence of a single layer of UCNPs, which is pretty important for emission coupling (especially due to the scattering effect). And the uniformity of UCNPs coated layer was much better than that obtained through conventional swelling-deswelling methods.

Then, a series of microcavity coated with various of UCNPs with Tm^{3+} doping concentration from 0.2 mol. % to 8 mol.% were prepared, and the lasing emission characteristic were measured using a home-built confocal system (Figure 3.19d).

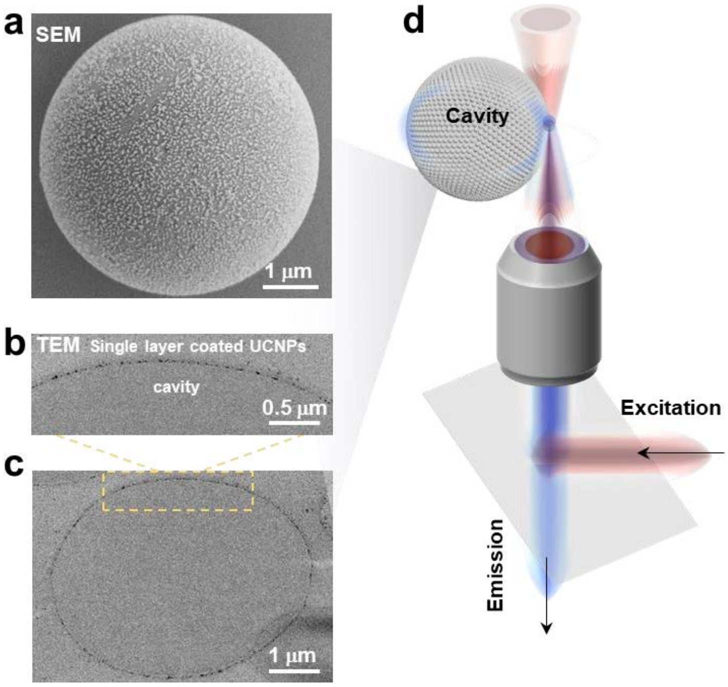

Figure 3.19 **a**, SEM image of a 5-μm polystyrene micro cavity coated with a single layer of self-assembled UCNPs. **b** and **c**, (enlarged-) Cross-sectional TEM images of micro cavity showing the distribution of UCNPs on the surface. **d**, Excitation and detection scheme.

3.3.5 Lasing emission related measurement

As shown in Figure 3.19d, the lasing emission was measured by focusing the 980 nm pump laser at the edge of the micro cavity. Multi-mode lasing emissions can be observed under the pumping of 10 kW/cm^2 (above the threshold, Figure 3.20a). And all the emission peaks fit well with the simulated optical modes at 800 nm band. The free spectral range (FSR) between two adjacent TE modes or TM modes also fit well with theoretical value ($\Delta\lambda_{FSR} = \frac{\lambda^2}{2\pi R}$, R is the radius of microcavity). Noting that, the simulated result is only used for positioning for cavity modes. In order to get result fast and reduce the computation, we set the meshes order as 10 nm. Thus, the linewidth of modes is a bit broad. Meanwhile, intense upconversion emissions (Figure 3.20b) can be observed at the excitation spot and the edge of its opposite end due to the propagation path inside the microsphere, which suggests the onset of whispering gallery modes emissions[63, 64]. The full width at half-maximum (FWHM) of the sharp lasing peaks is calculated to be 0.54 nm using the Lorentz function fitting. According to $Q \approx \lambda_0/\Delta\lambda$, where λ_0 and $\Delta\lambda$ are the centre wavelength and FWHM of the peak profile, the measured quality factor Q of whole laser is estimated as ~1500. Noting that, the measured Q factor is not only the quality of cavity alone. When the resonator coupled with gain medium to construct a laser, the Q factor contains the effect of radiative losses, scattering losses, absorption losses and other losses. Both the narrow FWHM and high Q benefit from the small size of ca. 24 nm of the UCNPs and the homogenous coating of a single layer of UCNPs. As the contrast, the results of uneven coating shown in Figure 3.21 exhibit broad FWHM and small signal to noise ratio. The aggregated nanoparticles at the surface increase the scattering cavity losses, in which the corresponding spectrum shows a strong background of spontaneous emission and increased FWHM of ~1.6 nm.

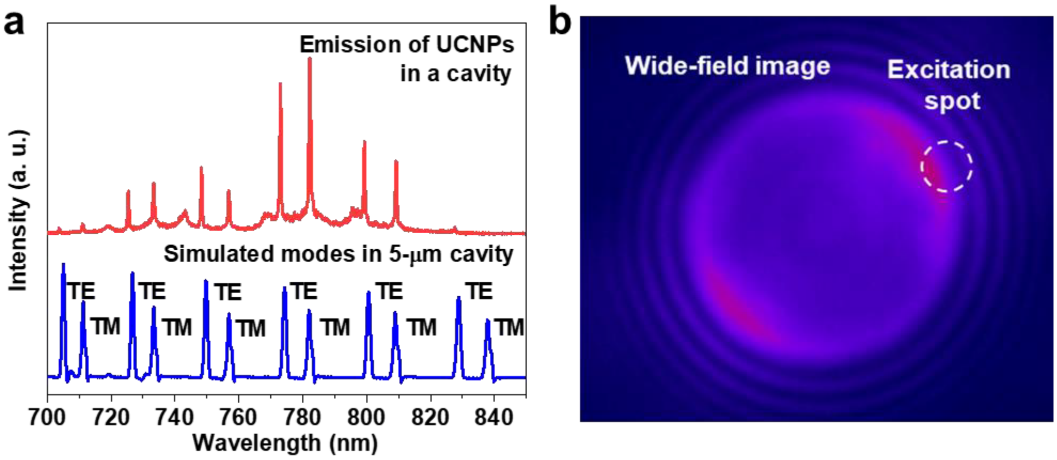

Figure 3.20 a, Numerical simulations of resonance spectrum and experimental emission spectrum (10 kW/cm^2). **b**, Wide-field pseudocolor image of a lasing micro cavity pumped by the laser excitation of a diffraction-limited spot on the side of the microsphere.

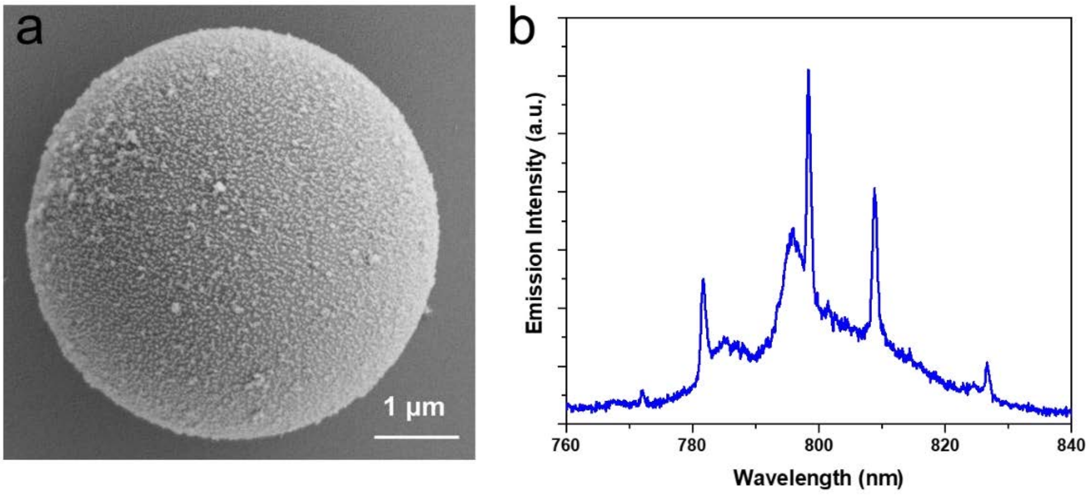

Figure 3.21 a, SEM image and **b**, upconversion spectrum under the excitation of 980

nm laser (100 kW/cm^2) of the microcavity coated with 24 nm UCNPs.

Besides, as the refractive index of PS beads is about 1.59, similar with UCNPs (n=1.5), which leads to an effective coupling of upconversion emissions within the cavity modes (Figure 3.22a). Noting that the tiny variation of the microcavity diameter would lead to pretty large mode shifts as shown in Figure 3.21b. The slight difference of experimental lasing peaks is attributed to the imperceptible slight variations of each cavity, as the mode position will move more than 8 nm when the size of this cavity changes for only 1%.

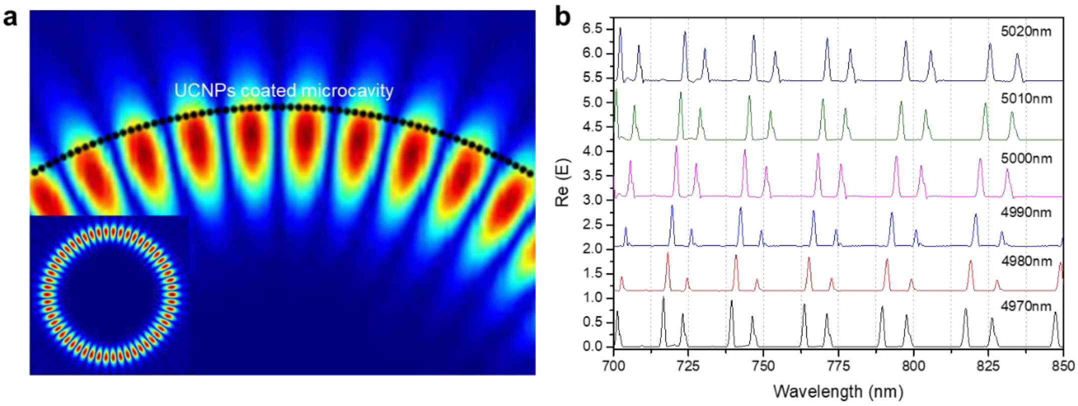

Figure 3.22 a, Numerical simulation of the electrical-field distributions at 800 nm (eigenmode) within a major plane. Note that the black spots indicate upconversion nanoparticles coated on the surface of microcavity. **b**, Numerical simulations of resonance spectra of microcavity with different sizes.

To further explore the characters of the lasing emissions, the emission spectra at the polarization angle from 0° to 360° were collected. The characterized polarization properties of both the TE and TM mode emissions exhibiting linear polarization with orthogonal periodicity as observed by the different polarization angles collection in Figure 3.23a. The polarization degree (ρ) can be calculated according to $\rho = \frac{I_{max}-I_{min}}{I_{max}+I_{min}}$, which indicate the excellent linear polarization of microlasing emissions.

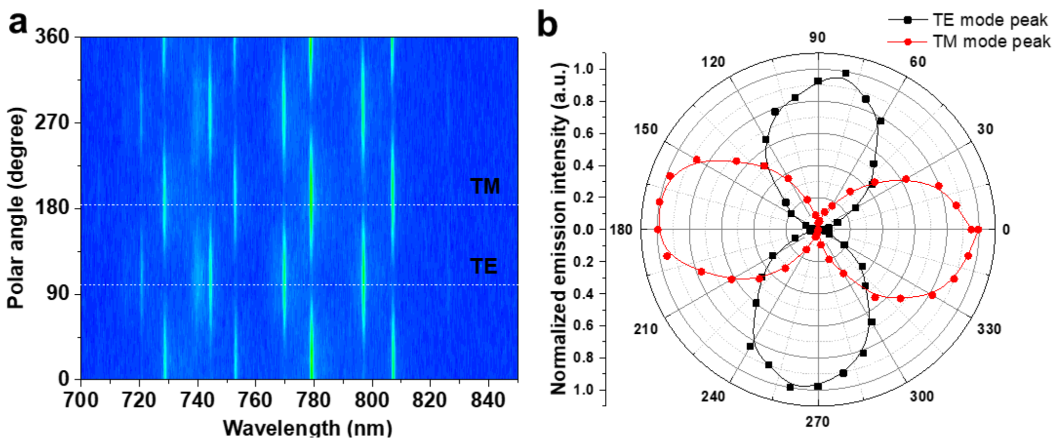

Figure 3.23 a, Emission polarization angle dependent intensities of the lasing peaks. b, Lasing emission intensity of the TE and TM modes (796 nm and 806 nm peak) plotted as a function of the polarization angle. The data are presented in a polar plot over a 360° range for clarity.

To investigate the pumping threshold that the lasing emission arise, power dependent emission spectra were collected. The transition from below, near, and at the threshold lasing emissions can be seen in Figure 3.24a. The onset of lasing emissions with the characteristic sharp and regularly spaced emission peaks can be observed when increase the pumping powers. The narrow peaks that indicative of increased coherence and laser emissions are emerging above the threshold at pump intensities of 120 W/cm^2 for the laser mode at 805 nm. Both the slopes for the intensity and linewidth curves (Figure 3.24b) display a non-linear change characteristic at the ultra-low pumping threshold of ~150 W/cm^2 achieved for the homogeneously coated 2 mol.% Tm^{3+} doped UCNPs sample, which all indicate a threshold of hundred watt per square centimeter.

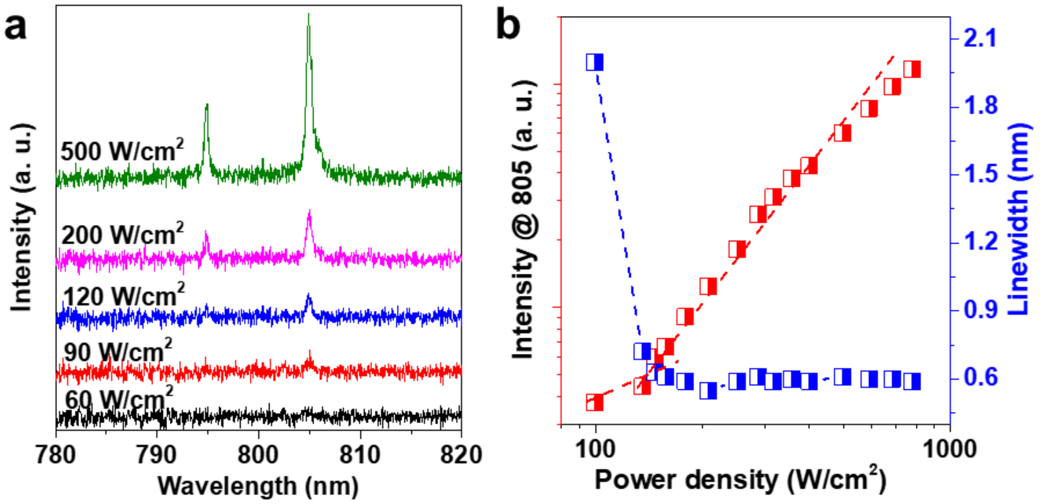

Figure 3.24 a, Power dependent upconversion emission spectra (below, near and above the threshold) showing the gradual appearance of lasing peaks. **b,** The pumping power dependent plots of emission intensities and spectral linewidth narrowing, showing the onset of upconversion lasing emissions.

To further confirm the stimulated lasing emission, power dependent lifetime was measured and shown in Figure 3.25. Hundreds of microseconds decay time shorter (from 291 μs to 158 μs) is observed when power density above the threshold, which indicated the transformation from spontaneous to simulated emission. However, due to the broad bandpass filter (800/40 nm) and spontaneous emission background, the measured lifetime decay contains spontaneous emission backgrounds, multi-mode lasing emissions, which cover up the expected very sharp decrease of stimulated emissions. If we could measure the lifetime of lasing emission peak with a faster response pumping laser and detector, the decay curve will be much sharp.

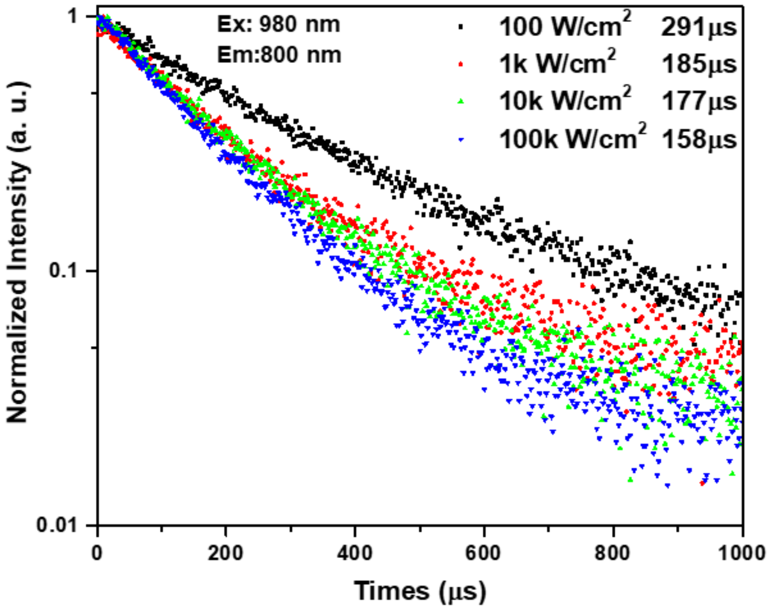

Figure 3.25 Power dependent lifetime of 800/40 nm bandpass emissions.

For the comparison characterizations of other UCNPs samples, the power dependent spectra and light-to-light curves of each related UCNPs coated microlaser were plotted in Figure 3.26. Normally, the threshold would increase with the increasing of activator doping concentration, when one just considers about the needed power for more emitters to achieve population inversion. However, the threshold reduces when the Tm^{3+} doping concentration increase from 0.2 mol% to 2 mol.% due to the dominant of

CR induced energy accumulation at $^3H_4$ level. The CR process between nearby Tm^{3+} ions play an important role in excited energy distribution, and thus modulate the threshold. However, when keep increasing the Tm^{3+} doping concentration to 8 mol.%, the threshold experiences an upward tendency due to the concentration quenching and energy back transfer (Tm^{3+} to Yb^{3+}) effects. Thus, it indicates 2 mol.% Tm^{3+} doped UCNPs as the most effective gain medium as a result of the CR induced efficient population inversion at low pumping power. Noting that, the accurate laser threshold should be ideally determined by using the absorbed pump power instead of incident pump power. We reason that the actual laser threshold should be much lower than the current values once the absorbed power could be measured, though it's inaccessible in our experimental conditions.

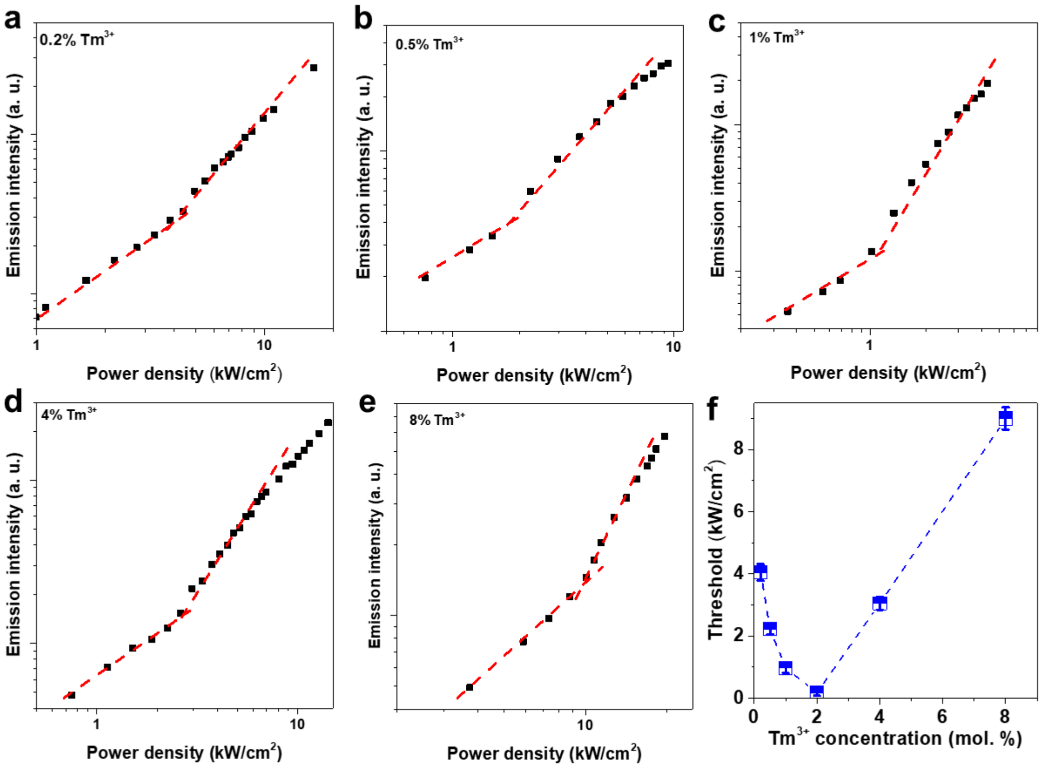

Figure 3.26 The systematic characterizations of the lasing threshold for the cavities coated with UCNPs at Tm^{3+} doping of **a-e**, 0.2%, 0.5%, 1%, 4%, 8%. **f,** Tm^{3+}concentration-dependent thresholds for the onsets of upconversion lasing emissions.

Furthermore, the stability of these microlasers was explored by measuring the lasing spectrum each ten minutes. As shown in Figure 3.27, the intensity and position of lasing emission are all pretty stable over 30 mins of continuous pumping at 10 kW/cm^2. No obvious spectral shift was observed under longtime CW pumping, which is barely observed for organic dyes, quantum dots, and semiconductor nanoparticles[65, 66]. On account of NIR optical window pumping, high signal-to-noise ratio, and optical stability, the upconverting microlaser show great potential in the application of long time labeling, tracking and sensing at complex biological conditions.

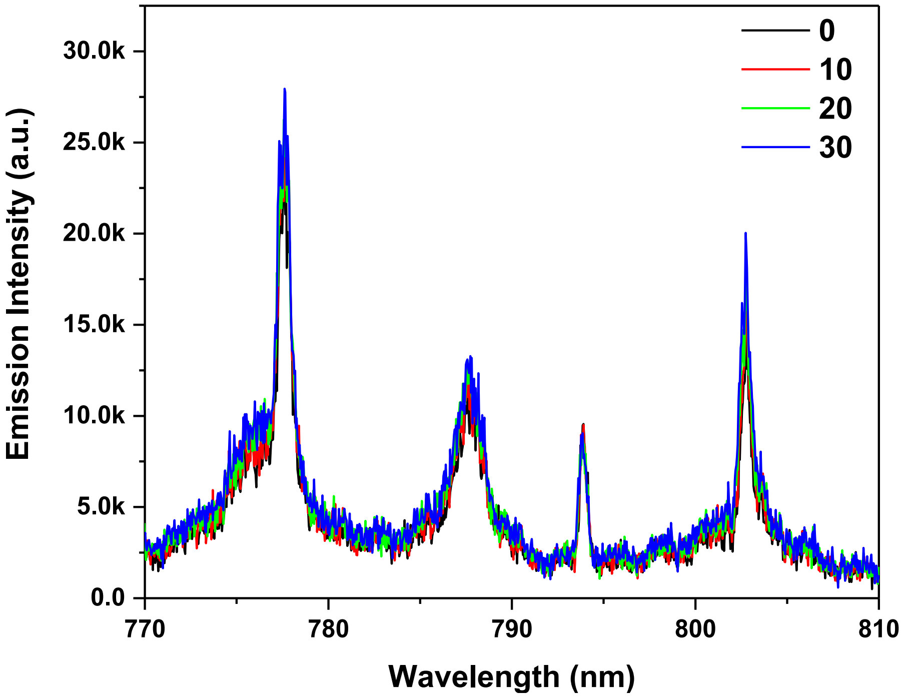

Figure 3.27 Lasing Emission spectra recorded each ten minutes under continuous pumping at 10 kW/cm^2.

3.4 Conclusion

In summary, we have achieved ultra-low threshold lasing by controlling CR in an upconversion energy transfer system and thereby the easy establishment of population inversion in single upconversion nanoparticles. Doping 20 mol. % Yb^{3+} and 2 mol. % Tm^{3+} has been identified as the appropriate concentration to produce moderate CR at relatively low power range. By using the doping-concentration-optimized UCNPs as gain medium and single-layer coating of monodispersed UCNPs on the cavity with minimized scattering loss, strong absorption and high efficiencies for both upconversion and population inversion establishement have been achieved. Compared with conventional swelling and deswelling deposition, the novel electrostatic force driven coating strategy exhibit multiple advantages, for example, smooth surface of microcavity, uniform single layer of gain media, *etc*. Employing a 5-µm cavity and homogenous coating architecture, we have achieved lasing emissions with a threshold of ~150 W/cm^2, nearly two orders of magnitude lower than the recently reported[57] benchmark value of 14 kW/cm^2. This study suggests great potential to using the concentration tunable UCNPs as an efficient gain medium for room temperature CW microscale and nanoscale lasers.

3.5 References

1. Auzel, F. Upconversion and anti-stokes processes with f and d ions in solids. *Chem Rev* **2004,** 104 (1), 139-174.
2. Liu, Y.; Lu, Y.; Yang, X.; Zheng, X.; Wen, S.; Wang, F.; Vidal, X.; Zhao, J.; Liu, D.; Zhou, Z.; Ma, C.; Zhou, J.; Piper, J. A.; Xi, P.; Jin, D. Amplified stimulated emission in upconversion nanoparticles for super-resolution nanoscopy. *Nature* **2017,** 543 (7644), 229-233 DOI: 10.1038/nature21366.
3. Zhu, H.; Chen, X.; Jin, L. M.; Wang, Q. J.; Wang, F.; Yu, S. F. Amplified spontaneous emission and lasing from lanthanide-doped up-conversion nanocrystals. *Acs Nano* **2013,** 7 (12), 11420-11426.
4. Chen, X.; Sun, T.; Wang, F. Lanthanide-Based Luminescent Materials for Waveguide and Lasing. *Chemistry–An Asian Journal* **2019**.
5. Chen, X.; Jin, L.; Kong, W.; Sun, T.; Zhang, W.; Liu, X.; Fan, J.; Yu, S. F.; Wang, F. Confining energy migration in upconversion nanoparticles towards deep ultraviolet lasing. *Nature communications* **2016,** 7, 10304.
6. Fernandez-Bravo, A.; Yao, K.; Barnard, E. S.; Borys, N. J.; Levy, E. S.; Tian, B.; Tajon, C. A.; Moretti, L.; Altoe, M. V.; Aloni, S. Continuous-wave upconverting nanoparticle microlasers. *Nat Nanotechnol* **2018,** 13 (7), 572.
7. Fernandez-Bravo, A.; Wang, D.; Barnard, E. S.; Teitelboim, A.; Tajon, C.; Guan, J.; Schatz, G. C.; Cohen, B. E.; Chan, E. M.; Schuck, P. J. Ultralow-threshold, continuous-wave upconverting lasing from subwavelength plasmons. *Nat Mater* **2019,** 18 (11), 1172-1176.
8. Ma, R.-M. Lasing under ultralow pumping. *Nat Mater* **2019,** 18 (11), 1152-1153 DOI: 10.1038/s41563-019-0513-2.
9. Hill, M. T.; Gather, M. C. Advances in small lasers. *Nat Photonics* **2014,** 8 (12), 908.
10. Schuller, J. A.; Barnard, E. S.; Cai, W.; Jun, Y. C.; White, J. S.; Brongersma, M. L. Plasmonics for extreme light concentration and manipulation. *Nat Mater* **2010,** 9 (3), 193.
11. Stockman, M. I. Nanoplasmonic sensing and detection. *Science* **2015,** 348 (6232), 287-288.
12. Ma, R.-M.; Oulton, R. F. Applications of nanolasers. *Nat Nanotechnol* **2019,** 14 (1), 12-22.

13. Zhuge, M. H.; Pan, C.; Zheng, Y.; Tang, J.; Ullah, S.; Ma, Y.; Yang, Q. Wavelength-Tunable Micro/Nanolasers. *Adv Opt Mater* **2019**, 1900275.

14. He, L.; Özdemir, Ş. K.; Yang, L. Whispering gallery microcavity lasers. *Laser & Photonics Reviews* **2013,** 7 (1), 60-82.

15. Wang, T.; Yu, H.; Siu, C. K.; Qiu, J.; Xu, X.; Yu, S. F. White-light whispering-gallery-mode lasing from lanthanide-doped upconversion NaYF4 hexagonal microrods. *ACS photonics* **2017,** 4 (6), 1539-1543.

16. Wang, T.; Siu, C. K.; Yu, H.; Wang, Y.; Li, S.; Lu, W.; Hao, J.; Liu, H.; Teng, J. H.; Lei, D. Y. Influence of plasmonic effect on the upconversion emission characteristics of NaYF4 hexagonal microrods. *Inorganic chemistry* **2018,** 57 (14), 8200-8204.

17. Fan, H.; Hua, S.; Jiang, X.; Xiao, M. Demonstration of an erbium-doped microsphere laser on a silicon chip. *Laser Physics Letters* **2013,** 10 (10), 105809.

18. Ruan, Y.; Boyd, K.; Ji, H.; Ebendorff-Heidepriem, H.; Munch, J.; Monro, T. M. In *Upconversion lasing for index sensing and strong amplitude modulation of WGMs in Er-Yb co-doped tellurite spheres*, CLEO: 2013, 2013; IEEE: 2013; pp 1-2.

19. Mehrabani, S.; Armani, A. M. Blue upconversion laser based on thulium-doped silica m icrocavity. *Opt Lett* **2013,** 38 (21), 4346-4349.

20. Bian, W.; Lin, Y.; Wang, T.; Yu, X.; Qiu, J.; Zhou, M.; Luo, H.; Yu, S. F.; Xu, X. Direct identification of surface defects and their influence on the optical characteristics of upconversion nanoparticles. *Acs Nano* **2018,** 12 (4), 3623-3628.

21. Jin, L.; Wu, Y.; Wang, Y.; Liu, S.; Zhang, Y.; Li, Z.; Chen, X.; Zhang, W.; Xiao, S.; Song, Q. Mass-Manufactural Lanthanide-Based Ultraviolet B Microlasers. *Adv Mater* **2019,** 31 (7), 1807079.

22. Zhan, Q.; Liu, H.; Wang, B.; Wu, Q.; Pu, R.; Zhou, C.; Huang, B.; Peng, X.; Agren, H.; He, S. Achieving high-efficiency emission depletion nanoscopy by employing cross relaxation in upconversion nanoparticles. *Nature Communications* **2017,** 8 (1), 1058 DOI: 10.1038/s41467-017-01141-y.

23. Levy, E. S.; Tajon, C. A.; Bischof, T. S.; Iafrati, J.; Fernandez-Bravo, A.; Garfield, D. J.; Chamanzar, M.; Maharbiz, M. M.; Sohal, V. S.; Schuck, P. J. Energy-looping nanoparticles: harnessing excited-state absorption for deep-tissue imaging. *Acs Nano* **2016,** 10 (9), 8423-8433.

24. Wang, J.; Wang, F.; Wang, C.; Liu, Z.; Liu, X. Single-band upconversion emission in lanthanide-doped $KMnF_3$ nanocrystals. *Angewandte Chemie International Edition* **2011,** 50 (44), 10369-10372.

25. Liao, J. Y.; Jin, D. Y.; Chen, C. H.; Li, Y. M.; Zhou, J. J. Helix Shape Power-Dependent Properties of Single Upconversion Nanoparticles. *Journal of Physical Chemistry Letters* **2020,** 11 (8), 2883-2890 DOI: 10.1021/acs.jpclett.9b03838.

26. Shang, Y.; Hao, S.; Lv, W.; Chen, T.; Tian, L.; Lei, Z.; Yang, C. Confining excitation energy of Er 3+-sensitized upconversion nanoparticles through introducing various energy trapping centers. *J Mater Chem C* **2018,** 6 (15), 3869-3875.

27. Wang, F.; Deng, R.; Wang, J.; Wang, Q.; Han, Y.; Zhu, H.; Chen, X.; Liu, X. Tuning upconversion through energy migration in core–shell nanoparticles. *Nat Mater* **2011,** 10 (12), 968.

28. Su, Q.; Han, S.; Xie, X.; Zhu, H.; Chen, H.; Chen, C.-K.; Liu, R.-S.; Chen, X.; Wang, F.; Liu, X. The effect of surface coating on energy migration-mediated upconversion. *J Am Chem Soc* **2012,** 134 (51), 20849-20857.

29. Auzel, F. Upconversion and anti-stokes processes with f and d ions in solids. *Chem Rev* **2004,** 104 (1), 139-173 DOI: 10.1021/cr020357g.

30. Zhao, J.; Jin, D.; Schartner, E. P.; Lu, Y.; Liu, Y.; Zvyagin, A. V.; Zhang, L.; Dawes, J. M.; Xi, P.; Piper, J. A. Single-nanocrystal sensitivity achieved by enhanced upconversion luminescence. *Nat Nanotechnol* **2013,** 8 (10), 729.

31. Jackson, S. D. Cross relaxation and energy transfer upconversion processes relevant to the functioning of 2 μm Tm3+-doped silica fibre lasers. *Optics Communications* **2004,** 230 (1-3), 197-203.

32. Hebert, T.; Wannemacher, R.; Macfarlane, R.; Lenth, W. Blue continuously pumped upconversion lasing in Tm: YLiF4. *Appl Phys Lett* **1992,** 60 (21), 2592-2594.

33. Ermeneux, F.; Goutaudier, C.; Moncorge, R.; Cohen-Adad, M.; Bettinelli, M.; Cavalli, E. Growth and fluorescence properties of Tm3+ doped YVO4 and Y2O3 single crystals. *Optical materials* **1997,** 8 (1-2), 83-90.

34. Zhang, L.; Lin, H.; Zhang, G.; Mateos, X.; Serres, J. M.; Aguiló, M.; Díaz, F.; Griebner, U.; Petrov, V.; Wang, Y. Crystal growth, optical spectroscopy and laser action of Tm 3+-doped monoclinic magnesium tungstate. *Optics express* **2017,** 25 (4), 3682-3693.

35. Wen, S.; Zhou, J.; Zheng, K.; Bednarkiewicz, A.; Liu, X.; Jin, D. Advances in highly doped upconversion nanoparticles. *Nature Communications* **2018,** 9 (1), 2415 DOI: 10.1038/s41467-018-04813-5.

36. Lu, Y. Q.; Zhao, J. B.; Zhang, R.; Liu, Y. J.; Liu, D. M.; Goldys, E. M.; Yang, X. S.; Xi, P.; Sunna, A.; Lu, J.; Shi, Y.; Leif, R. C.; Huo, Y. J.; Shen, J.; Piper, J. A.; Robinson, J. P.; Jin, D. Y. Tunable lifetime multiplexing using luminescent nanocrystals. *Nat Photonics* **2014,** 8 (1), 33-37 DOI: 10.1038/Nphoton.2013.322.

37. Wang, F.; Han, Y.; Lim, C. S.; Lu, Y.; Wang, J.; Xu, J.; Chen, H.; Zhang, C.; Hong, M.; Liu, X. Simultaneous phase and size control of upconversion nanocrystals through lanthanide doping. *Nature* **2010,** 463 (7284), 1061-1065.

38. Liu, D.; Xu, X.; Du, Y.; Qin, X.; Zhang, Y.; Ma, C.; Wen, S.; Ren, W.; Goldys, E. M.; Piper, J. A. Three-dimensional controlled growth of monodisperse sub-50 nm heterogeneous nanocrystals. *Nature communications* **2016,** 7, 10254.

39. Gargas, D. J.; Chan, E. M.; Ostrowski, A. D.; Aloni, S.; Altoe, M. V. P.; Barnard, E. S.; Sanii, B.; Urban, J. J.; Milliron, D. J.; Cohen, B. E.; Schuck, P. J. Engineering bright sub-10-nm upconverting nanocrystals for single-molecule imaging. *Nat Nanotechnol* **2014,** 9 (4), 300-305 DOI: 10.1038/Nnano.2014.29.

40. Liu, Q.; Zhang, Y.; Peng, C. S.; Yang, T.; Joubert, L.-M.; Chu, S. Single upconversion nanoparticle imaging at sub-10 W cm^{-2} irradiance. *Nat Photonics* **2018,** 12 (9), 548-553.

41. Tian, B.; Fernandez-Bravo, A.; Najafiaghdam, H.; Torquato, N. A.; Altoe, M. V. P.; Teitelboim, A.; Tajon, C. A.; Tian, Y.; Borys, N. J.; Barnard, E. S. Low irradiance multiphoton imaging with alloyed lanthanide nanocrystals. *Nature Communications* **2018,** 9 (1), 3082.

42. Gu, Y.; Guo, Z.; Yuan, W.; Kong, M.; Liu, Y.; Liu, Y.; Gao, Y.; Feng, W.; Wang, F.; Zhou, J. High-sensitivity imaging of time-domain near-infrared light transducer. *Nat Photonics* **2019,** 13 (8), 525-531.

43. Wei, W.; Zhang, Y.; Chen, R.; Goggi, J.; Ren, N.; Huang, L.; Bhakoo, K. K.; Sun, H.; Tan, T. T. Y. Cross relaxation induced pure red upconversion in activator-and sensitizer-rich lanthanide nanoparticles. *Chem Mater* **2014,** 26 (18), 5183-5186.

44. Chen, Q. S.; Xie, X. J.; Huang, B. L.; Liang, L. L.; Han, S. Y.; Yi, Z. G.; Wang, Y.; Li, Y.; Fan, D. Y.; Huang, L.; Liu, X. G. Confining Excitation Energy in Er^{3+} -Sensitized Upconversion Nanocrystals through Tm^{3+} -Mediated Transient Energy Trapping. *Angew Chem Int Edit* **2017,** 56 (26), 7605-7609 DOI: 10.1002/anie.201703012.

45. Zhong, Y.; Ma, Z.; Zhu, S.; Yue, J.; Zhang, M.; Antaris, A. L.; Yuan, J.; Cui, R.; Wan, H.; Zhou, Y.; Wang, W.; Huang, N. F.; Luo, J.; Hu, Z.; Dai, H. Boosting the down-shifting luminescence of rare-earth nanocrystals for biological imaging beyond 1500 nm. *Nat Commun* **2017,** 8 (1), 737 DOI: 10.1038/s41467-017-00917-6.

46. Misiak, M.; Prorok, K.; Cichy, B.; Bednarkiewicz, A.; Stręk, W. Thulium concentration quenching in the up-converting α-Tm3+/Yb3+ NaYF4 colloidal nanocrystals. *Optical Materials* **2013,** 35 (5), 1124-1128.

47. Shang, Y.; Zhou, J.; Cai, Y.; Wang, F.; Fernandez-Bravo, A.; Yang, C.; Jiang, L.; Jin, D. Low threshold lasing emissions from a single upconversion nanocrystal. *Nature Communications* **2020,** 11 (1), 6156 DOI: 10.1038/s41467-020-19797-4.

48. Chen, C.; Wang, F.; Wen, S.; Su, Q. P.; Wu, M. C.; Liu, Y.; Wang, B.; Li, D.; Shan, X.; Kianinia, M. Multi-photon near-infrared emission saturation nanoscopy using upconversion nanoparticles. *Nature communications* **2018,** 9 (1), 3290.

49. Yu, D.; Yu, T.; van Bunningen, A. J.; Zhang, Q.; Meijerink, A.; Rabouw, F. T. Understanding and tuning blue-to-near-infrared photon cutting by the Tm^{3+}/Yb^{3+} couple. *Light: Science & Applications* **2020,** 9 (1), 107 DOI: 10.1038/s41377-020-00346-z.

50. Feng, Z. Q.; Bai, L. Advances of Optofluidic Microcavities for Microlasers and Biosensors. *Micromachines-Basel* **2018,** 9 (3), DOI: Artn 122
10.3390/Mi9030122.

51. Qiagedeer, A.; Yamagishi, H.; Hayashi, S.; Yamamoto, Y. Polymer Optical Microcavity Sensor for Volatile Organic Compounds with Distinct Selectivity toward Aromatic Hydrocarbons. *Acs Omega* **2021,** 6 (32), 21066-21070 DOI:

10.1021/acsomega.1c02749.

52. Toropov, N.; Cabello, G.; Serrano, M. P.; Gutha, R. R.; Rafti, M.; Vollmer, F. Review of biosensing with whispering-gallery mode lasers. *Light-Sci Appl* **2021,** 10 (1), DOI: Artn 42
10.1038/S41377-021-00471-3.

53. Du, Y. X.; Zou, C. L.; Zhang, C. H.; Wang, K.; Qiao, C.; Yao, J. N.; Zhao, Y. S. Tuneable red, green, and blue single-mode lasing in heterogeneously coupled organic spherical microcavities. *Light-Sci Appl* **2020,** 9 (1), DOI: ARTN 151
10.1038/s41377-020-00392-7.

54. Zhang, W.; Yao, J. N.; Zhao, Y. S. Organic Micro/Nanoscale Lasers. *Accounts Chem Res* **2016,** 49 (9), 1691-1700 DOI: 10.1021/acs.accounts.6b00209.

55. Jiang, X. F.; Qavi, A. J.; Huang, S. H.; Yang, L. Whispering-Gallery Sensors. *Matter* **2020,** 3 (2), 371-392 DOI: 10.1016/j.matt.2020.07.008.

56. Zhukov, A. E.; Kryzhanovskaya, N. V.; Moiseev, E. I.; Maximov, M. V. Quantum-dot microlasers based on whispering gallery mode resonators. *Light-Sci Appl* **2021,** 10 (1), DOI: Artn 80
10.1038/S41377-021-00525-6.

57. Fernandez-Bravo, A.; Yao, K.; Barnard, E. S.; Borys, N. J.; Levy, E. S.; Tian, B.; Tajon, C. A.; Moretti, L.; Altoe, M. V.; Aloni, S.; Beketayev, K.; Scotognella, F.; Cohen, B. E.; Chan, E. M.; Schuck, P. J. Continuous-Wave Upconverting Nanoparticle Microlasers. *Nat. Nanotechnol.* **2018,** 13, 572.

58. Liu, Y. W.; Teitelboim, A.; Fernandez-Bravo, A.; Yao, K. Y.; Altoe, M. V. P.; Aloni, S.; Zhang, C. H.; Cohen, B. E.; Schuck, P. J.; Chan, E. M. Controlled Assembly of Upconverting Nanoparticles for Low-Threshold Microlasers and Their Imaging in Scattering Media. *Acs Nano* **2020,** 14 (2), 1508-1519 DOI: 10.1021/acsnano.9b06102.

59. Yang, X. F.; Lyu, Z. Y.; Dong, H.; Sun, L. D.; Yan, C. H. Lanthanide Upconverted Microlasing: Microlasing Spanning Full Visible Spectrum to Near-Infrared under Low Power, CW Pumping. *Small* **2021,** 17 (41), DOI: Artn 2103140
10.1002/Smll.202103140.

60. Vahala, K. J. Optical microcavities. *Nature* **2003,** 424 (6950), 839.

61. Gorodetsky, M. L.; Savchenkov, A. A.; Ilchenko, V. S. ULTIMATE Q OF OPTICAL MICROSPHERE RESONATORS. *Opt Lett* **1996,** 21 (7), 453-455.

62. Boriskina, S. V.; Benson, T. M.; Sewell, P.; Nosich, A. I. Spectral shift and Q change of circular and square-shaped optical microcavity modes due to periodic sidewall surface roughness. *JOSA B* **2004,** 21 (10), 1792-1796.

63. Ward, J.; Benson, O. WGM microresonators: sensing, lasing and fundamental optics with microspheres. *Laser & Photonics Reviews* **2011,** 5 (4), 553-570.

64. Chiasera, A.; Dumeige, Y.; Feron, P.; Ferrari, M.; Jestin, Y.; Nunzi Conti, G.; Pelli, S.; Soria, S.; Righini, G. C. Spherical whispering-gallery-mode microresonators. *Laser & Photonics Reviews* **2010,** 4 (3), 457-482.

65. Grim, J. Q.; Christodoulou, S.; Di Stasio, F.; Krahne, R.; Cingolani, R.; Manna, L.; Moreels, I. Continuous-wave biexciton lasing at room temperature using solution-processed quantum wells. *Nat Nanotechnol* **2014,** 9 (11), 891-895 DOI: 10.1038/nnano.2014.213.

66. Fan, F.; Voznyy, O.; Sabatini, R. P.; Bicanic, K. T.; Adachi, M. M.; McBride, J. R.; Reid, K. R.; Park, Y.-S.; Li, X.; Jain, A.; Quintero-Bermudez, R.; Saravanapavanantham, M.; Liu, M.; Korkusinski, M.; Hawrylak, P.; Klimov, V. I.; Rosenthal, S. J.; Hoogland, S.; Sargent, E. H. Continuous-wave lasing in colloidal quantum dot solids enabled by facet-selective epitaxy. *Nature* **2017,** 544 (7648), 75-79 DOI: 10.1038/nature21424.

Chapter 4 Determinants for lowering threshold and achieving single nanoparticle upconverting microlaser

4.1 Preamble

In chapter 3, we explored the powerful ability of CR for modulating excited energy accumulation of each energy levels. Appropriate doping concentration of Tm^{3+} ions lead to the onset of population inversion at low excitation power, which is vital to achieve lasing emission with a low threshold. We found the appropriate doping concentration of 20 mol. % Yb^{3+} and 2 mol. % Tm^{3+} to produce moderate CR at a relatively low power range. Then, these UCNPs were used as gain media and coated on the cavity with a uniform single layer to suppress the scattering loss. Finally, a threshold of ~150 W/cm^2 was achieved through employing a 5-μm PS bead as WGM microcavity. Meanwhile, we also found that the gain media coating process plays an important role in the arising of lasing emission. For example, non-uniform coating with UCNPs aggregations induces the increase of threshold with broad FWHM/linewidth and small Q factor[1-3]. However, as we all know, large UCNPs show stronger emission intensity especially at single particle level due to more emitters and restrained surface quenching[4-6]. This brings another question: will the uniform coating of large UCNPs lower the pumping threshold of lasing emission?

In this chapter, gain media with same dopant but various sizes are used to explore the size-dominant scattering effect for Q factor and lasing threshold. The power dependent spectra, lasing emission linewidth as well as other key properties for lasing emission are studied. Furthermore, the possibility of single nanoparticle to achieve lasing emission is also investigated.

4.2 Introduction

Microlasers, producing coherent photons from a tiny cavity, show great potential for the application of intracellular sensing[7-9], tracking[10-12], on-chip integrated optoelectronics[13-15], high-density data storage[16-18], and so on. The emerging applications of microlasers has promoted the demands of more efficient microlasers with smaller cavity size and lower pumping threshold[16, 18, 19]. Although great progress of microlasers have achieved in the past decades, miniatured laser with CW pumped low threshold remains challenging. The miniaturization of cavity size gives rise to high optical losses and insufficient pump to gain interaction[20, 21], and thus lead to the increase of lasing threshold[17, 22, 23]. And nanoscale laser is also a big challenge for many gain media.

As for upconverting microlasers, several strategies have been employed to lower the threshold. The population inversion establishment of gain media are most explored[24-29]. Most recently, room temperature continuous-wave (CW) pumped upconverting lasing at blue and NIR band was obtained through the employ of single Tm^{3+} doped $NaYF_4$ energy-looping nanocrystals[30]. The avalanche-like energy looping mechanism provide an efficient strategy to achieve energy accumulation in the selected $^3H_4$ (Tm^{3+}) state, which would further facilitate the formation of low threshold (~14 kW/cm^2) lasing emission with a high-quality polystyrene microsphere acting as resonant cavity[2]. Furthermore, we also developed a kind of CR modulated gain media with a strong absorption coefficient and powerful energy accumulation ability to keep lower the threshold to ~150 W/cm^2 (chapter 3)[1]. The size of upconversion gain media used in recent works is smaller than 25 nm. The larger nanoparticles with more emitters and suppressive surface quenching often produce stronger brightness[31-33]. Does it possible to lower the threshold by using large upconversion nanoparticles?

As the intrinsic quality factor Q_{int} (here for spherical WGM resonator) arise from losses of many processes and can be written as[15, 23, 34, 35]:

$$1/Q_{int} = 1/Q_{rad} + 1/Q_{abs} + 1/Q_{sca}$$

Where the Q_{rad} describe the radiation loss of cavity especially at the looping node of total reflection, Q_{abs} contains intrinsic material absorption and surface coated gain media absorbing loss, Q_{sca} describes the scattering losses caused by intrinsic and surface scattering loss. The scattering scales is particles' diameter to the 6th power[36, 37].

Herein, the balance between the brightness and scattering effect was discussed in detail. Upconversion nanoparticles with larger size indeed show stronger brightness. However, the enlarged size, from 24 nm to 51 nm, induced severe scattering losses, resulting in an increase of lasing emission linewidth from ~0.5 nm to ~1.2 nm, and strong spontaneous emission background. The Q factor was also reduced from ~1900 to ~700 due to the scattering losses. On the consideration of brightness and scattering effect, lasing emission from single nanoparticle coupled microcavity was further explored. The narrow linewidth of ~0.45 nm indicates the single nanoparticle is bright enough to achieve lasing emission with negligible scattering loss.

4.3 Experimental Section

Upconversion nanoparticles with same dopants but various sizes were designed and synthesized to explore the size dependent scattering effect. To obtain the upconversion nanocrystals with various sizes, we employed the seed-mediated growth method for precise control[38-42].

4.3.1 Seed-mediated growth of nanocrystals with various sizes

Due to the same dopants in the core and shell layer, homoepitaxial growth was used. In our experiment, the seeds were obtained by the method introduced in chapter 2 and 3. The prepare of precursors for epitaxial growth is shown as follow[40, 43]:

$YCl_3 \cdot 6H_2O$ (0.78 mmol), $YbCl_3 \cdot 6H_2O$ (0.2 mmol) and $TmCl_3 \cdot 6H_2O$ (0.02 mmol) were added into a 50 mL three-necked flask containing 6 mL oleic acid (OA) and 15 mL 1-octadecene (ODE). The mixture was first heated to 160 °C under argon for 30 min to form a transparent solution and remove residual water. The solution was cooled down to room temperature, and 10 mL of a methanol solution containing NaOH (2.5 mmol) and NH_4F (4 mmol) was slowly dropped into the flask and stirred for 30 min. Then, the solution was heated to 70-80 °C and maintained for 30 min to evaporate methanol. And the reaction solution was further heated to 160 °Cfor 30 min to remove the residual water before cooling down to room temperature.

For the seed-mediated layer by layer growth of upconversion nanocrystals with needed size[44, 45]: A total of 0.2 mmol seed nanocrystals in cyclohexane were added to a 50 mL flask containing 4 mL OA and 10 mL ODE. The mixture was heated to 160 °C under argon for 30 min to remove cyclohexene before the solution was further heated to 300 °C. Then, an appropriate amount of shell precursors was injected into the reaction mixture step-by-step with an injection rate of 0.25 mL every 3 min. After finish the injection of precursors, the reaction solution was ripened at 300 °C for additional 5 min. Finally, the reaction solution was cooled down to room temperature, and the resulting products were precipitated by ethanol and collected by centrifugation at 6000 rpm for 5 min. The precipitate was then purified with ethanol three times, and finally dispersed in cyclohexane for further use.

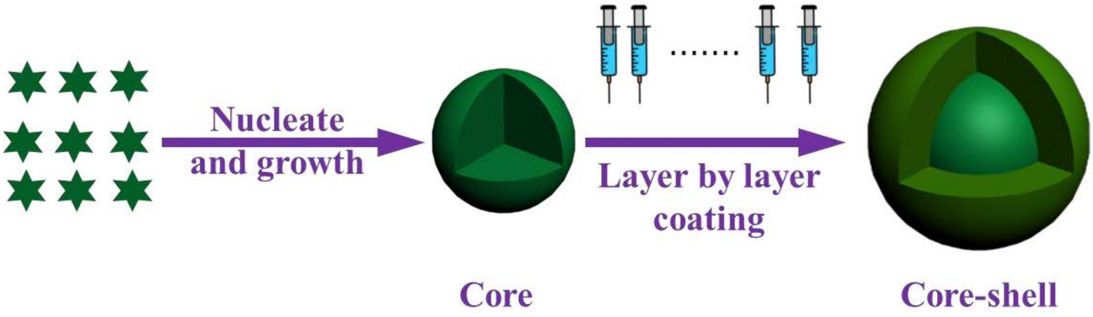

Figure 4.1 Schematic illustration of reaction equipment used in seed-mediated layer by layer growth method, and growth process of nanocrystals.

4.3.2 Simplified calculation of layer-by-layer growth

In this method, the upconversion nanocrystals with smaller size, serving as seeds, can be grown into the large one that we need by adding precursors continuously. When using the same core, the final size is decided by the amount of precursor that we added, and we can also calculate this simply as follow:

During the calculation, a spherical concentric model is applied to calculate the precursor dose. As the number of nanocrystals (*N*) would not change before and after epitaxial growth, we can simplify the calculation into the growth of one nanocrystal ($V_{\mathrm{total}} = V_{\mathrm{single}} \times N$).

In a single nanocrystal, the volume can be calculated by the following equation:

$$V = \frac{4}{3}\pi r^3$$

Where r is the radius of this spherical nanocrystal.

Then, the volume of precursor needed for a single nanocrystal is

$$V_{\mathrm{precursor}} = V_{\mathrm{target}} - V_{\mathrm{seed}}$$

Where V_{seed} and V_{target} are the volume of the nanocrystal before and after epitaxial growth.

Then, the volume ratio of precursor we needed *v.s.* the seed we added is:

$$\frac{V_{\mathrm{precursor}}}{V_{\mathrm{seed}}} = \frac{V_{\mathrm{target}} - V_{\mathrm{seed}}}{V_{\mathrm{seed}}} = \frac{r_{\mathrm{target}}^3}{r_{\mathrm{seed}}^3} - 1$$

As the mole number $n = \frac{m}{M} = \frac{\rho V}{M}$ and for homogeneous growth (same molar mass and density), the amount of precursor needed for target size is

$$n_{\text{precursor}} = [(\frac{r_{\text{target}}}{r_{\text{seed}}})^3 - 1] \times n_{\text{seed}}$$

Noting that the calculation process needs to be corrected, as the molar mass and density of seed and shell layer are not same for heterogeneous growth.

Then, we can estimate the amount of precursor by knowing the target size, the size and dose of added seeds. In this experiment, 24 nm core nanoparticles were used as seeds. As can be seen from table 4.1, the actual size fit well with the desired size. Normally, it's impossible to achieve 100% yield for the synthesis of core nanoparticles. The actual amount of core nanoparticles was a bit smaller than 0.2 mmol. Thus, the final size of core shell nanoparticles was slightly larger than designed ones.

Table 4.1 The calculation of added precursors for desired size.

Size of core	Amount of core	Desired size	Amount of precursor	Actual size
24 nm	0.2 mmol	50 nm	~1.60 mmol	51 nm
24 nm	0.2 mmol	40 nm	~ 0.75 mmol	43 nm

4.4 Results and discussion

4.4.1 Characteristic of upconversion nanoparticles with enlarged size

By using the seed-mediated layer by layer epitaxial growth method, upconversion nanoparticles with uniform morphology but different sizes were obtained. As shown in TEM images and particle size statistical distribution results, the upconversion nanoparticles with a diameter of 24 nm were grown into 43 nm and 51 nm. Due to the homogeneous growth process (core and shell layer have same dopants), we can only see the enlarged size without obvious contrast between core and shell layer. What's more, the dimensional homogeneity of each as-prepared sample is very good, which is vital for single nanoparticles imaging.

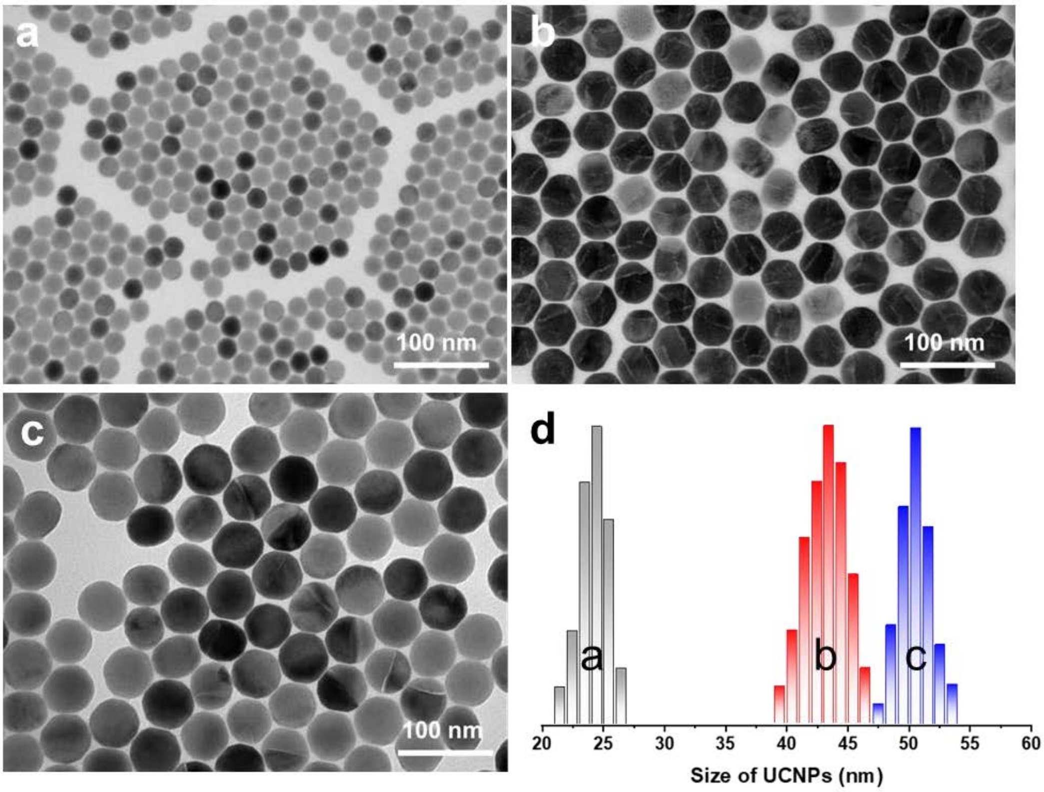

Figure 4.2 a-c, TEM images of NaYF$_4$:20%Yb^{3+},2%Tm^{3+} with various sizes, and **d** shows the sizes distribution of UCNPs shown in **a-c**.

The upconversion emission spectra of these nanoparticles were measured used the solution sample measurement set-up. As can be seen, the emission intensity enhanced a lot with the increase of size. The integrated emission intensity of 51 nm nanoparticles was ~12 times stronger than that of 24 nm ones. The enhancement mainly comes from two parts. One originates from the enlarged size, which means more sensitizers and emitters for upconversion emissions. On the other hand, there are lots of quenching sites on the surface, and the smaller size leads to higher surface to volume ratio, that excited state energy are easily be quenched by surface defects[46, 47]. With the increase of size, the specific surface area reduces, and the emission quenching arising from surface defects can be suppressed at some extent.

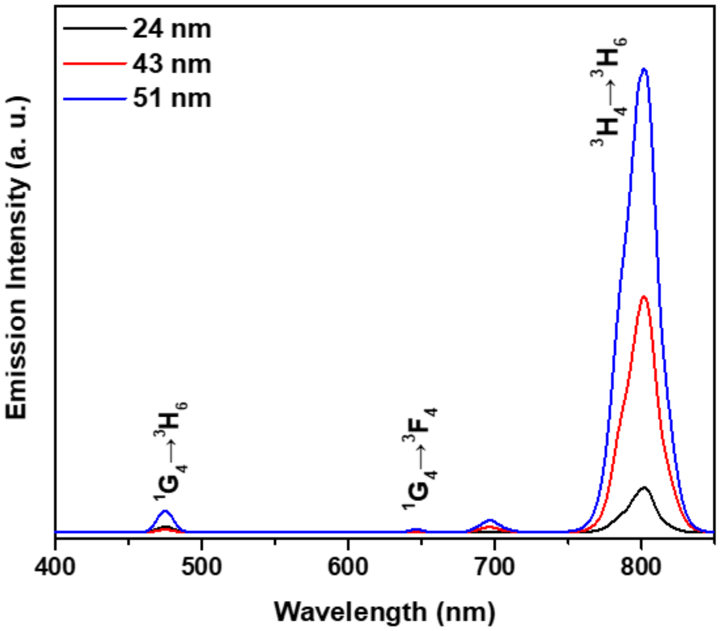

Figure 4.3 Upconversion emission spectra of NaYF$_4$:20%Yb^{3+},2%Tm^{3+} with various sizes under the excitation of 976 nm laser.

The brightness of single upconversion nanoparticles was then characterized by using a home-built confocal system with a resolution of about 450 nm. To measure the single nanoparticles with the distance between two nearby ones larger than the resolution, nanoparticles was diluted more than 10^4 times and dropped onto the cover glass. After point-by-point scanning, the emission intensity of each point is recorded and then emission distribution mapping is reconstructed. As can be seen, the brightness of each nanoparticle is almost than same in each batch of as-prepared UCNPs. The brightness of UCNPs increase from ~3100 counts/50ms to ~35200 counts/50ms as the size increase from 24 nm to 51 nm. At ultra-high-power density, the brightness of UCNPs is determined by the amount of doped emitters, while the surface quenching has very limited effect on the brightness. The amount of emitters contained in each nanoparticle is proportional to the volume, which is proportional to the radius to the third power. Thus, the final emission intensity of single nanoparticles increases with the same tendency of volume (number of emitters), as shown in Figure 4.4.

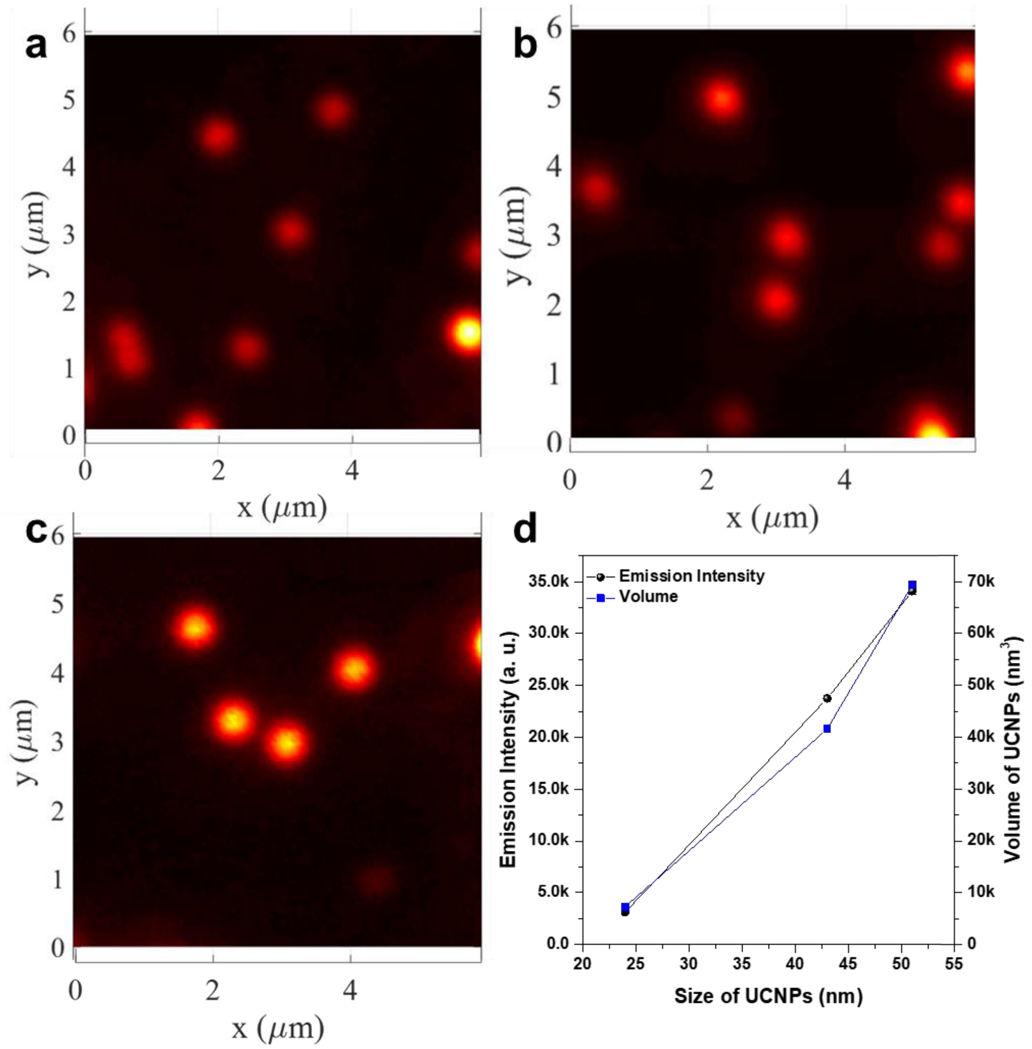

Figure 4.4 a-c, the single nanoparticle confocal images of $NaYF_4$:20%Yb^{3+},2%Tm^{3+} with a size of 24 nm, 43 nm, and 51 nm. **d**, the emission intensity and volume of UCNPs plotted with the function of size.

4.4.2 Lasing emission performances of microlaser

Although the larger nanoparticles often produce stronger brightness, the size induced scattering losses cannot be neglected. The effect of size on lasing emission, including threshold, linewidth, Q factor, is explored. As can be seen, the nanoparticles with various sizes are coated onto the surface of microcavity to form a uniform single layer (Figure 4.5 a-c). The single and smooth layer of gain media benefits emission coupling with the microcavity, which further facilitates the amplification by stimulated radiation. However, with the increase of nanoparticle size, from 24 nm, to 43 nm and 51 nm, the FWHM in the lasing spectra increases from ~0.5 nm to 0.8 nm and ~1.2 nm, with the increased spontaneous emission background (Figure 4.5e). These all indicate the scattering effects caused by size of gain media.

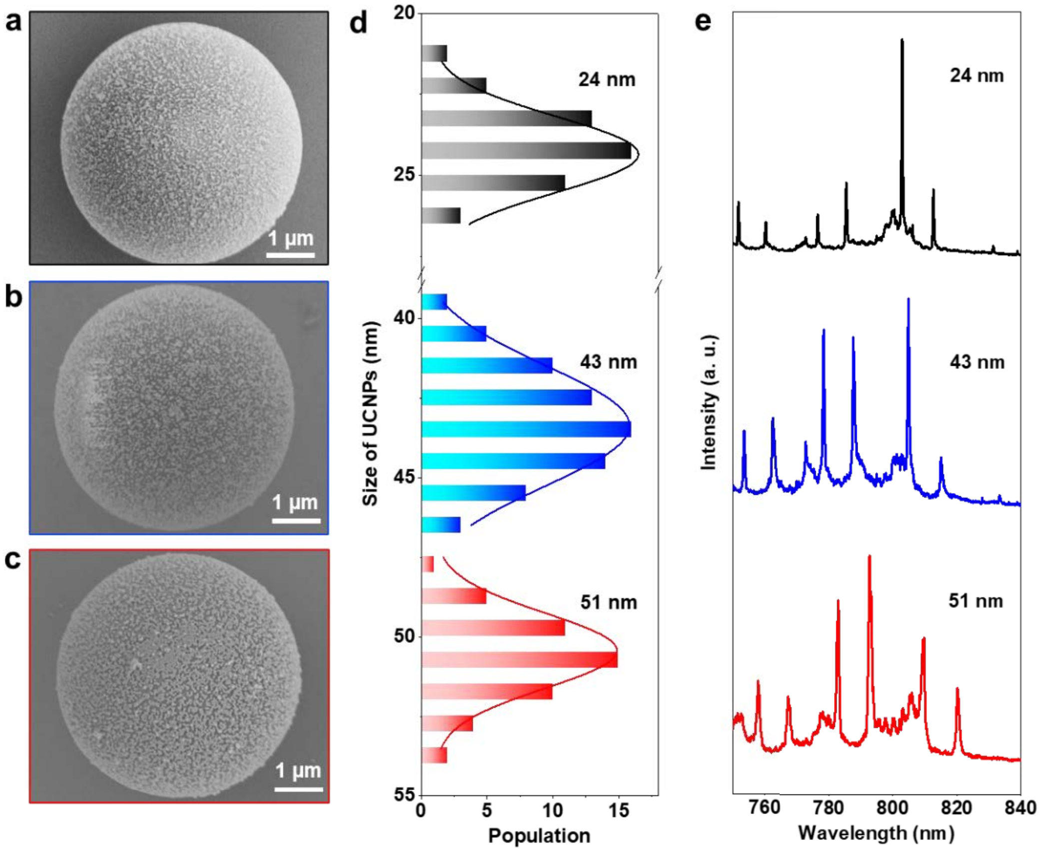

Figure 4.5 Size-dependent quality (Q) factors caused by the scattering losses when coating a single layer of nanoparticles in the micro cavity. a-c, SEM images of microspheres coated with $NaYF_4$:20%Yb^{3+},2%Tm^{3+} nanoparticles with sizes of 24 nm, 43 nm and 51 nm. Related **d**, upconversion nanoparticles size distribution and **e**, emission spectra of UCNPs coated microcavities in **a-c**.

Though larger sized UCNPs are brighter due to the increased emitters and reduced degree of surface-quenching, by testing more than 20 micro cavity lasers, the Q factor ($Q = \frac{\lambda}{\Delta\lambda}$) reduces from ~1900 to ~700 with the increased size of UCNPs (Figure 4.6). The reduction in the Q factor further indicates the increased size-induced scattering losses.

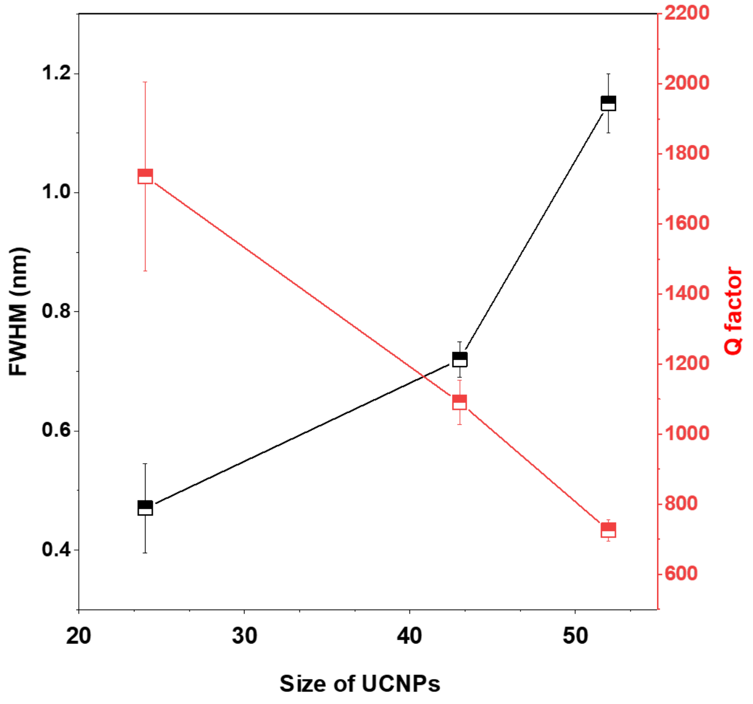

Figure 4.6 The related linewidth and Q factor of upconversion nanoparticles coated microlasers.

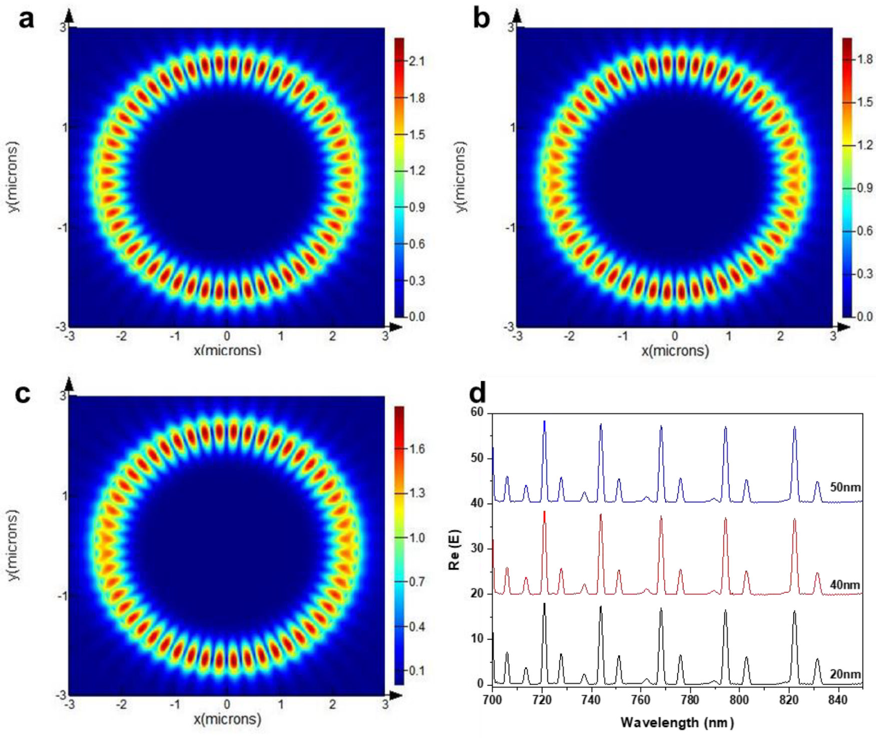

Figure 4.7 a-c, the numerical simulation of the electrical-field distributions at 794 nm within a major plane coated with various UCNPs. d, Numerical simulations of resonance spectra of microcavity coated with various UCNPs.

To further explore the effects of upconversion nanoparticles size, electrical fields simulations were carried out by using Lumerical FDTD solutions. As can be seen from the simulation results, the relatively electrical field intensity shows a slightly reduce when the coated UCNPs size increase. There is also a little disturbance at the looping node of 794 nm mode due to the particle scattering induced de-coupling. This indicates an increase of particle size induced scattering which would affect the light coupling and leaking during the looping paths. What's more, when the size of UCNPs becomes too large, the catchment area by the evanescent field of micro cavity modes also reduces (Figure 4.8).

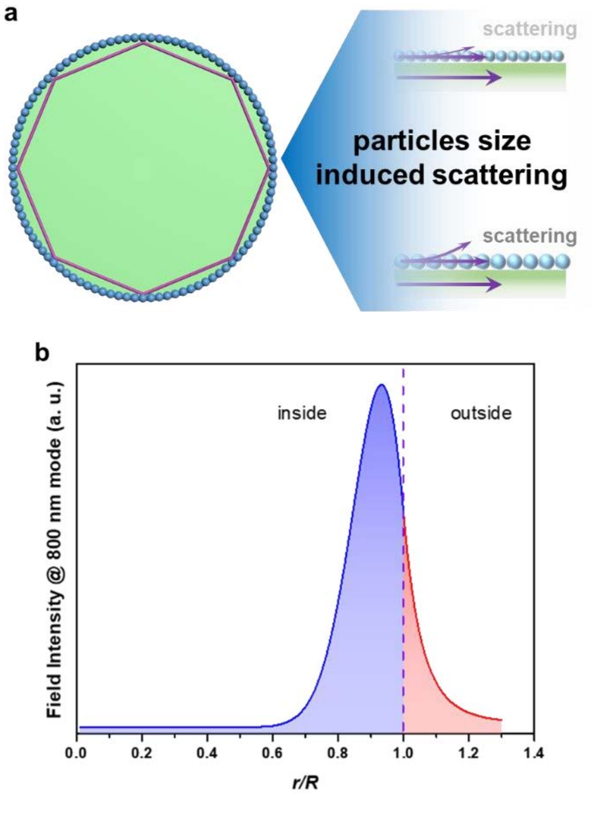

Figure 4.8 a, Schematic diagram of nanoparticles size induced scattering. **b**, The electrical-field distributions at 794 nm *v.s.* the distance to the center.

4.4.3 Single nanoparticle upconverting microlaser

As the single nanoparticle is bright enough for the collection of upconversion emission spectrum. Single nanoparticle coupled microlaser is constructed to further investigate the effect of nanoparticles size on the lasing emission performance. Upconversion nanoparticles with an average size of ~43 nm is chosen. Figure 4.9 a and b show that lanthanide ions doped single UCNPs are optically uniform and sufficiently bright, as there are 23640±832 confocal microscopy photon counts per 50 millisecond can collected from each nanoparticle, which are suitable for single particle lasing. And the size and brightness uniformity further provide optical error suppression.

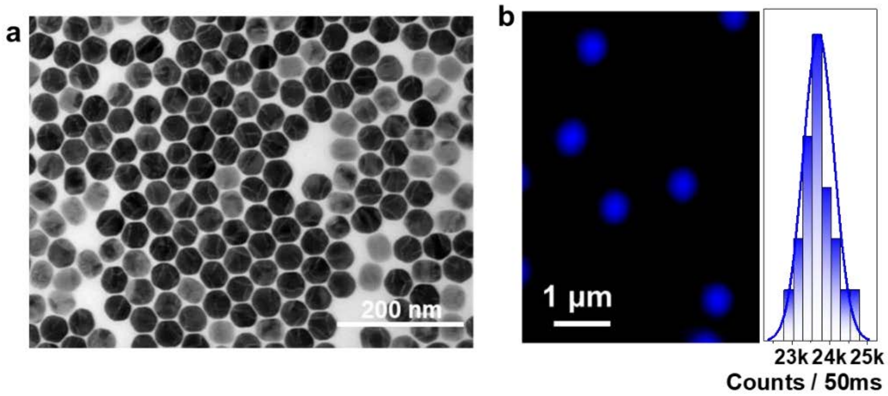

Figure 4.9 **a**, TEM image of 43 nm monodispersed $NaYF_4$:20%Yb^{3+},2%Tm^{3+} nanocrystals. **b**, Point-scanning confocal microscopic image of single UCNPs (in pseudocolour) and their brightness distribution at an excitation power density of 100 kW/cm^2.

With the precise control of the concentration ratio of UCNPs *v.s.* PS microcavity, single nanoparticle coated microcavity was achieved. As can be seen in Figure 4.10 a and the enlarged inset, there is only one nanoparticle with a size about 43 nm located at the edge of the microcavity, which is appropriate for the lasing emission measurement. Then, we focused the laser beam and pumped the single nanoparticle at the edge of this microcavity. Interestingly, obvious emission at the opposite of the excited spot can be seen from the wide field image, which indicates the successful coupling of upconversion emission. It is clear that the upconversion emissions can propagate along the inner surface of this microcavity. It is possible to achieve lasing emission when the gain is larger than losses.

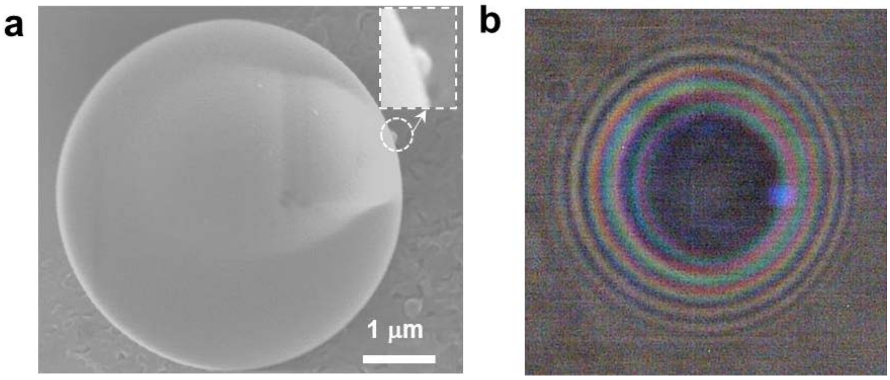

Figure 4.10 SEM image (**a**) and Wide field image (**b**) of a single UCNP in a micro cavity.

The spectra comparation of single nanoparticle with and without coupling with a microcavity is shown in Figure 4.11. The upconversion nanoparticle with a size of 43 nm is bright enough to be detected and the full emission spectrum of single nanoparticle is collected. Obvious sharp emission peaks around 800 nm appears when the upconversion nanoparticle is coupled with a microcavity. And the free spectral range (FSR) between two adjacent TE modes or TM modes fit well with theoretical value ($\Delta\lambda_{FSR} = \frac{\lambda^2}{2\pi R}$, R is the radius of microcavity). What's more, the emission intensity from the transition from $^3H_4$ to $^3H_6$ become much stronger than that without microcavity, which all indicate the possible stimulated emission of $^3H_4$ at selected modes.

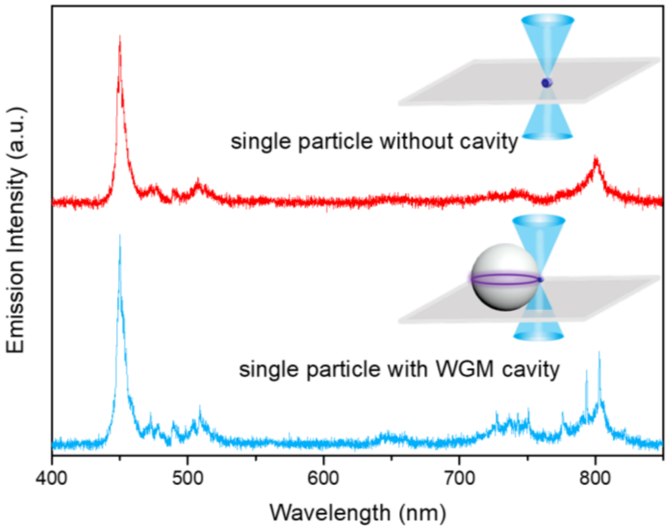

Figure 4.11 The upconversion spectra comparation of single nanoparticle with and

without coupling with a WGM microcavity.

The power dependent spectra of single nanoparticle coupled microlaser were measured and shown in Figure 4.12 a. Obvious sharp peak at 808 nm arises with the increase of pumping power. The narrowed linewidth and S shape light-to-light curve indicate the occurrence of stimulated emission, which confirmed the lasing emission from single nanoparticle coupled microcavity. However, due to the brightness of single nanoparticle and the limited light that confined within the cavity, the observed lasing threshold of single nanoparticle is much higher than the single layer coated ones.

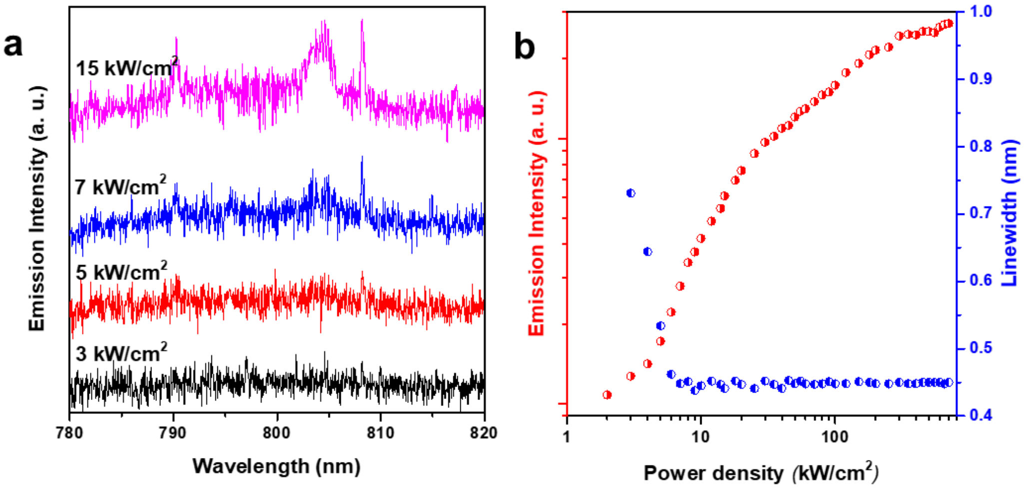

Figure 4.12 Lasing emissions from a single nanocrystal. a, Power dependent upconversion emission spectra showing the gradual appearance of lasing emission peaks at 808 nm. **b**, The pumping power-dependent plots of emission intensities and spectral linewidth narrowing (peak@808 nm), showing the onset of single UCNP's lasing emissions.

To further confirm the stimulated lasing emission, upconversion emission lifetimes at 800 nm band with and without microcavity were measured and shown in Figure 4.13. Tens of microseconds decay time shorter is observed when single nanoparticle is coupled with a microcavity. However, due to the broad bandpass filter (800/40 nm) and strong spontaneous emission background, the measured decay curve contains both spontaneous emission part and stimulated emission parts. As the spontaneous emission is much broad, the expected sharp decrease of lifetime is not observed. If we equip with fast responding pumping laser, much sensitive detector, and filter the emission with a very narrow band monochromator, a stimulated dominant decay curve can be obtained.

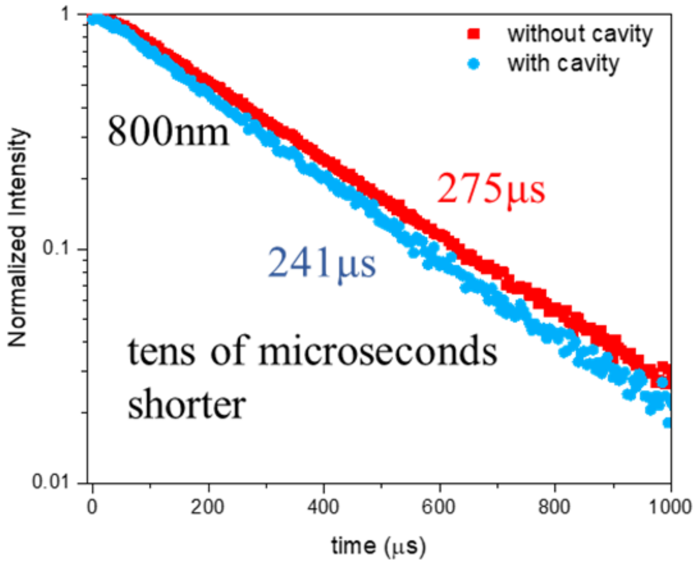

Figure 4.13 Lifetime of single nanoparticle with and without microcavity. Noting that the lifetime is measured through an 800/40 nm bandpass filter.

4.5 Conclusion

The scattering effect originate from the size of gain medium is investigated in this chapter. Upconversion nanoparticles with larger size show much brighter emission due to the suppressed surface quenching and increased number of emitters. However, the increased size leads to stronger scattering, which hinder the coupling of emission at the surface and increase the leaking of light inside the microcavity. Thus, a broad linewidth (from ~0.5 nm to ~1.2 nm) and reduced Q factor (from ~1900 to ~700) were observed when increase the sizes of upconversion nanoparticles coated on the surface of microcavity. Based on the brightness of upconverstion nanoparticles, we have further verified that the size of single nanoparticle does not affect the Q factor of micro cavity lasing. We demonstrate that CR assisted population inversion in single UCNPs as a highly efficient gain medium, which can be widely used in any photonics cavities for single nanoparticle lasers. Single 43 nm $NaYF_4$: 20 mol. % Yb^{3+}-2 mol.% Tm^{3+} UCNPs can lase at 808 nm with the sharp peaks and narrow FWHM of ~0.45 nm once in a cavity, which preserving the Q-factors of the cavity since scattering losses are reduced to the minimum. Due to the reduced scattering from single UCNP, it allows to use bigger particles and increase the total gain, compared to the uniform 24 nm single layer coating.

4.6 References

1. Shang, Y.; Zhou, J.; Cai, Y.; Wang, F.; Fernandez-Bravo, A.; Yang, C.; Jiang, L.; Jin, D. Low threshold lasing emissions from a single upconversion nanocrystal. *Nature Communications* **2020,** 11 (1), 6156 DOI: 10.1038/s41467-020-19797-4.
2. Fernandez-Bravo, A.; Yao, K.; Barnard, E. S.; Borys, N. J.; Levy, E. S.; Tian, B.; Tajon, C. A.; Moretti, L.; Altoe, M. V.; Aloni, S.; Beketayev, K.; Scotognella, F.; Cohen, B. E.; Chan, E. M.; Schuck, P. J. Continuous-Wave Upconverting Nanoparticle Microlasers. *Nat. Nanotechnol.* **2018,** 13, 572.
3. Liu, Y. W.; Teitelboim, A.; Fernandez-Bravo, A.; Yao, K. Y.; Altoe, M. V. P.; Aloni, S.; Zhang, C. H.; Cohen, B. E.; Schuck, P. J.; Chan, E. M. Controlled Assembly of Upconverting Nanoparticles for Low-Threshold Microlasers and Their Imaging in Scattering Media. *Acs Nano* **2020,** 14 (2), 1508-1519 DOI: 10.1021/acsnano.9b06102.
4. Kraft, M.; Würth, C.; Muhr, V.; Hirsch, T.; Resch-Genger, U. Particle-size-dependent upconversion luminescence of NaYF 4: Yb, Er nanoparticles in organic solvents and water at different excitation power densities. *Nano Res* **2018,** 11 (12), 6360-6374.
5. Ma, C.; Xu, X.; Wang, F.; Zhou, Z.; Liu, D.; Zhao, J.; Guan, M.; Lang, C. I.; Jin, D. Optimal Sensitizer Concentration in Single Upconversion Nanocrystals. *Nano Lett* **2017,** 17 (5), 2858-2864 DOI: 10.1021/acs.nanolett.6b05331.
6. Liu, Y. J.; Lu, Y. Q.; Yang, X. S.; Zheng, X. L.; Wen, S. H.; Wang, F.; Vidal, X.; Zhao, J. B.; Liu, D. M.; Zhou, Z. G.; Ma, C. S.; Zhou, J. J.; Piper, J. A.; Xi, P.; Jin, D. Y. Amplified stimulated emission in upconversion nanoparticles for super-resolution nanoscopy. *Nature* **2017,** 543 (7644), 229-233 DOI: 10.1038/nature21366.
7. Humar, M.; Hyun Yun, S. Intracellular microlasers. *Nat Photonics* **2015,** 9 (9), 572-576 DOI: 10.1038/nphoton.2015.129.
8. Gather, M. C.; Yun, S. H. Single-cell biological lasers. *Nat Photonics* **2011,** 5 (7), 406-410 DOI: 10.1038/Nphoton.2011.99.
9. Nizamoglu, S.; Lee, K. B.; Gather, M. C.; Kim, K. S.; Jeon, M.; Kim, S.; Humar, M.; Yun, S. H. A Simple Approach to Biological Single-Cell Lasers Via Intracellular Dyes. *Adv Opt Mater* **2015,** 3 (9), 1197-1200 DOI: 10.1002/adom.201500144.
10. Martino, N.; Kwok, S. J. J.; Liapis, A. C.; Forward, S.; Jang, H.; Kim, H.-M.; Wu, S. J.; Wu, J.; Dannenberg, P. H.; Jang, S.-J.; Lee, Y.-H.; Yun, S.-H. Wavelength-encoded laser particles for massively multiplexed cell tagging. *Nat Photonics* **2019,** 13 (10), 720-727 DOI: 10.1038/s41566-019-0489-0.
11. Tang, S.-J.; Dannenberg, P. H.; Liapis, A. C.; Martino, N.; Zhuo, Y.; Xiao, Y.-F.; Yun, S.-H. Laser particles with omnidirectional emission for cell tracking. *Light: Science & Applications* **2021,** 10 (1), 23 DOI: 10.1038/s41377-021-00466-0.
12. Pirnat, G.; Humar, M.; Musevic, I. Remote and autonomous temperature measurement based on 3D liquid crystal microlasers. *Optics Express* **2018,** 26 (18), 22615-22625 DOI: 10.1364/Oe.26.022615.

13. Vahala, K. J. Optical microcavities. *Nature* **2003,** 424 (6950), 839.

14. Ma, Y. G.; Guo, X.; Wu, X. Q.; Dai, L.; Tong, L. M. Semiconductor nanowire lasers. *Adv Opt Photonics* **2013,** 5 (3), 216-273 DOI: 10.1364/Aop.5.000216.

15. Foreman, M. R.; Swaim, J. D.; Vollmer, F. Whispering gallery mode sensors. *Adv Opt Photonics* **2015,** 7 (2), 168-240 DOI: 10.1364/AOP.7.000168.

16. Ma, R.-M.; Oulton, R. F. Applications of nanolasers. *Nat Nanotechnol* **2019,** 14 (1), 12-22.

17. Zhuge, M. H.; Pan, C.; Zheng, Y.; Tang, J.; Ullah, S.; Ma, Y.; Yang, Q. Wavelength-Tunable Micro/Nanolasers. *Adv Opt Mater* **2019**, 1900275.

18. Jeong, K.-Y.; Hwang, M.-S.; Kim, J.; Park, J.-S.; Lee, J. M.; Park, H.-G. Recent Progress in Nanolaser Technology. *Adv Mater* **2020,** 32 (51), 2001996 DOI: https://doi.org/10.1002/adma.202001996.

19. Azzam, S. I.; Kildishev, A. V.; Ma, R. M.; Ning, C. Z.; Oulton, R.; Shalaev, V. M.; Stockman, M. I.; Xu, J. L.; Zhang, X. Ten years of spasers and plasmonic nanolasers. *Light-Sci Appl* **2020,** 9 (1), DOI: ARTN 90
10.1038/s41377-020-0319-7.

20. Gorodetsky, M. L.; Savchenkov, A. A.; Ilchenko, V. S. ULTIMATE Q OF OPTICAL MICROSPHERE RESONATORS. *Opt Lett* **1996,** 21 (7), 453-455.

21. Jiang, X. F.; Zou, C. L.; Wang, L.; Gong, Q. H.; Xiao, Y. F. Whispering-gallery microcavities with unidirectional laser emission. *Laser & Photonics Reviews* **2016,** 10 (1), 40-61 DOI: 10.1002/lpor.201500163.

22. Hill, M. T.; Gather, M. C. Advances in small lasers. *Nat Photonics* **2014,** 8 (12), 908.

23. He, L.; Özdemir, Ş. K.; Yang, L. Whispering gallery microcavity lasers. *Laser & Photonics Reviews* **2013,** 7 (1), 60-82.

24. Ruan, Y.; Boyd, K.; Ji, H.; Ebendorff-Heidepriem, H.; Munch, J.; Monro, T. M. In *Upconversion lasing for index sensing and strong amplitude modulation of WGMs in Er-Yb co-doped tellurite spheres*, CLEO: 2013, 2013; IEEE: 2013; pp 1-2.

25. Chen, X.; Jin, L.; Kong, W.; Sun, T.; Zhang, W.; Liu, X.; Fan, J.; Yu, S. F.; Wang, F. Confining energy migration in upconversion nanoparticles towards deep ultraviolet lasing. *Nature communications* **2016,** 7, 10304.

26. Xu, X. H.; Zhang, W. F.; Yang, D. C.; Lu, W.; Qiu, J. B.; Yu, S. F. Phonon-Assisted Population Inversion in Lanthanide-Doped Upconversion Ba2LaF7 Nanocrystals in Glass-Ceramics. *Adv Mater* **2016,** 28 (36), 8045-8050 DOI: 10.1002/adma.201601405.

27. Wang, T.; Yu, H.; Siu, C. K.; Qiu, J.; Xu, X.; Yu, S. F. White-light whispering-gallery-mode lasing from lanthanide-doped upconversion NaYF4 hexagonal microrods. *ACS photonics* **2017,** 4 (6), 1539-1543.

28. Chen, X.; Jin, L. M.; Sun, T. Y.; Kong, W.; Yu, S. F.; Wang, F. Energy Migration Upconversion in Ce(III)-Doped Heterogeneous Core-Shell-Shell Nanoparticles. *Small* **2017,** 13 (43), DOI: Artn 1701479

10.1002/Smll.201701479.

29. Jin, L. M.; Wu, Y. K.; Wang, Y. J.; Liu, S.; Zhang, Y. Q.; Li, Z. Y.; Chen, X.; Zhang, W. F.; Xiao, S. M.; Song, Q. H. Mass-Manufactural Lanthanide-Based Ultraviolet B Microlasers. *Adv Mater* **2019,** 31 (7), DOI: Artn 1807079
10.1002/Adma.201807079.

30. Fernandez-Bravo, A.; Yao, K.; Barnard, E. S.; Borys, N. J.; Levy, E. S.; Tian, B.; Tajon, C. A.; Moretti, L.; Altoe, M. V.; Aloni, S. Continuous-wave upconverting nanoparticle microlasers. *Nat Nanotechnol* **2018,** 13 (7), 572.

31. Zhao, J. B.; Jin, D. Y.; Schartner, E. P.; Lu, Y. Q.; Liu, Y. J.; Zvyagin, A. V.; Zhang, L. X.; Dawes, J. M.; Xi, P.; Piper, J. A.; Goldys, E. M.; Monro, T. M. Single-nanocrystal sensitivity achieved by enhanced upconversion luminescence. *Nat Nanotechnol* **2013,** 8 (10), 729-734 DOI: 10.1038/nnano.2013.171.

32. Haro-Gonzalez, P.; del Rosal, B.; Maestro, L. M.; Rodriguez, E. M.; Naccache, R.; Capobianco, J. A.; Dholakia, K.; Sole, J. G.; Jaque, D. Optical trapping of NaYF4:Er3+,Yb3+ upconverting fluorescent nanoparticles. *Nanoscale* **2013,** 5 (24), 12192-12199 DOI: 10.1039/c3nr03644h.

33. Dong, H.; Sun, L. D.; Yan, C. H. Upconversion emission studies of single particles. *Nano Today* **2020,** 35, DOI: Artn 100956
10.1016/J.Nantod.2020.100956.

34. Chiasera, A.; Dumeige, Y.; Feron, P.; Ferrari, M.; Jestin, Y.; Nunzi Conti, G.; Pelli, S.; Soria, S.; Righini, G. C. Spherical whispering-gallery-mode microresonators. *Laser & Photonics Reviews* **2010,** 4 (3), 457-482.

35. Jiang, X. F.; Qavi, A. J.; Huang, S. H.; Yang, L. Whispering-Gallery Sensors. *Matter* **2020,** 3 (2), 371-392 DOI: 10.1016/j.matt.2020.07.008.

36. Hulst, H. C.; van de Hulst, H. C. *Light scattering by small particles*. Courier Corporation: 1981.

37. Bohren, C. F.; Huffman, D. R. Absorption and scattering of light by small particles. **1983**.

38. Li, X. M.; Shen, D. K.; Yang, J. P.; Yao, C.; Che, R. C.; Zhang, F.; Zhao, D. Y. Successive Layer-by-Layer Strategy for Multi-Shell Epitaxial Growth: Shell Thickness and Doping Position Dependence in Upconverting Optical Properties. *Chem Mater* **2013,** 25 (1), 106-112 DOI: 10.1021/cm3033498.

39. Liao, J. Y.; Jin, D. Y.; Chen, C. H.; Li, Y. M.; Zhou, J. J. Helix Shape Power-Dependent Properties of Single Upconversion Nanoparticles. *Journal of Physical Chemistry Letters* **2020,** 11 (8), 2883-2890 DOI: 10.1021/acs.jpclett.9b03838.

40. Liu, B. L.; Liao, J. Y.; Song, Y. L.; Chen, C. H.; Ding, L.; Lu, J.; Zhou, J. J.; Wang, F. Multiplexed structured illumination super-resolution imaging with lifetime-engineered upconversion nanoparticles. *Nanoscale Adv* **2021,** 4 (1), 30-38 DOI: 10.1039/d1na00765c.

41. Liao, J. Y.; Zhou, J. J.; Song, Y. L.; Liu, B. L.; Lu, J.; Jin, D. Y. Optical Fingerprint

Classification of Single Upconversion Nanoparticles by Deep Learning. *Journal of Physical Chemistry Letters* **2021,** 12 (41), 10242-10248 DOI: 10.1021/acs.jpclett.1c02923.

42. Chen, Y. H.; Shimoni, O.; Huang, G.; Wen, S. H.; Liao, J. Y.; Duong, H. T. T.; Maddahfar, M.; Su, Q. P.; Ortega, D. G.; Lu, Y. L.; Campbell, D. H.; Walsh, B. J.; Jin, D. Y. Upconversion nanoparticle-assisted single-molecule assay for detecting circulating antigens of aggressive prostate cancer. *Cytom Part A* **2021**, DOI: 10.1002/cyto.a.24504.

43. Shan, X. C.; Wang, F.; Wang, D. J.; Wen, S. H.; Chen, C. H.; Di, X. J.; Nie, P.; Liao, J. Y.; Liu, Y. T.; Ding, L.; Reece, P. J.; Jin, D. Y. Optical tweezers beyond refractive index mismatch using highly doped upconversion nanoparticles. *Nat Nanotechnol* **2021,** 16 (5), 531-537 DOI: 10.1038/s41565-021-00852-0.

44. Liu, D.; Xu, X.; Du, Y.; Qin, X.; Zhang, Y.; Ma, C.; Wen, S.; Ren, W.; Goldys, E. M.; Piper, J. A. Three-dimensional controlled growth of monodisperse sub-50 nm heterogeneous nanocrystals. *Nature communications* **2016,** 7, 10254.

45. Li, D.; Wen, S. H.; Kong, M. Y.; Liu, Y. T.; Hu, W.; Shi, B. Y.; Shi, X. Y.; Jin, D. Y. Highly Doped Upconversion Nanoparticles for In Vivo Applications Under Mild Excitation Power. *Anal Chem* **2020,** 92 (16), 10913-10919 DOI: 10.1021/acs.analchem.0c02143.

46. Gargas, D. J.; Chan, E. M.; Ostrowski, A. D.; Aloni, S.; Altoe, M. V. P.; Barnard, E. S.; Sanii, B.; Urban, J. J.; Milliron, D. J.; Cohen, B. E.; Schuck, P. J. Engineering bright sub-10-nm upconverting nanocrystals for single-molecule imaging. *Nat Nanotechnol* **2014,** 9 (4), 300-305 DOI: 10.1038/Nnano.2014.29.

47. Zhou, J. J.; Wen, S. H.; Liao, J. Y.; Clarke, C.; Tawfik, S. A.; Ren, W.; Mi, C.; Wang, F.; Jin, D. Y. Activation of the surface dark-layer to enhance upconversion in a thermal field. *Nat Photonics* **2018,** 12 (3), 154-+ DOI: 10.1038/s41566-018-0108-5.

Chapter 5 Upconverting microlasers govern by nanoparticles with high concentration of sensitizer

5.1 Preamble

In the previous chapter, we investigated the doping concentration of activator induced CR process, the uniformity of coated gain medium layer and the size of gain medium, as well as the possibility of single nanoparticle to achieve lasing emission. Besides, the sensitizer inside upconversion nanoparticles also play an important role in the modulation of emission intensity and excited energy distribution[1-5], which would further regulate the pumping power density to facilitate population inversion and lasing emission[6, 7]. Although we have realized NIR lasing emission with a threshold of ~150 W/cm^2, the desired demand of much lower pumping threshold and multifunctional lasing emission is still challenging[8-10].

In this result chapter, we focus on the realization of population inversion at lower power density, and the gain medium with multiple emission peaks at the full visible range. To accomplish this objective, upconversion nanoparticles with core-shell structure were designed and synthesized. The dependence of doping concentration of sensitizer and the multi-ions doping for lasing emissions were investigated. Then, these upconversion gain media were coated on the same microcavity. The lasing performance, including pumping threshold, Q factors, and emission modes, *etc.* were further explored. What's more, the energy migration modulated white lasing emission was demonstrated.

5.2 Introduction

The multiple energy levels and ultra-long radiative lifetimes (microseconds or milliseconds) of 4f electrons make the lanthanide ions doped material a kind of excellent gain medium to achieve lasing emissions[7, 9, 11-14]. The relatively long decay times with optical and thermal stability of lanthanide ions promote the accumulation of excited energy with CW pumping, which is barely occurs in the gain media system such as QDs or organic dyes. However, the 4f-4f transitions induced absorption and emission of lanthanide ions lead to intrinsic weak absorption ($\sim 10^{-20}$ cm^{-2}) and relatively low quantum yield[15-18]. To improve the absorption efficiency, two main strategies, including NIR dye sensitized[19-24] and highly sensitizer doped upconversion nanosystems[4, 5, 25-27], are widely used. Normally, the absorption cross-section of organic dye is $10^3 \sim 10^4$ times higher than that of Yb^{3+} sensitizer ions[28, 29] and the emission intensity of dye-sensitized upconversion nano-system can be enhanced by $10 \sim 10^5$ folds[19, 22, 24]. However, the organic-inorganic hybrid upconversion nano-systems suffer from poor stability, for example photobleaching, O_2 and H_2O quenching of organic dyes[30], which limited the usage in microlaser. The highly doped sensitizers (e. g. Yb^{3+}) can also strengthen the NIR energy harvesting ability by increasing the absorbing units. With the protection of an inert shell layer, highly Yb^{3+} (even 100%) doping with $10 \sim 10^3$ times enhancement of emission intensity was achieved[4, 25, 31].

In this chapter, we employed a novel core-shell structured upconversion nanoparticle, in which high concentration of Yb^{3+} was doped to improve the absorbing ability. Apart from the powerful energy distribution modulation of CR process, the doping concentration of Yb^{3+} ions inside $NaYF_4$@$NaYF_4$:x%Yb^{3+},2%Tm^{3+}@$NaYF_4$ nanoparticles also play an important role. The pumping threshold shows a downward trend (from ~2 kW/cm^2 to ~180 W/cm^2) as the increase of Yb^{3+} doping concentration, which indicate the improved harvesting ability of highly doped sensitizers. And the temperature dependent performance of upconverting lasing emission was also explored. Apart from NIR long time tracking, the obvious blue shift shows great potential for temperature sensing, especially in biological applications.

Furthermore, upcovnersion nanoparticles with multiple emission peaks, showing green, red and blue, were obtained by constructing an energy migration path between core and shell layer. The visible range upconversion emissions (450, 475, 650, 780, 800 nm) have been well investigated[5, 32, 33]. While the UV band emissions from higher energy level of Tm^{3+} ions ($^1I_6$) are often neglected and found useless in many researches. Here we provided a bridge to transfer these UV level excited energy (Tm^{3+}, $^1I_6$) to Gd^{3+} ($^6P_{7/2}$)

then to the outer layer Tb^{3+} ions ($^5D_4$) for green band emissions. Then, white lasing emissions from energy migration modulated $NaGdF_4:Yb^{3+}$, $Tm^{3+}@NaGdF_4:Tb^{3+}$ nanoparticles coated microcavity were achieved with a low threshold.

5.3 Experimental Section

5.3.1 Synthesis of lanthanide doped $NaYF_4$ core nanoparticles

The $NaYF_4$ based nanoparticles were synthesized using a modified coprecipitation method[34-36] and described in chapter 2. A batch of $NaYF_4$:x%Yb^{3+},2%Tm^{3+} (x increases from 20 to 98) upconversion nanoparticles were synthesized through the above-mentioned method.

Noting that, to ensure the same core for subsequent epitaxial growth, 2 mmol lanthanide doped $NaYF_4$ core nanoparticles were synthesized at one time. The synthesis process remains the same, except the amount of reactants were doubled.

5.3.2 Synthesis of multi core shell structured nanoparticles

The core shell structured $NaYF_4$@ $NaYF_4$:x%Yb^{3+},2%Tm^{3+}@$NaYF_4$ (x=20, 40, 60, 80,98) and $NaGdF_4$:40%Yb^{3+},2%Tm^{3+}@$NaGdF_4$:15%Tb^{3+} nanoparticles were obtained through seed modulated layer by layer epitaxial growth strategy[37-39]. The detailed description can be found in chapter 2. Noting that, for the precise control of nanoparticle sizes, calculation of injected precursor is needed.

Table 5.1 Summary of sandwich like core shell structured upconversion nanoparticles.

sample	Inert core	Active shell	Outermost inert shell
S1	$NaYF_4$	20%Yb^{3+},2%Tm^{3+}	$NaYF_4$
S2		40%Yb^{3+},2%Tm^{3+}	
S3		60%Yb^{3+},2%Tm^{3+}	
S4		80%Yb^{3+},2%Tm^{3+}	
S5		98%Yb^{3+},2%Tm^{3+}	

Besides, the microlaser mentioned in this chapter were constructed by using aqueous phase electrostatic force driven coating method. And before these nanoparticles being loaded onto the surface of microcavity, HCl assisted ligands free strategy was used for surface modification.

5.4 Results and discussion

5.4.1 Construction of high doping upconversion nanoparticles

In order to explore the performance of highly sensitizer doped upconversion nanoparticles for lasing emission, a batch of $NaYF_4$:x%Yb^{3+},2%Tm^{3+} (x increases from 20 to 98) nanoparticles were synthesized and investigated. However, as can be seen, with the increase of Yb^{3+} concentration, the size of nanoparticles become much larger and the morphology become nonuniform (Figure 5.1). Due to the smaller ionic radius of Yb^{3+} (0.858 Å) than Y^{3+} (0.893 Å), the growth rate of Yb^{3+} is much faster than Y^{3+}, and thus induce the larger size and nonuniformity[40, 41]. The average size increases from about 20 nm to 150 nm, and the morphology also changes from nanosphere to hexagonal nanoplatelet. As we mentioned that the size of gain media plays an important role in scattering and decoupling effect, the size and morphology of gain media need to be the same when we explore the function of highly sensitizer doping. Thus, novel core-shell structure with similar size and morphology is need to be constructed for nano gain media with various sensitizer doping concentrations.

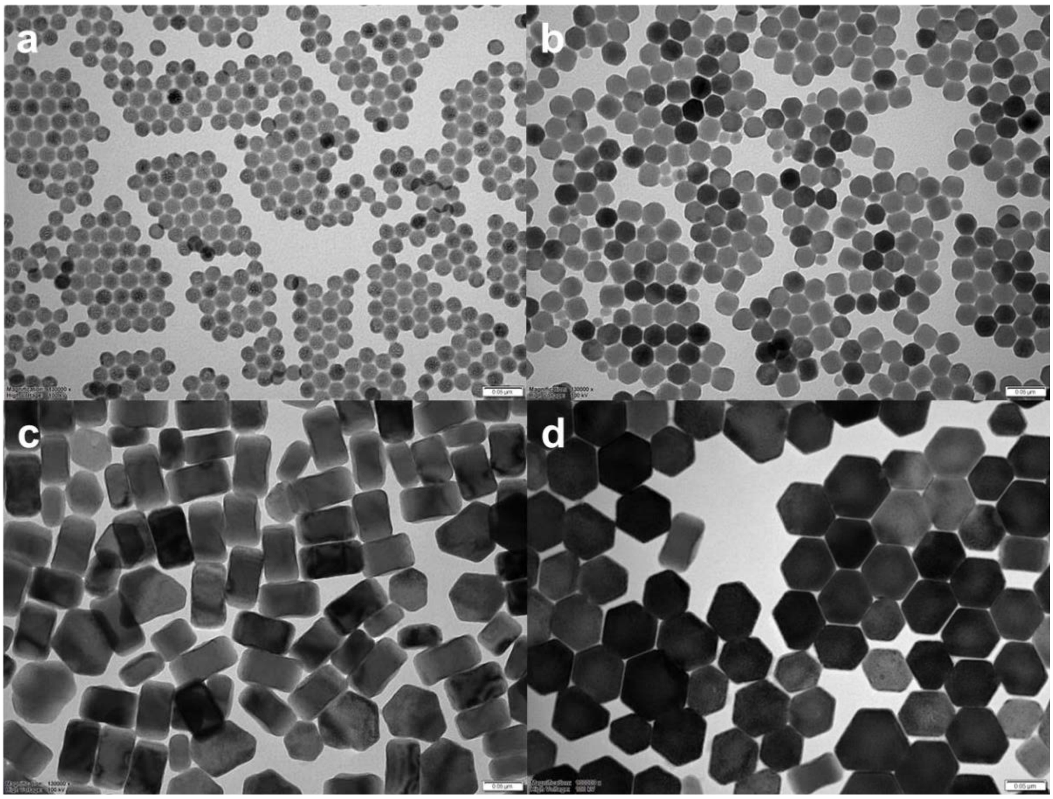

Figure 5.1 a-d, TEM images of $NaYF_4$:x%Yb^{3+},2%Tm^{3+} with x varying from 20, 40, 60 to 80.

Layer by layer coating method

To keep the size and morphology of upconversion nanoparticle at a consistent level, a templet modulated layer by layer coating method was employed[5]. As shown in Figure 5.2, the novel nanoparticles are constituted by three parts: the same templet core, concentration tunable interlayer, and the outermost inert shell layer. An inert core without any activator or sensitizer was used as templet for size-controllable epitaxial growth of active layer. To avoid interfering by the serious surface quenching of highly doped Yb^{3+}, an outermost inert shell layer was employed to isolate the surface quenchers[1, 42-45]. Based on this design, the doping concentration of Yb^{3+} ions in the intermediate active layer were tuned from 20% to 98% with an invariable thickness.

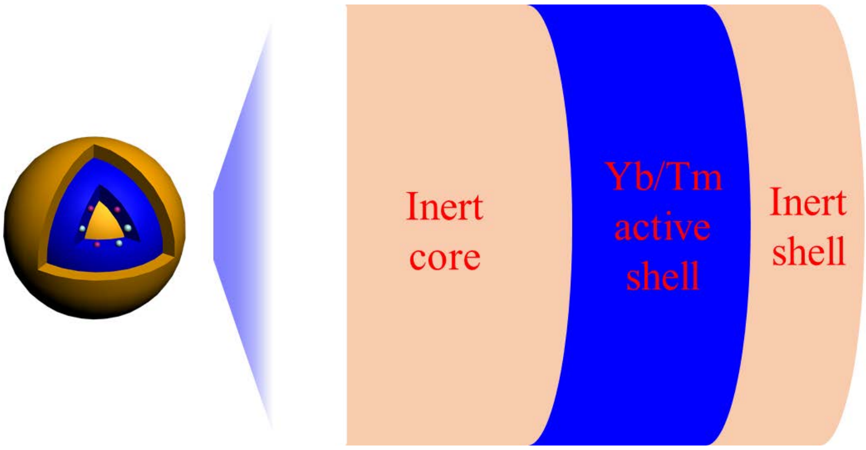

Figure 5.2 Diagram of the templet modulated sandwich core-shell nanostructure with a tunable concentration but a same size of interlayer.

As shown in Figure 5.3, an inert $NaYF_4$ core with a uniform morphology and an average diameter of ~25 nm was synthesized and chosen as templet seed. Then the active layer doped with Yb^{3+} and Tm^{3+} was coated on the templet core through layer-by-layer epitaxial grown method. The size increases to ~43 nm, indicating a successful coating process with a thickness of 9 nm. What's more, the contrast difference originating from Y^{3+} and Yb^{3+} in the core and shell layer also prove the successful construction of active shell layer (Figure 5.3 b). Then, an inert shell layer with a thickness of 2 nm was coated on the surface and the size increases to ~47 nm.

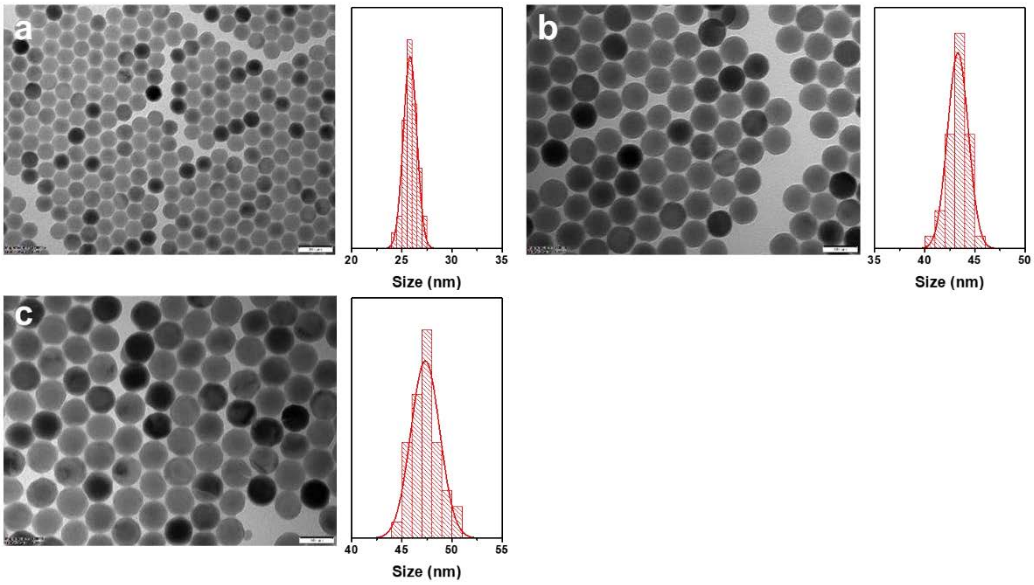

Figure 5.3 TEM image and size distributions of **a**, templet $NaYF_4$ core, **b**, epitaxial

grown $NaYF_4$@ $NaYbF_4$:2%Tm^{3+}, **c**, $NaYF_4$@ $NaYbF_4$:2%Tm^{3+}@$NaYF_4$

The upconversion emission spectra of nanoparticles with various Yb^{3+} doping concentration in the intermediate active layer were measured by using the solution sample measurement set-up. The emission intensity enhanced dramatically with the increase of Yb^{3+} doping concentration (Figure 5.4). The integrated emission intensity enhanced ~18 times as the doping concentration of Yb^{3+} ions increased from 20% to 98%. The enhanced absorption of pumping sources induced by increased sensitizers play an important role for the improved emission intensity. What's more, the highly doping of Yb^{3+} ions shortened the distance between Yb^{3+} ions and Tm^{3+} ions, which further lead to the increased energy transfer efficiency from Yb^{3+} ions to neighboring Tm^{3+} ions[4, 32, 46-48]. While the surface quenching was greatly suppressed by the outermost inert shell layer, which promoted the enhanced emission intensity[1, 26, 43, 49].

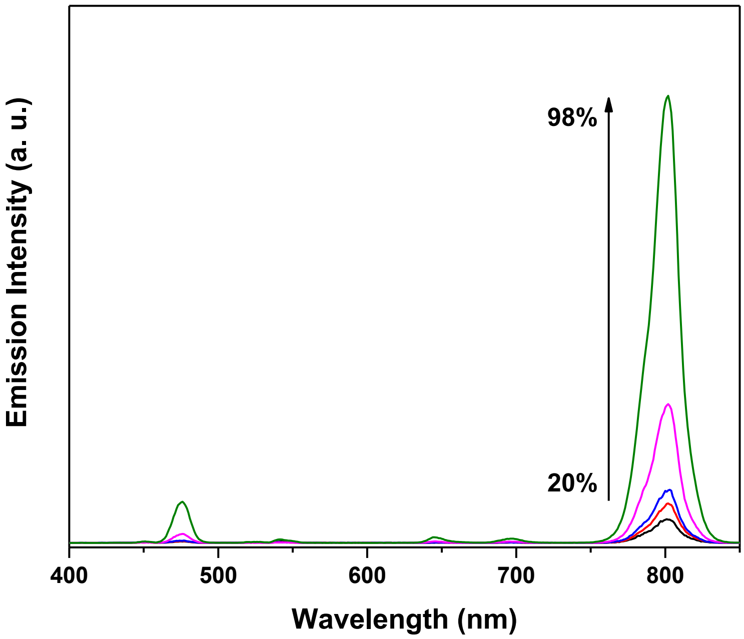

Figure 5.4 Upconversion emission spectra of $NaYF_4$@$NaYF_4$:x%Yb^{3+},2%Tm^{3+} @$NaYF_4$ (x =20, 40, 60, 80, 98) under the excitation of 976 nm laser. Concentration: 10 mg/ml in cyclohexane solution.

5.4.2 High doping upconversion nanoparticles for microlasers

As shown in Figure 5.5, $NaYF_4$@$NaYbF_4$:2%Tm^{3+}@$NaYF_4$ nanoparticles with an average size of ~47 nm is coated on the surface of microcavity to form a uniform single layer. No obvious aggregation was observed on the surface, which benefits the coupling of emission with microcavity. With the suppression of scattering loss, lasing emission arises at a relatively low power. As shown in Figure 5.6, sharp peak with a linewidth of ~0.8 nm arises with the increase of pumping power. From the light-to-light curve, we can get the threshold of ~180 W/cm^2, which almost the same with the one of 24 nm NaYF$_4$:20%Yb^{3+}2%Tm^{3+} coated microlaser[50].

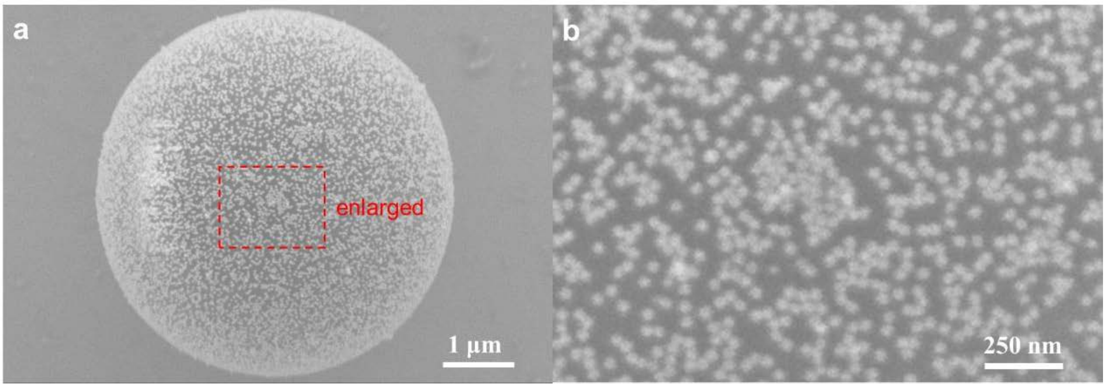

Figure 5.5 a, The SEM image and b, select enlarged SEM image of NaYF$_4$@NaYbF$_4$:2%Tm^{3+}@NaYF$_4$ coated microcavity.

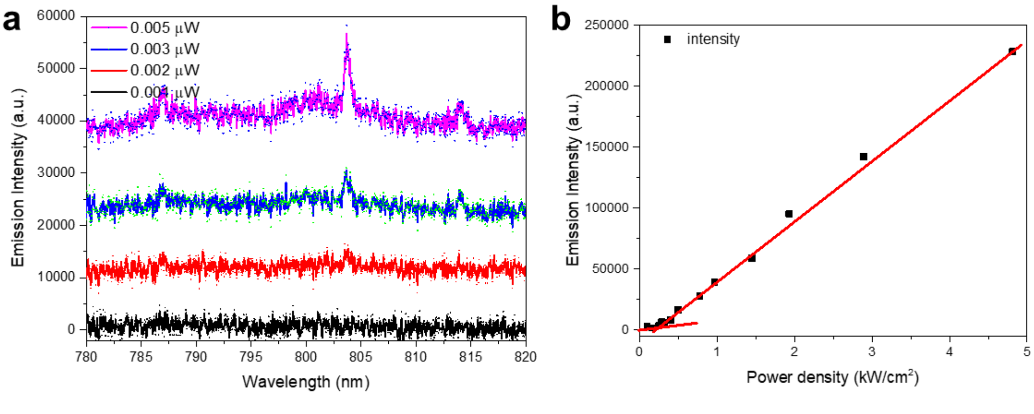

Figure 5.6 a, the power dependent spectra (below, near, above the threshold) of NaYF$_4$@NaYbF$_4$:2%Tm^{3+}@NaYF$_4$ coated microcavity. **b**, the light-to-light curve of related microlaser.

Then, the threshold of gain media with various Yb^{3+} doping concentration were compared and shown in Figure 5.7. The threshold shows a downward tendency with the increase of Yb^{3+} doping concentration, due to the enhanced NIR harvesting ability of gain media. More Yb^{3+} ions inside the nanoparticle improved the absorption and utilization of pumping light[51-53], and thus lower the power density needed to achieve the establishment of population inversion and onset of lasing emission. However, due to the size induced scattering and decoupling loss, the linewidth is a bit broader than that we reported in chapter 3. Although the pumping light harvesting ability is improved, the slightly reduced Q factor make the threshold still at the level of hundreds watt per square centimeter.

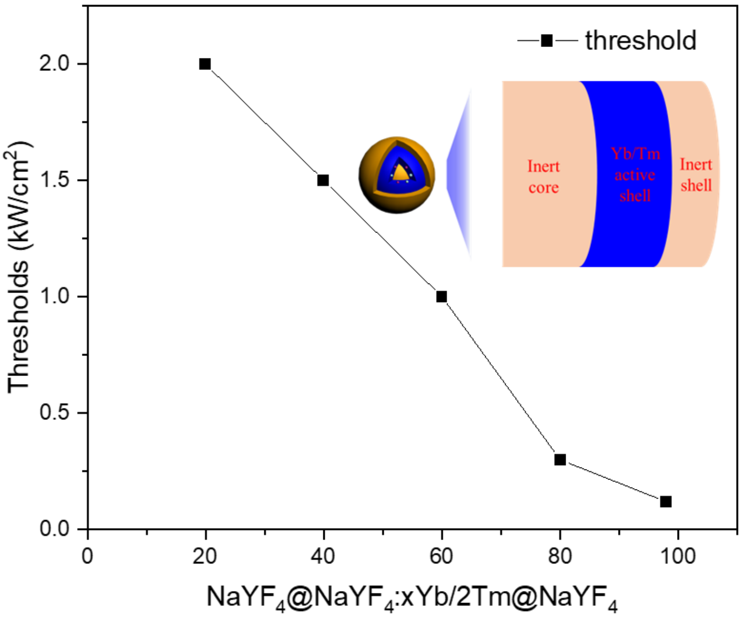

Figure 5.7 The tendency of threshold plotted by the function of Yb^{3+} doping concentration at the intermediate active layer.

5.4.3 Temperature sensing by upconverting microlasers

Normally, the resonant modes of a spherical WGM cavity followed a simplified law[54-59] of $2\pi n_{eff}R = m\lambda$, where n_{eff} refers the effective refractive index of WGM cavity *v.s.* the environment, R is the radius of this spherical microcavity, λ is the resonant mode and m is an integer. Thus, both the refractive index and size of microcavity are vital for the wavelength position of resonant modes. As we mentioned in chapter 3, the slightly difference of radius (R) would lead to a big different of resonant modes. The effective refractive index also plays an important role. As can be seen from Figure 5.8, the resonant mode at 817 nm would go through an obvious red shift (~14.6 nm) when the refractive index increases from 1.58 to 1.61. Therefore, the slight changes of microcavity, including size and refractive index, would be amplified by resonant mode shift.

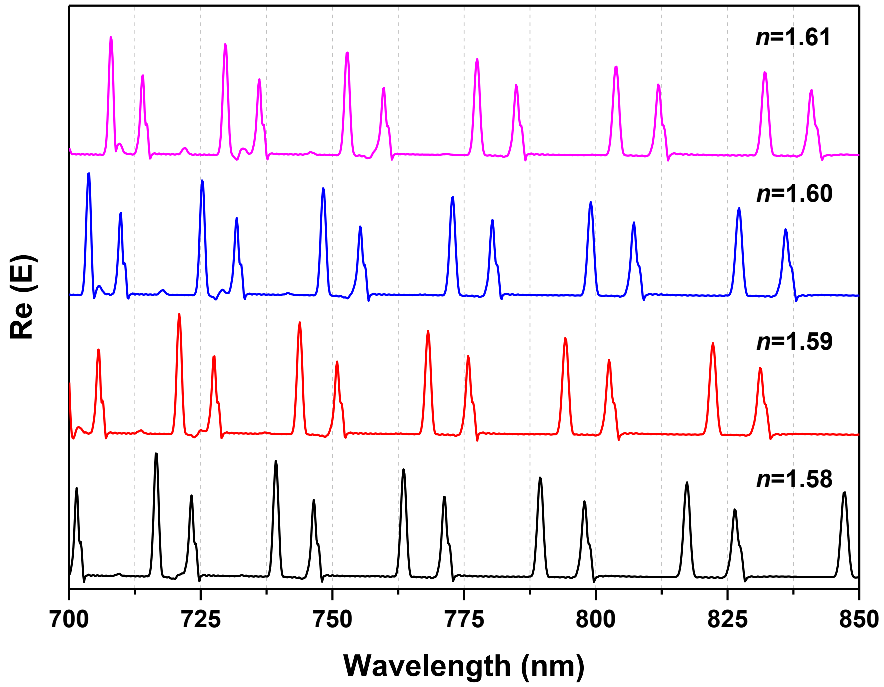

Figure 5.8 Numerical simulations of resonance spectra of microcavity with a fixed size (5 μm) but different refractive index (from 1.58 to 1.61).

As we have demonstrated the stability of lasing emission peaks under long time CW pumping in chapter 3. Herein, we explored the temperature dependent performance of these microlasers. Emission spectra at different temperatures were recorded and shown in Figure 5.9. Apparent blue shift was observed as the increase of temperature, which indicated the slightly reduce of effective refractive index[60, 61]. Although the increase of temperature would lead to thermal expansion of PS microspheres, the slight decrease of refractive index plays a more important role. Normally, the refractive index (n_{eff}) is proportional to the density (ρ)[62-66], while the density (ρ) is inversely proportional to the cubic power of the radius (R). Thus, the bule shift caused by refractive index reducing is larger than the red shift induced by radius expansion. As a result, the peak shift shows a net effect of these mentioned reasons.

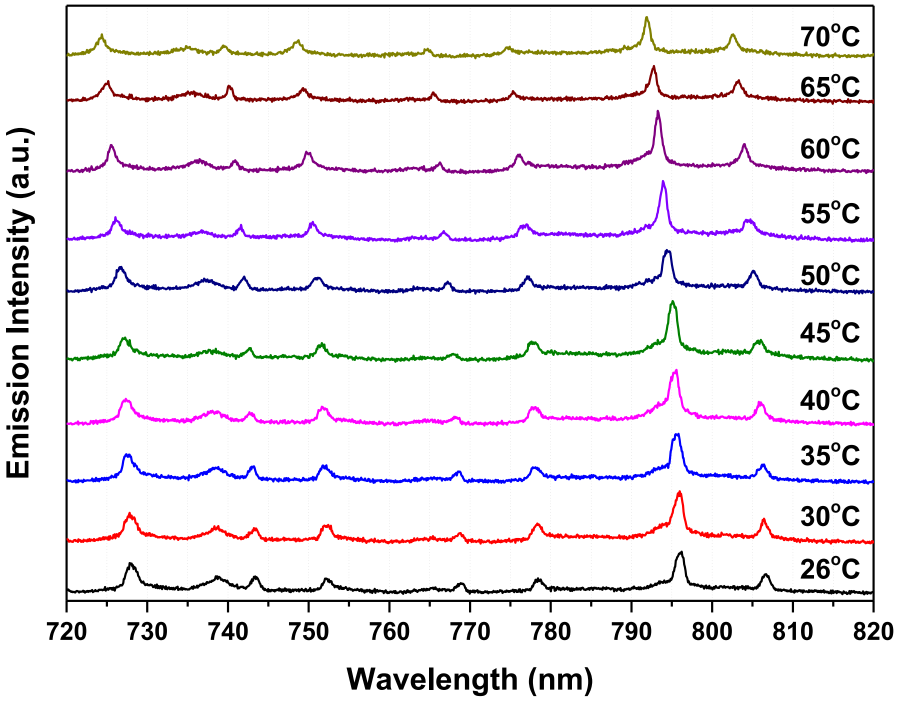

Figure 5.9 Temperature dependent spectra of an upconverting microlaser.

Therefore, the peak shift of lasing emission can be used to monitor temperature variation. Benefiting from the advantages of NIR optical window pumping, thermal effect of the laser is negligible. And anti-Stokes NIR lasing emission not only improves the signal-to-noise ratio, but also increases the penetration depth, especially in biological applications. As shown in Figure 5.10 a, all the lasing emission peaks were blue shifted with the increase of temperature (The set-up for in-situ temperature sensing is shown in chapter 2). The emission peak at ~796 nm was selected and monitored. As shown in Figure 5.10 b, an obvious shift of ~5 nm is observed when the temperature increased from 26 °C to 70 °C. And the tendency is also linear, which shows further application in temperature sensing.

What's more, the shape or the size of microlaser will go through a slightly variation under a certain force, thus make the lasing emission modes changing. So, the microlasers are also potential in sensing many other localized environments vibrations.

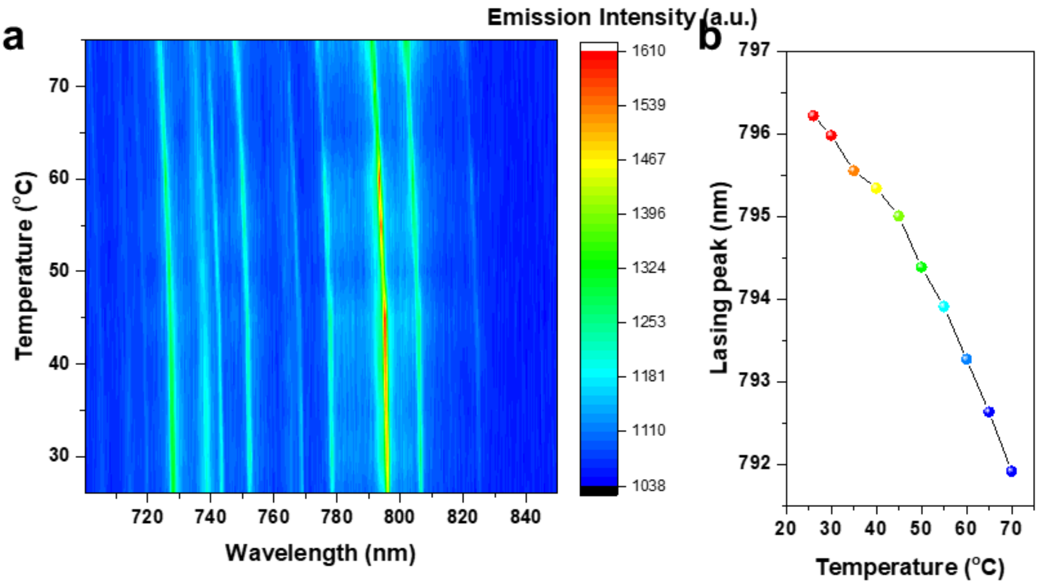

Figure 5.10 Temperature dependent **a**, spectra and **b**, emission peak shift of an upconverting microlaser.

5.4.4 Construction of energy migration upconversion nano-system

White-light laser, consisted of three primary colors with less divergence angle and high-power density, show great potential in the application of true color 3D holograms, lasing sources of microscopy, spotlights and so on[67-69]. As we mentioned above, there are almost three major emission peaks (450, 475, 650 nm) of Tm^{3+} at the visible range[70-72]. Green band emissions are needed to construct the three basic colors. The UV band emissions, such as ~291 nm ($^1I_6 \rightarrow {}^3H_6$), ~347 nm ($^1I_6 \rightarrow {}^3F_4$), ~362 nm ($^1D_2 \rightarrow {}^3H_6$) are often neglected and useless in many researches[73, 74]. Due to the large nonlinear slope and stable intermediate energy levels, the UV bands emission increase greatly at high pumping power density. Thus, we would like to construct a bridge like energy migration process to transfer the UV band excited energy to green ones. More importantly, compared with green emission ions of Er^{3+} and Ho^{3+}, the energy structure of Tb^{3+} is a typical four-level system, which benefits population inversion and lasing emissions. Based on the design shown in Figure 5.11, the energy could transfer through $^1I_6$ (Tm^{3+}) $\rightarrow {}^6P_{7/2}$ (Gd^{3+}) $\rightarrow {}^5D_4$ (Tb^{3+}), and then produce strong green emissions.

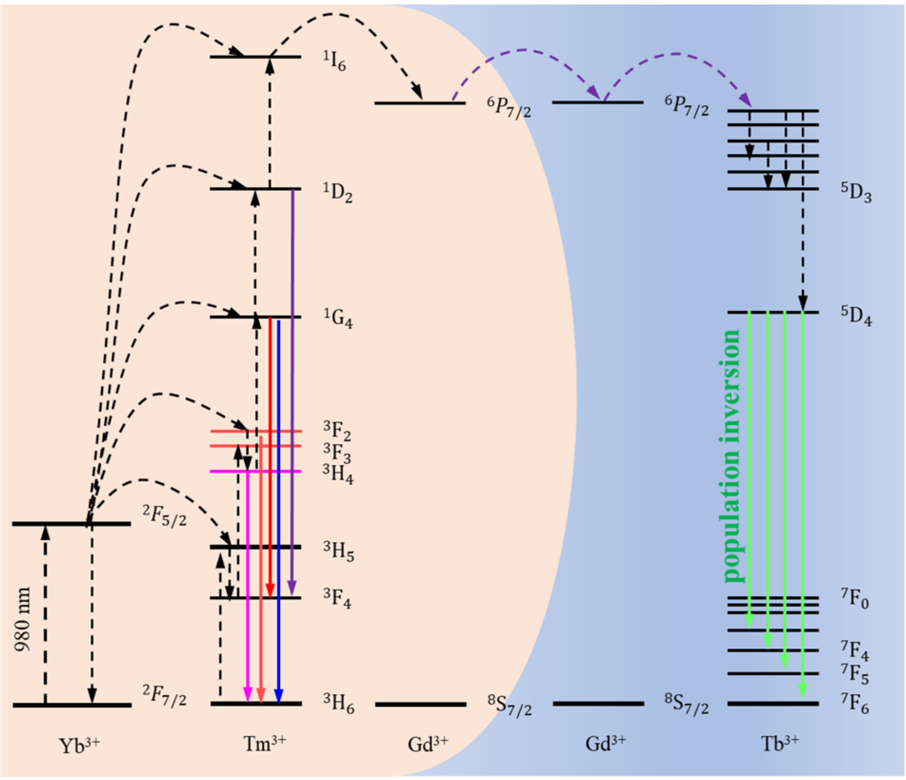

Figure 5.11 The schematic diagram of energy migration modulated core-shell upconversion nanoparticle.

As shown in Figure 5.12, uniform $NaGdF_4$:40%Yb^{3+},2%Tm^{3+} core with an average diameter of ~31 nm was synthesized through a coprecipitation method[34, 50]. Then, an active shell with a thickness of ~3 nm was coated through layer by layer grown strategy[75, 76]. The final $NaGdF_4$:40%Yb^{3+},2%Tm^{3+}@ $NaGdF_4$:15%Tb^{3+} nanoparticle with an average diameter of ~37 nm was obtained. The upconversion emission from UV to NIR is shown in Figure 5.13. Under the excitation of 980 nm laser, UV band emissions at ~291 nm (Tm^{3+}: $^1I_6 \rightarrow {}^3H_6$), ~347 nm ($Tm^{3+}$: $^1I_6 \rightarrow {}^3F_4$), ~362 nm ($Tm^{3+}$: $^1D_2 \rightarrow {}^3H_6$) and ~310nm ($Gd^{3+}$: $^6P_{7/2} \rightarrow {}^8S_{7/2}$) were observed. When coated with $NaGdF_4$:15%Tb^{3+} layer, the relative emission intensity of UV band reduces while the green emission peaks at ~544 nm, 580 nm from Tb^{3+} arise.

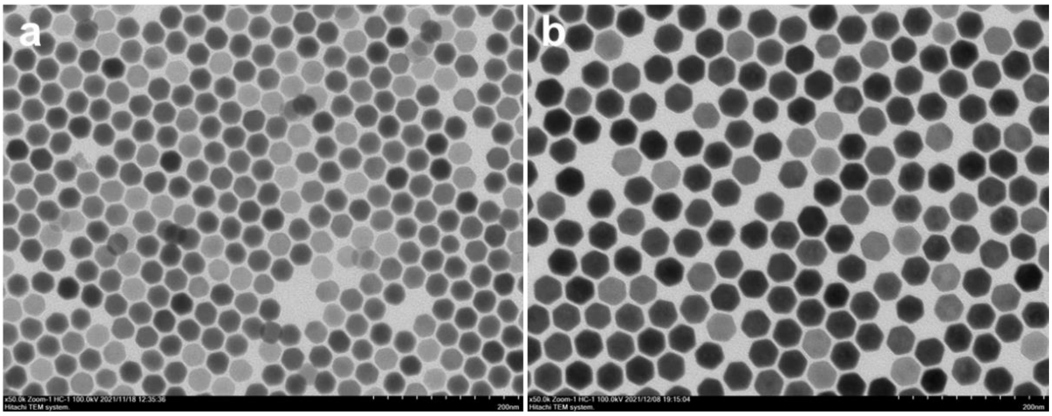

Figure 5.12 TEM image of **a**, $NaGdF_4$:40%Yb^{3+},2%Tm^{3+} and **b**, $NaGdF_4$:40%Yb^{3+},2%Tm^{3+}@ $NaGdF_4$:15%Tb^{3+}

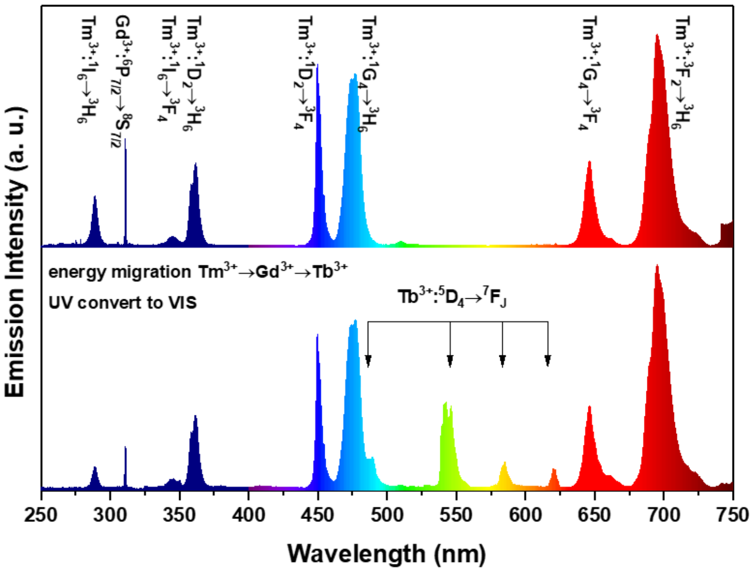

Figure 5.13 Upconversion emission spectrum of $NaGdF_4$:40%Yb^{3+},2%Tm^{3+} and $NaGdF_4$:40%Yb^{3+},2%Tm^{3+}@ $NaGdF_4$:15%Tb^{3+} under the excitation of 980 nm laser.

To further confirm the energy migration process, power dependent spectra were measured. As shown in Figure 5.14, the slopes of upconversion emission from Tb^{3+} ions are all above 4.2. While the slope of Tm^{3+}@450 nm band is about 3.6. These indicate a five-photon process of Tb^{3+} ions emission, which further verified the $^6P_{7/2}$ (Gd^{3+}) bridged energy transfer from $^1I_6$ (Tm^{3+}) to $^5D_4$ (Tb^{3+}) rather than the direct energy transfer from Tm^{3+} to Tb^{3+}. The energy migration path can be described as Figure 5.14 b. The decay curves of Tm^{3+}@450 nm and Tb^{3+}@544 nm are compared in Figure 5.14 c. The lifetime of $^5D_4$ (Tb^{3+}) is about 3600 μs that is 54 times longer than $^1D_2$ (Tm^{3+}).

The ultra-long radiative lifetime benefits the energy accumulation for achieving population inversion.

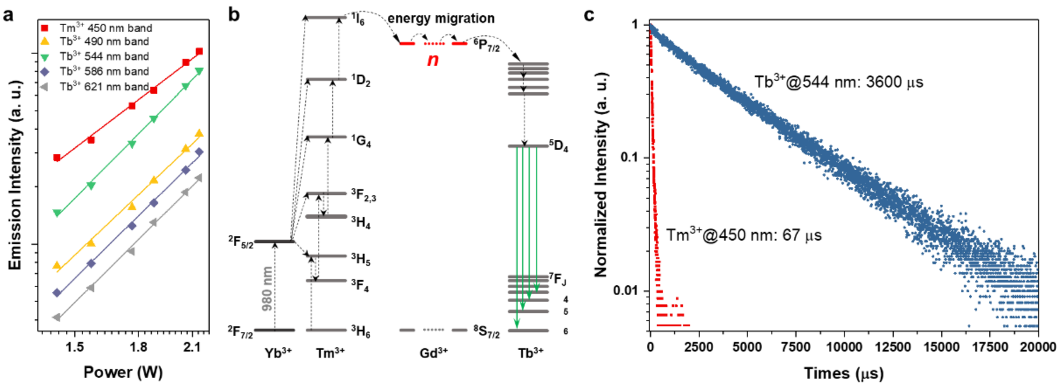

Figure 5.14 a, power dependent upconversion emission intensity of each peak. **b**, the possible energy transfer paths inside this upconversion core-shell nanoparticle. c, decay curves of Tm^{3+}@450 nm band and Tb^{3+}@544 nm band.

5.4.4 Upconverting microlaser with white lasing emission

The energy migration modulated nanoparticles are coated onto the surface of microcavity. As shown in Figure 5.15 a, the coating process made the particles uniformly distributed on the surface of the bead. The SEM image of single selected microcavity demonstrated a single layer of upconversion nanoparticles. Multiple upconverting lasing emissions, including blue, green, and red bands, were achieved under the excitation of a 980 nm laser (Figure 5.16). The linewidth of these lasing peaks varies from 0.5 nm to 0.8 nm, as the looping path of each mode are slightly different with the various Q factors. At higher pumping power density, in particular, at the power condition that is high enough to produce the 5 and 6-photon blue band emissions, the relative intensities of green band lasing emissions from $^5D_4$ (Tb^{3+}) reduce. This is because the energy migration process reaches a saturated state.

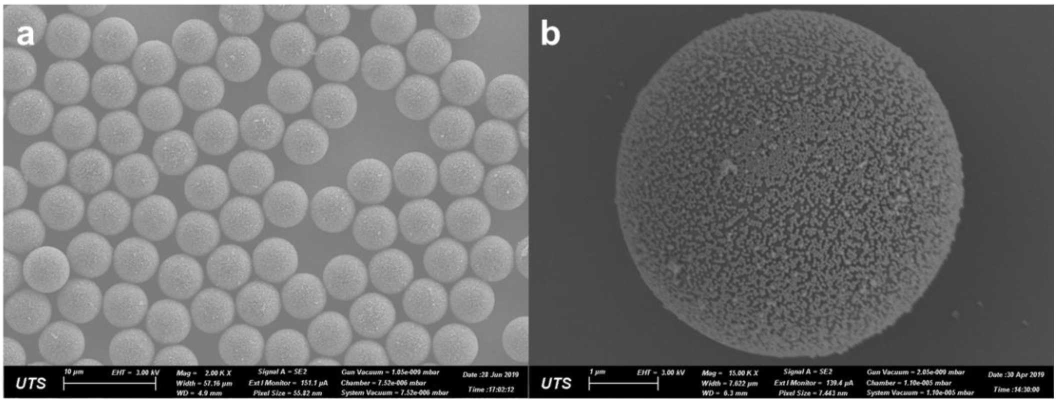

Figure 5.15 SEM images of upconversion nanoparticles coated microcavity: **a**, wide field, **b**, enlarged single microcavity.

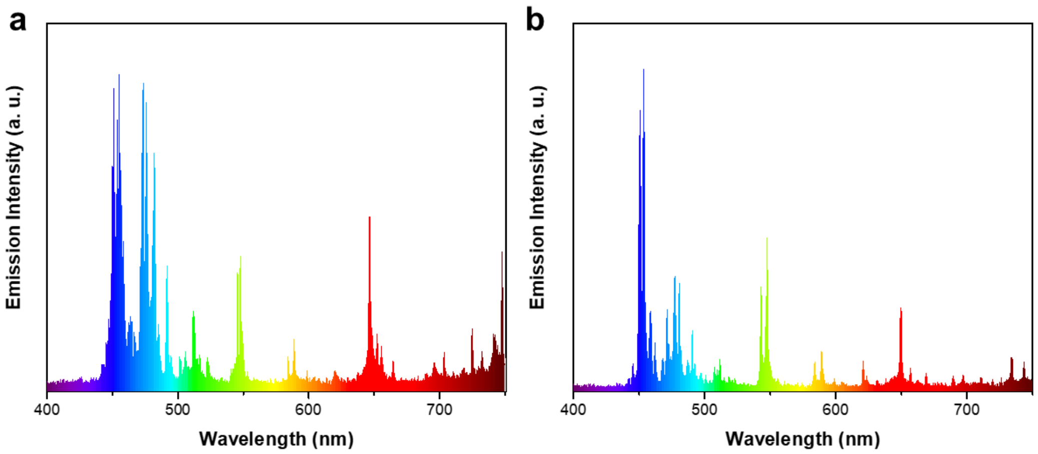

Figure 5.16 Lasing emission from $NaGdF_4$:40%Yb^{3+},2%Tm^{3+}@$NaGdF_4$:15%Tb^{3+} coated microcavity under the excitation power of **a**, 10 kW/cm^2 and **b**, 100 kW/cm^2.

More importantly, the lifetime shorten was observed for lasing emissions from $^5D_4$ (Tb^{3+}). When the pure UCNPs were measured without a microcavity, the decay curve of $^5D_4$ (Tb^{3+}) shows the single exponential decay feature with a long lifetime of ~3600 μs. Interestingly, when the UCNPs were coupled with a microcavity, a double exponential decay curve was observed, including a rapid decay process of ~47 μs and a slow decay process of ~1700 μs. The slow decay process originates from the possible amplification of spontaneous emission or the Purcell modulated spontaneous emission background, while the rapid decay process indicates the occurrence of stimulated radiation process. Noting that, the response time of the pumping laser used here is about 5 μs, and the bandpass filter used here is pretty broad (~40 nm) which covers several modes. Thus, the experimental measured decay lifetime is much longer than the actual value.

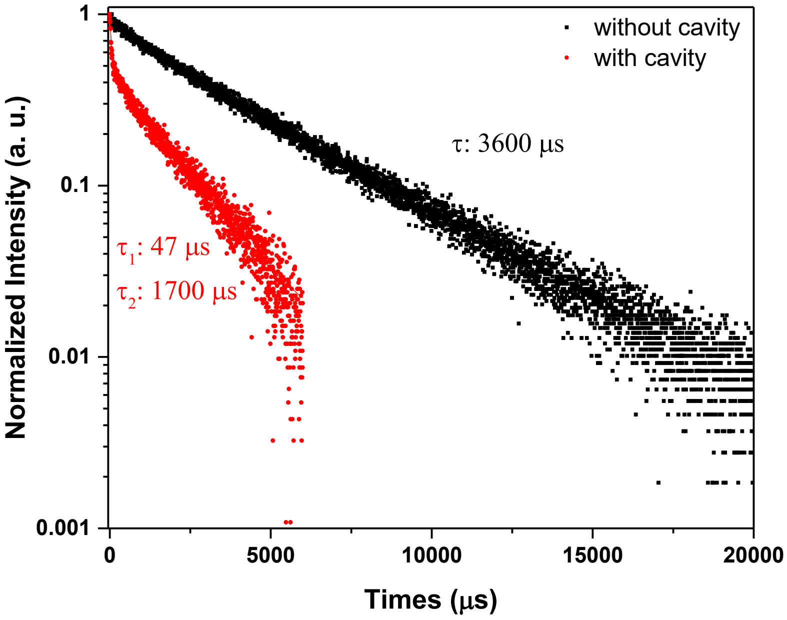

Figure 5.17 The decay curves of $NaGdF_4$:40%Yb^{3+},2%Tm^{3+}@$NaGdF_4$:15%Tb^{3+} coupled with and without microcavity (544 nm band).

5.5 Conclusion

In this chapter, Yb^{3+} highly doped sandwich core-shell structured upconversion nanoparticles with enhanced NIR harvesting ability were synthesized through a templet modulated layer-by-layer epitaxial growth strategy. With the increase of sensitizers doping concentration in the intermediate active layer, the pumping threshold of lasing emission (@800 nm band) was lowered from ~2 kW/cm^2 to ~180 W/cm^2. The improved absorption of pumping laser plays an important role in lowering the threshold, which indicated a potential direction for further reduce threshold by using the nanosystem with a powerful sensitizer, for example, inorganic hybrid sensitized upconversion nano-system, optical stable organic dye sensitized upconversion nano-system. Furthermore, the temperature dependent lasing emission peak shift was demonstrated, which showed a great potential to apply such microlaser for temperature sensing.

An energy migration modulated upconversion nano-system was employed to obtain white lasing emission. Apart from powerful CR modulated Tm^{3+} ions for blue and red band emissions, Tb^{3+} ions were introduced for green emission, which arise from the transition of $^5D_4$ to ^7F_J. It's worth noting that the ^7F_J (Tb^{3+}), especially $^7F_3$, $^7F_4$, and $^7F_5$, are not ground state level, which benefits the establishment of population inversion between $^5D_4$ and $^7F_{3,4,5}$. Finally, full visible spectrum lasing was achieved through using $NaGdF_4$:40%Yb^{3+},2%Tm^{3+}@$NaGdF_4$:15%Tb^{3+} nanoparticles as gain media. And the relative intensity of each band can be tuned by changing pumping power.

5.6 References

1. Johnson, N. J. J.; He, S.; Diao, S.; Chan, E. M.; Dai, H. J.; Almutairi, A. Direct Evidence for Coupled Surface and Concentration Quenching Dynamics in Lanthanide-Doped Nanocrystals. *J Am Chem Soc* **2017,** 139 (8), 3275-3282 DOI: 10.1021/jacs.7b00223.
2. Wei, W.; Chen, G. Y.; Baev, A.; He, G. S.; Shao, W.; Damasco, J.; Prasad, P. N. Alleviating Luminescence Concentration Quenching in Upconversion Nanoparticles through Organic Dye Sensitization. *J Am Chem Soc* **2016,** 138 (46), 15130-15133 DOI: 10.1021/jacs.6b09474.
3. Chen, G.; Ohulchanskyy, T. Y.; Kumar, R.; Ågren, H.; Prasad, P. N. Ultrasmall monodisperse $NaYF_4$: Yb^{3+}/Tm^{3+} nanocrystals with enhanced near-infrared to near-infrared upconversion photoluminescence. *Acs Nano* **2010,** 4 (6), 3163-3168.
4. Chen, G. Y.; Shen, J.; Ohulchanskyy, T. Y.; Patel, N. J.; Kutikov, A.; Li, Z. P.; Song, J.; Pandey, R. K.; Agren, H.; Prasad, P. N.; Han, G. (alpha-NaYbF4:Tm3+)/CaF2 Core/Shell Nanoparticles with Efficient Near-Infrared to Near-Infrared Upconversion for High-Contrast Deep Tissue Bioimaging. *Acs Nano* **2012,** 6 (9), 8280-8287 DOI: 10.1021/nn302972r.
5. Ma, C.; Xu, X.; Wang, F.; Zhou, Z.; Liu, D.; Zhao, J.; Guan, M.; Lang, C. I.; Jin, D. Optimal Sensitizer Concentration in Single Upconversion Nanocrystals. *Nano Lett* **2017,** 17 (5), 2858-2864 DOI: 10.1021/acs.nanolett.6b05331.
6. Shang, Y.; Chen, T.; Ma, T.; Hao, S.; Lv, W.; Jia, D.; Yang, C. Advanced lanthanide doped upconversion nanomaterials for lasing emission. *Journal of Rare Earths* **2022,** 40 (5), 687-695 DOI: https://doi.org/10.1016/j.jre.2021.09.002.
7. Chen, X.; Sun, T.; Wang, F. Lanthanide-Based Luminescent Materials for Waveguide and Lasing. *Chemistry – An Asian Journal* **2020,** 15 (1), 21-33 DOI: 10.1002/asia.201901447.
8. Jeong, K.-Y.; Hwang, M.-S.; Kim, J.; Park, J.-S.; Lee, J. M.; Park, H.-G. Recent Progress in Nanolaser Technology. *Adv Mater* **2020,** 32 (51), 2001996 DOI: https://doi.org/10.1002/adma.202001996.
9. Dong, H.; Sun, L. D.; Yan, C. H. Upconversion emission studies of single particles. *Nano Today* **2020,** 35, DOI: Artn 100956

10.1016/J.Nantod.2020.100956.

10. Azzam, S. I.; Kildishev, A. V.; Ma, R. M.; Ning, C. Z.; Oulton, R.; Shalaev, V. M.; Stockman, M. I.; Xu, J. L.; Zhang, X. Ten years of spasers and plasmonic nanolasers. *Light-Sci Appl* **2020,** 9 (1), DOI: ARTN 90
10.1038/s41377-020-0319-7.

11. Chen, Z.; Dong, G. P.; Barillaro, G.; Qiu, J. R.; Yang, Z. M. Emerging and perspectives in microlasers based on rare-earth ions activated micro-/nanomaterials. *Prog Mater Sci* **2021,** 121, DOI: ARTN 100814
10.1016/j.pmatsci.2021.100814.

12. Zhou, J.; Chizhik, A. I.; Chu, S.; Jin, D. Single-particle spectroscopy for functional nanomaterials. *Nature* **2020,** 579 (7797), 41-50 DOI: 10.1038/s41586-020-2048-8.

13. Sun, T. Y.; Chen, B.; Guo, Y.; Zhu, Q.; Zhao, J. X.; Li, Y. H.; Chen, X.; Wu, Y. K.; Gao, Y. B.; Jin, L. M.; Chu, S. T.; Wang, F. Ultralarge anti-Stokes lasing through tandem upconversion. *Nature Communications* **2022,** 13 (1), DOI: Artn 1032
10.1038/S41467-022-28701-1.

14. Jin, L. M.; Chen, X.; Wu, Y. K.; Ai, X. Z.; Yang, X. L.; Xiao, S. M.; Song, Q. H. Dual-wavelength switchable single-mode lasing from a lanthanide-doped resonator. *Nature Communications* **2022,** 13 (1), DOI: Artn 1727
10.1038/S41467-022-29435-W.

15. Auzel, F. Upconversion and anti-stokes processes with f and d ions in solids. *Chem Rev* **2004,** 104 (1), 139-173 DOI: 10.1021/cr020357g.

16. Chen, G.; Qiu, H.; Prasad, P. N.; Chen, X. Upconversion nanoparticles: design, nanochemistry, and applications in theranostics. *Chem Rev* **2014,** 114 (10), 5161-5214.

17. Sun, L.-D.; Dong, H.; Zhang, P.-Z.; Yan, C.-H. Upconversion of rare earth nanomaterials. *Annual review of physical chemistry* **2015,** 66, 619-642.

18. Zheng, K. Z.; Loh, K. Y.; Wang, Y.; Chen, Q. S.; Fan, J. Y.; Jung, T.; Nam, S. H.; Suh, Y. D.; Liu, X. G. Recent advances in upconversion nanocrystals: Expanding the kaleidoscopic toolbox for emerging applications. *Nano Today* **2019,** 29, DOI: Artn 100797
10.1016/J.Nantod.2019.100797.

19. Zou, W. Q.; Visser, C.; Maduro, J. A.; Pshenichnikov, M. S.; Hummelen, J. C. Broadband dye-sensitized upconversion of near-infrared light. *Nat Photonics* **2012,** 6 (8), 560-564 DOI: 10.1038/nphoton.2012.158.

20. Wu, X.; Lee, H.; Bilsel, O.; Zhang, Y.; Li, Z.; Chen, T.; Liu, Y.; Duan, C.; Shen, J.; Punjabi, A.; Han, G. Tailoring dye-sensitized upconversion nanoparticle excitation bands towards excitation wavelength selective imaging. *Nanoscale* **2015,** 7 (44), 18424-8 DOI: 10.1039/c5nr05437k.

21. Wang, X. D.; Valiev, R. R.; Ohulchanskyy, T. Y.; Agren, H.; Yang, C. H.; Chen, G. Y. Dye-sensitized lanthanide-doped upconversion nanoparticles. *Chemical Society Reviews* **2017,** 46 (14), 4150-4167 DOI: 10.1039/c7cs00053g.

22. Chen, G. Y.; Damasco, J.; Qiu, H. L.; Shao, W.; Ohulchanskyy, T. Y.; Valiev, R. R.; Wu, X.; Han, G.; Wang, Y.; Yang, C. H.; Agren, H.; Prasad, P. N. Energy-Cascaded Upconversion in an Organic Dye-Sensitized Core/Shell Fluoride Nanocrystal. *Nano Lett* **2015,** 15 (11), 7400-7407 DOI: 10.1021/acs.nanolett.5b02830.

23. Chen, G. Y.; Shao, W.; Valiev, R. R.; Ohulchanskyy, T. Y.; He, G. S.; Agren, H.; Prasad, P. N. Efficient Broadband Upconversion of Near-Infrared Light in Dye-Sensitized Core/Shell Nanocrystals. *Adv Opt Mater* **2016,** 4 (11), 1760-1766 DOI: 10.1002/adom.201600556.

24. Garfield, D. J.; Borys, N. J.; Hamed, S. M.; Torquato, N. A.; Tajon, C. A.; Tian, B.; Shevitski, B.; Barnard, E. S.; Suh, Y. D.; Aloni, S.; Neaton, J. B.; Chan, E. M.; Cohen, B. E.; Schuck, P. J. Enrichment of molecular antenna triplets amplifies upconverting nanoparticle emission. *Nat Photonics* **2018,** 12 (7), 402-407 DOI: 10.1038/s41566-018-0156-x.

25. Shen, J.; Chen, G. Y.; Ohulchanskyy, T. Y.; Kesseli, S. J.; Buchholz, S.; Li, Z. P.; Prasad, P. N.; Han, G. Tunable Near Infrared to Ultraviolet Upconversion Luminescence Enhancement in (alpha-$NaYF_4$:Yb,Tm)/CaF_2 Core/Shell Nanoparticles for In situ Real-time Recorded Biocompatible Photoactivation. *Small* **2013,** 9 (19), 3213-3217 DOI: 10.1002/smll.201300234.

26. Wen, S. H.; Zhou, J. J.; Zheng, K. Z.; Bednarkiewicz, A.; Liu, X. G.; Jin, D. Y. Advances in highly doped upconversion nanoparticles. *Nature Communications* **2018,** 9, DOI: Artn 2415
10.1038/S41467-018-04813-5.

27. Wei, W.; Zhang, Y.; Chen, R.; Goggi, J.; Ren, N.; Huang, L.; Bhakoo, K. K.; Sun, H.; Tan, T. T. Y. Cross relaxation induced pure red upconversion in activator-and sensitizer-rich lanthanide nanoparticles. *Chem Mater* **2014,** 26 (18), 5183-5186.

28. Deloach, L. D.; Payne, S. A.; Chase, L. L.; Smith, L. K.; Kway, W. L.; Krupke, W. F. Evaluation of Absorption and Emission Properties of Yb-3+ Doped Crystals for Laser Applications. *Ieee J Quantum Elect* **1993,** 29 (4), 1179-1191 DOI: Doi 10.1109/3.214504.

29. Schmidt, J.; Penzkofer, A. Absorption cross sections, saturated vapor pressures, sublimation energies, and evaporation energies of some organic laser dye vapors. *The Journal of chemical physics* **1989,** 91 (3), 1403-1409.

30. Wen, S.; Zhou, J.; Schuck, P. J.; Suh, Y. D.; Schmidt, T. W.; Jin, D. Future and challenges for hybrid upconversion nanosystems. *Nat Photonics* **2019,** 13 (12), 828-838.

31. Gu, Y.; Guo, Z.; Yuan, W.; Kong, M.; Liu, Y.; Liu, Y.; Gao, Y.; Feng, W.; Wang, F.; Zhou, J. High-sensitivity imaging of time-domain near-infrared light transducer. *Nat Photonics* **2019,** 13 (8), 525-531.

32. Chen, X.; Jin, L. M.; Sun, T. Y.; Kong, W.; Yu, S. F.; Wang, F. Energy Migration Upconversion in Ce(III)-Doped Heterogeneous Core-Shell-Shell Nanoparticles. *Small*

2017, 13 (43), DOI: Artn 1701479
10.1002/Smll.201701479.

33. Zhao, J.; Jin, D.; Schartner, E. P.; Lu, Y.; Liu, Y.; Zvyagin, A. V.; Zhang, L.; Dawes, J. M.; Xi, P.; Piper, J. A. Single-nanocrystal sensitivity achieved by enhanced upconversion luminescence. *Nat Nanotechnol* **2013,** 8 (10), 729.

34. Shang, Y.; Hao, S.; Lv, W.; Chen, T.; Tian, L.; Lei, Z.; Yang, C. Confining excitation energy of Er 3+-sensitized upconversion nanoparticles through introducing various energy trapping centers. *J Mater Chem C* **2018,** 6 (15), 3869-3875.

35. Ha, S. J.; Kang, J. H.; Choi, D. H.; Nam, S. K.; Reichmanis, E.; Moon, J. H. Upconversion-Assisted Dual-Band Luminescent Solar Concentrator Coupled for High Power Conversion Efficiency Photovoltaic Systems. *Acs Photonics* **2018,** 5 (9), 3621-3627 DOI: 10.1021/acsphotonics.8b00498.

36. Wu, Y. M.; Xu, J. H.; Poh, E. T.; Liang, L. L.; Liu, H. L.; Yang, J. K. W.; Qiu, C. W.; Vallee, R. A. L.; Liu, X. G. Upconversion superburst with sub-2 mu s lifetime. *Nat Nanotechnol* **2019,** 14 (12), 1110-1115 DOI: 10.1038/s41565-019-0560-5.

37. Chen, C. H.; Liu, B. L.; Liu, Y. T.; Liao, J. Y.; Shan, X. C.; Wang, F.; Jin, D. Y. Heterochromatic Nonlinear Optical Responses in Upconversion Nanoparticles for Super-Resolution Nanoscopy. *Adv Mater* **2021,** 33 (23), DOI: Artn 2008847
10.1002/Adma.202008847.

38. Shan, X. C.; Wang, F.; Wang, D. J.; Wen, S. H.; Chen, C. H.; Di, X. J.; Nie, P.; Liao, J. Y.; Liu, Y. T.; Ding, L.; Reece, P. J.; Jin, D. Y. Optical tweezers beyond refractive index mismatch using highly doped upconversion nanoparticles. *Nat Nanotechnol* **2021,** 16 (5), 531-537 DOI: 10.1038/s41565-021-00852-0.

39. Li, D.; Wen, S. H.; Kong, M. Y.; Liu, Y. T.; Hu, W.; Shi, B. Y.; Shi, X. Y.; Jin, D. Y. Highly Doped Upconversion Nanoparticles for In Vivo Applications Under Mild Excitation Power (vol 92, pg 10913, 2020). *Anal Chem* **2021,** 93 (32), 11346-11346 DOI: 10.1021/acs.analchem.1c03065.

40. Wang, F.; Han, Y.; Lim, C. S.; Lu, Y.; Wang, J.; Xu, J.; Chen, H.; Zhang, C.; Hong, M.; Liu, X. Simultaneous phase and size control of upconversion nanocrystals through lanthanide doping. *Nature* **2010,** 463 (7284), 1061-1065.

41. Yin, A.; Zhang, Y.; Sun, L.; Yan, C. Colloidal synthesis and blue based multicolor upconversion emissions of size and composition controlled monodisperse hexagonal NaYF 4: Yb, Tm nanocrystals. *Nanoscale* **2010,** 2 (6), 953-959.

42. Fischer, S.; Bronstein, N. D.; Swabeck, J. K.; Chan, E. M.; Alivisatos, A. P. Precise Tuning of Surface Quenching for Luminescence Enhancement in Core-Shell Lanthanide-Doped Nanocrystals. *Nano Lett* **2016,** 16 (11), 7241-7247 DOI: 10.1021/acs.nanolett.6b03683.

43. Zuo, J.; Li, Q. Q.; Xue, B.; Li, C. X.; Chang, Y. L.; Zhang, Y. L.; Liu, X. M.; Tu, L. P.; Zhang, H.; Kong, X. G. Employing shells to eliminate concentration quenching in photonic upconversion nanostructure. *Nanoscale* **2017,** 9 (23), 7941-7946 DOI:

10.1039/c7nr01403a.

44. Wang, M. Y.; Tian, Y.; Zhao, F. Y.; Li, R. F.; You, W. W.; Fang, Z. L.; Chen, X. Y.; Huang, W.; Ju, Q. Alleviating the emitter concentration effect on upconversion nanoparticles via an inert shell. *J Mater Chem C* **2017,** 5 (6), 1537-1543 DOI: 10.1039/6tc05289d.

45. Gu, Y. Y.; Guo, Z. Y.; Yuan, W.; Kong, M. Y.; Liu, Y. L.; Liu, Y. T.; Gao, Y. L.; Feng, W.; Wang, F.; Zhou, J. J.; Jin, D. Y.; Li, F. Y. High-sensitivity imaging of time-domain near-infrared light transducer. *Nat Photonics* **2019,** 13 (8), 525-+ DOI: 10.1038/s41566-019-0437-z.

46. Chen, B.; Liu, Y.; Xiao, Y.; Chen, X.; Li, Y.; Li, M. Y.; Qiao, X. S.; Fan, X. P.; Wang, F. Amplifying Excitation-Power Sensitivity of Photon Upconversion in a NaYbF4:Ho Nanostructure for Direct Visualization of Electromagnetic Hotspots. *Journal of Physical Chemistry Letters* **2016,** 7 (23), 4916-4921 DOI: 10.1021/acs.jpclett.6b02210.

47. Zhong, Y.; Ma, Z.; Zhu, S.; Yue, J.; Zhang, M.; Antaris, A. L.; Yuan, J.; Cui, R.; Wan, H.; Zhou, Y.; Wang, W.; Huang, N. F.; Luo, J.; Hu, Z.; Dai, H. Boosting the down-shifting luminescence of rare-earth nanocrystals for biological imaging beyond 1500 nm. *Nat Commun* **2017,** 8 (1), 737 DOI: 10.1038/s41467-017-00917-6.

48. Meng, Z. P.; Zhang, S. F.; Wu, S. L. Power density dependent upconversion properties of NaYbF4: Er3+@NaYbF4: Tm3+@NaYF4 nanoparticles and their application in white-light emission LED. *Journal of Luminescence* **2020,** 227, DOI: Artn 117566
10.1016/J.Jlumin.2020.117566.

49. Chen, B.; Wang, F. Combating Concentration Quenching in Upconversion Nanoparticles. *Accounts Chem Res* **2020,** 53 (2), 358-367 DOI: 10.1021/acs.accounts.9b00453.

50. Shang, Y.; Zhou, J.; Cai, Y.; Wang, F.; Fernandez-Bravo, A.; Yang, C.; Jiang, L.; Jin, D. Low threshold lasing emissions from a single upconversion nanocrystal. *Nature Communications* **2020,** 11 (1), 6156 DOI: 10.1038/s41467-020-19797-4.

51. Hao, S. W.; Shao, W.; Qiu, H. L.; Shang, Y. F.; Fan, R. W.; Guo, X. Y.; Zhao, L. L.; Chen, G. Y.; Yang, C. H. Tuning the size and upconversion emission of NaYF4:Yb3+/Pr3+ nanoparticles through Yb3+ doping. *Rsc Adv* **2014,** 4 (99), 56302-56306 DOI: 10.1039/c4ra11357h.

52. Li, D.; Wen, S. H.; Kong, M. Y.; Liu, Y. T.; Hu, W.; Shi, B. Y.; Shi, X. Y.; Jin, D. Y. Highly Doped Upconversion Nanoparticles for In Vivo Applications Under Mild Excitation Power. *Anal Chem* **2020,** 92 (16), 10913-10919 DOI: 10.1021/acs.analchem.0c02143.

53. Zhang, H. X.; Chen, Z. H.; Liu, X.; Zhang, F. A mini-review on recent progress of new sensitizers for luminescence of lanthanide doped nanomaterials. *Nano Res* **2020,** 13 (7), 1795-1809 DOI: 10.1007/s12274-020-2661-8.

54. Ilchenko, V. S.; Maleki, L. Novel whispering-gallery resonators for lasers, modulators, and sensors. *Laser Resonators Iv* **2001,** 4270, 120-130 DOI: Doi 10.1117/12.424663.

55. Jiang, X. F.; Qavi, A. J.; Huang, S. H.; Yang, L. Whispering-Gallery Sensors. *Matter* **2020,** 3 (2), 371-392 DOI: 10.1016/j.matt.2020.07.008.

56. Zamora, V.; Herter, J.; Wunderlich, V.; Nyugen, T.; Schroder, H.; Schneider-Ramelow, M. Sensor platform based on packaged whispering-gallery-resonators. *Frontiers in Biological Detection: From Nanosensors to Systems Xii* **2020,** 11258, DOI: Artn 112580b
10.1117/12.2545923.

57. Toropov, N.; Cabello, G.; Serrano, M. P.; Gutha, R. R.; Rafti, M.; Vollmer, F. Review of biosensing with whispering-gallery mode lasers. *Light-Sci Appl* **2021,** 10 (1), DOI: Artn 42
10.1038/S41377-021-00471-3.

58. Liu, Y.; Yang, H. H.; Lu, Y. L.; Di, K.; Guo, J. Q. A whispering gallery mode strain sensor based on microtube resonator. *Optoelectron Lett* **2021,** 17 (4), 199-204 DOI: 10.1007/s11801-021-0069-7.

59. Zhao, X. Y.; Guo, Z. H.; Zhou, Y.; Guo, J. H.; Liu, Z. R.; Li, Y. X.; Luo, M.; Wu, X. Optical Whispering-Gallery-Mode Microbubble Sensors. *Micromachines-Basel* **2022,** 13 (4), DOI: Artn 592
10.3390/Mi13040592.

60. Ioppolo, T.; Manzo, M. Dome-shaped whispering gallery mode laser for remote wall temperature sensing. *Appl Optics* **2014,** 53 (22), 5065-5069 DOI: 10.1364/Ao.53.005065.

61. Liu, Q.; Chiang, K. S.; Reekie, L.; Chow, Y. T. CO2 laser induced refractive index changes in optical polymers. *Optics Express* **2012,** 20 (1), 576-582 DOI: 10.1364/Oe.20.000576.

62. Liu, Y. G.; Daum, P. H. Relationship of refractive index to mass density and self-consistency of mixing rules for multicomponent mixtures like ambient aerosols. *J Aerosol Sci* **2008,** 39 (11), 974-986 DOI: 10.1016/j.jaerosci.2008.06.006.

63. Larsen, E. S. Relation between the refractive index and the density of some crystallized silicates and their glasses. *Am J Sci* **1909,** 28 (165), 263-274.

64. Burnett, D. The relation between refractive index and density. *P Camb Philos Soc* **1927,** 23, 907-911.

65. Ritland, H. N. The Relation between Refractive Index and Density in Glass. *Phys Rev* **1954,** 94 (5), 1434-1434.

66. Diguet, R.; Bonnet, P.; Barriol, J. Relation between the Refractive-Index and Density of a Fluid with Cavity Model of Invariable Radius - Application to the Study of the Permittivity .1. Study of Non Polar Liquids. *J Chim Phys Pcb* **1979,** 76 (1), 15-20 DOI: DOI 10.1051/jcp/1979760015.

67. Chiu, L. D.; Su, L.; Reichelt, S.; Amos, W. B. Use of a white light supercontinuum laser for confocal interference-reflection microscopy. *J Microsc-Oxford* **2012,** 246 (2), 153-159 DOI: 10.1111/j.1365-2818.2012.03603.x.

68. Kozacki, T.; Chlipala, M. Color holographic display with white light LED source and single phase only SLM. *Optics Express* **2016,** 24 (3), 2189-2199 DOI: 10.1364/Oe.24.002189.

69. Wang, T.; Yu, H.; Siu, C. K.; Qiu, J.; Xu, X.; Yu, S. F. White-light whispering-gallery-mode lasing from lanthanide-doped upconversion NaYF4 hexagonal microrods. *ACS photonics* **2017,** 4 (6), 1539-1543.

70. Zhao, J. B.; Jin, D. Y.; Schartner, E. P.; Lu, Y. Q.; Liu, Y. J.; Zvyagin, A. V.; Zhang, L. X.; Dawes, J. M.; Xi, P.; Piper, J. A.; Goldys, E. M.; Monro, T. M. Single-nanocrystal sensitivity achieved by enhanced upconversion luminescence. *Nat Nanotechnol* **2013,** 8 (10), 729-734 DOI: 10.1038/nnano.2013.171.

71. Shen, J.; Chen, G.; Ohulchanskyy, T. Y.; Kesseli, S. J.; Buchholz, S.; Li, Z.; Prasad, P. N.; Han, G. Tunable near infrared to ultraviolet upconversion luminescence enhancement in (alpha-NaYF4 :Yb,Tm)/CaF2 core/shell nanoparticles for in situ real-time recorded biocompatible photoactivation. *Small* **2013,** 9 (19), 3213-7 DOI: 10.1002/smll.201300234.

72. Liu, Y. J.; Lu, Y. Q.; Yang, X. S.; Zheng, X. L.; Wen, S. H.; Wang, F.; Vidal, X.; Zhao, J. B.; Liu, D. M.; Zhou, Z. G.; Ma, C. S.; Zhou, J. J.; Piper, J. A.; Xi, P.; Jin, D. Y. Amplified stimulated emission in upconversion nanoparticles for super-resolution nanoscopy. *Nature* **2017,** 543 (7644), 229-233 DOI: 10.1038/nature21366.

73. Jin, L. M.; Wu, Y. K.; Wang, Y. J.; Liu, S.; Zhang, Y. Q.; Li, Z. Y.; Chen, X.; Zhang, W. F.; Xiao, S. M.; Song, Q. H. Mass-Manufactural Lanthanide-Based Ultraviolet B Microlasers. *Adv Mater* **2019,** 31 (7), DOI: Artn 1807079
10.1002/Adma.201807079.

74. Quintanilla, M.; Cantarelli, I. X.; Pedroni, M.; Speghini, A.; Vetrone, F. Intense ultraviolet upconversion in water dispersible SrF2: Tm3+, Yb3+ nanoparticles: the effect of the environment on light emissions. *J Mater Chem C* **2015,** 3 (13), 3108-3113 DOI: 10.1039/c4tc02791d.

75. Johnson, N. J. J.; Korinek, A.; Dong, C. H.; van Veggel, F. C. J. M. Self-Focusing by Ostwald Ripening: A Strategy for Layer-by-Layer Epitaxial Growth on Upconverting Nanocrystals. *J Am Chem Soc* **2012,** 134 (27), 11068-11071 DOI: 10.1021/ja302717u.

76. Li, X. M.; Shen, D. K.; Yang, J. P.; Yao, C.; Che, R. C.; Zhang, F.; Zhao, D. Y. Successive Layer-by-Layer Strategy for Multi-Shell Epitaxial Growth: Shell Thickness and Doping Position Dependence in Upconverting Optical Properties. *Chem Mater* **2013,** 25 (1), 106-112 DOI: 10.1021/cm3033498.

Chapter 6 Conclusion and perspective

6.1 Conclusion

In this thesis, efficient lanthanide doped upconversion gain media and coupling strategies for upconverting microlaser were investigated. Powerful strategy for excited state energy accumulation to achieve population inversion was explored. Novel methods to load upconversion gain media uniformly on the surface of microcavity were developed. Inspired by the quality of coated gain media layer, scattering effect caused by size of nanoparticle, and the balance between brightness and scattering effect were discussed. Single upconversion nanoparticle was verified to achieve lasing emission when coupled with a microcavity. Meanwhile, upconversion gain media with highly sensitizers doping were employed to lower the pumping threshold. And the temperature dependent mode shift promoted the potential application of in-situ temperature sensing and monitoring. Moreover, energy migration modulated upconversion nanoparticles with tri-phosphor emissions were firstly employed for white lasing emissions. In summary, key points to obtain low threshold lasing emission based on lanthanide doped upconversion nanoparticles were explored and potential applications of temperature monitoring and white lasing emissions were further demonstrated.

The key results and findings of this PhD thesis can be summarized as follows:

(1) The author has verified that the cross-relaxation (CR) process is a powerful strategy for excited state energy accumulation and thereby can achieve population inversion at low power density. And doping 20 mol. % Yb^{3+} and 2 mol. % Tm^{3+} has been identified as the appropriate concentration to produce moderate CR at relatively low power range.

(2) The author has developed a novel aqueous phase processed loading strategy driven by electrostatic force. Compared with traditional swelling-deswelling method, the electrostatic force assembly strategy exhibits multiple advantages, for example,

smooth surface of microcavity, uniform single layer of gain media without aggregation, and easy controllable, which all benefit the coupling of upconversion gain media.

(3) By employing a 5-μm WGM cavity and homogenous coating architecture, we have achieved lasing emissions with a threshold of ~150 W/cm^2, nearly two orders of magnitude lower than the recently reported[1] benchmark value of 14 kW/cm^2. This result suggests a great potential to use the doping concentration tunable UCNP as an efficient gain medium for room temperature CW microscale and nanoscale lasers.

(4) The author has demonstrated the increased size leads to stronger scattering, which hinder the coupling of emission at the surface and increase the leaking of light inside the microcavity. A broad linewidth (from ~0.5 nm to ~1.2 nm) and reduced Q factor (from ~1900 to ~700) were observed when increase the sizes of upconversion nanoparticles (from 24 nm to 51 nm).

(5) Single 43 nm $NaYF_4$:20% Yb^{3+},2% Tm^{3+} UCNPs with bright emission were demonstrated can lase at 808 nm with the sharp peaks and narrow FWHM of ~0.45 nm once in a cavity, which preserving the Q-factors of the cavity since scattering losses are reduced to the minimum.

(6) High sensitizers doped sandwich core-shell structured upconversion gain media with enhanced NIR harvesting ability were synthesized through a templet modulated layer-by-layer epitaxial growth strategy. With the increase of Yb^{3+} sensitizers doping concentration from 20% to 98%, the pumping threshold of lasing emission (@800 nm band) was lowered from ~2 kW/cm^2 to ~180 W/cm^2.

(7) The temperature dependent lasing emission peak shift (~ 0.1 nm/°C) at the range of 26°C to 70°C has been demonstrated, which shown great potential in long time tracking and in-situ temperature variation monitoring, especially in the biological applications.

(8) Benefited from the CR process of Tm^{3+} ions and four energy levels system of Tb^{3+} ions, full visible spectrum lasing was firstly achieved through using excited state

energy migration modulated $NaGdF_4$:40%Yb^{3+},2%Tm^{3+}@$NaGdF_4$:15%Tb^{3+} core shell nanoparticles as gain media.

6.2 Perspective

The miniaturization of lasers exhibits great potential for the applications in high density data storage, optical interconnects, nanoscale tracking and sensing, super-resolution imaging and so on[2-7]. The fast development of material science enabled novel micro- and nano-laser output with new optical properties[7, 8]. The outstanding frequency conversion properties of upconversion nanoparticles provide numerous opportunities for upconverting lasering, especially for the background free biological applications. Nowadays, the emission wavelength of upconverting microlaser has already expanded from deep UV to NIR region[9-13]. The CW pumped ultra-stable upconversion lasing emissions were achieved by the design of efficient gain media and novel microcavity with WGM and lattice plasmon modes, which promote potential long-time-tracking and sensing in biological applications[1, 11, 14].

Although great progresses have been developed in recent years, challenges are still remained. For instance, the reduced resonator sizes lead to increased optical losses, which requires greater pumping power to reach the lasing thresholds[10, 15-17]. And as we mentioned in this thesis, the scattering effect of upconversion nanoparticles can't be neglected. Thus, small but bright upconversion nanoparticles are demanded for low threshold lasing emission. Smart cavities with high Q factor, such as WGM, FP cavity and plasmon enhanced cavity, should be further developed for various applications[17, 18]. Deepening regulatory mechanism studies on highly efficient upconversion luminescence output and threshold reduction in microlaser need to be further revealed.

Apart from the strategies to keep lowering the pumping threshold, the unique properties of lanthanide doped upconversion nanoparticles would enable fantastic lasing emissions. Nd^{3+} ion with a larger absorption cross section at ~800 nm was often used to switch the excitation wavelength of upconverison nanoparticles[19-21]. Orthogonal emissions under various pumping wavelength were also achieved by constructing multi core shell structures with well-designed dopants[22-24]. Thus, it's possible to obtain excitation switchable lasing emissions by equipping with these upconversion gain media[25]. What's more, new sensitizers, such as Tm^{3+} and Er^{3+} ions with longer excitation wavelength (1064 nm, 1532 nm), were reported for efficient upconversion process[26-28]. Alternative excitation wavelengths with desired emissions are available for practical applications[29]. These all provide great promises in the emerging application for next-generation micro-/nanoscale photonics and optoelectronics.

6.3 References

1. Fernandez-Bravo, A.; Yao, K.; Barnard, E. S.; Borys, N. J.; Levy, E. S.; Tian, B.; Tajon, C. A.; Moretti, L.; Altoe, M. V.; Aloni, S.; Beketayev, K.; Scotognella, F.; Cohen, B. E.; Chan, E. M.; Schuck, P. J. Continuous-Wave Upconverting Nanoparticle Microlasers. *Nat. Nanotechnol.* **2018,** 13, 572.

2. Genet, C.; Ebbesen, T. W. Light in tiny holes. *Nature* **2007,** 445 (7123), 39-46 DOI: 10.1038/nature05350.

3. Schuller, J. A.; Barnard, E. S.; Cai, W.; Jun, Y. C.; White, J. S.; Brongersma, M. L. Plasmonics for extreme light concentration and manipulation. *Nat Mater* **2010,** 9 (3), 193.

4. Stockman, M. I. Nanoplasmonic sensing and detection. *Science* **2015,** 348 (6232), 287-288.

5. Kim, T. I.; McCall, J. G.; Jung, Y. H.; Huang, X.; Siuda, E. R.; Li, Y. H.; Song, J. Z.; Song, Y. M.; Pao, H. A.; Kim, R. H.; Lu, C. F.; Lee, S. D.; Song, I. S.; Shin, G.; Al-Hasani, R.; Kim, S.; Tan, M. P.; Huang, Y. G.; Omenetto, F. G.; Rogers, J. A.; Bruchas, M. R. Injectable, Cellular-Scale Optoelectronics with Applications for Wireless Optogenetics. *Science* **2013,** 340 (6129), 211-216 DOI: 10.1126/science.1232437.

6. Ma, R.-M.; Oulton, R. F. Applications of nanolasers. *Nat Nanotechnol* **2019,** 14 (1), 12-22.

7. Jeong, K.-Y.; Hwang, M.-S.; Kim, J.; Park, J.-S.; Lee, J. M.; Park, H.-G. Recent Progress in Nanolaser Technology. *Adv Mater* **2020,** 32 (51), 2001996 DOI: https://doi.org/10.1002/adma.202001996.

8. Azzam, S. I.; Kildishev, A. V.; Ma, R. M.; Ning, C. Z.; Oulton, R.; Shalaev, V. M.; Stockman, M. I.; Xu, J. L.; Zhang, X. Ten years of spasers and plasmonic nanolasers. *Light-Sci Appl* **2020,** 9 (1), DOI: ARTN 90
10.1038/s41377-020-0319-7.

9. Chen, Z.; Dong, G. P.; Barillaro, G.; Qiu, J. R.; Yang, Z. M. Emerging and perspectives in microlasers based on rare-earth ions activated micro-/nanomaterials.

Prog Mater Sci **2021,** 121, DOI: ARTN 100814
10.1016/j.pmatsci.2021.100814.

10. Chen, X.; Sun, T.; Wang, F. Lanthanide-Based Luminescent Materials for Waveguide and Lasing. *Chemistry – An Asian Journal* **2020,** 15 (1), 21-33 DOI: 10.1002/asia.201901447.

11. Liu, Y. W.; Teitelboim, A.; Fernandez-Bravo, A.; Yao, K. Y.; Altoe, M. V. P.; Aloni, S.; Zhang, C. H.; Cohen, B. E.; Schuck, P. J.; Chan, E. M. Controlled Assembly of Upconverting Nanoparticles for Low-Threshold Microlasers and Their Imaging in Scattering Media. *Acs Nano* **2020,** 14 (2), 1508-1519 DOI: 10.1021/acsnano.9b06102.

12. Shang, Y. F.; Zhou, J. J.; Cai, Y. J.; Wang, F.; Fernandez-Bravo, A.; Yang, C. H.; Jiang, L.; Jin, D. Y. Low threshold lasing emissions from a single upconversion nanocrystal. *Nature Communications* **2020,** 11 (1), DOI: Artn 6156
10.1038/S41467-020-19797-4.

13. Yang, X. F.; Lyu, Z. Y.; Dong, H.; Sun, L. D.; Yan, C. H. Lanthanide Upconverted Microlasing: Microlasing Spanning Full Visible Spectrum to Near-Infrared under Low Power, CW Pumping. *Small* **2021,** 17 (41), DOI: Artn 2103140
10.1002/Smll.202103140.

14. Fernandez-Bravo, A.; Wang, D.; Barnard, E. S.; Teitelboim, A.; Tajon, C.; Guan, J.; Schatz, G. C.; Cohen, B. E.; Chan, E. M.; Schuck, P. J. Ultralow-threshold, continuous-wave upconverting lasing from subwavelength plasmons. *Nat Mater* **2019,** 18 (11), 1172-1176.

15. Feng, Z. Q.; Bai, L. Advances of Optofluidic Microcavities for Microlasers and Biosensors. *Micromachines-Basel* **2018,** 9 (3), DOI: Artn 122
10.3390/Mi9030122.

16. Tang, S.-J.; Dannenberg, P. H.; Liapis, A. C.; Martino, N.; Zhuo, Y.; Xiao, Y.-F.; Yun, S.-H. Laser particles with omnidirectional emission for cell tracking. *Light: Science & Applications* **2021,** 10 (1), 23 DOI: 10.1038/s41377-021-00466-0.

17. Shang, Y.; Chen, T.; Ma, T.; Hao, S.; Lv, W.; Jia, D.; Yang, C. Advanced lanthanide doped upconversion nanomaterials for lasing emission. *Journal of Rare Earths* **2022,** 40 (5), 687-695 DOI: https://doi.org/10.1016/j.jre.2021.09.002.

18. Zhang, W.; Yao, J. N.; Zhao, Y. S. Organic Micro/Nanoscale Lasers. *Accounts Chem Res* **2016,** 49 (9), 1691-1700 DOI: 10.1021/acs.accounts.6b00209.

19. Dibaba, S. T.; Ge, X. Q.; Ren, W.; Sun, L. N. Recent progress of energy transfer and luminescence intensity boosting mechanism in Nd3+-sensitized upconversion nanoparticles. *Journal of Rare Earths* **2019,** 37 (8), 791-805 DOI: 10.1016/j.jre.2019.02.001.

20. Zhou, B.; Li, Q. Q.; Yan, L.; Zhang, Q. Y. Controlling upconversion through interfacial energy transfer (IET): Fundamentals and applications. *Journal of Rare Earths* **2020,** 38 (5), 474-482 DOI: 10.1016/j.jre.2020.01.009.

21. Su, Q. Q.; Wei, H. L.; Liu, Y. C.; Chen, C. H.; Guan, M.; Wang, S.; Su, Y.; Wang,

H. F.; Chen, Z. G.; Jin, D. Y. Six-photon upconverted excitation energy lock-in for ultraviolet-C enhancement. *Nature Communications* **2021,** 12 (1), DOI: Artn 4367 10.1038/S41467-021-24664-X.

22. Li, X. M.; Guo, Z. Z.; Zhao, T. C.; Lu, Y.; Zhou, L.; Zhao, D. Y.; Zhang, F. Filtration Shell Mediated Power Density Independent Orthogonal Excitations-Emissions Upconversion Luminescence. *Angew Chem Int Edit* **2016,** 55 (7), 2464-2469 DOI: 10.1002/anie.201510609.
23. Zhang, Z.; Zhang, Y. Orthogonal Emissive Upconversion Nanoparticles: Material Design and Applications. *Small* **2021,** 17 (11), DOI: Artn 2004552 10.1002/Smll.202004552.
24. Hong, A. R.; Kyhm, J. H.; Kang, G.; Jang, H. S. Orthogonal R/G/B Upconversion Luminescence-based Full-Color Tunable Upconversion Nanophosphors for Transparent Displays. *Nano Lett* **2021,** 21 (11), 4838-4844 DOI: 10.1021/acs.nanolett.1c01510.
25. Jin, L. M.; Chen, X.; Wu, Y. K.; Ai, X. Z.; Yang, X. L.; Xiao, S. M.; Song, Q. H. Dual-wavelength switchable single-mode lasing from a lanthanide-doped resonator. *Nature Communications* **2022,** 13 (1), DOI: Artn 1727 10.1038/S41467-022-29435-W.
26. Zhou, B.; Yan, L.; Huang, J. S.; Liu, X. L.; Tao, L. L.; Zhang, Q. Y. NIR II-responsive photon upconversion through energy migration in an ytterbium sublattice. *Nat Photonics* **2020,** 14 (12), 760-+ DOI: 10.1038/s41566-020-00714-6.
27. Liu, S. B.; Yan, L.; Huang, J. S.; Zhang, Q. Y.; Zhou, B. Controlling upconversion in emerging multilayer core-shell nanostructures: from fundamentals to frontier applications. *Chemical Society Reviews* **2022,** 51 (5), 1729-1765 DOI: 10.1039/d1cs00753j.
28. Levy, E. S.; Tajon, C. A.; Bischof, T. S.; Iafrati, J.; Fernandez-Bravo, A.; Garfield, D. J.; Chamanzar, M.; Maharbiz, M. M.; Sohal, V. S.; Schuck, P. J. Energy-looping nanoparticles: harnessing excited-state absorption for deep-tissue imaging. *Acs Nano* **2016,** 10 (9), 8423-8433.
29. Sun, T. Y.; Chen, B.; Guo, Y.; Zhu, Q.; Zhao, J. X.; Li, Y. H.; Chen, X.; Wu, Y. K.; Gao, Y. B.; Jin, L. M.; Chu, S. T.; Wang, F. Ultralarge anti-Stokes lasing through tandem upconversion. *Nature Communications* **2022,** 13 (1), DOI: Artn 1032 10.1038/S41467-022-28701-1.